Multi-level Analysis and Optimization for Resource-Efficient High Temperature Gas Phase Processes

Dissertation
zur Erlangung des akademischen Grades

Doktoringenieur
(Dr.-Ing.)

von M.Sc. Georg Liesche
geboren am 17. Februar 1989 in Göppingen

genehmigt durch die Fakultät für Verfahrens- und Systemtechnik der Otto-von-Guericke-Universität Magdeburg

Promotionskommission: Prof. Dr.-Ing. Eckehard Specht (Vorsitz)
Prof. Dr.-Ing. Kai Sundmacher (Gutachter)
Prof. Anthony Dixon, PhD (Gutachter)
Prof. Dr.-Ing. Viktor Scherer (Gutachter)

eingereicht am: 21. Juni 2019
Promotionskolloquium am: 06. Dezember 2019

Abstract

The targets of the Paris agreement for the mitigation of climate change require a drastic reduction of the per capita resource consumption in particular in the developed countries. New lifestyles, products and production processes are key measures in this context but the reduction of resource consumption cannot be achieved without a significant increase in resource productivity across all industrial sectors including the chemical industry. This increase in resource efficiency is achievable only through the analysis and optimization of each lengthscale: the screening of promising process units at a high hierarchical level and targeted measures for the improvement of the mass and energy efficiency at smaller lengthscales and lower hierarchical levels. At the same time, overall gains in efficiency through non-intuitive combinations of different process units are enabled at the plant level. It is evident, that systemic, multi-level approaches are required that take all these aspects into account in order to exploit the full process intensification potential.

This dissertation addresses this multi-level problem at the reactor and plant levels for the example of high temperature catalytic gas phase processes. These processes include endothermic reactions like the reforming of methane and synthesis of hydrogen cyanide as prominent examples that are key intermediate processes of the chemical supply chain. Production of HCN serves as a case study in this thesis motivated by a collaboration with Evonik Industries but the reactor analysis and design methods of this work have been equally applied to steam reforming of methane. At first, a general literature overview combined with the methodological foundations in chapter 2 is provided. Following the introduction of the application background in chapter 3 this thesis is structured into three parts: the first two chapters address the reactor level and the third chapter focuses on the plant level of the process hierarchy.

At the level of the single synthesis compartment in a bundle of multiple compartments in chapter 4, the underlying physical transport mechanisms for momentum and heat are analyzed in order to identify the reactor intensification potential. At this level the modeling of radiative heat transfer is emphasized. It is found that radiation accounts for approximately $20\,\%$ of total heat transferred to the reacting fluid for dimensions similar to the industrial reactor design. Furthermore, radiation becomes the dominant mode of heat transfer for

channel widths greater than 1×10^{-2} m. The heat transfer at this level can be enhanced through an increase in the surface emissivity of the catalytic wall material for example through integrating SiC in the ceramic material: with an increase in the surface emissivity from 0.45 to 0.90, an increase in the reactor outlet temperature by 30 K can be achieved in the HCN synthesis example. Vice versa, decreasing the width or diameter of the single synthesis compartment by $1 - 2$ mm results in an increase in product yield by $2 - 3 \%$. It is demonstrated that space time yield, yield and fuel efficiency are competing objectives at this scale which can hardly be prioritized without the overall process context at the plant level.

At the next higher level of the tube bundle in chapter 5 the furnace design is optimized emphasizing the arrangement of the individual tubes of the tube bundle. To achieve this target a reduced two-dimensional model of the furnace is selected over a high fidelity CFD modeling of the three-dimensional furnace. It is shown that convective heat transfer is negligible unless a tube is placed directly within the main flow regime. Two key design parameters are identified for the optimal tube bundle design: inter-tube view factors that represent the shadowing between tubes and the hot flue gas emissivity. View factors are a good indicator of the performance of a bundle arrangement but do not suffice due to the impact of the flue gas emissivities: increasing inter-tube distances is beneficial as long as the gas layer emissivities are sufficiently high. If the tube shadowing is decreased beyond a certain tipping point, the overall bundle performance declines. For the HCN case study, the optimal inter-tube distance is identified as 0.052 m which is a slight improvement in average product yield and in inter-tube standard deviation compared to the industrial benchmark scenario. Staggered bundle arrangements are more favorable for radiative heat transfer than aligned tube arrangements because they have lower total inter-tube view factors.

The emphasis at the plant level is to identify the overall most resource-efficient – in terms of mass and energy consumption – production process for the case study of HCN. State-of-the-art procedures for design of efficient chemical processes, however, are either limited in terms of problem size or have to solve the mass and energy integration consecutively which may lead to suboptimal process designs. For this reason the FluxMax approach which is a method for simultaneous process synthesis and heat integration was developed in collaboration with Dominik Schack and it is outlined in chapter 6. Through a discretization of the thermodynamic state space and a description of process units as stoichiometric reaction equations, a linear feasible region is created. The most resource efficient process for HCN production is then identified using multi-objective optimization through weighing of linear objective functions for atom efficiency, waste minimization, heating and total duty as well as variable cost minimization. Non-intuitive process alternatives such as the negligibility of column design for the HCN case study are identified with the FluxMax approach and it is shown that atom efficiency can be improved by 39.5 % through recycling of the byproduct H_2 to synthesize the reactant NH_3. Furthermore, variable cost are reduced by 67.6 %.

Nonetheless, it is demonstrated that no unique optimum exists – both optimal process designs result in higher overall duty requirements. Instead, careful weighing of the objectives for specific site conditions is required.

The results of the individual levels show that a multi-level approach is essential in order to increase the resource efficiency of the chemical industry. The methods that are demonstrated in this dissertation have been successfully transferred to reactor design in methane steam reforming. The FluxMax approach is particularly versatile because it is level-independent and not limited to high temperature processes. As such it has been applied to process unit and plant design for methanol production. This thesis shows that high temperature processes of the chemical industry can contribute to an increase in resource productivity but the global targets can only be achieved as a combined effort of all industries, individuals and societies as a whole.

Zusammenfassung

Das Erreichen der Ziele des Pariser Klimaschutzabkommens – die Erderwärmung auf zwei Grad zu begrenzen – erfordert eine starke Reduktion des Resourcenverbrauchs der Industrienationen. Dafür sind ein umweltbewusstes Verhalten jedes Einzelnen und nachhaltigere Produktionsprozesse gleichermaßen wichtig. Die Reduktion der Treibhausgasemissionen in der Produktion sind beispielsweise durch den Umstieg auf Strom aus erneuerbaren Quellen und die Verwendung nachwachsender Rohstoffe möglich. Nichtsdestotrotz ist für die geforderte Minderung des Rohstoffverbrauchs auch eine kurzfristige Steigerung der Resourceneffizienz in allen Industriesektoren erforderlich. Für die chemische Industrie werden in diesem Zusammenhang Lösungsansätze auf jeder hierarchischen Betrachtungsebene – vom effizienten Kompressor bis hin zum Auslegen ressourcensparender Prozessnetzwerke – immer wichtiger. Systemische Ansätze sind hier von Vorteil, da sie Effekte auf verschiedenen Längenskalen im Zusammenspiel betrachten und so die insgesamt größte Steigerung der Resourceneffizienz ermöglichen.

In dieser Dissertation wird diese systemische Perspektive durch Betrachtung einzelner Ebenen innerhalb einer Prozesseinheit und durch eine ganzheitliche Betrachtung des Gesamtprozesses am Beispiel von katalytischen Hochtemperaturprozessen dargestellt. Wichtige Vertreter dieser Prozessgattung sind die Dampfreformierung von Methan sowie die Synthese von Cyanwasserstoff nach dem BMA – Blausäure aus Methan und Ammoniak – Verfahren, die beide Schlüsselprozesse innerhalb der organischen Chemie darstellen, da sie der Gewinnung wichtiger chemischer Intermediate dienen. Die Modellhierarchien und Lösungsansätze dieser Dissertation werden am Beispiel der Synthese von Cyanwasserstoff HCN gezeigt, da der Prozess mit mehr als einer Million Jahrestonnen Produktion eine große industrielle Relevanz hat. Darüber hinaus sind hier größere Effizienzsteigerungen zu erwarten, da die Reaktorkonzepte aus der Mitte des 20. Jahrhunderts stammen und dieser Prozess seither kaum beforscht wurde. Die Methoden für Reaktordesign, die im Kontext dieser Arbeit entwickelt wurden, wurden zusätzlich zum HCN Beispiel auch auf die Dampfreformierung von Methan angewandt. Nach einer methodischen Einordnung in Kapitel 2 und der Diskussion der Anwendungsbeispiele in Kapitel 3 ist diese Dissertation in drei Hauptkapitel gegliedert: zwei Kapitel je eines für eine Betrachtungsebene im Reaktor und ein Kapitel für den Gesamtprozess.

Auf der untersten betrachteten Ebene einer einzelnen Prozesseinheit, die zusammengenommen ein Rohrbündel bilden, werden die zugrundeliegenden physikalischen Transportmechanismen für die Geschwindigkeits- und Temperaturverteilung analysiert. Hierbei liegt der Schwerpunkt auf Wärmetransportmechanismen und insbesondere auf der Modellierung von Wärmestrahlung. Wärmestrahlung ist für etwa 20 % des gesamten Wärmetransports in das Gasgemisch bei industriellen Reaktorabmessungen verantwortlich. Strahlung dominiert darüber hinaus den Wärmetransport ab Breiten eines Einzelkompartments von 1×10^{-2} m. Für die Steigerung des Wärmetransports, dem limitierenden Faktor für Hochtemperatur-reaktoren, bestehen zwei Möglichkeiten: durch eine Erhöhung der Oberflächenemissivität des keramischen Trägermaterials von $\epsilon_{(\mathrm{w})} = 0.45$ auf $\epsilon_{(\mathrm{w})} = 0.90$ beispielsweise durch einen Siliziumcarbid-Anteil im Material kann die Reaktoraustrittstemperatur um 30 K gesteigert werden. Alternativ kann man die Breite bzw. den Durchmesser eines Einzelkompartments um wenige Millimeter reduzieren, um die Produktausbeute um zwei bis drei Prozentpunkte zu erhöhen. Es wird darüber hinaus gezeigt, dass sich Ausbeute, Raumzeitausbeute sowie Energieeffizienz bei der Größenordnung eines Einzelrohres gegenüber stehen, was eine Abwägung auf der Gesamtprozessebene erforderlich macht.

Die Kopplung mehrerer Einzelrohre in einem Rohrbündel und die damit verbundene Frage nach der effizientesten Anordnung der Einzelrohre wird in Kapitel 5 untersucht. Anstelle einer detaillierten, dreidimensionalen numerischen Strömungssimulation wird das Brennkammer-Rohrbündel-System auf die wesentlichen Transportmecha-nismen und ein zweidimensionales Modell reduziert, da dadurch die Optimierung der Bündelanordnung ermöglicht wird. Strahlung dominiert den Wärmetransport in der Brennkammer unter der Bedingung, dass kein Rohr direkt im Brenngasstrom positioniert wird. Zwei Parameter sind entscheidend für einen effizienzen Wärmetransport zu den einzelnen Rohren im Bündel: Die Sichtfaktoren der Rohre untereinander und die damit verbundenen Abschattungseffekte sowie die Emissivität des Heizgases, die sowohl vom Partialdruck der strahlenden Komponenten CO_2 und H_2O als auch von der Schichtdicke der strahlenden Gasschicht abhängt. Versetzte Rohranordnungen sind für die Brennkammer geringfügig von Vorteil gegenüber einer fluchtenden Rohranordnung, da hier die Abschattung minimiert wird. Für das Beispiel der Cyanwasserstoffsynthese und eine industrielle Brennkammerabmaße von 0.2 m auf 0.3 m ist der optimale Rohrabstand 0.052 m, was einer Steigerung der Produktausbeute um 0.5 % und eine Reduktion der Standardabweichung zwischen den einzelnen Rohren um 0.2 % entspricht.

Der Schwerpunkt auf der Gesamtprozessebene in Kapitel 6 liegt auf der Identifikation des insgesamt resourceneffizientesten Produktionsprozesses für Cyanwasserstoff unter Einbeziehung von sowohl Massen- als auch Energieströmen. Gegenwärtig sind Methoden zum Prozessentwurf entweder limitiert in Bezug auf die maximal kombinierbaren Prozesseinheiten oder sie verfolgen einen sequenziellen Lösungsansatz, bei dem nicht immer die global optimale Lösung identifiziert werden kann. Bei sequenziellen Methoden werden im Unterschied zu

simultanen Lösungsansätzen zunächst individuelle Prozesseinheiten optimiert und dann die Wärmeintegration auf Gesamtprozessebene abgeschätzt. Beispielhaft hierfür ist das Design der Rektifikationskolonne. Es ist für die Prozessgüte bei der HCN-Produktion irrelevant, da heiße und kalte Ströme für die Wärmeintegration in hohem Maße zur Verfügung stehen. Um einen simultanen Lösungsansatz zu entwickeln, bei dem die Größe der betrachteteten Problemstellung nicht limitiert ist, wurde in Kollaboration mit Dominik Schack die FluxMax-Methode entwickelt: durch eine Diskretisierung des thermodynamischen Zustandsraums und das Beschreiben jedweder stofflichen oder energetischen Umwandlung in diesem Zustandsraum über stöchiometrische Reaktionsgleichungen wird ein linearer Lösungsraum aufgespannt. Der effizienteste Prozess für die Cyanwasserstoffproduktion wird dann durch multi-kriterielle Optimierung identifiziert. Dafür werden die Zielgrößen Atomeffizienz, Abfallströme, Heiz- sowie Gesamtwärmeleistungsbedarf und gesamte variable Kosten gewichtet. Die Atomeffizienz der HCN-Produktion kann mit dieser Methode um 39.5 % durch stoffliches Recycling des Nebenprodukts H_2 gesteigert werden. Darüber hinaus können variable Kosten insgesamt um 67.6 % reduziert werden. Es wird aber auch gezeigt, dass kein eindeutiges Optimum existiert – beide optimalen Prozessentwürfe erfordern eine höhere Kühlleistung als der Grundprozess. Stattdessen ist die Gewichtung der Zielgrößen auch auf der Gesamtprozessebene erforderlich.

Die Ergebnisse auf den einzelnen Größenskalen verdeutlichen die Relevanz eines mehrskaligen Lösungsansatzes, um die Effizienz der chemischen Industrie zu erhöhen. Die Methoden, die in diesem Zusammenhang entwickelt wurden, konnten bereits teilweise auf die Dampfreformierung angewandt werden. Insbesondere die FluxMax-Methode ist weder auf Hochtemperatur- noch auf die Gesamtprozessebene beschränkt und wurde sowohl auf den Entwurf einer einzelnen Prozesseinheit als auch auf den Gesamtprozess der Methanolsynthese angewandt. Diese Dissertation zeigt insgesamt, wie Hochtemperaturprozesse zur Steigerung der Resourcenproduktivität beitragen können. Die globalen Ziele für einen nachhaltigen Resourcenkonsum stellen jedoch eine gesamtgesellschaftliche Herausforderung dar, die nur gesamtgesellschaftlich und international zu lösen ist.

Preface

Several publications were prepared in the context of this dissertation and four of them are partly included in this manuscript. The chapters that are partly based on these publications are listed here and their connection to the individual journal articles is highlighted.

- High temperature processes that motivate this thesis and are used as case studies are introduced in **Chapter 3**. The comparison of the BMA and Andrussow reactors for HCN synthesis was partly taken from Liesche and Sundmacher [1].

- The analysis of the single synthesis compartment in **Chapter 4** is partly based on Liesche and Sundmacher [1] where momentum and heat transport phenomena in a single synthesis compartment were investigated. The model derivation, simulation parameters and boundary conditions, however, are different in this thesis. The second part of this chapter is inspired by the reactor design analysis for methane steam reforming microchannel reactors in Liesche and Sundmacher [2] and contains its application for the HCN synthesis case study.

- The optimization of the tube bundle arrangement in **Chapter 5** is based to a large extent on Liesche and Sundmacher [4]: the method description and results for the tube diameter of $\delta = 0.018\,\mathrm{m}$ originate from the journal article. The introduction, simulation parameters, the analysis of the prevalence of radiative heat transfer and the comparison of different tube diameters at the end of the results section, however, are different in this thesis context. In addition, studies with respect to the optimal furnace geometry are provided in the appendix in Sec. C.2.

- **Chapter 6** is largely based on Liesche et al. [3]: the FluxMax method description as well as the application to the HCN case study are taken from the journal article whereas the introduction and interpretation of the results have been adapted to the thesis context.

[1] **Liesche, G.**, Sundmacher, K. (2018). Identification of Key Transport Phenomena in High-Temperature Reactors: Flow and Heat Transfer Characteristics, *Industrial & Engineering Chemistry Research*, **57**, 15884-15897.

[2] **Liesche, G.**, Sundmacher, K. (2018). Productivity versus Product Quality: Exploring the Limits of Autothermal Microchannel Reactors in Methane Steam Reforming, *Chemical Engineering Journal*, DOI: 10.1016/j.cej.2018.09.209.

[3] **Liesche, G.**, Schack, D., Sundmacher, K. (2019). The FluxMax Approach for Simultaneous Process Synthesis and Heat Integration: Production of Hydrogen Cyanide, *AIChE Journal*, **65**, 7, e16554.

[4] **Liesche, G.**, Sundmacher, K. (2019). Radiation-Based Model Reduction for the Optimziation of High Temperature Tube Bundle Reactors: Synthesis of Hydrogen Cyanide, *Computers & Chemical Engineering*, accepted article.

Contents

Nomenclature

Latin Symbols

$\mathbf{A}$	coefficient matrix in chapter 6	
A_i	surface area of tube i	m^2
A_s	catalyst surface area	m^2
A$_j$	absorber process node j	
$\mathbf{b}$	solution vector	
Bo	convection-to-radiation ratio, dimensionless Boltzmann number	-
D_{ij}	distance between two tube centers i and j	m
D$_j$	temperature state changer process node j	
E$_j$	elementary process node j	
e	entrainer-to-feed ratio	-
f	objective function in chapter 6	
f_{ij}	function describing the angle of visibility between tubes i and j	
$\Delta_R g$	molar Gibbs energy of reaction	kJ mol^{-1}
$\Delta_{\mathrm{M}} g$	molar Gibbs energy of mixing	kJ mol$^-$1
g	gravitational acceleration	m s^{-2}
G$_j$	generic process node j	
Gr	Grashoff number	-
$\Delta_R h^{\ominus}$	molar reaction enthalpy at standard conditions	kJ mol^{-1}
I_η	radiative intensity at wavenumber η	W m^{-2}
$I_{\mathrm{b}\eta}$	blackbody radiative intensity at wavenumber η	W m^{-2}
$j_{y,\alpha}$	diffusion flux in y direction of component α	kg m^{-2} s^{-1}
L	channel reactor length	m

L_j	mixing process node j	
$\tilde{M}$	molar mass of the gas mixture	$\mathrm{kg\,mol^{-1}}$
$\tilde{M}_\alpha$	molar mass of component α	$\mathrm{kg\,mol^{-1}}$
M_i	thermodynamic substance node i	
$\dot{N}_{(\mathrm{E}_j)}^{(\mathrm{M}_i)}$	molar flux linking TSN M_i with EPN E_j	$\mathrm{mol\,s^{-1}}$
n	refractive index	-
N/C	nitrogen to carbon ratio in HCN synthesis	-
N_A	Avogadro constant	$6.022 \times 10^{23}\ \mathrm{mol^{-1}}$
N_c	number of components in a gas mixture	-
N_r	number of chemical reactions	-
N_t	number of tubes in bundle	-
N_w	number of walls of a furnace	-
$n_{\mathrm{atom},i}$	number of atoms of TSN i	$\mathrm{mol^{-1}}$
N_k	number of discretized solid angles	
N_y	number of discretization elements in transverse direction y	
N	conduction-to-radiation ratio, dimensionless Planck number	-
p	pressure	Pa
p_α	partial pressure of component α	Pa
$p_{\dot{W},\mathrm{ext,in}}$	cost of work duty	$\mathrm{EUR\,kJ^{-1}}$
$\mathrm{pK_a}$	negative logarithm of the acid dissociation constant	-
Pr	Prandtl number	-
$\dot{Q}_{(\mathrm{E}_j)}^{(\mathrm{U}_l)}$	heat flux from UN U_l towards EPN E_j	kW
$\dot{Q}_i^{(cv)}$	convective heat flow towards tube i	kW
R	radiative resistance	$\mathrm{m^{-2}}$
r	reaction rate	$\mathrm{mol\,m^{-3}\,s^{-1}}$
R_i	radius of tube i	m
Re	Reynolds number	-
Δs	thickness of gas layer	m
$\hat{\mathbf{s}}$	vector of direction of radiative intensity	
S_k	work utility node k	
S/C	steam to carbon ratio in MSR	-
S_α	selectivity toward component α	-

STY	space time yield	$\mathrm{mol\,m^{-3}\,s^{-1}}$
Sc	Schmidt number	-
$\bar{T}_{(\mathrm{w})}$	mean tube wall surface temperature of the tube bundle	K
T	temperature	K
t	wall thickness of a synthesis compartment	m
U_l	utility node l	
V	volume	$\mathrm{m^3}$
v	velocity	$\mathrm{m\,s^{-1}}$
$\dot{W}_{(\mathrm{E}_j)}^{(\mathrm{ext})}$	external work flux to process node E_j	kW
W	channel reactor width	m
w_α	mass fraction of component α	-
$\mathbf{x}$	vector of decision variables in chapter 6	
x_α	molar fraction of component α	% / -
x_i, y_i	tube center position in x and y coordinates in chapter 5	m
$X_{\mathrm{NH_3}}$	conversion of $\mathrm{NH_3}$ as defined in Eq. (4.35a)	-
$\bar{Y}$	mean tube yield of a tube bundle	-
Y_{HCN}	yield of HCN	-
$Z(T)$	partition sum at temperature T	-

Greek Symbols

α	pure component index	
$\alpha_{\mathrm{g},i}^{(cv)}$	convective heat transfer coefficient	$\mathrm{W\,m^{-2}K^{-1}}$
β_η	spectral extinction coefficient	$\mathrm{bar\,m^{-1}}$
$\dot{\Gamma}$	variable of the process extent number	mol/s
δ	surface area equivalent tube diameter	m
δ_{iw}	minimum tube-wall distance	m
ϵ	emissivity	-
ζ	general thermodynamic coordinate in chapter 6	a.u.
η	wavenumber in chapter 4	$\mathrm{cm^{-1}}$
$\eta_{(\mathrm{E}_j)}^{\mathrm{in}}$	efficiency factor of work consuming EPN E_j in chapter 6	-
$\eta_{(\mathrm{E}_j)}$	separation efficiency of E_j in chapter 6	-
$\bar{\theta}_{ij}$	upper bound of view angle of tube i toward tube j	-

θ	polar angle for radiative direction	-
θ_C	surface coverage with carbon containing species	-
$\underline{\theta}_{ij}$	lower bound of view angle of tube i toward tube j	-
κ_η	spectral absorption coefficient	$\mathrm{bar\,m^{-1}}$
$\nu_{\alpha,i}$	stoichiometric coefficient of component α in reaction i	-
$\dot{\xi}$	extent of reaction	$\mathrm{mol/s}$
ξ_1, ξ_2, ξ_3	parameters of the tanh function for view factor calculation	-
ρ	density	$\mathrm{kg\,m^{-3}}$
σ	Stefan-Boltzmann constant	$\mathrm{W\,m^{-2}\,K^{-4}}$
σ_α	source term of component α	$\mathrm{kg\,m^{-3}\,s^{-1}}$
$\sigma_{s\eta}$	spectral scattering coefficient	$\mathrm{bar\,m^{-1}}$
τ	space time defined as $\tau := V_{(s)}/F_{(s)}(z=0)$	s
$\hat{\varphi}$	total inter-tube view factor in a tube bundle	-
Φ_η	spectral scattering phase function	-
φ	molar heat duty of a EPN in chapter 6	$\mathrm{kJ\,mol^{-1}}$
φ	view factor in chapter 5	-
χ_i	integrated term i of the energy balance	$\mathrm{W\,m^{-1}}$
$\chi_{(E_j)}^{(M_i)}$	stoichiometric coefficient of M_i in E_j	-
ψ	azimuthal angle for radiative direction	-
Ω	solid angle for radiative intensity	-
ω	molar work duty of a EPN in chapter 6	$\mathrm{kJ\,mol^{-1}}$
ω	normalized grid spacing $\omega := N_{\max}/N_i$ in chapter 4	-
Ω_k	discretized solid angle $k \in [1, 2, ..., N_k]$	-

Indices

(c)	conductive heat transfer
(cv)	convective heat transfer
(dif)	differential
eq	equality constraints
ext	external: in- and outward directed
ext,in	external inward directed
iq	inequality constraints

(f)	furnace compartments of the reactor
g, ij	of hot flue gas between tube j and tube i toward tube i
g, iw	of hot flue gas between wall w and tube i toward tube i
g, j	related to hot flue gas and tube j
g, w	related to hot flue gas and wall
ij	between tube i and j
(int)	integral
in	inner
$\ominus$	at standard conditions: $T^{\ominus} = 298$ K and $p^{\ominus} = 1013$ hPa
out	outer
(r)	radiative heat transfer
(s)	synthesis compartment of the reactor
sim	based on simulations
(w)	wall between synthesis and furnace compartments

Other Symbols

$\mathcal{E}$	set of all elementary process nodes
$\mathcal{F}$	set of all molar, heat and work flux edges of the digraph
$\mathcal{M}$	set of all thermodynamic substance nodes
$\mathcal{N}_c$	set of all components
$\mathcal{N}_t$	set of all tubes of the tube bundle
$\mathcal{N}_w$	set of all walls of the furnace
$\mathbb{R}$	set of all real numbers
$\mathcal{S}$	set of all work utility nodes
$\mathcal{U}$	set of all utility nodes

Acronyms

AE	algebraic equation
BLF	boundary layer flow
BMA	"Blausäure aus Methan und Ammoniak", Ger.: hydrogen cyanide from methane and ammonia
CB	component balance (component continuity equation)
CFD	computational fluid dynamics

DAE	differential algebraic equation
ENRTL-RK	electrolyte non-random-two-liquid model combined with the Redlich-Kwong equation of state
EPF	elementary process function
EPN	elementary process node
FMA	FluxMax approach
FVM	finite volume method
HCN	hydrogen cyanide
HITEMP	high-temperature molecular spectroscopic database
HITRAN	high-resolution transmission molecular absorption database
IDEAS	infinitely dimensional state space framework
LCA	life cycle analysis
LP	linear programming
MILP	mixed integer linear programming
MINLP	mixed integer nonlinear programming
MPI	Max Planck Institute for Dynamics of Complex Technical Systems in Magdeburg
MSR	methane steam reforming
NIST	National Institute of Standards and Technology
NLP	nonlinear programming
ODE	ordinary differential equation
OvGU	Otto-von-Guericke University in Magdeburg
PDE	partial differential equation
PEN	process extent number
PSE	process systems engineering
RDS	rate determining step
RTE	radiative transfer equation
TSN	thermodynamic substance node
UN	utility node
WHEN	work and heat exchanger networks
WUN	work utility node

Chapter 1

Introduction

1.1 Global Challenge

Planet earth provides natural boundaries of resource availability except for energy which is supplied continuously by the sun. Resources in this context include all matter ranging from freshwater to minerals, trees and feedstock. Historically, the annual resource consumption of humankind has been below the planet's capabilities of regeneration until the 20th century. Within that century, however, technological progress in all fields led to high standards of living and an exponential increase in world population. These high standards of living that an increasing number of people enjoys today, however, is responsible for a dramatic increase in the annual resource consumption beyond our planet's regeneration capabilities. One illustrative example for this development is the carbon cycle illustrated using the global earth overshoot day. The global earth overshoot day marks the date of each year when annual regeneration equals global resource consumption. Whereas this date was at the end of December in the 1970s – corresponding to a balanced consumption-regeneration – it is currently at the end of July meaning that humankind currently consumes 1.7 earths instead of one [1]. Apart from the carbon cycle, closing material cycles is equally relevant for non-renewable resources such as metals [2, 3]. It is evident that the increasing resource consumption is not sustainable – neither from an ecological nor from a societal point of view. In addition, the depletion of natural resources is strongly related to other dimensions of sustainability that need to be addressed such as the loss of biodiversity, the climate change and the acidification of oceans [4–6].

To return to a sustainable level of resource consumption while maintaining good standards of living for humankind is one of the current global challenges. It is our duty to find solutions toward this goal that refrain from going back to the 1970s in terms of technologies and

world population. According to the factor-10-institute, providing equal opportunities for all humankind requires a reduction of resource consumption of the developed countries by a factor of 10 [7]. This decrease in resource consumption affects all areas of life: individual lifestyles, businesses and societies as a whole. While every single one of us can contribute to this objective through increased awareness about and change of our own resource consumption, key leverage remains in politics: clever policies have to be designed that integrate resource efficiency targets into our economic system, i.e. making it economically desirable to act resource-efficient. Policies are crucial because they provide the framework for both individual people's lives and the market economy that businesses operate in. Examples for incentives for the reduction of energy and material resources include subsidies (e.g. for the construction of efficient buildings) and penalties (e.g. for greenhouse gas emissions or resource consumption). They aim at an increase the productivity of an industry since the product output level is maintained while resource utilization is reduced. This reduces the ecological footprint of a production process and its cost thus making the process economically more competitive.

The chemical industry is an intermediary between the business-to-consumer industries and the consumer as they provide materials and material solutions for their business customers. Therefore, the sustainability goals affect the chemical industry twofold: on the one hand, intelligent chemical products are required that reduce final customer's resource utilization for example through lightweight and recyclable materials for the mobility sector. On the other hand, resource consumption of the chemical industry itself has to be reduced through a productivity increase. On the mid to longterm, this includes alternative production processes and feedstock. On the short term, however, growth in productivity has to be achieved via an increase in the efficiency of existing plants and equipment. The German society for chemical- and biotechnology (DECHEMA) estimates that despite a reduction of $59\,\%$ in 2014 compared to greenhouse gas emissions of 1990, up to $20-30$ megatonnes of annual carbon dioxide emissions can still be reduced by energy efficiency measures in the European chemical industry alone [8]. This corresponds to an emission of total CO_2 emissions of the chemical industry of $17-25\,\%$. In order to achieve this target a systemic perspective toward chemical processes is required that links mechanistic understanding at small lengthscales with macro-scale decision making perspective.

Chemical processes that are both highly relevant for the chemical value chain and have high energy consumptions are reforming processes, in particular methane steam reforming (MSR) and a less-known relative – the synthesis of hydrogen cyanide in the BMA route from methane and ammonia (HCN). Their high energy demands originate from their high operating temperatures in order to shift the equilibria of the endothermic chemical synthesis reactions that account for $206\,\mathrm{kJ\,mol^{-1}}$ (MSR) and $251\,\mathrm{kJ\,mol^{-1}}$ (HCN) toward the product side. While MSR is a globally abundant process for synthesis gas and hydrogen production, HCN is a chemical intermediate for various target products: it is required for the production

of poly(methyl methacrylate), the production of polyisocyanates which are precursors for polyurethanes as well as for the production of the amino acid methionine. Both HCN and reforming products are important chemical processes today and are expected to remain essential pillars of the value chain in the near future: reforming of methane is under current market conditions the most economical pathway toward hydrogen [8].

While the chemical industry – let alone reforming processes – cannot achieve the factor-10 goal by themselves, they do constitute significant contributors to resource consumption of the chemical industry due to their relevance and high energy consumption. Thus, resource-efficient reforming processes are a key requirement in order to achieve a sustainable production. Despite plentiful research in the field for MSR, a systemic perspective on the reactor and process design is promising because improvements in the range of fractions of percent in resource efficiency have a potentially large impact on the footprint of these processes at a global scale. With respect to HCN production, recent literature is practically non-existent which raises suspicions that efficiency gains are possible in these processes because industrial processes rely on historical reactor developments. In addition, with a production capacity of HCN of more than a million annual tons in 1998 that has been growing since due to new products such as methionine, HCN constitutes a highly relevant chemical intermediate. Therefore, the production of HCN is an ideal case study for the systemic study of these processes. Relevant literature for the more prominent case of MSR is reviewed where necessary and parts of the methods of this thesis have been successfully demonstrated for the example of MSR as well.

1.2   Contribution of This Thesis

Embedded in this global context, it is the objective of this dissertation to perform a multi-level analysis and optimization of high temperature catalytic gas phase processes from a systemic perspective exemplified for the case study of HCN synthesis. Tools for the systematic investigation of these types of processes and beyond are developed that address the following questions:

(I)   What are the dominating heat transfer mechanisms in high temperature reactors?

(II)   How dependent are the heat transfer phenomena on the various lengthscales in the reactor for example at the single compartment and at the bundle level?

(III) How can performance and resource efficiencies of high temperature reactors be improved based on these transport mechanistic insights?

(IV)   What is a suitable method for the design of resource-efficient chemical processes?

(V)   What implications does this design method have on the high temperature process case studies?

It is evident that the aspects (I), (II) and (III) need to be addressed at the reactor levels whereas the last two aspects (IV) and (V) concern the overall process. High temperature processes are challenging to investigate experimentally due to their harsh reaction conditions. While it is feasible to investigate reaction kinetics experimentally, the analysis of pilot-plant reactors or even industrial-scale reactors is limited to modeling studies in academia. Pure in-silico models, however, often suffer from insufficient experimental validation as a benchmark for the model. For this reason, experimental validation of the reactor models with literature data was used wherever possible. In addition, the aspects (I), (II) and (III) regarding reactor design and optimization were accompanied by a dialogue with Evonik Industries as an industrial partner. In the context of this work, a collaboration project regarding reactor design was launched and completed successfully. In order to identify answers to the research questions (I) to (V), this thesis is structured into six chapters as illustrated in Fig. 1.1.

Chapter 2 lays the theoretical foundation of this dissertation with a review of all relevant literature for multiscale and multi-level modeling approaches. In the context of this chapter, the title of this thesis is defined using previous contributions in literature and characteristic solution methods to multi-level and multiscale problems are discussed.

Chapter 3 discusses the applications to high temperature processes. HCN synthesis is characterized with respect to relevance, process contexts and reactor designs and compared with MSR. A thermodynamic analysis of the chemical reactions is presented and the reaction kinetics for the case of HCN that are available in literature are discussed. The hierarchical levels that are discussed in this thesis are justified based on these reaction kinetics.

As shown at the center and bottom of Fig. 1.1, the reactor scale is split into two subdomains: the single synthesis compartment and the design of the tube bundle. The single synthesis compartment is analyzed in Chapter 4 with an emphasis on both momentum and heat transport in order to address the aspects (I) and (III). The relevance of all three modes of heat transfer is discussed and intensification aspects are derived. It is shown that enhancing the energy efficiency comes at the expense of reducing raw material efficiency and vice versa requiring decision making at superordinate levels.

The entire reactor that consists of a bundle of individual synthesis compartments or tubes is discussed in chapter 5. Correlations of wall heat flux versus wall boundary temperature of chapter 4 are applied to link the single compartment and the tube bundle in order to avoid having to solve the synthesis compartment simultaneously. As for the synthesis compartment, mechanistic aspects (I) and their scale dependency (II) are discussed first emphasizing the

Chapter 6: Optimal Plant Design for the Production of HCN

Chapter 5: Optimal Design of the Tube Bundle in the Furnace

Chapter 4: Characteristics of the Single Synthesis Compartment

H_2

HCN

Pt on Al_2O_3

CO_2

H_2O

CH_4

NH_3

N_2

Chapter 3: High Temperature Gas Phase Processes

HCN Synthesis $\quad\quad\quad CH_4 + NH_3 \rightleftharpoons HCN + 3H_2$

Methane Steam Reforming $\quad CH_4 + H_2O \rightleftharpoons CO + 3H_2$

Chapter 2: Multi-level Analysis, Optimization, Resource Efficiency

process hierarchy

characteristic lengthscale

km

m

cm

mm

high

low

Fig. 1.1 Dissertation in a nutshell highlighting the chapter structure.

analysis of heat transfer mechanisms on the furnace side. Simulation-based optimization is utilized to identify the most optimal bundle arrangement inside the furnace (III).

Chapter 6 presents the FluxMax approach (FMA) for process synthesis that was created in a collaborative project with Dominik Schack where process synthesis and heat integration are solved simultaneously. With this methodology, the research questions (IV) and (V) are addressed. Upon the introduction of the method, the strengths of the method are illustrated for the case study of HCN synthesis. Using the case study of HCN production, it is demonstrated that simultaneous heat integration is substantial for design of efficient processes and that the FMA can design a priori non-intuitive process which are superior in overall material and energy efficiencies.

Chapter 7 summarizes the findings and interprets the results from a systemic perspective and concludes the thesis.

Chapter 2

Multi-level Modeling, Analysis, Optimization and Resource Efficiency

It is the primary purpose of models to understand an aspect of the real world in order to make a prediction or informed decision. Models are thus not the reality but instead have the purpose to be applicable as George Box framed it in his famous statement: "All models are wrong, but some are useful" [9].

2.1 Multi-level Modeling

In the past, simulations were bound to narrow time- and lengthscale intervals due to the limitations in computational power and algorithms for example a chemical reactor model based on ordinary differential equations (ODE) could not take elementary atomistic chemical reactions at shorter time- and lengthscales into account. The increase in computational power of the recent past, however, has enabled the solution of problems with larger time and length intervals and has led to improvements in the predictive power of models. This bridging of formerly separate scales is referred to as multi-level and multi-scale modeling.

At this point a distinction is required: multi-level modeling is hierarchy-oriented and refers to scenarios where a holistic, systemic perspective is essential for example the inclusion of higher hierarchical levels for decision making. This is represented by a pyramid denoting the process hierarchy from low to high in Fig. 2.1 (right). On the other hand, multi-scale is more oriented toward the coupled solution of problems and refers explicitly to the bridging of different time- and lengthscales illustrated with characteristic lengthscales from small to large in Fig. 2.1

(left). Multi-scale modeling could thus be interpreted as a part of multi-level modeling – different time- and lengthscales compose hierarchical levels by themselves – but it is evident, that both terms can hardly be separated rigorously. Instead, typically a combination of scales and hierarchical levels exist which is the reason why both terms are often used synonymously across the scientific community.

In resource supply planning of cities, lengthscales range from single house blocks to districts and eventually the entire city whereas timescales vary from days to years [10–12]. Examples from the field of mechanical and material engineering include atomistic aspects and their impact on device performance such as the design of hard-drives or nano-structured surfaces [13, 14]. Systems biology and also biotechnology are another prominent example where multiple length- and timescales are significant: starting from gene expression at an atomistic scale to proteins, cellular organelles, cells and eventually tissues, organs and up to the scales of entire organisms in systems biology or bioreactors in biotechnology [15–18]. All these examples demonstrate that multi-level and multi-scale modeling is a widely used concept within the scientific community.

2.1.1 Multi-level Modeling in Process Systems Engineering

Levels and scales of interest that are of interest for the process systems engineering (PSE) community are illustrated in Fig. 2.1: starting with elementary reaction steps at the molecular level via coupled reaction-diffusion systems at the particle level up to phases that constitute process units, plants and eventually entire production systems. In addition to the synonymous use of levels and scales, undisputed designations for the individual levels do not exist. For example the meso-scale refers to reactor units in contributions by Grossmann et al. whereas it addresses transport processes at the particle scale for reaction engineers [19, 20]. The level and scale perspective may coarsely related to the academic background of researchers in the field: while reaction engineers emphasize the scale aspect, the hierarchical level perspective is frequently used by researchers in systems and control theory [17, 21–24]. As the title of the thesis implies, the level perspective is selected in this thesis.

Beside these different perspectives, the PSE community agrees that multi-level modeling and optimization are among the key challenges in chemical engineering in the future [26–28]. The following three sections highlight recent work in multi-level and multi-scale modeling. The contributions are structured into three groups using the illustration in Fig. 2.1: (i) reaction engineering from the molecular up to the phase and process unit level, (ii) the interface between PSE and economics at the plant and production system levels and beyond and (iii) the process unit – plant interface which is expanded further in the context of this thesis.
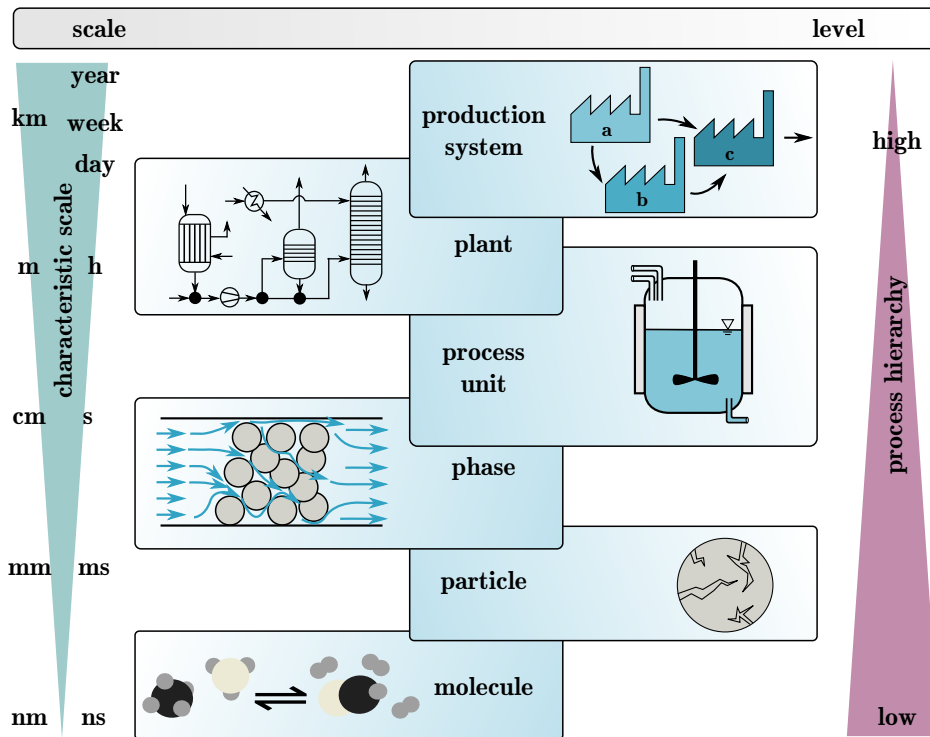
Fig. 2.1 Multi-scale with characteristic length- and timescales (left) and multi-level with hierarchy pyramid (right) perspectives on classical PSE research questions in the center: from molecules to particles, phases, process units, plants up to production systems [19, 25].

(i) Molecular to Process Unit Levels

Several reviews emphasize the relevance of multi-scale modeling for reaction engineering from the molecular up to the phase and process unit level in Fig. 2.1: from calculation of bond energies at the molecular level up to continuum simulations in the reactor at the process unit level in order to link mechanistic insights into chemical reactions at a catalyst surface to internal and external transport phenomena quantitatively [29–32, 17, 20]. The terms micro-, meso- and macroscale are clearly defined within this community referring to molecular interactions with catalyst atoms using intrinsic kinetics, pore transport and lattice interactions that are described by diffusion models and eventually macroscopic flow behavior which is modeled with continuum mechanics. These hierarchical levels are at the origin of multi-scale modeling in reaction engineering and they serve well to illustrate the development from single- to multi-scale simulation approaches: formerly, kinetic and transport limitations such as the rate determining step identification within a reaction network where extracted first and then utilized in the reactor model. Nowadays these aspects can be partly addressed simultaneously [20]. The main reason why scales are emphasized over levels in reaction engineering is that the calculation horizons of time- and length-scales are strongly different ranging from fractions of meters and seconds for molecular simulations up to hours and

meters in reactor simulations. The principle obstacle in bridging these scales is therefore a smart connection of different levels of details.

In heterogeneous catalysis for example, ab-initio and semi-empirical calculations of rate parameters of elementary reaction steps using density functional theory and transition state theory are decoupled from simulations of the entire reactor. They are calculated a priori and then fed into solvers specifically designed to include surface reaction mechanisms into computational fluid dynamics (CFD) calculations [33–35]. In addition to surface chemical reactions, kinetic Monte Carlo simulations are used to include information of surface structure of catalyst and carrier into the model [36, 37]. Besides heterogeneous catalysis, particle information through coupling of population balances with continuum simulations is significant in crystallization and bioreactors: impact of macroscopic parameters such as flow rate and temperature are thus related to microscopic parameters such as the size distribution of crystals and cells [38–40].

Alongside the strategies above and despite the increase in computational capabilities, intelligent coupling of models at different time- and length-scales remain essential to enable the combined solution of both [35]. Examples include the assumption of the most abundant reaction intermediate in the analysis of reaction rates and sensitivity analyses for microkinetic reaction mechanisms [41–43].

(ii) Plant to Production System Levels

PSE is linked to economics at the plant and production system levels that correspond to the maximum length- and timescales in Fig. 2.1. Research questions like cost-efficient plant design, scheduling of batch processes and the optimal supply chain for an entire enterprise or country arise at these levels [44, 27, 45]. Here, the hierarchical structure referred to by process levels is emphasized over the difference in time- and lengthscales. Examples at this plant and production system levels include life cycle analyses (LCA) and the identification of optimal processes from a thermo-economic perspective using thermodynamic efficiencies and economics-based targets [46, 47]. Solutions at this level can be identified using optimization techniques where the structure of a process or supply chain is represented by integer variables and flows with continuous variables leading to mixed integer linear (MILP) or nonlinear (MINLP) programming problem formulations [48, 49]. Besides, parameter uncertainties such as fluctuating electricity prices are accounted for using robust optimization [50, 51].

(iii) Process Unit − Plant Interface

The third cluster of research bridges process unit and plant levels. Based on the schematic representations of a process unit and a plant in Fig. 2.1, the plant level refers to a connection of process units. Several multi-level modeling approaches exists in this area and the modeling approaches are introduced from a loose to more close level coupling.

Utilization of results from separate lower order models is done in the modeling study of a fuel cell stack ranging from single channels to single cells up to an integrated fuel cell system [52–54]. In a separate approach, modeling platforms for separate hierarchical levels are linked with software interfaces in order to obtain a coupled multi-level model [55–57]. Iterative approaches solve optimization problems with increasing complexity in a sequential way: Kravanja and Grossmann [58] introduce a three-step approach starting from the single reactor up to the entire process using MINLP whereas Pouransari et al. [59] structure their step-wise approach based on hierarchies integrating the heat fluxes in subsystems first and a subsequent overall heat integration. The last group of contributions contains multi-level models where different time- and length-scales are connected in a single model. This is achieved either via the reduction of the modeling complexity at the unit scale – for example through simplified reactor models instead of CFD-based computations – or with a model reduction prior to the multi-level simulation – for example through the use of surrogate models. The latter is demonstrated with CFD simulations that are reduced to a data-driven model that is in turn included in a plant-wide optimization [60–62]. The group of Maréchal emphasizes economic and efficiency consideration over detailed fluid dynamics considerations in their thermo-economic optimization examples [47, 63]. Similar emphasis on the systems perspective is placed in LCA [64]. Examples for process design without CFD simulations include contributions where the focus is set on reactor design and where the impacts of the design parameters are investigated using simplified downstream processing such as distillation and absorption columns [65–67].

2.1.2   Multi-level Modeling in This Thesis

Multi-level modeling in this thesis addresses the three levels for high temperature gas phase reactors that are illustrated in Fig. 2.2. The single compartment reactor level and the tube bundle reactor level relate to the process unit level and to a lesser extent phase level of Fig. 2.1 because the overall reactor for high temperature catalytic gas phase reactions is composed of a furnace with individual tubes. At the plant level, different reactor types and configurations are considered in the reactor-separator-recycle context.
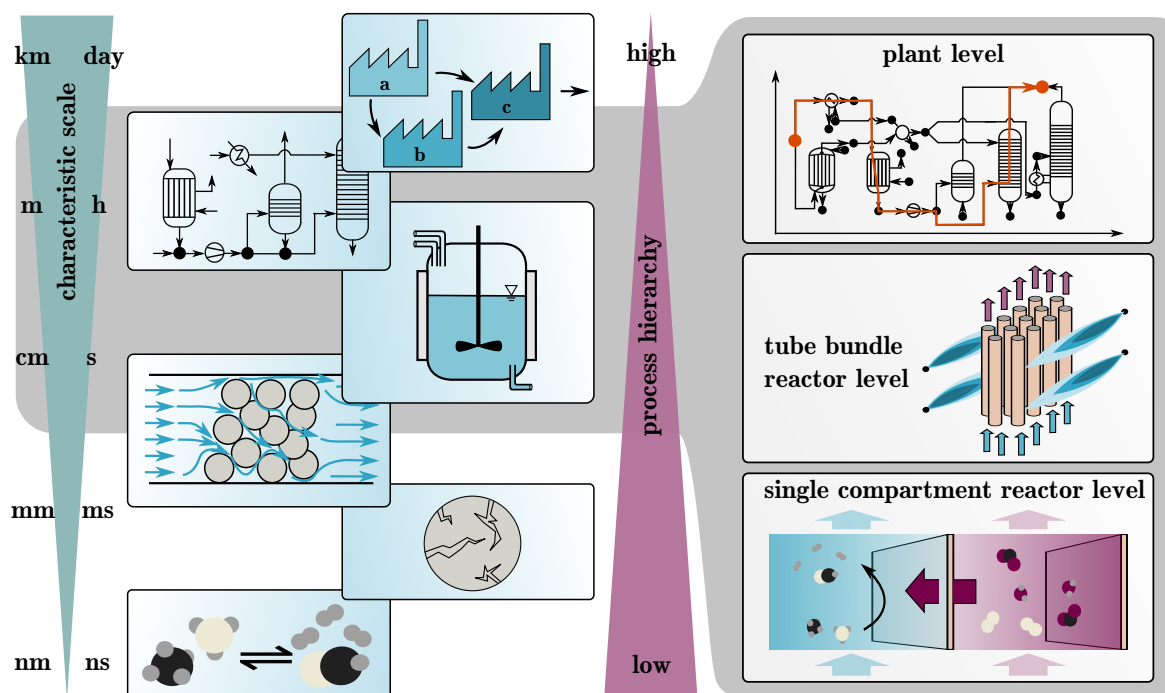
Fig. 2.2 Multi-level modeling in this thesis: single compartment reactor level, tube bundle reactor level and plant level.

Literature on multi-level and multi-scale modeling for high temperature reactors emphasizes the most prominent example of fixed bed reactors for steam reforming applications: the chemical synthesis reaction occurs at active sites of catalyst pellets that provide the surface area inside a tube bundle reactor. As such, previous contributions focused on the connection of continuum mechanics with meso- and micro-scale transport and reaction phenomena as shown by a number of publications from MSR and chemical looping processes with the latest publications also including dynamic models [36, 37, 68–71, 21]. At the plant level, studies include the integration of a reforming process into a larger plant network where for example Onel et al. [62] used simulation results from their reformer CFD simulation in the design of the overall plant [66, 54, 72].

The three hierarchical levels in this thesis are in between the levels of these examples. Motivated by the case study of HCN synthesis and to a lesser extent MSR emphasis is set on the transport phenomena in the reactor and their impact on the tube bundle and on the entire process performance which is quantified using resource efficiency objectives. Single compartment reactor simulations are utilized to generate characteristic heat duty profiles that are used at the two higher levels: for the optimization of the tube bundle and of the plant designs. As such, the modeling hierarchies and their connection is emphasized instead of the simultaneous solution of a model across all three hierarchical levels.

2.2 Multi-level Analysis and Optimization

A multitude of solution strategies exist in order to solve the multi-level and multi-scale problems that were introduced above. The hierarchical level perspective illustrated in Fig. 2.3 provides an orientation in this regard: the analysis typically requires the consideration of effects at lower hierarchical levels – i.e. more details – that can then be used for the design and optimization at superordinate hierarchical levels. Despite the strong increase in computational power over the last decades, macroscopic phenomena can hardly be calculated via increasing the calculation time and domain dimensions due to the sheer amount of computations that such a strategy would involve. All solution methodologies thus involve strategies that enable the computational handling of the multi-level complexity.
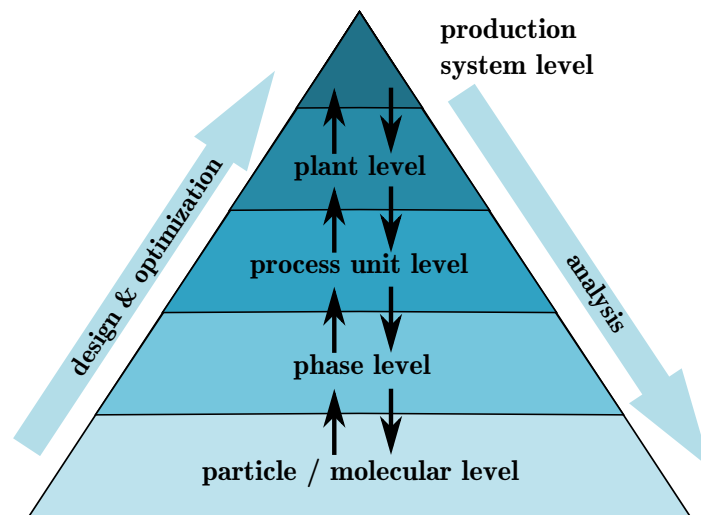
Fig. 2.3 Process analysis requires information from low hierarchical levels that is used for process design and optimization at high levels within the process hierarchy.

2.2.1 Solution Strategies

Solution strategies for multi-level problems can be generally grouped into one-way and two-way methodologies [17]. In one-way approaches, a sequential approach is utilized where tasks at one length-scale are completed first and the results are subsequently utilized for calculations at different levels. Besides, two-way strategies include feedback mechanisms between both lengthscales investigating mutual interactions of the levels that are involved [15].

Two-way Solution Methods

The versatility of two-way approaches ranges from integrating levels into a single model via parallel computations on several models to iterative approaches where results are passed back and forth between levels [15]. Examples for two-way methods spanning from atomistic up to continuum simulations include for example equation free models where macroscopic models are replaced by a grid-wise evaluation of microscopic levels and iterative approaches [32, 73–75]. Key questions include the understanding of the interplay of levels in order to identify potential improvements at the continuum scale for example for the design of a process unit. The analysis aspect is thus emphasized over the optimization aspect. At the plant and production system levels, key questions include the optimal process design and optimization of supply chain networks [27]. In contrast to lower levels, optimization techniques and comparative methods such as LCA are applied to address these questions. Either the process unit models that interact with the plant level are simplified or high-fidelity CFD simulations are utilized. Reduced process unit models enable the use of deterministic optimization tools whereas optimization of processes that involve CFD computations rely typically on stochastic or simulation-based optimization methods. In addition, hybrid and mixed strategies exist in order to combine stochastic and deterministic optimization approaches [76, 77, 47, 78].

One-way Solution Methods

In one-way solution methods results are passed from one hierarchical level to another without simultaneous feedback in order to avoid complexity. While two-way models are required for example to link fluid flow and meso-scalic transport behavior, one-way methods are suitable for example to derive reaction kinetics for continuum simulations [17]. Historic examples of are the rate determining step (RDS) and quasi-equilibrium assumptions in order to identify reaction kinetics that can be used for reaction kinetic expressions at larger scales to predict reactor behavior while reducing the complexity at the microscale [79]. A separate example includes molecular design via the screening of promising molecule candidates to reduce the multi-scale complexity [80–82]. Hybrid solution methods are equally used such as the sensitivity analysis-based reduction of a model for intrinsic reaction kinetics that maintains the information about active catalytic sites for a diffusion model [43].

2.2.2   Model Relaxation

The reduction of the modeling complexity plays a key role in enabling the simultaneous consideration of different levels. This can be achieved first and foremost by designing a model based on know-how of the system of interest employing the right level of complexity. This

is attainable either by setting up simplified model or by relaxation of an existing model for example through introduction of additional modeling assumptions. Besides, model order reduction techniques are relevant for fast computations for example in data analysis or optimal control and surrogate models are increasingly used as computationally inexpensive yet predictive replacement models for microscopic phenomena [83–87]. Surrogate models require training data that could originate from experiments, plants or simulations. Strictly speaking, discretization techniques such as the reduction of partial differential equations (PDE) to ordinary, differential (DAE) and eventually algebraic (AE) equations also relax the modeling complexity [17].

2.2.3 Optimization

The previous sections have shown that design optimization problems arise at plant and production system levels. A general, static MINLP problem is provided in Eq. (2.1) where the decision variables $\mathbf{x}$ and $\mathbf{y}$ denote vectors of continuous and of binary integer variables and the objective function f as well as the constraint functions h and g are nonlinear.

$$
\begin{aligned}
\min_{\mathbf{x}, \mathbf{y}} \quad & J = f(\mathbf{x}, \mathbf{y}) \\
\text{s.t.} \quad & h(\mathbf{x}, \mathbf{y}) = 0 \\
& g(\mathbf{x}, \mathbf{y}) \leq 0 \\
& \mathbf{x} \in \mathbb{R}, \mathbf{y} \in \{0, 1\} \quad .
\end{aligned}
\tag{2.1}
$$

If no integer decision variables exist, a purely continuous nonlinear (nonlinear programming – NLP) or linear (linear programming – LP) optimization problem is obtained.

Biegler and Floudas provide overviews over the types of optimization problems and their applicability to different multiscale problems in the PSE community [27, 88]. Plant design for production of chemicals is frequently solved using NLP or MINLP approaches in literature and will remain a key area of future research [47, 28, 19]. Solution approaches to the plant design optimization problem are reconsidered in the literature context of chapter 6.

2.2.4 Multi-level Analysis and Optimization Throughout This Work

In this thesis, a combination of these methods is utilized. The analytic aspect is emphasized at the lowest hierarchical level of a single synthesis compartment and to a lesser extent at the tube bundle level. Here, optimization is utilized to identify the optimal arrangement of tubes. At the superordinate plant level, optimization is utilized for resource-efficient process design. In order to account for the fluid-dynamical complexity of the reaction compartments

at the synthesis compartment level without utilizing simplified reactor models, a one-way solution strategy is pursued in this work: at the single compartment reactor level (chapter 4), information on the heat duty requirements is generated which is then utilized at both superordinate levels: for the tube bundle (chapter 5) and plant design (chapter 6). At all levels, the model complexity is relaxed: In chapter 4, physics-based flow assumptions and the finite volume method (FVM) in combination with the method of lines are used to formulate a boundary layer model and in order to solve a system of PDEs. In chapter 5, physical assumptions as well as the model analysis lead to the reduction of a three-dimensional PDE system to AEs that are accessible to optimization techniques. Lastly, in chapter 6, a method for design of resource-efficient plants is proposed where the overall process synthesis problem is formulated as a LP instead of a MINLP.

2.3   Resource Efficiency

According to the American Heritage dictionary, "efficient" means to cause "less waste or" requires "less effort than comparable devices or methods" [89]. In the PSE community, the term is often used as a synonym for energy efficiency but it is not limited to energy [90]. The term can be equally applied to other resources such as raw materials, economical cost and sustainability metrics as utilized in LCA such as global warming potential and CO_2 equivalents. In this dissertation, the technological aspects of resource efficiency – material and energy efficiency – are emphasized over economical parameters and it is utilized particularly for the tube bundle optimization in chapter 5 and at the plant level in chapter 6.

At the single compartment and tube bundle reactor levels, raw material efficiency is considered from the perspective of chemistry and chemical engineering: conversion, selectivity, yield as well as space time yield. These terms are complemented with energy efficiency through relating yields to the energy input at the single reactor compartment reactor level. At the plant scale, resource efficiency is analyzed as the efficient use of energy, materials and financial resources: work, heating and cooling duties for the energy efficiency, raw material usage and waste generation for the material efficiency and lastly variable cost efficiency.

Chapter 3

High Temperature Gas Phase Processes

As outlined in chapter 1, the methods that are developed in this thesis are illustrated with the case study of HCN synthesis. Besides, design aspects at the single synthesis compartment level have been successfully investigated for microchannel reactors for MSR and the tube bundle design has been extended to MSR in collaboration with Sebastian Engel of the Otto-von-Guericke University (OvGU) [91, 92]. Therefore, the introduction of high temperature catalytic processes in this chapter focuses on HCN synthesis and is supplemented with a discussion of the analogies between HCN synthesis and MSR.

3.1   Synthesis of HCN

Hydrogen cyanide, HCN, is a colorless liquid at standard conditions ($p = 1013$ hPa, $T = 298$ K). The substance is a weak acid with a pK_a of 9.21. Major hazards include its low boiling point at 299 K, its high toxicity and high reactivity in the presence of moisture or bases [93]. Consequently, cooling, monitoring and ventilation of production facilities as well as the addition of stabilizing agents – typically acids such as sulfuric acid – are required. Furthermore, transportation is restricted and as such it must often be produced on-site and it is not a tradable good. HCN can be synthesized from a large variety of feedstock containing C, N and H atoms given that the required energy for the synthesis reaction is provided [93].

3.1.1   Reactor Technologies

Synthesis pathways toward HCN that are of economic relevance include typically reactions of alkanes with ammonia in the presence or absence of oxygen. Other processes such as the formamide dehydration are competitive due to the specific production site conditions. The five main production processes toward HCN include [94]:

- **Shawinigan Process**: In the Shawinigan process, HCN is synthesized from short alkanes (C1-C5) and NH_3 [95–97]:

$$C_xH_{2x+2} + xNH_3 \longrightarrow xHCN + (2x+1)H_2$$
$$\Delta_R h^\ominus = 210 - 251 \, \mathrm{kJ \, mol_{HCN}^{-1}} \quad . \tag{3.1}$$
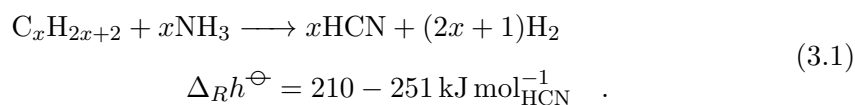
  The reactants enter a fluidized bed of coke particles which is heated electrically using electrodes. The reaction takes place at around $1800 \, \mathrm{K}$ and no catalyst is required. Based on the electric heating, the Shawinigan process is applied only at sites with a scarce availability of CH_4 and inexpensive electricity.

- **Formamide Process**: The formamide process describes the dehydration of formamide to yield HCN and H_2O at around $700 \, \mathrm{K}$ and in a mild vacuum:

$$HCONH_2 \longrightarrow HCN + H_2O \qquad \Delta_R h^\ominus = 75 \, \mathrm{kJ \, mol_{HCN}^{-1}} \quad . \tag{3.2}$$

  Its comparatively mild reaction conditions and high partial pressure of the product HCN are advantageous and this process is applied at sites where formamide is available. The formamide route was developed and applied at the Ludwigshafen site of BASF [98, 99].

- **Sohio Process**: Acrylonitrile is synthesized via the exothermic ammoxidation of propylene with air and NH_3 and yields HCN as a byproduct with $0.15 \, \mathrm{kg_{HCN}/kg_{acrylonitrile}}$. It is estimated that this byproduct stream accounts for 20% of the total production of HCN in Western Europe and the USA [93, 100, 94].

- **Andrussow Process**: In this millisecond reactor that was invented in the 1930's, CH_4, NH_3 and O_2 react on a Pt gauze according to the net reaction equation [101–103]:

$$CH_4 + NH_3 + \frac{3}{2}O_2 \longrightarrow HCN + 3\,H_2O$$
$$\Delta_R h^\ominus = -627 \, \mathrm{kJ \, mol_{HCN}^{-1}} \quad . \tag{3.3}$$
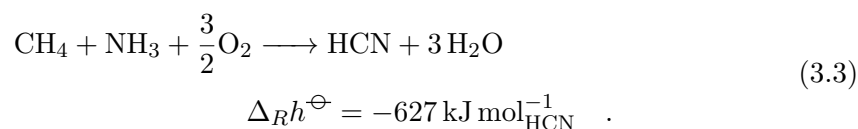
  The presence of O_2 leads to multiple byproducts and reaction times need to be short in order to prevent total oxidation of the reactants CH_4 and NH_3. The strong exothermicity

of the reaction is thus accompanied by a low partial pressure of the product HCN in the reactor outlet stream that requires a comparably expensive separation.

- **BMA Process**: The reactants of the BMA ("Blausäure aus Methan und Ammoniak", Ger.: hydrogen cyanide from methane and ammonia)) reactor are equally CH_4 and NH_3 but the energy of formation of HCN is supplied via combustion in an adjacent compartment leading to limited byproduct formation [104–107]

$$CH_4 + NH_3 \longrightarrow HCN + 3\,H_2$$
$$\Delta_R h^{\ominus} = 251\,\mathrm{kJ\,mol_{HCN}^{-1}} \quad . \tag{3.4}$$
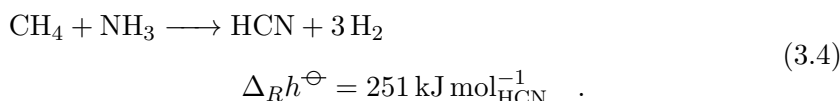
As a consequence, the product partial pressures in the reactor outlet stream are high making the product separation inexpensive.

Apart from these main HCN synthesis reactors, additional reactor concepts with less economic importance exist for example monolith reactors as well as electric arc variants of the BMA reactor [108, 109]. In addition, reactor concepts using alternative raw materials from the ones described above ranging from CO to alcohols have been patented [110, 111]. In the 1990s, DuPont developed a reactor that is heated with microwaves for small-scale applications [112]. Exploiting the analogy to acetylene synthesis according to the Sachse-Bartholome partial oxidation process, Herbertz et al. [113] investigated HCN synthesis in a flame reaction [114].

Among the HCN production routes above, the Andrussow and the BMA reactor are compared further since they do not necessarily require specific site conditions in a Verbund like the formamide, Sohio and Shawinigan routes. While the Andrussow reactor is the most widely used reactor for the synthesis of HCN, the BMA reactor was developed by Evonik Industries and is used in the context of methionine production [93]. These reactors are thus analyzed in more detail in the following section.

3.1.2 Thermodynamic Analysis for BMA and Andrussow Reactors

The two major competing reactor technologies for HCN synthesis are illustrated schematically in Fig. 3.1. In the BMA reactor, the synthesis reaction occurs at the tube wall surfaces which are impregnated with a Pt catalyst (Fig. 3.1 A) while the heat of reaction is supplied through the tube wall. Catalyst materials have been screened systematically in the past and Pt was identified as stable and effective at the high temperatures of reaction. The two principle reactions in the BMA reactor – synthesis of HCN and decomposition of NH_3 into its elements – are formulated as equilibrium reactions as:

$$CH_4 + NH_3 \rightleftharpoons HCN + 3\,H_2 \qquad \Delta_R h^{\ominus} = 251\,\mathrm{kJ\,mol^{-1}} \tag{3.5a}$$
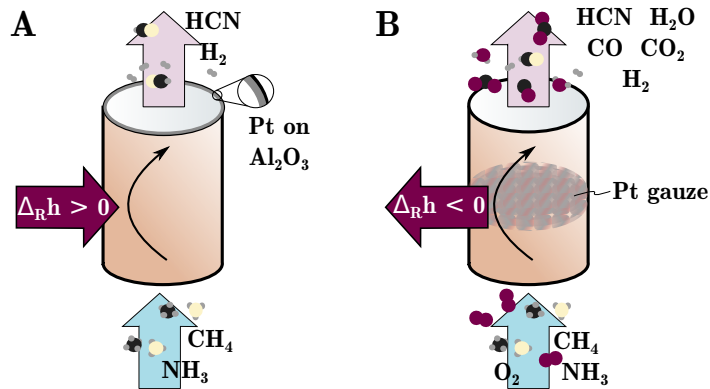
Fig. 3.1 BMA (A) and Andrussow (B) reactors for synthesis of HCN. Endothermic BMA reactors produce a higher purity product than Andrussow reactors that are exothermic instead.

$$\text{NH}_3 \rightleftharpoons 0.5\,\text{N}_2 + 1.5\,\text{H}_2 \quad \Delta_R h^{\ominus} = 45\,\text{kJ}\,\text{mol}^{-1} \quad . \tag{3.5b}$$
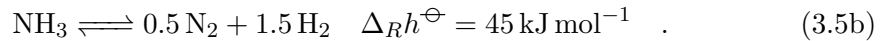
The identification of superior catalysts than the Pt catalyst is challenging because it must fulfill four criteria: the optimal catalyst should catalyze the synthesis reaction, inhibit coke formation and should not catalyze the decomposition of NH_3 to N_2 and H_2 while being stable at the harsh reaction conditions [115]. Reaction temperatures are around 1500 K and the reactor is operated at ambient pressure or slight vacuum as a safety measure in case of HCN leakage [94].

In the Andrussow reactor (Fig. 3.1 B), the chemical reactions of the gas mixture occur on a Pt gauze with 10 % Rh at around 1300-1400 K. The contact times of the reacting gas flow with the catalyst are maintained in the millisecond range due to the extremely fast reaction toward HCN. Due to the availability of O_2 a variety of oxidation reactions occur as shown in the appendix in Sec. A.2. In both the BMA and Andrussow reactors, the hot reactor gas effluents are quenched rapidly at the reactor outlet to prevent further reactions of the product such as dimerization and hydrolysis. In theory, a stoichiometric feed composition according to the reaction equation (Eq. (3.3)) is optimal to maximize the yield of HCN. In practice, however, O_2 is added sub-stoichiometrically to prevent oxidation of the reactants CH_4 and NH_3. For this reason and due to oxidation reactions of the reactants, the outlet gas stream of the Andrussow reactor contains H_2. In addition to that, experiments indicate that small nitrogen to carbon (N/C) ratios favor high yields of HCN but at the same time cause low product outlet gas concentrations [94].

Industrial outlet gas concentrations of both reactor types are compared in Tab. 3.1 [94]. Product molar fractions of the BMA reactor are approximately three times higher than of the Andrussow reactor due to the large spectrum of byproducts of the Andrussow reactor. H_2 accounts for 71.8 % in the BMA outlet and 12.0 % in the Andrussow reactor outlet stream.

Tab. 3.1 Typical outlet molar fractions of the BMA and Andrussow reactors [94].

reactor	component molar fraction x_α / %							
	HCN	NH$_3$	CH$_4$	N$_2$	H$_2$	H$_2$O	CO	CO$_2$
BMA	22.9	2.5	1.7	1.1	71.8	-	-	-
Andrussow	7.0	1.7	0.2	52.5	12.0	23.0	3.3	0.3

Beside the production of HCN, recycling of H$_2$ may be of interest in the plant context. This aspect is considered in detail in chapter 6.
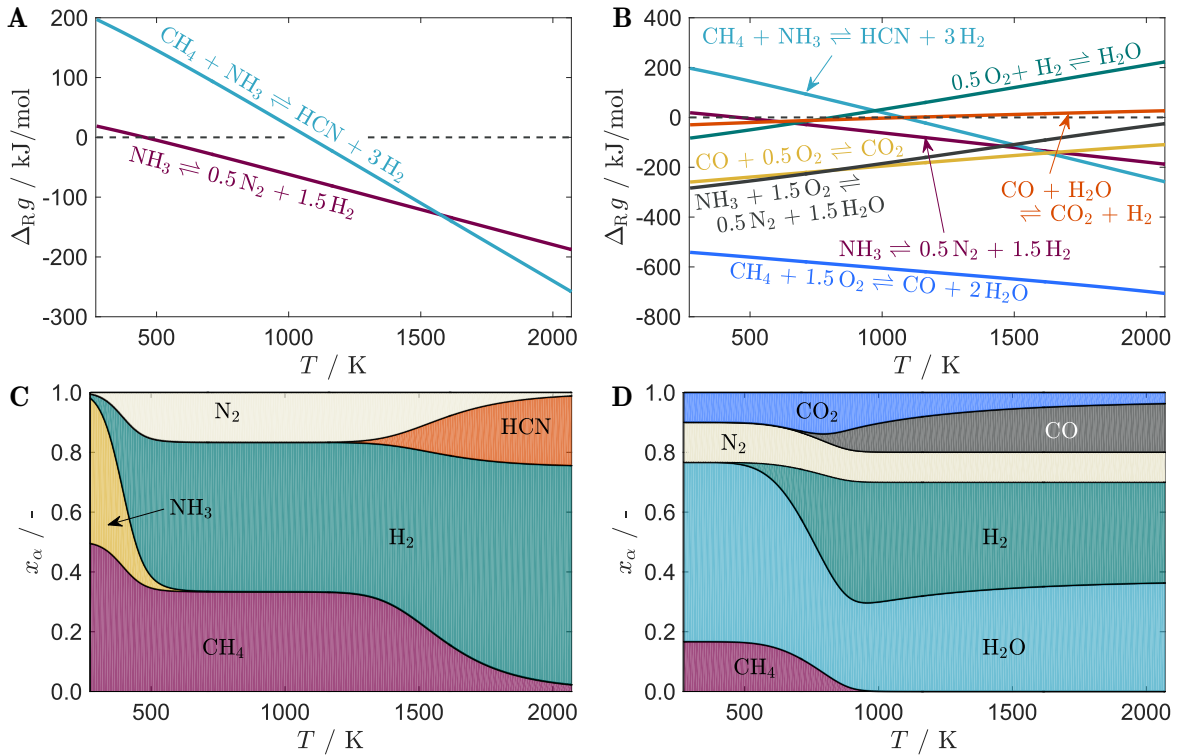
Fig. 3.2 Molar Gibbs energy of reaction $\Delta_R g$ for the principle reactions in the BMA (A) and Andrussow (B) reactors versus temperature (top). Synthesis and NH$_3$ decomposition reactions are displayed using the same colors. Molar fractions at thermodynamic equilibrium of all components in the BMA (C) and Andrussow (D) reactors (bottom).

The BMA and Andrussow reactors are compared with respect to Gibbs free energies of the principle reactions and the thermodynamic equilibrium molar fractions in Fig. 3.2 which is based on thermochemistry data of the NIST webbook [116]: thermochemistry data on HCN is scarce and apart from the NIST webbook not provided in literature [117–120]. The two net reaction equations in the BMA reactor are shown in Fig. 3.2 A. The Gibbs free energies of reactions intersect at 1520 K favoring thermodynamically the formation of HCN at high temperatures. Molar fractions at thermodynamic equilibrium starting from a stoichiometric composition of reactants CH$_4$ and NH$_3$ illustrate this further in Fig. 3.2 C. N$_2$

is the equilibrium product up to 1400 K. Beyond, HCN is the thermodynamically favored product. Comparison with literature of the temperature at which this shift from N_2 to HCN occurs indicates that, in practice, the equilibrium shift is likely to occur around 100 K below the values that are identified in Fig. 3.2 A and C [94, 93]. The kinetic expressions that are used for the reactor modeling seem to reflect the equilibrium shift that is predicted in literature but the exact transition temperatures could not be fully elucidated due to the lack of data in publicly available literature. Nonetheless, the temperature dependent yield of the BMA reactor raises the question, whether sacrificing yield for reduced energy costs is an attractive reactor alternative in the overall process context. This aspect is discussed in chapter 6.

The situation is more complex for the Andrussow reactor as illustrated with the Gibbs free energies of reaction of the most relevant chemical reactions in the Andrussow reactor in Fig. 3.2 B. The reactions that occur in the BMA and Andrussow reactors are displayed using the same colors. The oxidation reactions of both reactants NH_3 and CH_4 have low Gibbs free energies of reaction and are favored thermodynamically over the HCN synthesis in the Andrussow reactor. Despite the fact that the synthesis reaction of HCN is strongly exergonic at temperatures above 1700 K ($\Delta_R g \leq -300\,\mathrm{kJ\,mol^{-1}}$), the partial oxidation of CH_4 remains more favorable with Gibbs free energies of reaction below $-650\,\mathrm{kJ\,mol^{-1}}$. As a consequence, no HCN is present in the thermodynamic equilibrium molar fractions in Fig. 3.2 D. The synthesis of HCN in the Andrussow reactor is thus based on the kinetically faster reaction to the target product and not favored thermodynamically.

In summary, formation of HCN is limited thermodynamically in the BMA reactor and kinetically in the Andrussow reactor: the fast reaction toward the product HCN and extremely low contact times prevent the gas mixture from attaining equilibrium concentrations. The rapid quenching of the reactor gas effluents which is essential for both reactor types to mitigate further product reactions is thus even more significant in the Andrussow reactor.

3.1.3 Reaction Rate Expressions for BMA and Andrussow Reactors

Obtaining reliable reaction kinetic expressions for the HCN synthesis reactions is challenging due to the high temperatures and fast reaction times that are involved. In addition, the catalyst of BMA reactors requires specific pretreatments prior to the actual catalysis [94]. Early investigations of the reaction mechanism in the BMA reactor assumed the N-H bond cleavage as rate determining for the overall reaction [121]. Koberstein later suspected methane adsorption and a subsequent Eley-Rideal mechanism for the formation of HCN with gas phase NH_3 reacting with the adsorbed carbon species [115]. This idea was adopted and quantified in the comprehensive studies on HCN formation by the group of Schmidt which constitute

the sole quantitative reaction rate expressions available in literature [122–124]. The group suggests a mixture of a Langmuir-Hinshelwood and an Eley-Rideal type of surface kinetics: both reactant species CH_4 and NH_3 adsorb and are present in the rate expression but the rate expression is also a function of the partial pressure of gas phase NH_3: $r_{HCN} = f(\theta_C, \theta_N, p_{NH_3})$ where θ describes the surface coverage of carbon and nitrogen containing species. In their kinetic expressions, Schmidt et al. make two assumptions: that the surface reaction is irreversible and that the surface reaction is the rate determining step. Thus, these rate expressions describe the chemical reactions in Eq. (3.6) instead of the equilibrium chemical reactions in Eq. (3.5). The kinetic expressions are successfully validated using industrial data but nonetheless, their reaction kinetics are thermodynamically inconsistent [125]. The two reaction rate expressions for the synthesis of HCN and the decomposition of NH_3 in the BMA and Andrussow reactors are formulated as

$$R_1: \quad CH_4 + NH_3 \longrightarrow HCN + 3\,H_2$$

$$r_1 = \frac{7.8 \times 10^{18} \exp\left(\frac{-1950}{T}\right) p_{CH_4} p_{NH_3}^{1/2}}{\left(1 + 0.044 \exp\left(\frac{2390}{T}\right) p_{CH_4}/p_{NH_3}^{1/2}\right)^4} \tag{3.6a}$$

$$R_2: \quad NH_3 \longrightarrow \frac{3}{2} H_2 + \frac{1}{2} N_2$$

$$r_2 = \frac{4.9 \times 10^{18} \exp\left(\frac{-2130}{T}\right) p_{NH_3}}{\left(1 + 0.044 \exp\left(\frac{2390}{T}\right) p_{CH_4}/p_{NH_3}^{1/2}\right)^3} \tag{3.6b}$$

where the partial pressures of the components are in Torr. The complete set of chemical reactions for the Andrussow reactor including the additional oxidation reactions is provided in the appendix in Sec. A.2.

HCN synthesis in the BMA reactor constitutes a selectivity problem: it is desirable to maximize the selectivity toward HCN instead of the byproduct N_2. In this context, the selectivity can be considered either from a differential or from an integral perspective: the differential selectivity $S_{HCN}^{(dif)}$ provides information about the instantaneous formation of product and byproduct and the integral form $S_{HCN}^{(int)}$ quantifies the accumulated product formation:

$$S_{HCN}^{(dif)} := \frac{\frac{dn_{HCN}}{dz}(z)}{\frac{dn_{N_2}}{dz}(z)} \quad \text{and} \quad S_{HCN}^{(int)} := \frac{n_{HCN}(z) - n_{HCN}(0)}{n_{HCN}(z) - n_{HCN}(0) + n_{N_2}(z) - n_{N_2}(0)} \quad . \tag{3.7}$$

Using the two reaction rate expressions (3.6a) and (3.6b), the differential selectivity is formulated as:

$$S_{HCN}^{(dif)} = \frac{r_1}{r_2} = \frac{k_1(T) p_{CH_4}}{k_3(T) p_{NH_3}^{1/2} + k_2(T) k_3(T) p_{CH_4}} \tag{3.8}$$

where the three temperature dependent coefficients k_1, k_2 and k_3 correspond to the kinetic coefficients of the reaction rates according to the appendix Sec. A.3. The integral selectivity is obtained at each distance z through simulation of an isothermal, infinitely long plug flow reactor with no radial gradients until full reactant conversion is obtained.
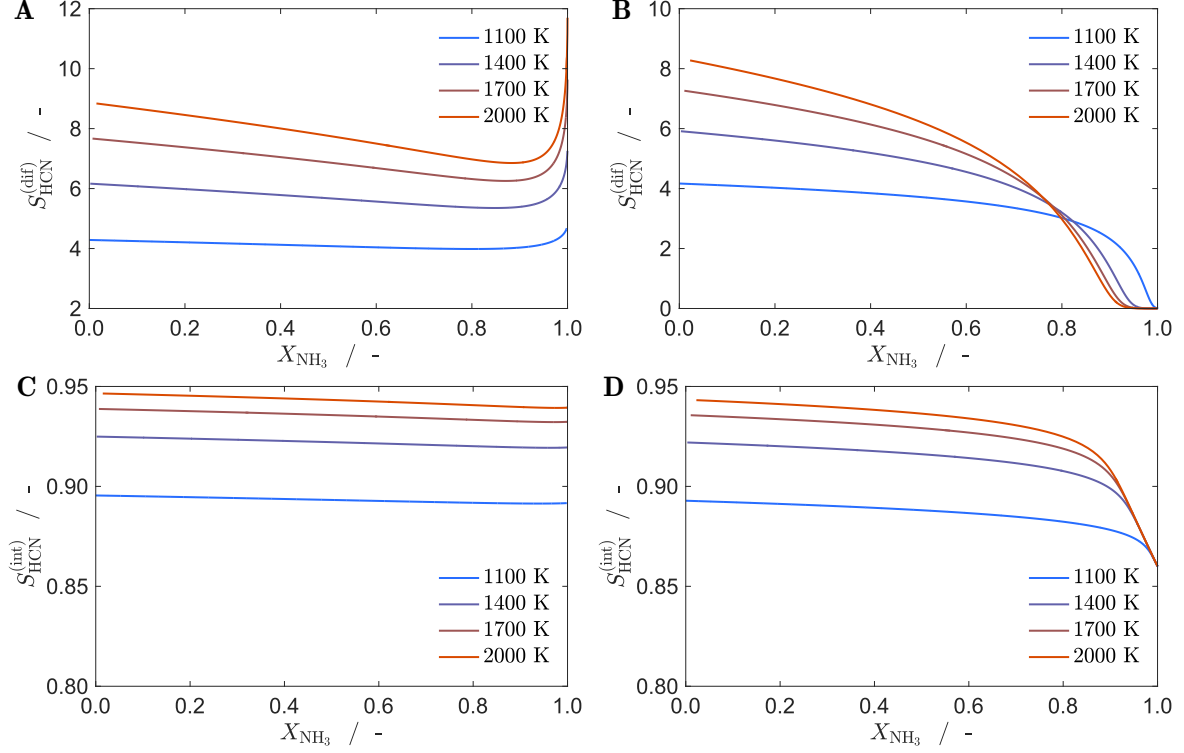
Fig. 3.3 Differential (A,B) and integral (C,D) selectivities of HCN versus conversion of NH_3 for different feed N/C ratios in an infinitely long BMA reactor: stoichiometric i.e. $N/C = 1.0$ (A,C) and excess of NH_3 with $N/C = 1.26$ (B,D).

A comparison of the differential and integral selectivities toward HCN formation is illustrated using conversion of NH_3 X_{NH_3} versus selectivity S_{HCN} graphs for four different temperatures and two feed compositions in Fig. 3.3. The graphs on the left hand side correspond to simulations with molar feed flows of $n_{CH_4} = 0.50\,\mathrm{mol\,m^{-2}\,s^{-1}}$ and $n_{NH_3} = 0.50\,\mathrm{mol\,m^{-2}\,s^{-1}}$ (Fig. 3.3 A,C) whereas the right hand side graphs to feed flows with a strong excess of NH_3 of 27 %: $n_{CH_4} = 0.44\,\mathrm{mol\,m^{-2}\,s^{-1}}$ and $n_{NH_3} = 0.56\,\mathrm{mol\,m^{-2}\,s^{-1}}$ (Fig. 3.3 B,D). Based on the expression (3.8) the limits of the differential selectivity for maximum conversion of NH_3 can be identified:

$$\frac{n_{NH_3}(z_0)}{n_{CH_4}(z_0)} = 1.00: \qquad \lim_{X_{NH_3} \to 1} S_{HCN}^{(dif)} = \frac{k_1(T)}{k_2(T)k_3(T)} \tag{3.9}$$

$$\frac{n_{NH_3}(z_0)}{n_{CH_4}(z_0)} = 1.27: \qquad \lim_{X_{NH_3} \to 1} S_{HCN}^{(dif)} = 0 \quad . \tag{3.10}$$

For stoichiometric feed conditions and toward maximum conversion of NH_3, unreacted CH_4 remains and the differential selectivity equals the ratio of the kinetic coefficients. If NH_3 is added in excess, however, $S_{HCN}^{(dif)}$ approaches zero for full conversion of NH_3. As a consequence, integral selectivities toward the target product HCN are approximately constant for stoichiometric feed and increase with temperature whereas they approach 0.87 at maximal conversion for feed with excess NH_3. Thus, integral selectivities decrease with increasing conversion and turn toward the same number irrespective of the reactor temperature.

An excess of NH_3 is essential to prevent coking of the catalyst and reactor tube but the chemical reactions that lead to coking are not reflected in the reaction kinetic expressions. Therefore, it is not reasonable to identify the optimal feed composition using these kinetics. Besides, comparison of the equilibrium concentration of HCN at $1100\,K$ in Fig. 3.2 C with the integral selectivity toward HCN in Fig. 3.3 C shows clearly that the kinetic expressions are not thermodynamically consistent: The equilibrium concentration of HCN is zero whereas an integral selectivity of $90\,\%$ toward HCN is obtained from the kinetic expressions. The integral selectivity is used for the evaluation of reactor designs in chapter 4 and 5. Therefore, the integral selectivity is referred to as S_{HCN} and the index (int) is neglected from here onward.

Despite being the sole quantitative reaction kinetics available, recent investigations focused on the intrinsic reaction mechanisms of HCN synthesis and two ideas of the synthesis mechanism of HCN over Pt exist: (i) the adsorption of both reactant species, their dehydrogenation and surface reaction and subsequent hydrogenation [126, 127] and (ii) adsorption of CH_x and NH_x species, their reaction and subsequent desorption and dehydrogenation as well as the Eley-Rideal reaction of NH_3 with adsorbed CH_x species [128–130]. The second pathway (ii) is reflected in the Schmidt kinetics and the presence of Pt^+ clusters as active sites is likely [94].
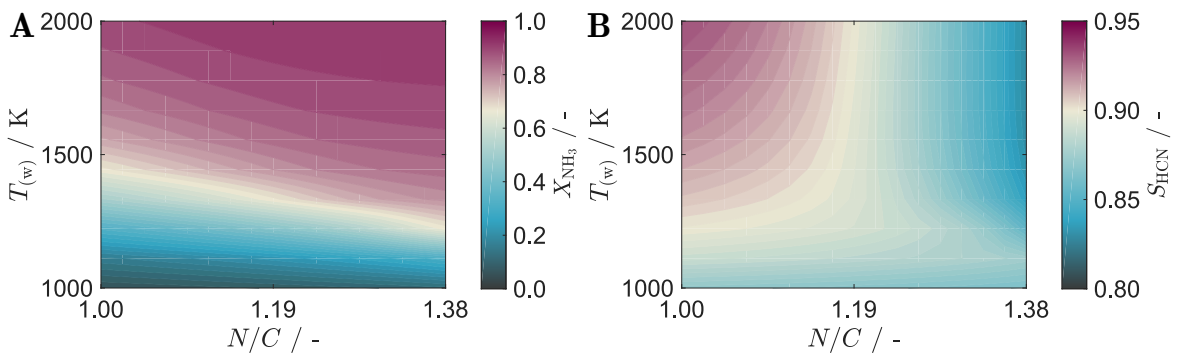
Fig. 3.4 Conversion of NH_3, X_{NH_3} (A), and integral selectivity of HCN, S_{HCN} (B), for different wall temperatures $T_{(w)}$ and ratios of the two feed components N/C at the reactor inlet.

Simulation results of the BMA reactor with $2\,m$ reactor length based on the reactor model of chapter 4 are shown in Fig. 3.4. Constant reactor wall temperatures $T_{(w)} \in [1000\,K, 2000\,K]$

and feed reactant ratios $N/C := n_{\mathrm{NH_3}}(0)/n_{\mathrm{CH_4}}(0) \in [1.00, 1.38]$ are illustrated to demonstrate the impact of an excess of $\mathrm{NH_3}$ in the feed on the product selectivity S_{HCN}. $X_{\mathrm{NH_3}}$ increases with wall temperature but S_{HCN} increases with wall temperature for a stoichiometric feed composition and levels off for higher N/C ratios until it decreases with wall temperature for N/C ratios beyond 1.20. In practice N/C ratios up to 1.10 are utilized [93, 94]. Since coking is not reflected in the reaction kinetic expressions, however, it is not possible to provide model-based recommendations on the optimal amount of excess $\mathrm{NH_3}$. Fig. 3.4 shows that the excess of $\mathrm{NH_3}$ should be kept at a minimum to achieve optimal product selectivities.

3.2 Comparison of BMA and Methane Steam Reforming Reactors

Steam reforming of hydrocarbons and particularly methane is a key process of the chemical industry because it is essential for both synthesis gas – a mixture of CO and $\mathrm{H_2}$ in variable ratios – and hydrogen production [131]. The former is the building block for the synthesis of methanol and other liquid fuels for example via Fischer-Tropsch synthesis but also used for reduction of metals. Synthetic fuels were historically relevant at the beginning of the 20th century but may play a key role as storage molecules for volatile renewable energies (Power-to-X). The origins of reforming date back to the 19th century, when reforming reactions over calcium oxide where observed, catalyst poisons sulfur and coke where identified and the nowadays most relevant catalyst for MSR – Ni – was identified [132–134]. In addition, production of $\mathrm{H_2}$ is important for the synthesis of $\mathrm{NH_3}$. In the context of a more sustainable use of resources, the importance of steam reforming is potentially increasing due to synthetic fuel production or $\mathrm{H_2}$ usage in the mobility sector to power proton-exchange membrane (PEM) fuel cells for heavy-duty vehicles [8].

3.2.1 Reaction Thermodynamics and Kinetics

Analog to the synthesis of HCN, a drawback of MSR is its high energy consumption due to its two principle endothermic reactions: partial (Eq. (3.11a)) and total reforming (Eq. (3.11b)). The water-gas-shift reaction (Eq. (3.11c)) constitutes the third most important reaction in a MSR reactor. All three reaction equations are formulated as:

$$\mathrm{CH_4 + H_2O \rightleftharpoons 3\,H_2 + CO} \qquad \Delta_{\mathrm{R}} h^{\ominus} = 206.1 \text{ kJ\,mol}^{-1} \qquad (3.11a)$$

$$\mathrm{CH_4 + 2\,H_2O \rightleftharpoons 4\,H_2 + CO_2} \qquad \Delta_{\mathrm{R}} h^{\ominus} = 165.0 \text{ kJ\,mol}^{-1} \qquad (3.11b)$$

$$\mathrm{CO + H_2O \rightleftharpoons H_2 + CO_2} \qquad \Delta_{\mathrm{R}} h^{\ominus} = -41.2 \text{ kJ\,mol}^{-1} \quad . \qquad (3.11c)$$
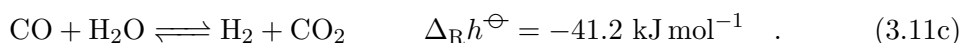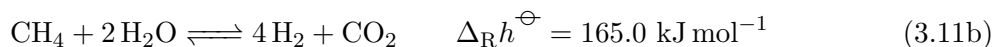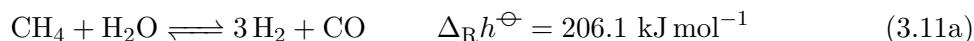
In spite of the high reaction enthalpies of partial and total reforming, they are lower than the reaction enthalpy of the synthesis reaction of HCN (Eq. (3.5a)). As a consequence, the equilibrium shift toward synthesis gas for the MSR reactions occurs at 900 K as shown in Fig. 3.5 A. Methane partial reforming and total reforming to CO_2 have similar reaction enthalpies and Gibbs enthalpies of reaction (Eq. (3.11a), (3.11b)). Both reactions are endergonic up to 900 K and above 1100 K, partial reforming is the thermodynamically favored reaction. In addition to the competitive formation of CO and CO_2 from CH_4, CO formation is also preferred thermodynamically via the water-gas-shift reaction at temperatures higher than 1050 K. As a consequence, maximum temperatures favor the target product CO as well as the formation of H_2 because both reforming reactions are strongly exergonic at high temperatures which is evident from Fig. 3.5 B. This figure displays equilibrium molar fractions of all relevant species for a steam-to-carbon feed ratio $S/C = 1/1$ and a pressure of 1 bar which is often investigated in microchannel reactors [135].
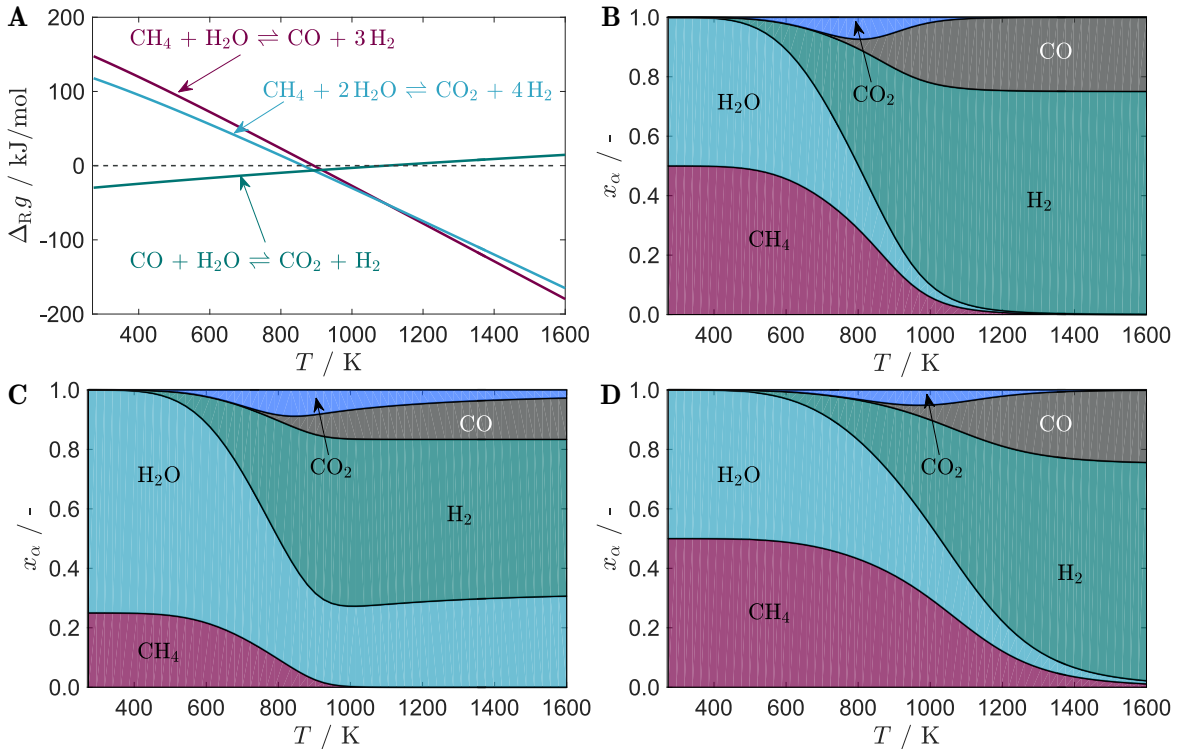
Fig. 3.5 Molar Gibbs energy of reaction $\Delta_R g$ for the principle reactions in MSR (A) and corresponding molar fractions at thermodynamic equilibrium versus temperature: stoichiometric feed ($S/C = 1/1$) and $p = 1$ bar (B), excess H_2O in the feed ($S/C = 3/1$) and $p = 1$ bar (C) and industrially applied pressure ($S/C = 1/1$) and $p = 30$ bar (D).

Two challenges exist in MSR – prevention of coking using higher S/C ratios as well as higher pressures to reduce the reactor volume and increase productivity – which are highlighted with Fig. 3.5 C and D. In Fig. 3.5 C, the S/C feed ratio is changed to a typical industrial

steam-to-carbon ratio of $S/C = 3/1$. The excess of H_2O shifts the equilibrium toward higher fractions of CO_2. In Fig. 3.5 D, the pressure is increased to 30 bar which is a typical pressure of fixed bed tube reactors in the industry. Then, the equilibrium molar composition shifts toward CO_2 and the reactants CH_4 and H_2O following the principle of Le Chatelier because the total mole number increases in the reforming reactions. This increase in molar amount is stronger in partial than in total reforming which penalizes the formation of CO [133].

Several reaction kinetics for MSR are proposed in literature due to the high relevance of this process. A widely used reaction kinetic model contains the rate expressions by Xu and Froment. The model dates back to the 1980's and diffusion limitations are discussed alongside [136, 137]. More recent studies propose either microkinetic reaction mechanisms with elementary step kinetics – that have also been applied to MSR with a boundary layer flow (BLF) model on a Rh catalyst – or more simplified kinetics based on a single RDS which is the activation of CH_4 [138–141]. Because of its wide acceptance and its application for both packed bed and wall reactor models, the kinetics of Xu and Froment are utilized for the model transfer from HCN to MSR [142]. A detailed discussion of the reaction kinetics and validation is out of scope in this chapter but the single compartment model is validated with microchannel experimental data for MSR in the appendix in Sec. B.2 [91].

Both the MSR and HCN reactions have in common, that the prevention of coking is important which is achieved via the excess of the oxidizing agent NH_3 for HCN synthesis and H_2O in MSR. Nonetheless, both kinetic rate expressions lack the consideration of coking in their models hindering the investigation of the necessary but sufficient excess of oxidizing agent. Consequently, the optimal reactor design with respect to feed composition or reactant dosing is not possible with these kinetic expressions. In contrast to the kinetics for HCN synthesis, the MSR kinetics by Xu and Froment are thermodynamically consistent and can be used to model both MSR and methanation reactions [83].

3.2.2 Comparison of Reactor Designs

Similar to HCN synthesis, the reactors for MSR must ensure good heat transfer to the endothermic reaction sites. Since synthesis gas and H_2 are commodity products – thus produced in large quantities – and MSR requires lower reaction temperatures, MSR reactors for large-scale production in industry are significantly larger than BMA reactors with synthesis tubes of up to 12 m length. In contrast to the catalytic wall reactor in the BMA process, fixed bed reactors are applied in MSR to increase the catalytic active surface area. One of the main reasons why fixed beds are applied in MSR but not BMA is that MSR is not as prone to coking as BMA because a large amount of excess oxidizing agent is added in MSR with $S/C = 3/1$. This is a strong contrast to the BMA reactor where the oxidizing agent NH_3

is added in lesser excess with $N/C \leq 1.1$ because it is a comparatively expensive reactant. Instead of adding it in large excess amounts, it is desired that NH_3 is consumed entirely in the synthesis reaction because recycling of NH_3 is hardly possible – ammonia is typically separated from the product stream via absorption in sulfuric acid yielding an ammonium sulfate solution with little economic value [93, 131].

Four distinct types of furnace designs exist in MSR that are differentiated according to their different firing patterns: (i) co- and (ii) counter-current as well as (iii) side- and (iv) terrace-fired furnaces. All four furnace types are applied in industry in different companies, but the terrace- and side-fired furnace types have the advantage that the temperature profile along the synthesis tubes can be adjusted through the burner loads [133, 143, 131]. As such, the maximum allowable temperatures can be set at the tube inlet. For these reasons, this design was investigated for the tube bundle optimization of MSR furnaces in collaboration with Sebastian Engel [92]. In this context, heat flux versus wall temperature correlations of a single tube were identified in the master thesis of Adrian Krummnow that was supervised during this thesis [144].

Fixed bed reactors aside, microchannel reactors provide a promising candidate for reactor intensification for both MSR and HCN synthesis and they may be used for small-scale production such as decentralized fuel production [145]. In addition to numerical and experimental studies, a commercial microchannel reactor is demonstrated by Tonkovich et al. [135, 146, 147]. The advantage of high surface areas and autothermal reactor concepts through simultaneous catalytic combustion in an adjacent channel provide an interesting alternative to tube bundle furnaces. Design aspects and heat transfer limitations of microchannel reactors for MSR were investigated in the context of this thesis [91]. For HCN synthesis, however, a patent on a monolith reactor exists but it is not foreseeable that this reactor will replace conventional reactor designs in the near future [108]: the construction and operation of a high temperature monolith reactor is challenging and in addition to that, coking of small channel widths would disrupt the operation of the entire reactor whereas the dysfunction of single tubes in the conventional tube bundle design does not affect the operation of adjacent tubes.

3.3   Chapter Summary

MSR and synthesis of HCN are among the most important high temperature gas phase processes. Both processes require high energy inputs due to their underlying endothermic chemical synthesis reactions. Major industrially applied reactor types – industrial furnaces for MSR and the BMA reactor for HCN synthesis – are designed as tube bundle furnaces where the combustion in the furnace compartment provides the required heat for the endothermic

synthesis reaction inside the tubes. The reactors are operated with a stoichiometric excess of the oxidizing agent to prevent coking of the reaction compartments. Catalytic wall reactors are utilized in HCN synthesis and fixed bed reactors in MSR where larger quantities of the oxidizing agent H_2O prevent coking. The analysis and design methods of this thesis are exemplified for the case study of HCN synthesis. Beyond that, the heat transfer analysis and design of a single reaction compartment and of a tube bundle have been successfully applied to MSR as well [91, 92].

The BMA and Andrussow reactors are the two most industrially relevant reactors to produce HCN from CH_4 and NH_3. While the BMA reactor is endothermic and heat is provided externally in a tube bundle furnace, the Andrussow reactor is exothermic but has inferior product yields. The analysis of the rate expressions by Schmidt et al. shows that the available reaction kinetics are useful for the prediction of industrially relevant scenarios but their drawbacks – thermodynamic inconsistency, absence of key reactions such as coking or product decomposition – prohibit the identification of the mass transfer limitations and the optimal feed and temperature control for the BMA reactor. It is nonetheless evident, that for the BMA reactor, heat transfer into the synthesis compartment shall be maximized. Production processes of HCN that involve a BMA reactor are of interest for two reasons: understanding of the key heat transfer mechanisms may lead to intensified reactor concepts and in addition, there is the possibility to operate the reactor at different temperatures in order to weigh product yield and heat duties which may be desirable for the overall resource-efficiency in the plant context.

Chapter 4

Characteristics of the Single Synthesis Compartment

In order to propose intensified reactor design concepts for MSR and HCN reactors, an understanding of the governing design and operating parameters for high temperature catalytic wall reactors is required. It is the objective of this chapter, address the research questions (I), (II) and (III) that were formulated in chapter 1 at the single compartment reactor level (comp. Fig. 1.1). Therefore, the underlying flow and heat transfer characteristics are analyzed and the potential for reactor intensification is evaluated. The analysis of transport phenomena in high temperature reactors poses several challenges but is essential for improved reactor designs [145]: experimental studies are difficult because the high temperatures hinder measurements inside of the reactor and are limited to concentration measurements in the quenched reactor outlet gas stream. High reaction kinetic constants that often lead to fast reactions are an additional consequence of the high temperatures in the reactor. In addition to that, radiative heat transfer is often not negligible and has to be taken into account for reactor design. Besides, HCN is hazardous due to its high toxicity, reactivity and volatility and requires additional safety measures in the laboratory. For all these reasons, the analysis of transport phenomena in this chapter is limited to model-based investigations.

At first, the literature for single reactor compartment design for MSR and HCN is reviewed. Then, the model for the single compartment reactor is derived with a constant wall temperature boundary condition and with an adjacent furnace compartment. Subsequently, results for both modeling scenarios are discussed followed by a chapter summary that contains the key findings at the single compartment level.

4.1   Literature Context

Literature for heat transfer in high temperature catalytic reactors is more abundant for MSR than for HCN synthesis. Therefore, their literature is discussed together beginning with experimental and leading over to modeling investigations.

Experimental contributions include the work by Ricca et al. [148] who used SiC as a wall material to increase the thermal conductivity of the wall. Mass transfer limitations were investigated in combination with the formulation of reaction kinetic expressions by Xu and Froment [136]. As a result, they introduced efficiency factors depending on the catalyst type [137]. In addition to that, Irani et al. [142] suggested that no diffusional limitations exist for MSR in channel reactors. Venkataraman and Wanat investigated different channel couplings of exo- and endothermal reaction compartments to increase heat transfer rates [149, 146]. Karakaya et al. [135] performed experimental studies of MSR on a Ni catalysts and their work is used for model validation in the appendix in Sec. B.2. Periodic operation of a two layer catalytic reactor was investigated by Galvita and Sundmacher [150] which lead to an increase of H_2 production. There exists also an industrial application of MSR microchannel reactors whose dimensions were used as benchmark in the microchannel design study that is related to this chapter [147, 91].

In modeling studies for MSR and HCN reactors, modeling assumptions are crucial for example radiative heat transfer is treated differently depending on the reactor type and application: in fixed bed reactors radiation was long considered negligible and was thus combined with conductive heat transfer into an effective conductivity [151, 83]. An increase in accuracy of the model-based temperature predictions, however, was reported in a recent contribution: Wehinger [152] proposed that surface-to-surface radiation plays a role also for reforming applications in the lower temperature range [153]. With respect to the BMA reactor for HCN synthesis, a single model reactor study exists which emphasizes the importance of the warm-up zone of the reactor and that the reactor performance is mass-transfer limited once the reactants near the wall achieve their reaction temperature. Furthermore, the conductivity of the wall separating reaction compartment and furnace is high enough such that the thermal resistance of the wall can be neglected [115]. High-fidelity models were used for the modeling of industrial fixed bed reforming reactors [154–156]. Frauhammer et al. [157] and later Kolios et al. [158] investigated the operation of autothermal reactors with separate compartments for combustion and reforming in order to identify the best operating point [159].

The identification of the optimal reactor design was a key objective of the MSR community in the past and it is still today. For conventional fixed bed reactors, optimal heat flux profiles along the reactor have been identified and also feed composition as well as flowrates have been optimized [160, 161]. A simulation- and an optimization-based study on operating

conditions for a single tube have been reported as well [162, 163]. For microchannel geometries, Mundhwa et al. [164] recommended a segmented instead of a continuous catalyst impregnation to enhance the reactor performance. Arzamendi et al. [165] assumed a constant channel width to compare co- and cross-current microchannel designs and Karim et al. [166] claimed that the channel geometry has no impact on the reactor performance at all. Beside these contributions, parameter studies by Zhai and Stutz compared selected different channel widths and identified optimal design candidates within the considered interval of dimensions in their studies [167, 168].

4.2   Model Formulation

The transport characteristics in the synthesis compartments are analyzed with a locally distributed model of a system of coupled channels as illustrated in Fig. 4.1. Two scenarios are considered: a constant wall temperature boundary condition and an adjacent furnace compartment with a flow of hot flue gases. The same model is applied for the description and design of microchannels for MSR [91]. Fig. 4.1 illustrates both compartments – the
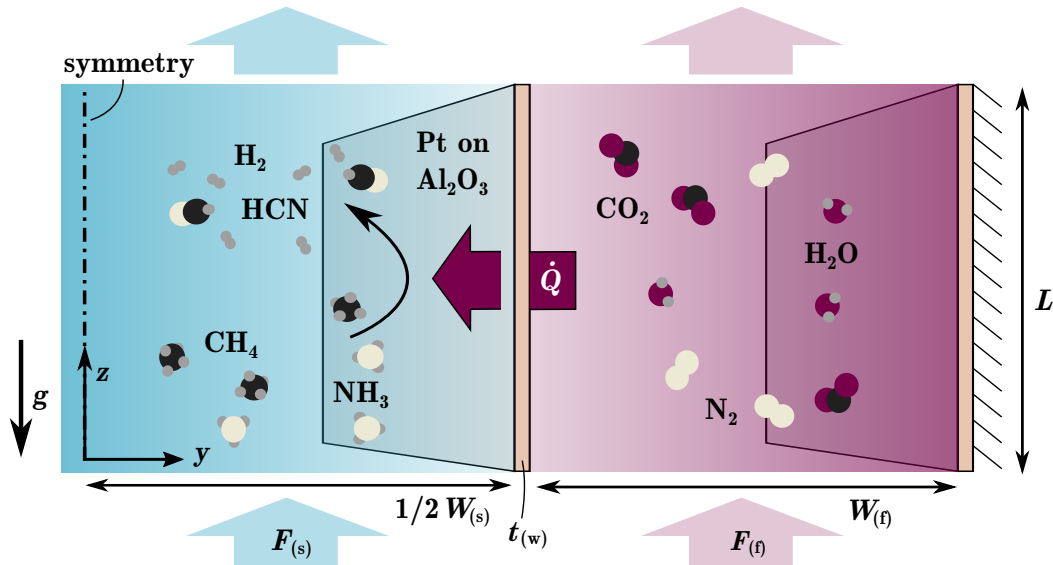
Fig. 4.1 Sketch of the two compartment reactor model: synthesis compartment (s) with the catalytic surface reaction (left) and furnace compartment (f) with a hot flue gas flow (right).

synthesis compartment (left) and the furnace compartment (right) which are separated by a wall of thickness $t_{(w)}$ that transmits the heat flux $\dot{Q}$. Key design parameters of the channel system are the widths of synthesis and furnace compartments $W_{(s)}$ and $W_{(f)}$, the volume flows in both compartments $F_{(s)}$ and $F_{(f)}$ and the length of the single compartment L. In order to accelerate the computation, the symmetry of the synthesis compartment is exploited

as indicated by the dash-dotted symmetry line whereas the furnace compartment is bounded by an adiabatic wall. At first, the model for the synthesis compartment and a constant wall boundary condition is derived followed by the coupled model of synthesis and furnace compartments.

4.2.1   Channel Model for a Single Compartment

Two single synthesis compartment geometries are relevant for the HCN and MSR reactor catalytic wall reactors: a channel for MSR microreactors and a cylinder for the tubes of the BMA reactor and for fixed bed tubes of MSR. Throughout this chapter, single compartments for HCN synthesis are modeled as channel flow in Cartesian coordinates. It is evident, that the channel model results do not equal results of cylinders. The findings of this chapter are nonetheless relevant because this chapter emphasizes the investigation of the transport phenomena which remains valid qualitatively irrespective of the specific geometry which the study on MSR with a cylinder model shows [92]. The channel wall heat fluxes are utilized below for the tube bundle optimization and are converted using equal surface areas as shown in the appendix in Sec. C.1. Even with a cylindrical model at the single synthesis compartment level, accurate quantitative information cannot be obtained at the tube bundle level due to the additional relaxation of the modeling complexity that is required for the handling of the furnace tube bundle reactor. These assumptions are discussed with the tube bundle furnace model in chapter 5. The cylinder model is thus omitted in this thesis. Instead, it was set up within the master thesis project of Adrian Krummnow [144]. Subsequently, it was utilized for the tube bundle design for MSR in collaboration with Sebastian Engel [92].

Modeling Assumptions

In order to analyze the transport phenomena inside the reactive gas flow the following modeling assumptions are applied:

(i)   The channel is described in two dimensions: z in principle flow direction and y transverse to the principle direction of flow.

(ii)   A boundary layer model is justified due to Reynolds numbers much greater than one across the channel cross section (Re$\gg$ 1).

(iii)   No body forces are relevant except gravity g due to the upright reactor orientation for the case of HCN synthesis in the BMA reactor (Fig. 4.1).

(iv)   The change of kinetic and potential energies are neglected.

(v)   The reactor is in steady state.

(vi)   The reactor inlet gas mixture is composed of reactants.

(vii)   The ideal gas assumption holds due to the near ambient pressures for both HCN synthesis and microchannel design for MSR.

(viii) Backmixing, i.e. diffusion in z direction is neglected.

(ix)   Fluid flow is laminar and compressible (thermally-dilatant).

(x)   Radiative heat transfer is accounted for with a participating medium.

(xi)   Radiation in the gas mixture is described with multiple absorbing-emitting gray gases.

(xii)   Scattering of radiative intensity is negligible.

(xiii) The inner reactor walls are modeled as gray walls.

(xiv)   Species diffusion is described using Fick diffusion and an effective diffusion coefficient.

(xv)   Thermodiffusion is neglected.

(xvi)   Heat transfer due to concentration gradients (Dufour effect) is neglected.

(xvii) Chemical reactions occur only at the catalytic wall surface and not in the gas phase.

The derivation of the BLF equations was pioneered by Ludwig Prandtl in 1904 and their derivation is omitted here. Instead, BLF is discussed in detail in the textbooks by Jischa and Krause [169, 170].

Total Mass Balances

All conservation laws are formulated for the Cartesian coordinate system that is indicated in Fig 4.1. For an arbitrary control volume, the steady state total mass balance in two Cartesian coordinates assuming compressible flow (ix)is formulated as

$$\frac{\partial}{\partial z}\left(\rho_{(s)} v_{z,(s)}\right) + \frac{\partial}{\partial y_{(s)}}\left(\rho_{(s)} v_{y,(s)}\right) = 0 \quad .$$

(4.1)

where $\rho_{(s)}$, $v_{z,(s)}$ and $v_{y,(s)}$ denote the density and velocity magnitudes in z and y directions within the synthesis compartment indicated with the index "(s)". Based on assumption (vii), the ideal gas equation of state is used for the calculation of the density:

$$\rho_{(s)} = \frac{p_{(s)} \tilde{M}_{(s)}}{R T_{(s)}} \quad .$$

(4.2)

$p_{(s)}$, $\tilde{M}_{(s)}$, $T_{(s)}$ and R represent pressure, mixture molar mass and temperature of the control volume as well as the universal gas constant.

Component Balances

In addition to the total mass balance, N_c component balances – one per component α – are formulated as

$$\rho_{(s)} v_{z,(s)} \frac{\partial w_{\alpha,(s)}}{\partial z} + \rho_{(s)} v_{y,(s)} \frac{\partial w_{\alpha,(s)}}{\partial y_{(s)}} = -\frac{\partial j_{y,\alpha,(s)}}{\partial y_{(s)}} + \sigma_{\alpha,(s)}$$

$$\alpha \in \mathcal{N}_c := \{1, 2, ..., N_c\} \quad . \tag{4.3}$$

Mass fractions of component α are indicated as $w_{\alpha,(s)}$ whereas $\mathcal{N}_c$ and N_c are the set of all components and the total number of components in the gas mixture. The transverse diffusion flux is denoted with $j_{y,\alpha,(s)}$ whereas diffusion in z is negligible according to assumption (viii). $\sigma_{\alpha,(s)}$ denotes the species source term which is zero except for at the wall surface (xvii). The diffusion flux $j_{y,\alpha,(s)}$ is calculated assuming Fick's law (xiv) using the effective diffusivity approach of Wilke for a multicomponent mixture [171]:

$$j_{y,\alpha,(s)} = -D_{\alpha,\text{eff},(s)} \rho_{(s)} \frac{\partial w_{\alpha,(s)}}{\partial y_{(s)}} \quad . \tag{4.4}$$

The effective diffusivity $D_{\alpha,\text{eff},(s)}$ is based on binary diffusion coefficients $\mathcal{D}_{\alpha\beta}$ that are obtained from kinetic theory of gases using the Fuller equation and molar fractions of the species x_α [171]:

$$D_{\alpha,\text{eff},(s)} = (1 - x_\alpha) \left(\sum_{\beta=1, \beta \neq \alpha}^{N_c} \frac{x_\beta}{\mathcal{D}_{\alpha\beta}} \right)^{-1} \quad . \tag{4.5}$$

For the example of HCN synthesis using the reaction rate expressions by Schmidt et al. (Eq. (3.6a)), the volumetric source term near the walls $\sigma_{\alpha,(s)}$ is derived as:

$$\sigma_{\alpha,(s)} = \frac{A_s}{V} \frac{\tilde{M}_\alpha}{N_A} \sum_{i=1}^{N_r} \nu_{\alpha,i} r_i \quad . \tag{4.6}$$

In this equation the catalyst surface A_s divided by V denotes the catalyst surface to volume ratio, $\tilde{M}_\alpha$ the molar mass of component α and N_A the Avogadro constant. $\nu_{\alpha,i}$, r_i and N_r are the stoichiometric coefficient of component α in reaction i, the reaction rate of reaction i and the total number of reactions.

Momentum Balances

The velocity distribution in the reactor is obtained from the momentum conservation equations which result in two equations for each control volume – for the y (Eq. (4.8)) and z (Eq. (4.7)) coordinates. As a result of the boundary layer model assumption, the pressure in y-direction is constant as shown in Eq. (4.8):

$$\rho_{(s)}\left(v_{z,(s)}\frac{\partial v_{z,(s)}}{\partial z} + v_{y,(s)}\frac{\partial v_{z,(s)}}{\partial y_{(s)}}\right) = -\frac{\partial p_{(s)}}{\partial z} + \frac{\partial \tau^*_{(s)}}{\partial y_{(s)}} + \rho_{(s)}g \tag{4.7}$$

$$0 = \frac{\partial p_{(s)}}{\partial y_{(s)}} \quad . \tag{4.8}$$

g is the gravitational acceleration and $\tau^*_{(s)}$ denotes the modified stress tensor because the BLF assumption reduces the stress tensor of the momentum conservation $\tau_{jk,(s)}$ to the single term

$$\tau^*_{(s)} = \eta_{(s)}\frac{\partial v_{z,(s)}}{\partial y_{(s)}} \quad . \tag{4.9}$$

$\eta_{(s)}$ is the viscosity of the gas mixture which is obtained from pure component viscosities and the mixing rule according to Wilke [169, 172, 173].

Energy Balances

The temperature of each volume element is obtained from the energy balance

$$\rho_{(s)}c_{p,(s)}\left(v_{z,(s)}\frac{\partial T_{(s)}}{\partial z} + v_{y,(s)}\frac{\partial T_{(s)}}{\partial y_{(s)}}\right) = v_{z,(s)}\frac{\partial p_{(s)}}{\partial z} - \frac{\partial q^{(c)}_{y,(s)}}{\partial y_{(s)}} - \frac{\partial q^{(r)}_{y,(s)}}{\partial y_{(s)}} +$$
$$- \sum_{\alpha=1}^{N_c} h^0_{\alpha,(s)}\sigma_{\alpha,(s)} - \sum_{\alpha=1}^{N_c} j_{y,\alpha,(s)}\frac{\partial h^0_{\alpha,(s)}}{\partial y_{(s)}} + \sum_{\alpha=1}^{N_c} g j_{y,\alpha,(s)} + \tau^*_{(s)}\frac{\partial v_{z,(s)}}{\partial y_{(s)}} \quad . \tag{4.10}$$

Here, $c_{p,(s)}$ and $h^0_{\alpha,(s)}$ denote the heat capacity of the gas mixture and the enthalpy of pure component α in the synthesis compartment. The terms in the first line correspond to convection, pressure work as well as temperature change due to conductive $\partial q^{(c)}_{y,(s)}/\partial y_{(s)}$ and radiative $\partial q^{(r)}_{y,(s)}/\partial y_{(s)}$ heat transfer in y direction. Conductive and radiative heat flux vectors in z cancel out as a consequence of the BLF assumption. The second line of Eq. (4.10) contains the enthalpy difference due to the chemical reaction, enthalpy diffusion, work of gravity as well as dissipation losses of the flow. The conductive heat flux is modeled using Fourier's law as

$$q^{(c)}_{y,(s)} = -\lambda_{(s)}\frac{\partial T_{(s)}}{\partial y_{(s)}} \quad . \tag{4.11}$$

The thermal conductivity of the gas mixture $\lambda_{(s)}$ is calculated – analog to the viscosity – from pure component data using Wilke's mixing rule.

The radiative heat flux vector in y direction $q^{(r)}_{y,(s)}$ is directly related to the radiative intensities that are obtained from the radiative transfer equations (RTE):

$$q^{(r)}_{y,(s)} = \int_0^\infty \int_{4\pi} I_\eta \hat{\mathbf{s}} \, \mathrm{d}\Omega \, \mathrm{d}\eta \quad . \tag{4.12}$$

In Eq. (4.12), I_η denotes the wavenumber-dependent intensity, $\hat{\mathbf{s}}$ the unit direction vector. The radiative heat flux equals the radiative intensities integrated over the entire solid angle space $[0, 4\pi]$ and over the entire wavenumber range. The solid angles and directional dependence of the radiative intensities are discussed next.

Radiative Transfer Equations

The RTE models the conservation of radiative energy along the unit direction $\hat{\mathbf{s}}$ as sketched in Fig. 4.2 A. Along the distance $\mathrm{d}s$, intensity changes due to emission, absorption and in- and out-scattering which is reflected in the three terms that constitute the RTE. In addition
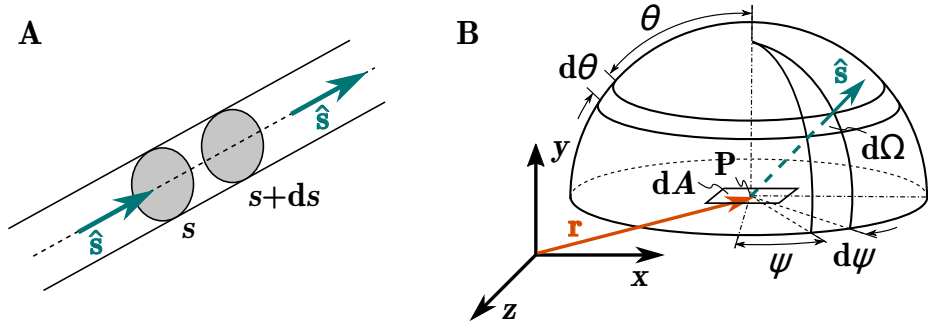
Fig. 4.2 Illustration of pencil of rays for the radiative energy balance (A) and the three spatial and two directional coordinates of the RTE (B) [174].

to this directional dependence, radiative intensity is dependent on the location described by $\mathbf{r}$ and the wavenumber η which is described by Planck's law. The local RTE in the unit direction $\hat{\mathbf{s}}$ is formulated as

$$\frac{\mathrm{d}I_\eta}{\mathrm{d}s} = \kappa_\eta(\mathbf{r})I_{\mathrm{b},\eta}(\mathbf{r}) - \beta_\eta(\mathbf{r})I_\eta(\mathbf{r},\hat{\mathbf{s}}) + \frac{\sigma_{s\eta}(\mathbf{r})}{4\pi} \int_{4\pi} I_\eta(\mathbf{r},\hat{\mathbf{s}}')\Phi_\eta(\mathbf{r},\hat{\mathbf{s}}',\hat{\mathbf{s}})\mathrm{d}\Omega' \tag{4.13}$$

where I_η and $I_{b\eta}$ denote the radiative intensity and blackbody intensity at wavenumber η. The coefficients κ_η, β_η and $\sigma_{s\eta}$ represent the absorption, extinction and scattering coefficients with $\beta_\eta := \kappa_\eta + \sigma_{s\eta}$. In contrast to $\hat{\mathbf{s}}$ the direction vector $\hat{\mathbf{s}}'$ denotes inward-pointing directions into the local pencil of rays that are scattered into the direction $\hat{\mathbf{s}}$. As shown in Fig. 4.2 B,

the directional discretization is described using solid angles Ω that correspond to a surface fraction of the hemisphere that is created by all unit direction vectors $\hat{\mathbf{s}}$. Solid angles are expressed in terms of a polar angle θ and an azimuthal angle ψ.

$$\mathrm{d}\Omega = \sin\theta \, \mathrm{d}\theta \, \mathrm{d}\psi \quad . \tag{4.14}$$

Φ_η in Eq. (4.13) represents the scattering phase function. Overall, equation (4.13) is a five-dimensional (three in space and two in direction) integro-differential equation that is simplified using the modeling assumptions that were described above: Negligence of scattering (xii) – i.e. $\sigma_{s\eta} \equiv 0$ – for small optical thicknesses and the gray gas assumption (xi) – i.e. I_η is simplified to I – reduce Eq. (4.13) to

$$\frac{\mathrm{d}I_{(s)}}{\mathrm{d}s} = \kappa_{(s)}(\mathbf{r})I_{\mathrm{b},(s)}(\mathbf{r}) - \kappa_{(s)}(\mathbf{r})I_{(s)}(\mathbf{r}, \hat{\mathbf{s}}) \tag{4.15}$$

for the single synthesis compartment. The gray gas assumption means that the absorption of the gas is a constant fraction of the blackbody spectrum for all wavelengths. The blackbody intensity in $\mathrm{W\,m^{-2}\,rad^{-1}}$ is given by the Stefan-Boltzmann law:

$$I_{\mathrm{b}} = \sigma \frac{T^4}{\pi} \tag{4.16}$$

More background on radiation modeling and the detailed derivation of the RTE is provided for example in Modest [174] or Howell et al. [175]. In addition to the spatial discretization scheme that is required for the solution of the mass, momentum and energy balances, a directional discretization is required for the solution of the RTEs.

Planck Mean Absorption Coefficients

In order to solve the RTEs (4.15), the gray gas assumption (xi) is applied which is justified for the quantification of radiative heat transfer for most engineering applications but not for analytical purposes where the quantized nature of the absorption/emission bands is explicitly exploited. Despite the gray gas assumption, the species and temperature dependence of the absorption coefficients have to be taken into account. For CO_2 and H_2O that are relevant in combustion and furnaces, tabulated data exists [175, 174]. In order to quantify radiative heat transfer for the synthesis compartment of HCN, however, absorption of additional species such as NH_3, HCN and CH_4 need to be considered. Therefore, Planck mean absorption coefficients are derived from high resolution spectroscopic data that are contained in databases such as the high-resolution transmission molecular absorption database (HITRAN) and the high-temperature molecular spectroscopic database (HITEMP) [176–179]. The Planck mean

absorption coefficient is defined as:

$$\kappa_{P,\alpha} := \frac{\int_0^\infty \kappa_{\eta,\alpha} I_{b,\eta} d\eta}{\int_0^\infty I_{b,\eta} d\eta} = \frac{1}{I_b} \int_0^\infty \kappa_{\eta,\alpha} I_{b,\eta} d\eta \quad . \tag{4.17}$$

Data in HITEMP do not include all species of interest and data in HITRAN is available at standard conditions of $T^\ominus = 298$ K and $p^\ominus = 1013$ hPa. However, the band emissivities S_{ij} can be translated to higher temperature emissivities through the ratio of partition sums Z at the target and at the reference temperature level according to Eq. (4.18) [180].

$$S_{ij}(T) = S_{ij}(T^\ominus) \frac{Z(T^\ominus)}{Z(T)} O(T) \tag{4.18}$$

where the term $O(T)$ contains additional effects such as stimulated emission that are described in detail in literature [176]. Using equations (4.17) and (4.18), species and temperature dependent absorption coefficients are derived and illustrated in Fig. 4.3. All components have
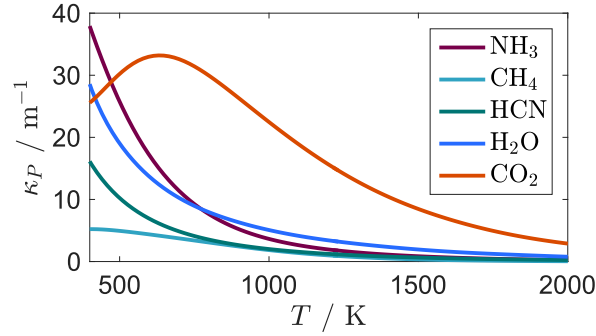
Fig. 4.3 Planck mean absorption coefficients versus temperature for the absorbing/emitting species inside a HCN synthesis reactor compared with absorption coefficients of CO_2 and H_2O.

higher absorption coefficients at lower than at higher temperature. The main reason is that the wavelength at the peak of emission shifts to higher wavenumbers as the temperature increases while the gas absorption spectra remain at their discrete positions. The impact of additional molecular rotational-vibrational energy states that become accessible at higher temperatures is overcompensated by this shift to higher wavenumbers and thus decline of absorption coefficients. Elementary gases are not taken into account because they absorb significantly less than gases of molecules that consist of different atoms. Considering Fig. 4.3, it is evident that both CH_4 and HCN play minor roles for radiative heat transfer and absorb/emit significantly less than H_2O and CO_2. The reactant NH_3, however, has an absorption coefficient similar to H_2O due to the similarity of their atomic structures. Therefore, it is expected that radiative heat transfer is crucial near the reactor entrance where high concentrations of the reactant NH_3 prevail. Toward the center and outlet of the reactor, the contribution of

radiation to the total heat transfer is expected to diminish as the synthesis gas mixture heats up and the products HCN and H_2 with lower absorption coefficients are formed.

Boundary Conditions

Formulation of the conservation laws for the synthesis compartment with the constant wall temperature boundary condition in Fig. 4.1 requires one boundary condition each in z dimension for $v_{z,(s)}$, $w_{\alpha,(s)}$, $p_{(s)}$ and $T_{(s)}$. They are formulated as:

$$v_{z,(s)} \left(z = 0, y_{(s)} \right) = v_{z0,(s)}$$
$$w_{\alpha,(s)} \left(z = 0, y_{(s)} \right) = w_{\alpha 0,(s)} \qquad \alpha \in \{1, 2, ..., N_c\}$$
$$p_{(s)} \left(z = 0, y_{(s)} \right) = p_{0,(s)}$$
$$T_{(s)} \left(z = 0, y_{(s)} \right) = T_{0,(s)} \quad .$$

In addition to that, boundary conditions in the direction $y_{(s)}$ are required. They are characterized by the symmetry plane at $y_{(s)} = 0$ and the channel wall at $y_{(s)} = y_{\mathrm{max},(s)}$. At the wall, the velocity magnitude is zero, there is no concentration gradient due to the volumetric source term and the temperature takes the wall temperature $T_{(w)}$:

$$v_{y,(s)} \left(z, y_{(s)} = y_{\mathrm{max},(s)} \right) = v_{z,(s)} \left(z, y = y_{\mathrm{max},(s)} \right) = 0$$
$$\frac{\partial w_{\alpha,(s)}}{\partial y_{(s)}} \left(z, y_{(s)} = y_{\mathrm{max},(s)} \right) = 0$$
$$T_{(s)} \left(z, y_{(s)} = y_{\mathrm{max},(s)} \right) = T_{(w)} \quad .$$

At the symmetry plane, velocity, concentration and temperature gradients equal zero:

$$\frac{\partial v_{z,(s)}}{\partial y_{(s)}} \left(z, y_{(s)} = 0 \right) = \frac{\partial w_{\alpha,(s)}}{\partial y_{(s)}} \left(z, y_{(s)} = 0 \right) = \frac{\partial T_{(s)}}{\partial y_{(s)}} \left(z, y_{(s)} = 0 \right) = 0 \quad .$$

Boundary conditions for the RTE are required for each direction $\hat{\mathbf{s}}$ of the directional discretization and are discussed in combination with the discretization of the RTE below.

4.2.2 Coupled Model of Synthesis and Furnace Compartments

In order to enable simulations of the second scenario – the coupled synthesis channel and furnace model as illustrated in Fig. 4.1 – additional conservation equations for the furnace side and the separating wall are introduced.

Modeling Assumptions

No chemical reactions are considered for the furnace side i.e. the furnace side fluid is modeled as a hot flue gas. The flue gas composition is assumed constant and originates from a complete combustion of methane without soot formation. As for the synthesis compartment channel model, a laminar steady-state two-dimensional representation of the fluid flow is selected that exploits the BLF model formulation.

Furnace and Wall Conservation Laws

In addition to the conservation laws of the synthesis compartment, local conservation laws for total mass, momentum, energy and radiative energy in the furnace compartment are formulated based on the modeling assumptions as

$$\frac{\partial}{\partial z}(\rho_{(f)} v_{z,(f)}) + \frac{\partial}{\partial y_{(f)}}(\rho_{(f)} v_{y,(f)}) = 0 \tag{4.19a}$$

$$\rho_{(f)}\left(v_{z,(f)}\frac{\partial v_{z,(f)}}{\partial z} + v_{y,(f)}\frac{\partial v_{z,(f)}}{\partial y_{(f)}}\right) = -\frac{\partial p_{(f)}}{\partial z} + \frac{\partial \tau^*_{(f)}}{\partial y_{(f)}} + \rho_{(f)} g \tag{4.19b}$$

$$0 = \frac{\partial p_{(f)}}{\partial y_{(f)}} \tag{4.19c}$$

$$\rho_{(f)} c_{p,(f)}\left(v_{z,(f)}\frac{\partial T_{(f)}}{\partial z} + v_{y,(f)}\frac{\partial T_{(f)}}{\partial y_{(f)}}\right) = v_{z,(f)}\frac{\partial p_{(f)}}{\partial z} - \frac{\partial q^{(c)}_{y,(f)}}{\partial y_{(f)}} - \frac{\partial q^{(r)}_{y,(f)}}{\partial y_{(f)}} +$$
$$+ \tau^*_{(f)}\frac{\partial v_{z,(f)}}{\partial y_{(f)}} \tag{4.19d}$$

$$\frac{\mathrm{d}I_{(f)}}{\mathrm{d}s} = \kappa_{(f)}(\mathbf{r})I_{b,(f)}(\mathbf{r}) - \kappa_{(f)}(\mathbf{r})I_{(f)}(\mathbf{r}, \hat{\mathbf{s}}) \tag{4.19e}$$

where the subscript (f) denotes the furnace system. In addition to the two systems of PDEs for the synthesis and furnace compartments, a PDE is used to describe the temperature $T_{(w)}$ of the wall that separates both compartments and which is no longer constant:

$$0 = \frac{\partial q^{(c)}_{y,(w)}}{\partial y_{(w)}} + \frac{\partial q^{(r)}_{y,(w)}}{\partial y_{(w)}} \quad . \tag{4.20}$$

Boundary Conditions

The furnace compartment is bounded by two walls, hence the velocities at both boundaries must equal zero due to the no-slip boundary condition. The temperature boundary conditions

are given as

$$T_{(s)}\left(z, y_{(s)} = y_{\max,(s)}\right) = T_{(f)}\left(z, y_{(f)} = 0\right) = T_{(w)} \quad \text{and}$$
$$\frac{\partial T_{(f)}}{\partial y_{(f)}}\left(z, y_{(f)} = y_{\max,(f)}\right) = 0 \quad . \tag{4.21}$$

4.3 Model Solution

Spatial Discretization Scheme

The model solution strategy for the system of PDEs (Eq. (4.1) (4.3), (4.7), (4.8), (4.10), (4.15), (4.19)) exploits the boundary layer nature of the flow because the equation system is solved as a parabolic flow system using the method of lines [181]: The PDEs are transformed into ordinary differential equations using the FVM as shown in Fig. 4.5. At first, the PDEs are discretized manually in the transverse direction y for each control volume Λ^j. Subsequently, the resulting DAE is integrated along the reactor coordinate z using state-of-the-art integrators such as IDAS of the Sundials solver suite [182]. The channel models for the single synthesis compartment and the coupled synthesis-furnace compartments are implemented and solved in Matlab/CasADi [183]. The discretization scheme is exemplified for the species mass balance for a non-wall element (Eq.(4.3)) in the appendix in Sec. B.1.

The key to solving this strongly coupled DAE system is the discretization of transverse velocities in a staggered fashion: the discretized momentum balances in z-direction are used to solve for v_z velocities whereas total continuity equations are used for determination of transverse velocity magnitudes v_y: Considering the synthesis compartment, there are $N_{y,(s)}+1$ transverse velocities among which $v_{y,(s)}\left(y_{(s)} = 0\right) = v_{y,(s)}\left(y_{(s)} = y_{\max,(s)}\right) = 0$. Therefore, $N_{y,(s)}-1$ total continuity equations are used for transverse velocity and one continuity balance is available for the pressure drop correction analog to SIMPLE(R) algorithms [184].
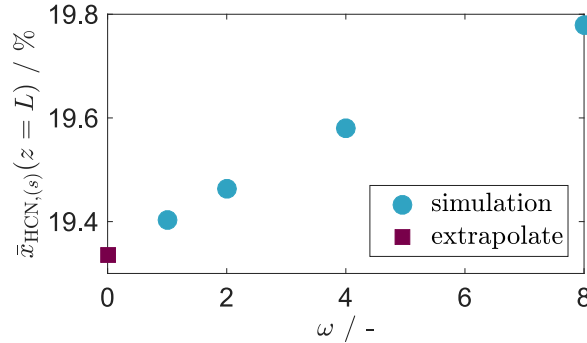
Fig. 4.4 Grid dependence study with the average HCN molar fraction at the reactor outlet $\bar{x}_{\mathrm{HCN}}$ versus normalized grid spacing ω.

The impact of the spatial discretization mesh size on the solution precision is analyzed with a grid dependence study that is shown in Fig. 4.4 with the example of mass average HCN molar fractions at the reactor outlet [185]. A constant grid refinement ratio of $\omega = 2$ is used and the normalized grid spacing ω is defined as $\omega := N_{\max}/N_i$ [186]. As a consequence, the point at a normalized grid spacing of $\omega = 1$ corresponds to for example 80 elements, at a grid spacing of $\omega = 2$ to 40 elements and so forth. Then, the data point at $\omega = 0$ – the Richardson extrapolate – corresponds to an infinitely fine mesh. The difference between Richardson extrapolate and the coarsest grid value is 2.3%. Consequently, errors that originate from the mesh sizing are negligible.
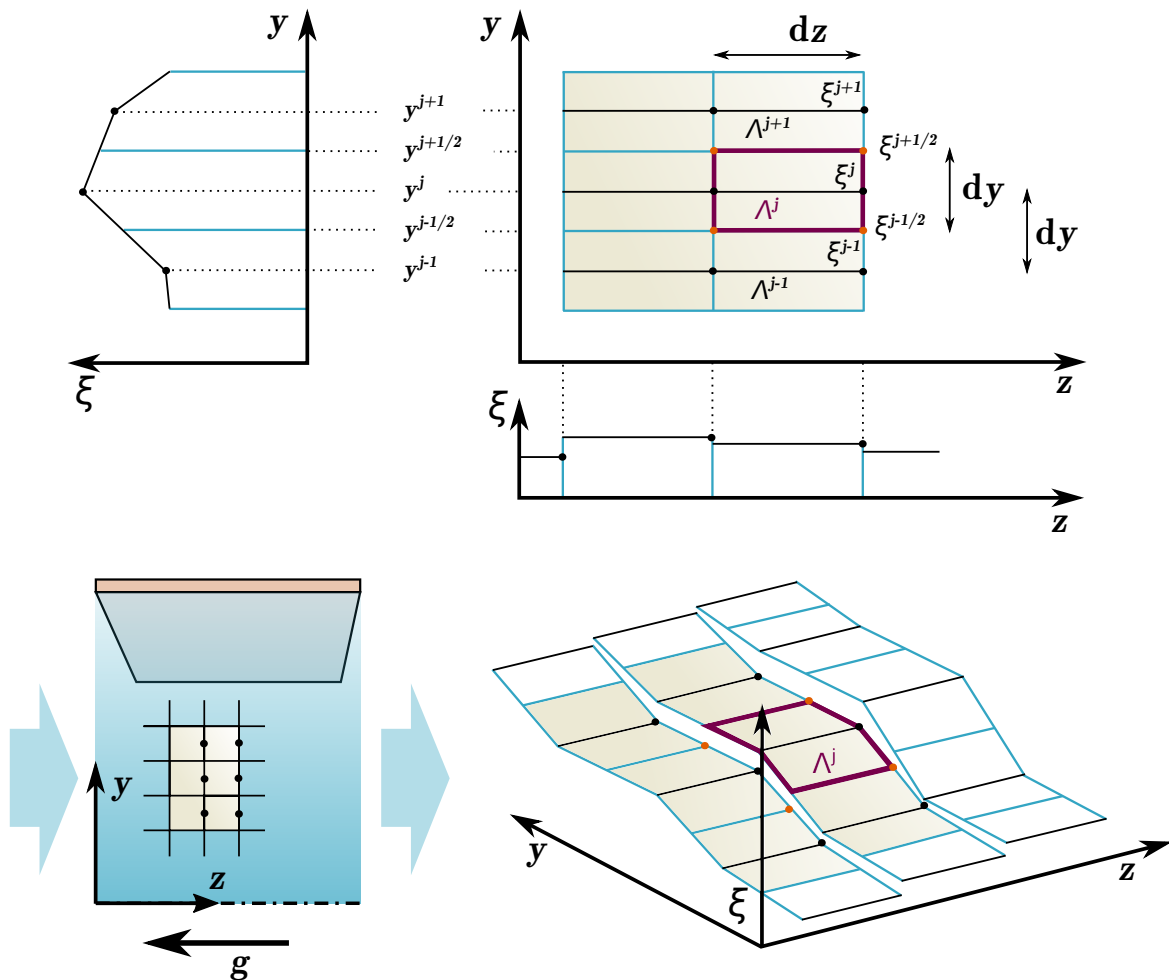
Fig. 4.5 Discretization scheme using the method of lines Brenan et al. [181]: A piecewise linear function is assumed in transverse y direction and piecewise constant states ξ are assumed in z. ξ represents an arbitrary state.

4.3.1 Directional and Spatial Discretization of RTEs

The directional and spatial discretization of the RTEs is structured into two parts: at first, the discretization scheme is demonstrated for the general three-dimensional case. Consecutively, it is applied to the channel reactor geometry and the boundary conditions for radiative intensities are discussed. The indices "(s)" and "(f)" are omitted because the discretization scheme is identical for both compartments.

General Directional and Spatial Discretization of RTE

The left hand side of Eq. (4.15) – $\mathrm{d}I/\mathrm{d}s$ – may be written in symbolic notation as $\hat{\mathbf{s}} \cdot \boldsymbol{\nabla} I$ where $\boldsymbol{\nabla}$ denotes the spatial gradient in three coordinates because spatial and directional coordinates are independent. Complementary to the FVM scheme of the spatial discretization, the directional domain (Fig. 4.2) is discretized into N_k solid angles Ω_k, $k \in \{1, 2, ..., N_k\}$ with the FVM assumption of a constant intensity per solid angle Ω_k [174]. Using

$$\mathbf{s}_k = \int_{\Omega_k} \hat{\mathbf{s}}\,\mathrm{d}\Omega \quad , \tag{4.22}$$

Eq. (4.15) is integrated for solid angle Ω_k as

$$\mathbf{s}_k \cdot \boldsymbol{\nabla} I_k = \Omega_k \kappa (I_\mathrm{b} - I_k) \qquad k \in \{1, 2, ..., N_k\} \quad . \tag{4.23}$$

Comparison with Eq. (4.12) shows the link between divergence of the radiative heat flux and intensities for the general three-dimensional case:

$$\boldsymbol{\nabla} \cdot \mathbf{q}^{(r)} = \sum_{k=1}^{N_k} \mathbf{s}_k \cdot \boldsymbol{\nabla} I = \sum_{k=1}^{N_k} \Omega_k \kappa (I_\mathrm{b} - I_k) \quad . \tag{4.24}$$

Spatial integration of Eq. (4.23) using Gauss' integral law and an UPWIND step scheme for the control volume Λ leads to

$$\sum_{j=1}^{N_A} I_{jk}(\mathbf{s}_k \cdot \hat{\mathbf{n}}_j) A_j = \Omega_k \kappa_\Lambda V_\Lambda (I_{bp} - I_{\Lambda k}) \tag{4.25}$$

where $j \in \{1, 2, ..., N_A\}$ denotes all surfaces of the control volume Λ. Eq. (4.25) is equivalent to

$$I_{\Lambda k} = \frac{\Omega_k \kappa_\Lambda V_\Lambda I_{b\Lambda} + \displaystyle\sum_{j,\,\mathrm{in}} I_{jk}|\mathbf{s}_k \cdot \hat{\mathbf{n}}_j| A_j}{\Omega_k \kappa_\Lambda V_\Lambda + \displaystyle\sum_{j,\,\mathrm{out}} (\mathbf{s}_k \cdot \hat{\mathbf{n}}_j) A_j} \tag{4.26}$$

resulting in an algebraic equation for every intensity $I_{\Lambda k}$ of element Λ and direction k. In the numerator, the summation is over all inward pointing intensities $I_{jk}\left(\mathbf{s}_k \cdot \hat{\mathbf{n}}_j < 0\right)$ and in the denominator for outward pointing intensities that take the value $I_{\Lambda k}\left(\mathbf{s}_k \cdot \hat{\mathbf{n}}_j > 0\right)$. As a consequence, N_k algebraic equations are obtained for each control volume Λ that are solved simultaneously during the integration of the DAE system.

RTE Discretization and Boundary Conditions for the Channel Geometry

For the channel reactor geometry, the directional discretization of the RTE is straightforward: the angular space is discretized into two solid angles Ω_k with $k \in \{+, -\}$ as sketched for the furnace compartment in Fig. 4.6 A. Each solid angle Ω_k thus covers a hemisphere of the total
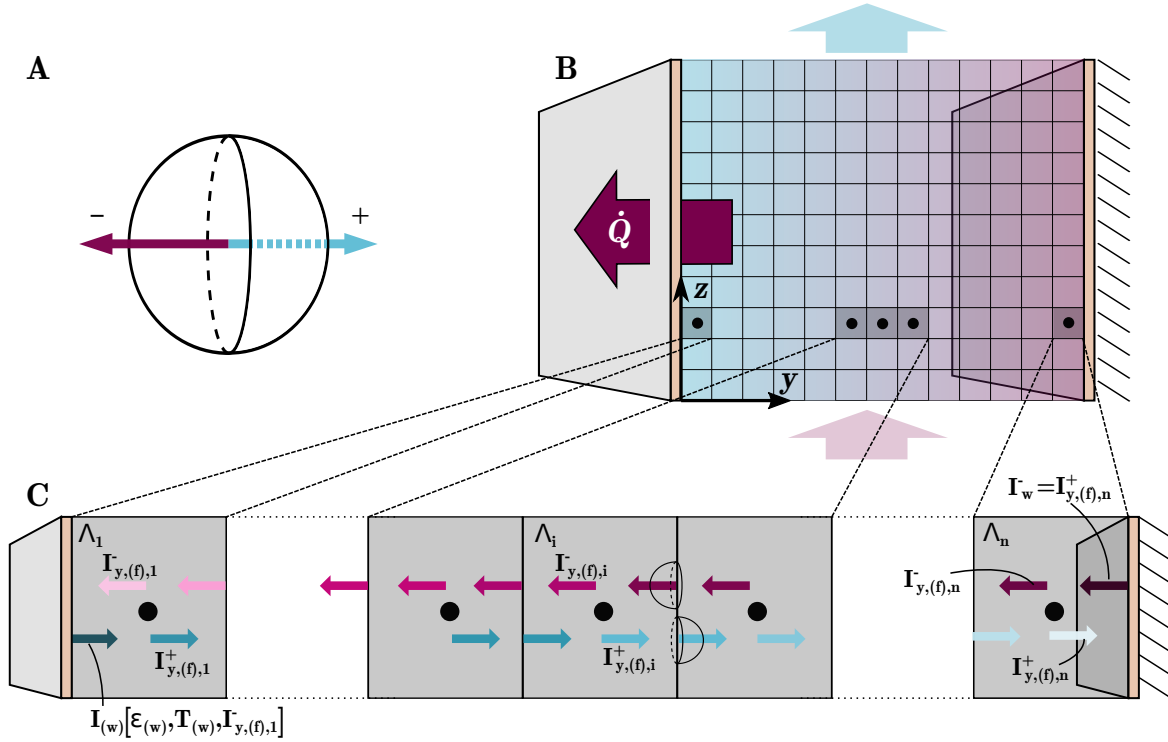
Fig. 4.6 Illustration of the directional (A) and spatial (B) FVM discretization of the RTE for the furnace channel compartment (C).

solid angle space. As a consequence, two boundary conditions – one for each discretized solid angle – are required for each reactor compartment. Fig. 4.6 B and C illustrate the spatial FVM discretization and the formulation of boundary conditions based on both discretization schemes. The radiative heat flux at the symmetry plane equals zero, therefore

$$I_{y,(\mathrm{s})}^+\left(y_{(\mathrm{s})} = 0\right) = I_{y,(\mathrm{s})}^-\left(y_{(\mathrm{s})} = 0\right) \quad . \tag{4.27}$$

The same boundary condition holds for the adiabatic wall of the furnace channel (Fig. 4.6 C, right):

$$I_{y,(f)}^{-}\left(y_{(f)} = y_{\max,(f)}\right) = I_{y,(f)}^{+}\left(y_{(f)} = y_{\max,(f)}\right) \quad . \tag{4.28}$$

At the channel wall, however, the boundary condition is calculated using the emissivity of the channel wall $\epsilon_{(w)}$ (Fig. 4.6 C, left) resulting in the following expression for the intensity leaving the wall in the furnace compartment:

$$I_{y,(f)}^{+}\left(y_{(f)} = 0\right) = I_{(w)} = \epsilon_{(w)}I_{b,(w)} - \left(1 - \epsilon_{(w)}\right)I_{y,(f)}^{-}\left(y_{(f)} = 0\right) \tag{4.29}$$

which is formulated analog for the synthesis compartment.

4.4   Results for the Single Compartment of the BMA Reactor

At first, the model for the single synthesis compartment with a constant wall temperature boundary condition is validated and the transport phenomena are investigated. Subsequently, the extended model – i.e. the coupled model of synthesis and furnace compartment – is analyzed.

4.4.1   Concentration Profile and Validation for HCN Synthesis

The reactor design and operating parameters for all simulations of the HCN synthesis compartment in this chapter are summarized in Table 4.1. Reactor length as well as inlet flow, composition and pressure are selected similar to the Endter reactor and a NH_3/CH_4 ratio of 1.08 is selected [104]. The diameter of the synthesis tubes of the Endter reactor is used as channel width. Wall emissivities of alumina decrease from 0.6 to 0.4 for temperatures between from 1600 K to 1000 K [120]. Throughout this chapter, emissivities are assumed as $\epsilon_{(w)} = 0.45$. A preheated feed at 373 K and a constant wall boundary temperature at 1500 K are assumed. In the absence of a surface characterization of the catalyst on the carrier material, the catalyst surface area is assumed to be equal to the wall surface area. The results are generated using 50 discretization elements in y directions and are displayed for 200 elements in z.

Concentration profiles of the five species CH_4, NH_3, HCN, H_2 and N_2 are depicted in Fig. 4.7. The graphs of the two reactants CH_4 (A) and NH_3 (B) are almost identical: the species react at the catalytic wall surface and enter the reactor in similar quantities. In addition to that, both molecules are similar in size and thus have similar diffusion coefficients. The concentration of NH_3, however, decreases more rapidly compared to CH_4 due to the byproduct formation

Tab. 4.1 Parameters for synthesis compartment simulations in this chapter.

design parameters				
channel length	L	$=$	2	m
channel width	$W_{(s)}$	$=$	1.8×10^{-2}	m
operating parameters				
molar fraction CH_4 at inlet	$x_{CH_4,(s)}(z=0)$	$=$	0.48	-
molar fraction NH_3 at inlet	$x_{NH_3,(s)}(z=0)$	$=$	0.52	-
average inlet velocity in z direction	$\bar{v}_{z,(s)}(z=0)$	$=$	2.0	$m\,s^{-1}$
nominal space time	$\tau_{(s)}$	$=$	0.8	s
inlet temperature	$T_{(s)}(z=0)$	$=$	373	K
inlet pressure	$p_{(s)}(z=0)$	$=$	1013	hPa
constant wall boundary temperature	$T_{(w)}$	$=$	1500	K
wall surface emissivity	$\epsilon_{(w)}$	$=$	0.45	-

of N_2. Molar fractions of the two main products HCN and H_2 are shown below in Fig. 4.7 C and D. Both graphs illustrate product formation with the sharpest gradients in reactant concentration in the first half of the reactor and less pronounced product formation after 1 m length. Cross-sectional gradients in HCN concentrations are more persistent because of its higher molecular weight than H_2 which results in lower diffusion coefficients. Additionally, H_2 experiences the highest concentration gradients due to the stoichiometry of the HCN synthesis reaction. This is clearly evident from both graphs as the concentration of H_2 evens out across the cross-sectional area rapidly whereas sharp gradients of HCN remain until the reactor outlet. The molar fraction of byproduct N_2 is illustrated in Fig. 4.7 E: It has the lowest diffusion rates due to its low diffusion coefficients and low driving force due to the slight concentration difference in the reactor.

Normalized reaction rates $\hat{r}$ for the two reactions R_1 (Eq. (3.6a)) and R_2 (Eq. (3.6b)) as well as cross-sectional average species molar fractions in combination with literature data are illustrated in Fig. 4.8 A and B: The reaction rate expressions r_1 and r_2 are normalized with their respective maximum values because r_2 is five orders of magnitude smaller than r_1. The side reaction R_2 is less endothermic than R_1. Therefore, the rate of the side reaction has its maximum directly at the reactor inlet decreasing exponentially with the onset of the synthesis reaction and the consumption of NH_3. The HCN synthesis reaction has a higher enthalpy of reaction. Therefore, the rate of R_1 exhibits its maximum value at $z = 7 \times 10^{-2}$ m. Both reaction rates decrease exponentially due to the quick consumption of the reactants NH_3 and CH_4 but the rate of the side reaction R_2 decreases more rapidly due to the lower reaction enthalpy.

In order to validate the reactor model, cross-sectional average molar fractions at the reactor outlet obtained from the channel model are compared with literature data that are based on industrial plant data in Fig. 4.8 B [104]. Reactor outlet concentrations of the model
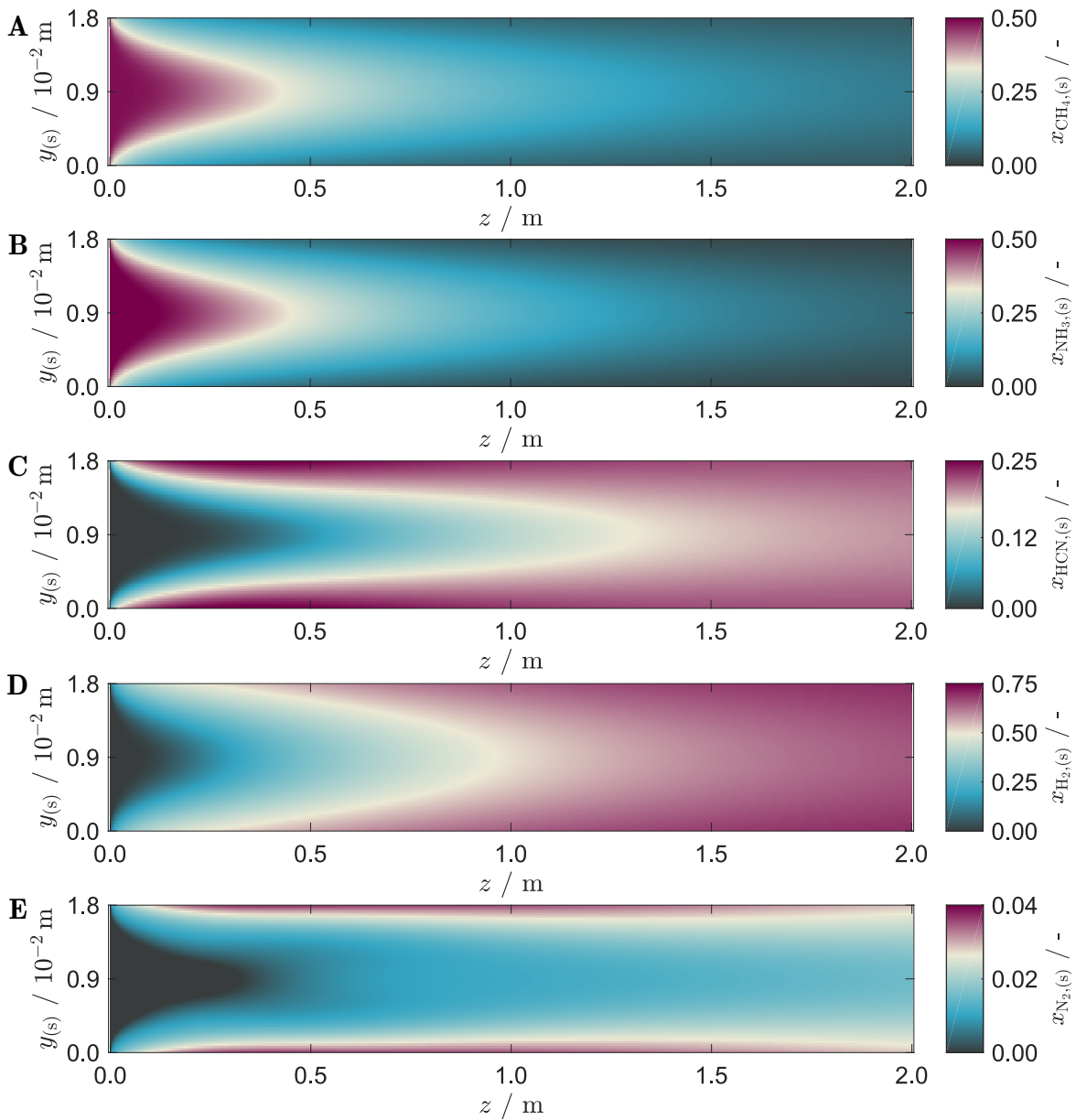
Fig. 4.7 Molar fractions of the reactants CH_4 (A), NH_3 (B) and products HCN (C), H_2 (D) and the byproduct N_2 (E).

match the plant data well but the predicted product yields underestimate the literature data by 6 % for the selected space time. A more rigorous validation for HCN is impossible due to the scarce availability of data. The deviations in the reactor outlet concentrations may originate from three aspects: the flow rate and thus space time of the industrial reactor is not clearly indicated in the literature source, the catalyst surface area is guessed to equal the wall surface in the absence of a surface analysis and the reaction kinetic expressions have some shortcomings as explained above in chapter 3. A separate model validation study at
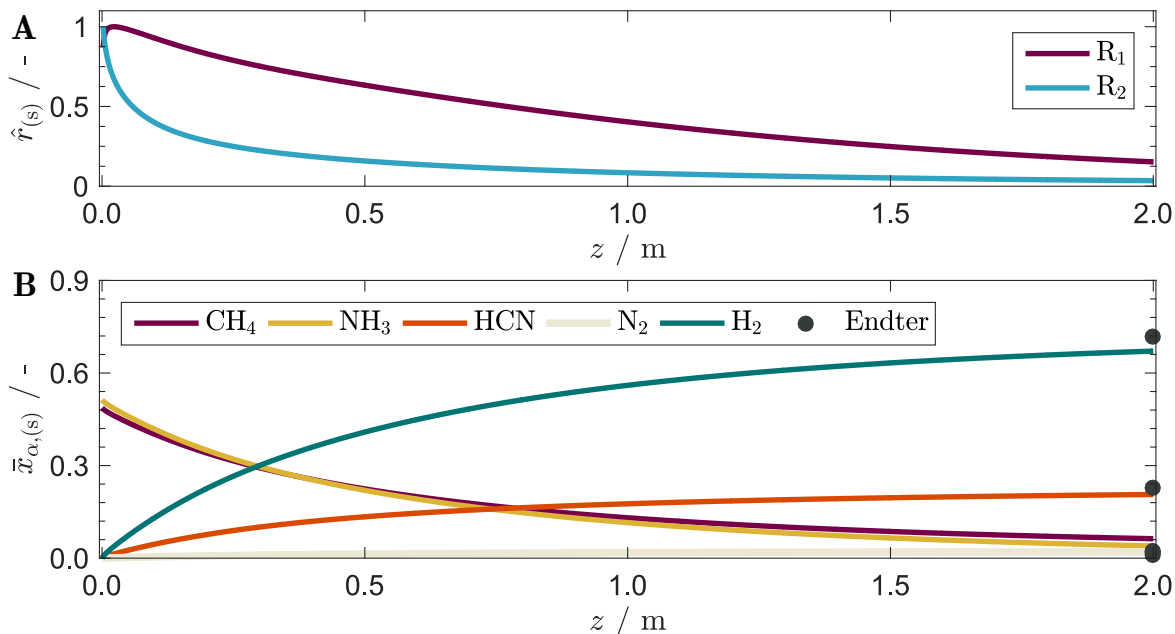
Fig. 4.8 Normalized reaction rates $\hat{r}_1$ and $\hat{r}_2$ (A) for HCN formation (R$_1$, Eq. (3.6a) and R$_2$, Eq. (3.6b)) and validation of cross-sectional average molar fractions with literature data (B) [104].

greater depth is done for MSR where more experimental data for microchannels and different space times and feed ratios is available in literature. This validation is illustrated in the appendix in Sec. B.2 which confirms the principle accuracy of the model.

4.4.2   Flow Characteristics

Boundary Layer Formation

As shown in the model derivation, the density is modeled using the ideal gas law. Reconsidering Eq. (4.2), the temperature is in the denominator and the molar mass of the mixture in the numerator. Based on the formation of hydrogen and heat uptake of the reacting gas mixture, the density is thus expected to decrease over the reactor length. As a consequence of the continuity equation, the velocity increases strongly from $2\,\mathrm{m\,s^{-1}}$ up to $20\,\mathrm{m\,s^{-1}}$. This is illustrated with the temperature, molar mass and velocity distribution in the reactor in Fig. 4.9 A, B and C. The pressure drop inside the reactor contributes to an additional decrease in density but accounts solely for few Pascals and is therefore negligible compared to the change in molar mass and temperature.

The cold reactants heat up and are converted to HCN and H$_2$ quickly upon entering the reactor. After about $1\,\mathrm{m}$ length, both temperature and concentration profiles do not alter as drastically compared to the first half of the reactor. Therefore, the acceleration of the gas
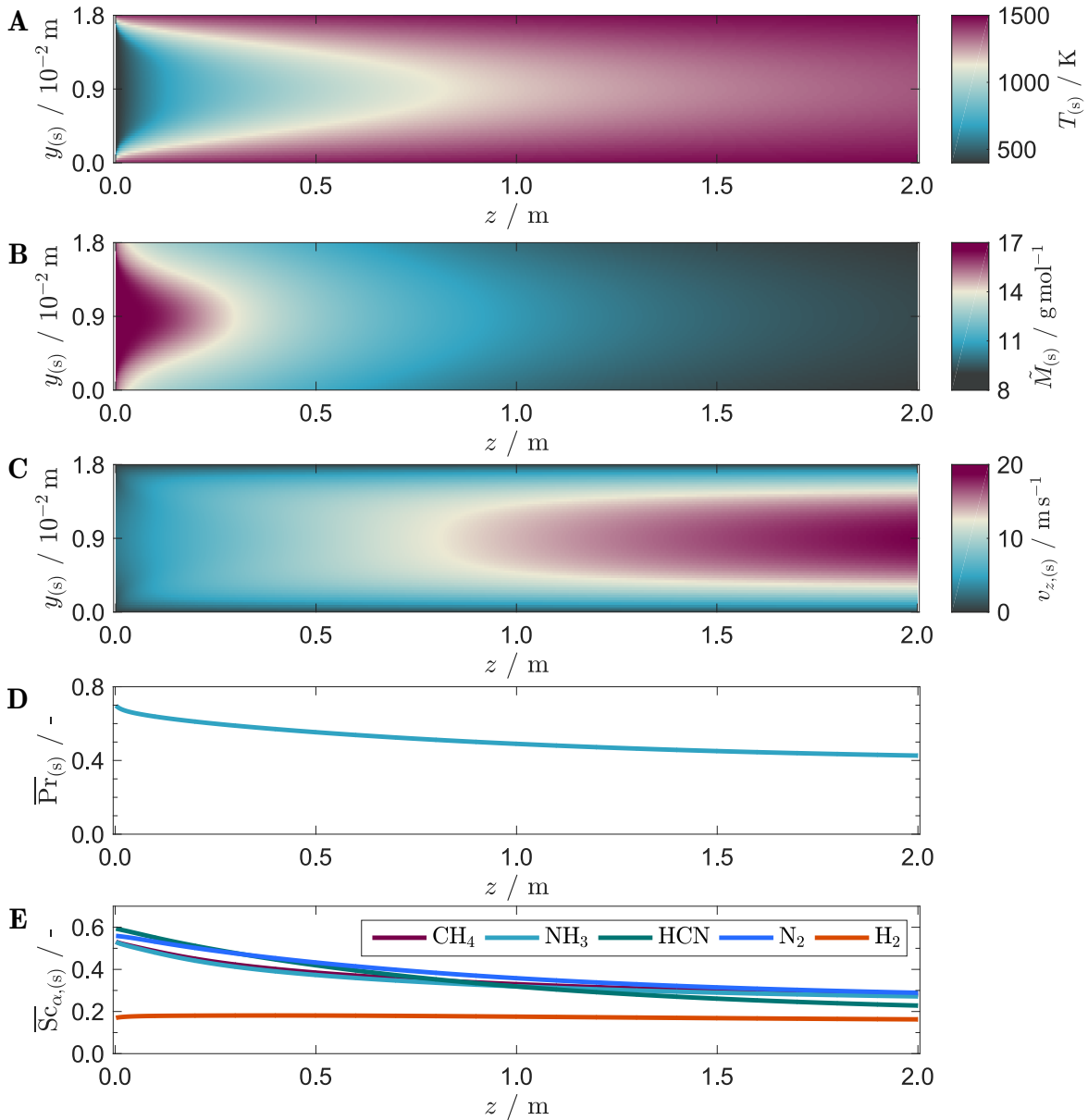
Fig. 4.9 Temperature (A), molar mass of the gas mixture (B), velocity magnitude in principle flow direction (C) as well as cross-sectional average Prandtl (D) and Schmidt numbers (E).

mixture slows down almost reaching a fully established flow profile toward the reactor outlet. Modeling of thermally dilatant flow is thus highly relevant because assuming an established Hagen-Poiseuille profile from the start would strongly overestimate residence times inside the reactor. Whereas the fluid-dynamical boundary layer forms along the reactor coordinate, the thermal and concentration boundary layers can be approximated using the Prandtl and Schmidt numbers. The Prandtl number, Pr, represents the ratio of momentum to thermal diffusivity or the ratio of the fluid-dynamical to the thermal boundary layer δ/δ_{th} and the Schmidt number, Sc, is its analog for mass transfer. The two dimensionless numbers are

defined as

$$\mathrm{Pr} := \frac{\nu}{a} = \frac{\eta c_p}{\lambda} \qquad \text{and} \qquad \mathrm{Sc}_\alpha := \frac{\nu}{D_{\alpha,\mathrm{eff}}} = \frac{\eta}{\rho D_{\alpha,\mathrm{eff}}} \quad . \tag{4.30}$$

The cross-sectional average Prandtl and Schmidt numbers from simulations of the synthesis channel model, $\overline{\mathrm{Pr}}_{(s)}$ and $\overline{\mathrm{Sc}}_{\alpha,(s)}$, are depicted in Fig. 4.9 D and E: The Pr number is calculated using mixture data whereas the effective diffusion coefficients of each species are used to calculate individual $\mathrm{Sc}_{\alpha,(s)}$ numbers for each component α. Generally, Pr numbers are in the range of 1 for gases and 0.8 for air and similar for Sc numbers. The formation of H_2, however, leads to a decrease in the Pr number from 0.7 at the inlet toward 0.4 at the reactor outlet because the overall thermal conductivity of the gas mixture increases more than its heat capacity. Consequently, diffusive heat transport (conduction) is favored over momentum transport near the outlet of the reactor.

Sc numbers also decrease along the reactor as a consequence of the chemical reactions: the change in effective diffusion coefficients is larger than the change in density except for hydrogen where the increase in the diffusion coefficient is similar to the decrease in density. H_2 has the lowest effective diffusivity and thus the lowest $\overline{\mathrm{Sc}}_{\alpha,(s)}$ values.

Impact of Turbulence and Buoyancy Forces

The flow profile is analyzed with the Reynolds number which can be interpreted as momentum convection to momentum diffusion and is defined as

$$\mathrm{Re} := \frac{vL}{\nu} = \frac{\rho vL}{\eta} \quad . \tag{4.31}$$

Despite the strong increase in velocity in Fig. 4.9 C, the flow pattern is adequately described as laminar since the cross-sectional averaged Reynolds number remains below its critical value for parallel plate internal flow of $\mathrm{Re}_{\mathrm{crit}} \approx 1200$ as shown in Fig. 4.10 A and B [187]. Whereas the local Re number indicates flow close to the transition regime at the inlet center of the reactor and toward the outlet of the reactor, Re drop sharply upon entering the reactor due to the increase in temperature: the viscosity of the gas mixture increases more than the gas velocity and thus Re values decline. The increase in Re towards the outlet of the reactor originates from the formation of hydrogen in the chemical reaction which has a lower viscosity than the reactants.

The identification of the flow regime near the inlet region and close to the reactor wall is challenging due to the large temperature gradients involved and either forced convection, mixed or free flow exist. A categorization can be made with the ratio of Grashoff number Gr versus Re squared: $\mathrm{Gr}/\mathrm{Re}^2$ [188]. Values below 0.3 are considered forced flow, in between
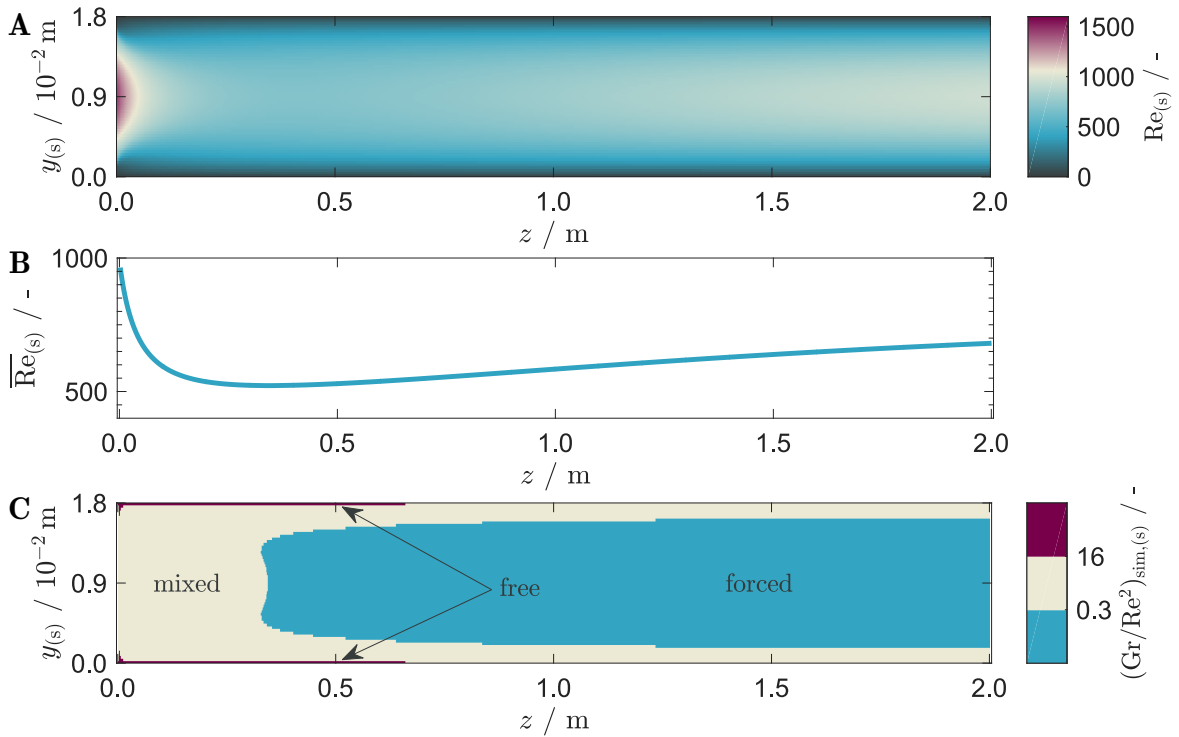
Fig. 4.10 Local Reynolds number Re (A), cross-sectional average Reynolds number (B) and Gr/Re^2 ratio from simulation to quantify the impact of buoyancy (C).

0.3 and 16 mixed flow and ratios beyond 16 free convection. This ratio is calculated using simulation and demonstrated in Fig. 4.10 C: Both mixed and forced flow play a role whereas free flow exists within the first 0.5 mm of the wall. Following the definition of the three flow regimes, mixed flow prevails close to the reactor walls and near the reactor inlet up to $z = 0.36$ m. Beyond this value, forced flow can be assumed. Overall, the largest part of the reactor is dominated by forced convection but buoyancy plays a minor role at the reactor inlet and near the reactor walls.

4.4.3   Heat Transfer Characteristics

It is the target of this section to identify the key heat transfer mechanisms in the synthesis and furnace compartments because it can lead to reactor intensification strategies. At first, the relevance of conductive, convective and radiative heat transfer is estimated using dimensionless numbers. Subsequently, the individual terms in the energy balance (4.10) are analyzed. At last, the prevalence of the heat transfer mechanisms is quantified for both synthesis and furnace compartments.

Estimation Using Dimensionless Numbers

Two dimensionless numbers help to approximate the relevance of radiative heat transfer compared to conductive and convective heat transfer: the Boltzmann number Bo and the Planck number N representing the ratio of convective-to-radiative and the ratio of conductive-to-radiative heat transfer:

$$\text{Bo} := \frac{\rho c_p v_\infty}{n^2 \sigma T_\infty^3} \qquad \text{N} := \frac{\lambda \kappa}{4 n^2 \sigma T_\infty^3} \tag{4.32}$$

where n, and σ represent the refractive index and the Stefan-Boltzmann constant whereas v_∞ and T_∞ denote the velocity and temperature in the continuum adjacent to the boundary layer. Bo and N numbers are calculated for pure reactant and product gas mixtures and transverse heat transfer in y direction. Both are illustrated in semilogarithmic graphs in Fig. 4.11 versus temperature T_∞. The Boltzmann number (Fig. 4.11 A) is well below unity
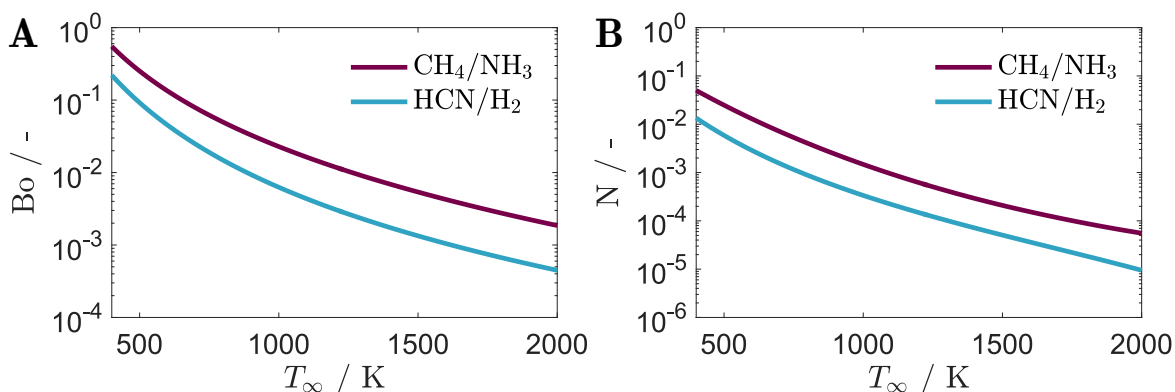
Fig. 4.11 Boltzmann Bo (A) and Planck N (B) numbers versus T_∞ for pure reactant and product gas mixtures ($1/1 = \text{CH}_4/\text{NH}_3$ (red) and $1/3 = \text{HCN}/\text{H}_2$ (blue).

for the transverse velocities that attain maximum values up to $0.1\,\text{m}\,\text{s}^{-1}$. With increasing temperature, Bo numbers decrease due to the T_∞^3 factor for both sample gas compositions. Convective heat transfer is therefore expected to be significantly lower in y direction than radiative heat transfer.

The Planck number N is calculated using both temperature and composition dependent Planck mean absorption coefficients and illustrated in Fig. 4.11 B. Similar to Bo numbers, N remains well below unity due to the low gas mixture absorption coefficients and thermal conductivities. Similar to the Boltzmann number, this effect is emphasized at higher temperatures indicating that conduction is negligible compared to radiation.

Analysis of the Energy Balance of the Synthesis Side

In order to identify the relevant heat transfer mechanisms in the reactor, all nine contributing terms χ_i with $i \in \{1, ..., 9\}$ of Eq. (4.10) are integrated and ranked in a semilogarithmic graph in Fig. 4.12. The simulation results are shown for a constant radiative absorption coefficient $\kappa = 4.0$ bar^{-1}m^{-1} which is an approximate value for a 50:50 mixture of CH_4:NH_3 and read from Hottel charts [120]. The buoyancy term (χ_9) is in the order of 10^{-5} and therefore not visualized in Fig. 4.12. Red color is used for terms with magnitudes larger
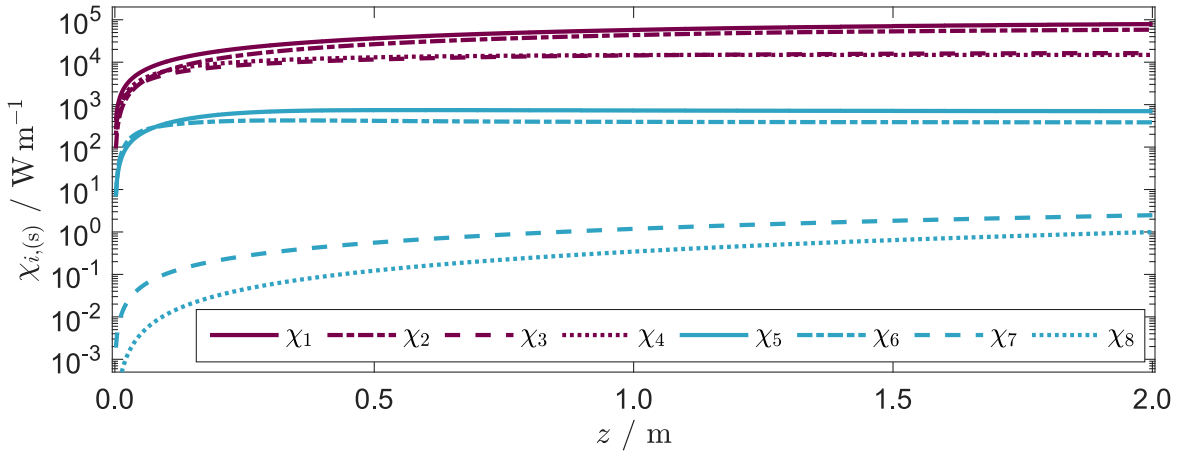
Fig. 4.12 Integration of the energy balance in separate terms (χ_i) split into terms of major (red) and minor (blue) importance: χ_1...conduction in y direction, χ_2...heat of reaction, χ_3...convection in z direction, χ_4...radiative heat transfer in y direction, χ_5...enthalpy diffusion, χ_6...convection in y direction, χ_7...pressure loss term, χ_8...dissipation (comp. Eq. (4.10)).

than 10^3 while blue color highlights all terms of smaller magnitudes. Enthalpy diffusion (χ_5), convection in $y_{(s)}$ direction (χ_6), pressure work (χ_7) as well as dissipation losses (χ_8) are of minor magnitudes compared to the other terms in the energy balance. The small contributions of enthalpy diffusion, pressure work and dissipation losses in gas flows confirm standard literature where these terms are often neglected a priori [189]. The irrelevance of convective heat transfer in transverse direction $y_{(s)}$ is in agreement with the estimates of the Bo number.

The main contributors of the energy balance that are highlighted in red color in Fig. 4.12 represent conductive heat transfer in y direction (χ_1), heat of reaction (χ_2), convection in z direction (χ_3) and radiative heat transfer in y direction (χ_4). The importance of conductive heat transfer into the synthesis compartment is in contrast to the estimations using the Planck number. This difference originates from the fact that the catalytic synthesis reaction occurs directly at the channel wall surface. The major fraction of the heat of reaction is thus supplied by conductive heat transfer. The prevalence of conductive and radiative heat

transfer in transverse direction y are analyzed next but prior to that the impact of the absorption coefficient model on the simulation results is demonstrated.

Impact of the Absorption Coefficient Model on Reactor Temperature Profiles

Average temperature levels and absorption coefficients along the reactor coordinate z are shown in Fig. 4.13 for four different assumptions regarding the radiative absorption coefficient: a constant $\kappa_{P,(s)}$ of 4 m^{-1} in the entire reactor (scenario I, green); a composition dependent but temperature independent $\kappa_{P,(s)}$ of 4 bar^{-1}m^{-1} (scenario II, blue) are compared with data using correct temperature and species dependence of the absorption coefficient (scenario III, red). All results are compared with the average temperature if radiative heat transfer is neglected (scenario IV, black). If radiation is neglected, the gas mixture heats up significantly slower
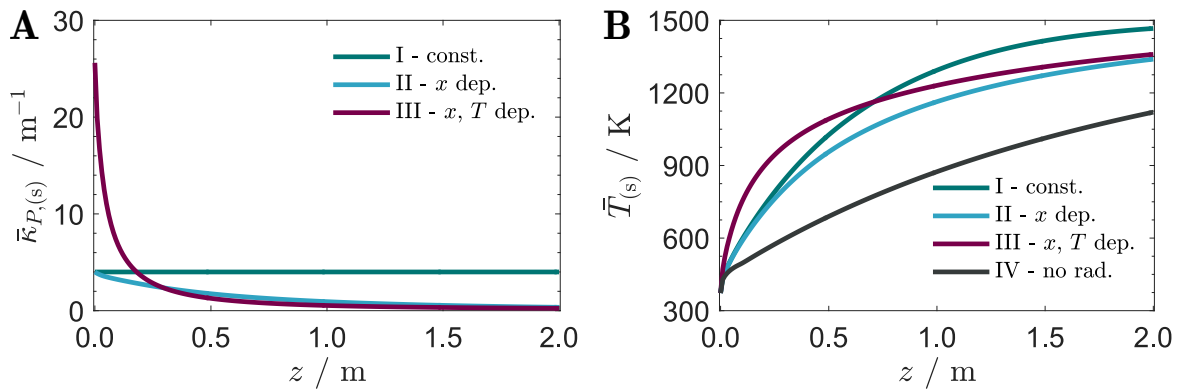
Fig. 4.13 Cross-sectional average temperature $\overline{T}_{(s)}$ (A) and average $\overline{\kappa}_{P,(s)}$ (B) along the reactor coordinate z for four radiation model scenarios: "I - const.": constant $\kappa_{P,(s)}$ of 4 m^{-1} (green), "II - x dep.": species but not temperature dependent, $\kappa_{P,(s)} = 4$ bar^{-1}m^{-1} for NH$_3$ and CH$_4$ (blue), "III - x, T dep.": species and temperature dependent $\kappa_{P,(s)}$ (red) and "IV - no rad.": no radiative heat transfer (black).

compared to the models that take radiation into account achieving an outlet temperature of 1120 K compared to 1360 K for the correct species and temperature dependent model (Fig. 4.13 B). Comparing the constant absorption coefficient approximation (I) and the correct species and temperature dependent model (III) in Fig. 4.13 (A), the constant coefficient approximation (I) underestimates radiative absorption near the inlet of the reactor and overestimates $\kappa_{P,(s)}$ for $z > 0.23$ m. This is clearly visible in the temperature graph in Fig. 4.13 (A) where the temperature of (I) increases more slowly than (III) at the inlet but keeps increasing until the reactor outlet. Modeling of the species but not temperature dependency illustrated by scenario (II) also underestimates radiative absorption near the inlet region but leads to slightly higher overall absorption coefficients compared to the correct substrate and temperature dependent scenario (III) beyond $z = 0.28$ m. The correct species and temperature dependent model (III) exhibits the highest absorption coefficient values

near the reactor inlet. Consequently, the highest temperature slope in Fig. 4.13 (B) out of all scenarios occurs before $z = 0.23$ m. Caused by the sharp decline of $\kappa_{P,(s)}$ with increasing temperature in model (III), however, $\kappa_{P,(s)}$ drops below (I) and (II) after $z = 0.23$ m leading to the most shallow temperature slope of all three scenarios. Coincidentally, the second modeling scenario (II) results in similar outlet temperatures as model (III) due to the switch from under- to overestimation of $\kappa_{P,(s)}$.

Identification of Key Heat Transfer Mechanisms for Synthesis and Furnace Sides

The four absorption coefficient scenarios show the importance of radiative heat transfer for the heat uptake of the gas mixture on the synthesis side. Based on simulation data of the rigorous physical reactor model, the key heat transfer mechanisms for the reactor are identified. For this purpose, a local and an integral conduction-to-radiation ratio N_{sim} are defined based on local conductive and radiative wall heat fluxes as well as the integrated terms of the energy balance that were shown in Fig. 4.12 as:

$$N_{sim}(y, z) := \frac{q_y^{(c)}(y, z)}{q_y^{(r)}(y, z)} \qquad \text{and} \qquad N_{sim,int} := \frac{\chi_1(L)}{\chi_4(L)} \quad . \tag{4.33}$$

They are illustrated in Fig. 4.14 for the furnace (A) and synthesis sides (B and C). Starting with the synthesis compartment, the dark gray region at the center and inlet of the reactor in Fig. 4.14 B indicates that radiative heat transfer is the dominant mode of heat transfer in this region whereas conduction dominates right at the walls providing heat to the chemical reaction and in particular in the inlet region where the thermal boundary layer starts to form (until $z = 0.15$ m). The second half of the reactor where the flow profile is more established ($z > 1$ m) is dominated by conductive heat transfer. However, 70% of the cumulative heat transferred via the walls into the reactor occurs in the first half of the reactor as shown in Fig. 4.14 C.

Overall, the cumulative wall heat fluxes into the synthesis compartment are governed by conduction with 79.9% whereas radiative heat transfer accounts for 20.1%. These findings seem to contradict the Planck number results in Fig. 4.11 B at first glance that showed a clear dominance of radiative heat transfer in the temperature range of interest. The main reason is that both parameters do not describe the same scenario: Whereas the original Planck number N indicates the heat transport through the gas, N_{sim} indicates the heat uptake of the gas itself. Radiation propagates to much higher extents through the gas compared to conduction as indicated in Fig. 4.11 B. The low optical thickness of the gas mixture minimizes resistance to radiative heat transfer through the fluid but as a consequence, it is mostly transparent to radiation absorbing only little heat itself. Therefore, heat uptake of the gas mixture due to

synthesis compartment   furnace compartment
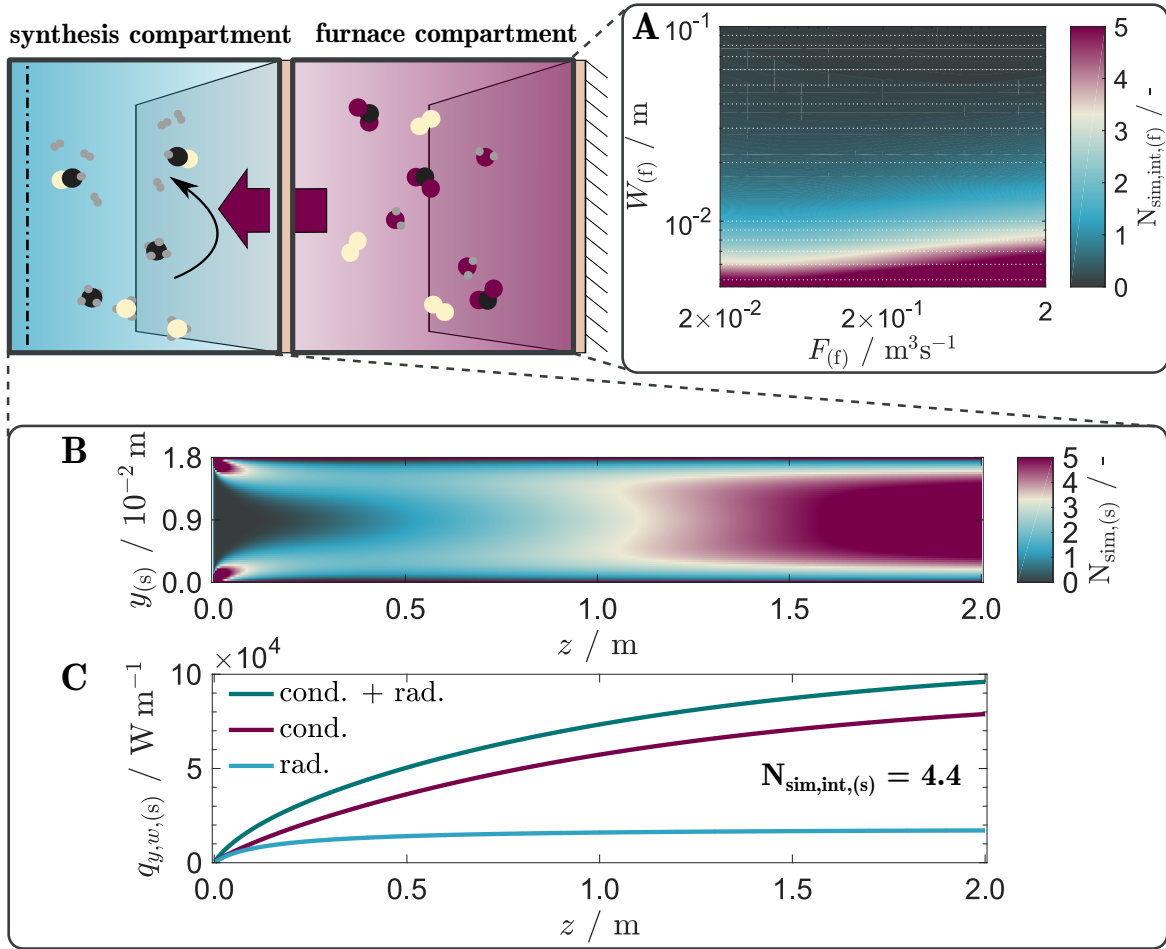
Fig. 4.14 Analysis of conductive and radiative heat transfer: local conductive fraction $N_{sim,(s)}$ (B) and conductive and radiative wall heat fluxes (C) on the synthesis side and the integral conductive fraction $N_{sim,int,(f)}$ for non-reactive flow on the furnace side versus furnace width and flue gas volume flows (A).

radiative heat transfer is of second order importance compared to conduction. In addition, the catalytic synthesis reaction occurs at the surface of the wall where heat is supplied directly through conduction leading to high overall conductive heat fluxes into the synthesis compartment summing up to an integral Planck number of $N_{sim,int} = 4.4$. Consequently, both Planck number results complement each other.

Expanding the analysis of conductive versus radiative heat transfer to channel compartments in general is done using the furnace compartment in Fig. 4.14 A: The integrated Planck number is illustrated versus volume flows $F_{(f)}$ and versus channel width $W_{(f)}$. The furnace inlet temperature is $T_{(f)}(z = 0) = 1800\,\mathrm{K}$ and the flue gas composition is based on the complete combustion of CH_4 with air: $x_{N_2,(f)} = 0.73$, $x_{H_2O,(f)} = 0.18$, $x_{CO_2,(f)} = 0.09$. The volume flows are indicated per meter channel depth and a wall thickness $t_{(w)}$ of $1 \times 10^{-3}\,\mathrm{m}$ is selected. From this perspective, the synthesis compartment flow of the previous simulations

would be at a $1.8 \times 10^{-2}\,\mathrm{m}$ and at a volume flow of $3.6 \times 10^{-2}\,\mathrm{m^3\,s^{-1}}$ yielding an integrated Planck number of $N_{\mathrm{sim,int}} = 0.9$ on the furnace side versus the actual value of $N_{\mathrm{sim,int}} = 4.4$. This strong difference between synthesis and furnace side originates from the catalytic wall reaction. Integral Planck numbers for hot gas flows without chemical reactions are almost independent of the volume flow in the furnace channel and a function of channel width as shown by the horizontal edge in Fig. 4.14 A. As a rule of thumb for non-reactive flows, conductive heat transport dominates below $1 \times 10^{-2}\,\mathrm{m}$ and radiation beyond $2 \times 10^{-2}\,\mathrm{m}$.

4.4.4 Reactor Design with Enhanced Heat Transfer

Having completed the heat transfer analysis, the model is used to identify reactor designs with enhanced heat transfer. As mentioned in chapter 3, the reaction kinetic expressions are not suitable for the optimization of the feed conditions or temperature and concentration profiles along the reactor. Instead of mathematical optimization, a simulation-based approach is chosen at this point because the optimality criteria cannot be defined unambiguously in the absence of the bundle and plant context. The target product quality is indicated using the product yield of HCN (Fig. 4.15 A,B) which is defined as the product of selectivity of HCN and conversion of NH_3:

$$Y_{\mathrm{HCN}} \;:=\; X_{\mathrm{NH_3}} S_{\mathrm{HCN}} \quad . \tag{4.34}$$

Selectivity and conversion are defined as

$$X_{\mathrm{NH_3}} := \frac{n_{\mathrm{NH_3}}(z=0) - n_{\mathrm{NH_3}}(z=L)}{n_{\mathrm{NH_3}}(z=0)} \tag{4.35a}$$

$$S_{\mathrm{HCN}} := \frac{n_{\mathrm{HCN}}(z=L) - n_{\mathrm{HCN}}(z=0)}{\sum\limits_{\mathrm{prod.i}} n_{\mathrm{i}}(z=L) - n_{\mathrm{i}}(z=0)} \quad . \tag{4.35b}$$

In addition, the space time yield of the designs are compared as quantitative indicators. The space time yield STY_{HCN} is defined as

$$STY_{\mathrm{HCN}} := \frac{n_{\mathrm{HCN}}(z=L) - n_{\mathrm{HCN}}(z=0)}{V_{\mathrm{cat}}} \quad . \tag{4.36}$$

In the absence of reliable information about the catalyst volume, the thickness of the catalyst layer is assumed to equal $1 \times 10^{-4}\,\mathrm{m}$ which is a typical value in microchannel MSR reactors [147]. With respect to the synthesis side, a parameter design study is presented in Fig. 4.15 A,B,C and D: Variation of half-width on the ordinate and space time on the abscissa are selected over reactor length because the amount of catalytic active material remains constant. Space time is defined for the synthesis side as $\tau := V_{(\mathrm{s})}/F_{(\mathrm{s})}(z=0)$. The channel design of the simulations above that corresponds to industrial values is highlighted with a box
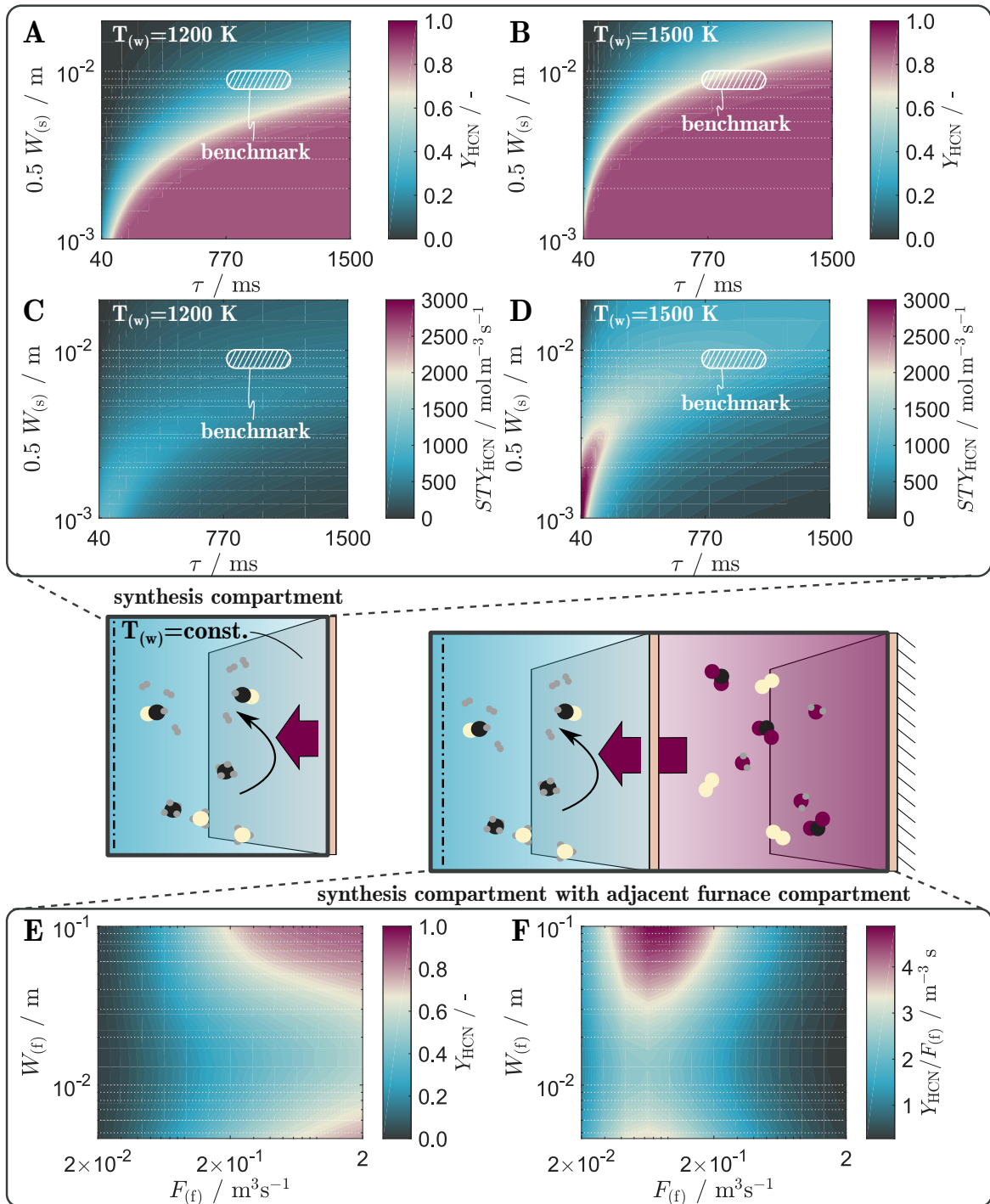
Fig. 4.15 Design aspects of the synthesis (A,B,C,D) and furnace side (E,F): yield and space time yield versus half-width and space time for wall temperatures of 1200 K (A,C) and 1500 K (B,D) and yield (E) and yield per flue gas flow (F) for a grid of furnace volume flows and widths.

("benchmark") in all four graphs because a precise value of the space time in BMA reactors for HCN synthesis is not available in literature [104]. In addition, tube and channel geometries

are not directly comparable. In scenarios Fig. 4.15 A and C, the bounding wall temperature of the single compartment is set to $1200\,\mathrm{K}$ whereas in B and D to $1500\,\mathrm{K}$ as in the studies above.

Maintaining the operating parameters as indicated in Tab. 4.1, a high yield above $Y_{\mathrm{HCN}} \geq 0.80$ is attained for the high wall temperature but it can be improved by $2-3\,\%$ via a reduction of the channel width by $1 \times 10^{-3}\,\mathrm{m}$ (Fig. 4.15 B). Reducing the wall temperature to $1200\,\mathrm{K}$ leads to decrease in yield to $0.4-0.6$ within the benchmark region (Fig. 4.15 A). With respect to space time yields (Fig. 4.15 C, D), STY_{HCN} decreases approximately by a factor of three if the wall temperature is reduced from $1500\,\mathrm{K}$ to $1200\,\mathrm{K}$ throughout the design space of widths and space times: space time yields decrease for larger widths because the yield decreases and for longer space times because the product volume flow is reduced. As a consequence, maximum values of STY_{HCN} are found at the most narrow reactor width and at the shortest residence times. In summary, lower reactor wall temperatures result in lower yields and space time yields but also in a reduction in the energy requirements of the reactor. High yields compete with high space time yields because space time yields decrease with increasing space times. This interplay of product quality, quantity and energy requirement is addressed in the context of the plant design in chapter 6.

The coupling of the synthesis and furnace models is used to study the impact of variations of furnace width and of flue gas flow on the yield in the synthesis compartment as illustrated in Fig. 4.15 E. For this purpose, the design parameters of the benchmark of the synthesis compartment are selected. The graph demonstrates, that high yields are attainable for flue gas volume flows greater than $2 \times 10^{-1}\,\mathrm{m^3\,s^{-1}}$ and two furnace width designs: for narrow flue gas channels below $8 \times 10^{-3}\,\mathrm{m}$ width resulting in high flue gas velocities and for widths that are larger than $3 \times 10^{-2}\,\mathrm{m}$ with corresponding long residence times of the hot flue gases. With the latter, maximum yields of $Y_{\mathrm{HCN}} \approx 0.85$ are attainable.

Fig. 4.15 F illustrates the yield per flue gas volume flow ratio indicating the fuel efficiency of the reactor-furnace coupling: despite the high yields that are attainable for narrow flue gas channels around the synthesis compartment, the corresponding fuel efficiency is low because only a fraction of the heat of the fast-flowing flue gas can be transferred to the synthesis compartment. Maximum fuel efficiency is located where the flue gas channel width attains its maximum and flue gas residence times are long. The optimal coupled design from the fuel efficiency perspective would thus be with a channel of $1 \times 10^{-1}\,\mathrm{m}$ and gas flows in the range $3 \times 10^{-2} - 2 \times 10^{-1}\,\mathrm{m^3\,s^{-1}}$. A compromise between high yield and fuel efficiency of the reactor design is with maximum width and a flue gas volume flow of $3 - 4 \times 10^{-1}\,\mathrm{m^3\,s^{-1}}$.

Overall, the results show that weighing of objectives is required to identify the adequate reactor design and operating point for a specific scenario with either high product purity

but high energy costs involved or reduced energy cost at the expense of a decline in product purity not to mention effects on space time yields.

4.5 Chapter Summary

This chapter presented a two-dimensional steady channel reactor model for high temperature catalytic gas phase reactions with an emphasis on modeling of radiative heat transfer. Two scenarios of the synthesis compartment – with a constant wall temperature boundary condition and with an adjacent furnace compartment – are modeled in order to quantify the underlying transport mechanisms and propose reactor intensification strategies. The model was validated successfully using literature data for the two examples of HCN synthesis and MSR. The reactive flow accelerates rapidly inside of the reactor due to the temperature increase and mole number increasing chemical reaction that yields large amounts of H_2 for both case study examples. Therefore, fluid-dynamical, thermal and concentration boundary layers undergo continuous changes along the reactor length. It is shown that the flow is in the laminar region and buoyant forces play a minor role for an upright orientation of the HCN reactor. Heat flow in axial direction is – by design – governed by convection whereas radiative and conductive heat transfer are both significant for the heat uptake of the gas mixture in the synthesis compartment accounting for $20\,\%$ and $80\,\%$ of total heat transferred into the synthesis compartment. Considering a hot flue gas flow on the furnace side yields a radiation-dominated heat transfer for channel widths larger than $1 \times 10^{-2}\,\mathrm{m}$ for any flow rate. For both reactor compartments, species and temperature dependent modeling of the absorption coefficient is necessary for an accurate description of the temperature profile in the reactor. Through doubling of the emissivity of the bounding walls of the synthesis compartment from 0.45 to 0.90, an increase in $30\,\mathrm{K}$ of the outlet temperature is achievable for example through the use of silicon carbide instead of alumina as a wall support material. Design studies for the synthesis side show that a reduction in channel width by $1 \times 10^{-3}\,\mathrm{m}$ results in an increase in yields by $2-3\,\%$. Space time yield and yield are competing objectives because the space time yield decreases for increasing residence times in the reactor tubes. Upon reduction of the wall temperature from $1500\,\mathrm{K}$ to $1200\,\mathrm{K}$, space time yields decrease by factor of three for any reactor design. As a rule of thumb, any long and narrow channel design with high wall temperature is good to achieve high yields.

In summary, there exist three competing objectives: either high yields – i.e. product quality – or high space time yields at the expense of yields are attainable. An additional objective comes into play if the fuel efficiency of the furnace is taken into account: one has to balance between high yields and high fuel efficiency i.e. yield per flue gas flow invested. As a consequence, no specific design is favored at this hierarchical level but promising parameter

variations are identified for decision making at the higher-order levels: comparison of channel widths are addressed at the level of the tube bundle in chapter 5. The interplay of yield, space time yield and energy requirement is reconsidered at the plant level in chapter 6.

Chapter 5

Optimal Design of the Tube Bundle in the Furnace

The research questions (I), (II) and (III) are addressed at the tube bundle level in this chapter. The previous chapter revealed that heat transfer mechanisms at the single compartment level are conduction and radiation dominated and this is scrutinized at the bundle level in this chapter. The identification of the reactor intensification potential of the overall tube bundle furnace is challenging using mathematical optimization: individual solutions of the full-scale CFD model are obtained at the expense of high computational cost due to the size and complexity of the entire tube bundle furnace system. In addition, experimental validation of the overall reactor is hardly possible. Operating parameters aside, the optimal design and topology of a tube bundle furnace is thus scarcely addressed in literature using optimization techniques. In order to maximize heat transfer to the individual tubes of the bundle, multiple design parameters of the tube bundle furnace system can be optimized ranging from material properties like surface emissivities, to tube bundle arrangements and furnace topologies in two up to three dimensions using a full-scale model. To begin with, the scope of this chapter is set to a suitable reduction of the modeling complexity to enable the design optimization. By means of the simplified model, surface emissivities and the arrangement of the individual tubes inside the furnace are investigated utilizing results of chapter 4. Consecutively, an outlook on furnace topology is provided in the appendix in Sec. C.2.

Out of the three performance indicators that were used at the single compartment level – product purity in terms of yield Y_{HCN}, quantity described by space time yield STY_{HCN} and fuel efficiency – attaining a high product purity is emphasized over the other two aspects at the tube bundle level for two reasons: the weighing of yield and space time yield is more suitable at the plant scale and fuel efficiency of the furnace design cannot be investigated unless the energy balance for the furnace is considered. As shown in the following section, the

first design step is achieved using flow field assumptions and neglecting flue gas flow in the furnace. The consecutive solution of the flow field in the furnace to validate the assumptions of the first step is addressed in collaboration with the laboratory of fluid dynamics at OvGU and first results are currently under review [92]. As a consequence, the yield of HCN is a key performance indicator of the tube bundle designs in this chapter.

As in the previous chapter, the literature for tube bundle reactor design is reviewed first followed by the model development for the tube bundle. After that, a strategy for tube bundle design is identified and applied to the BMA Endter reactor [104]. The findings at the tube bundle level are summarized in a brief summary at the end of this chapter.

5.1   Literature Context

While furnace models that incorporate radiative heat transfer are abundant in literature, the characterization, comparison and optimization of tube bundle arrangements in furnaces are addressed scarcely. Instead, it is limited to view factor calculation and Nusselt number correlations in textbooks in order to approximate convective heat transfer in bundles [174, 120, 190, 191]. More information can be found in recent journal publications that focus on reforming as the most relevant furnace bundle design: the identification of optimal heat flux profiles for single reforming tubes using a physics-based PDE model was published in 2001 and Olivieri and Vegliò [192] investigated the fuel distribution in the furnace along the reactor coordinate splitting the furnace length into "firing" and "non-firing" zones [160]. The first three-dimensional CFD-based reformer model was published two years later and Zheng et al. [193] discussed the ideal number of flue gas exhaust channels at the bottom of a top-fired reactor in order to manipulate the temperature profile in the furnace. Higher fidelity CFD-based models based on single-tube reforming models were published by Tran et al. [156] who validated their model against industrial data [194]. Based on this model they modified gas flows across the cross section of their reformer in order to homogenize the temperature profile along the reformer length. This is important because a limiting factor of reforming design is the temperature stability of the individual reforming tubes that suffer from large temperature gradients along the reactor length [195]. Kumar et al. [61] performed a similar study by grouping tubes into clusters and by utilizing reduced order but physics-based models.

Besides the recent progress in modeling and understanding of reforming furnaces the contributions that have addressed the reformer optimization are limited to operational optimization which refers to the identification of the optimal operating parameters of the reformer to improve the overall performance [193, 61]. Beyond operating parameters, the scrutiny of existing designs and the design optimization for an entire tube bundle have not been ad-

dressed. In order to do so, a reduction of the full-scale modeling complexity is essential due to high computational costs of the optimization of the full-scale model. For example, the bundle of a heat exchanger was optimized in CFD under the assumption of few tubes, two-dimensional flow and a narrow temperature window with constant fluid properties [78]. For high temperature reactors, careful selection of modeling assumptions is thus significant in order to identify the key design parameters for the optimization which is often not reported in a detailed way: for example Olivieri and Vegliò [192] and Tran et al. [156] refer to Yu et al. [196] to justify that radiation dominates heat transfer on the furnace side with 95 % of total heat transferred. As shown in Chap. 4, such modeling assumptions require scrutiny in order to reduce a model to its essential constituents [91, 197]. Therefore, the modeling assumptions are emphasized in the derivation of the tube bundle furnace model in the following section.

5.2 Tube Bundle Furnace Model

Optimization of the tube bundle furnaces in MSR and HCN BMA reactors is equivalent to the maximization of heat transfer to the individual tubes of the bundle. The furnace-bundle system exhibits several modeling challenges such as chemical reactions both within the gas phase (furnace) and on the surface (synthesis), radiation and complex geometries causing turbulence and often unsteady flows. In order to optimize the tube bundle furnace, a reduction
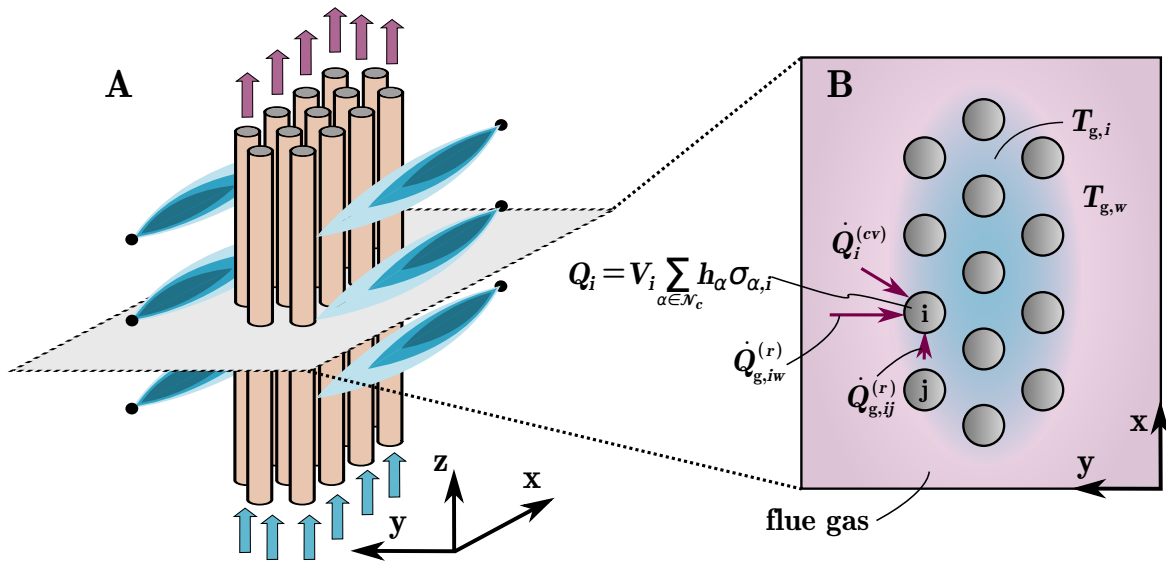
Fig. 5.1 Sketch of a tube bundle furnace for HCN synthesis according to Endter [104] with the three coordinates x, y and z (A) and two-dimensional cut in the x-y plane illustrating the heat flows toward tube i from tube j and the furnace enclosure walls, the temperatures between tubes $T_{g,i}$ and between burners and tubes $T_{g,w}$ (B).

of the modeling complexity is useful: the model is narrowed down to its key aspects that govern design decisions while accuracy is sacrificed.

The tube bundle furnace in Fig. 5.1 A is therefore modeled according to the schematic illustration in Fig. 5.1 B: a quasi-homogeneous temperature along the reactor height (z-coordinate) is assumed enabling the formulation of a two-dimensional model. The staggered bundle arrangement in this illustration corresponds to tube positions inside the historic BMA Endter reactor [104]. The tube bundle with tubes $i \in \mathcal{N}_t := \{1, 2, ..., j, ..., N_t\}$ is bounded by a rectangular furnace cross section and $\mathcal{N}_t$ denotes the set of all tubes whereas N_t the total number of all tubes in the bundle. The furnace walls are contained in the set $\mathcal{N}_w$: $w \in \mathcal{N}_w := \{1, 2, ..., N_w\}$. This two-dimensional cut represents a significant simplification, but it is justified by the larger gradients in the furnace-tube system in the x,y-plane compared with the z direction. In addition, the aforementioned key features such as the shadowing between tubes as well as the impact of the emissivity of the flue gas are maintained in the two-dimensional model. The two-dimensional model is then used to address the design objective: to maximize heat transfer from the flue gas toward each individual tube of the tube bundle. The correlations of wall heat fluxes and yields of the desired product HCN versus tube wall surface temperature are taken from the single compartment model that is described in chapter 4 [197].

5.2.1   Wall Temperature Correlations for HCN Synthesis

The system of PDEs for a single compartment in Sec. 4.2.1 describes a channel reactor but the heat uptake of a cylinder geometry is required for the bundle optimization in this chapter. The wall heat flux is thus converted for a cylinder using an equivalent wall surface for heat transfer from the outer compartment which is explained in the appendix in Sec. C.1. As discussed in the model introduction for the single synthesis compartment, this assumption of equal heat transfer and yield of channel and cylinder for equal heat transfer areas is not accurate because the reactor volume of the channel reactor is twice as large as the cylinder reactor under these assumptions. However, this systematic difference does not affect the qualitative findings at the tube bundle level. As a consequence of the different reactor volumes of channel and cylinder at the single compartment level the use of space time yield as a reactor performance indicator is not recommendable at the tube bundle level. Instead, tube surface temperatures and product yields are used to evaluate the bundle designs in this chapter. The tube bundle design strategy that is presented in this chapter was transferred to MSR in Engel et al. [92] using a cylindrical tube model for single reaction compartments.

The solution of the PDE system of Sec. 4.2.1 for different constant wall surface temperatures $T_{(w)}$ results in correlations for heat transferred to a single channel Q_i and product yield Y_{HCN}

as shown in Fig. 5.2 A and B. Based on Fig. 4.15 A and B, four inner channel widths are selected
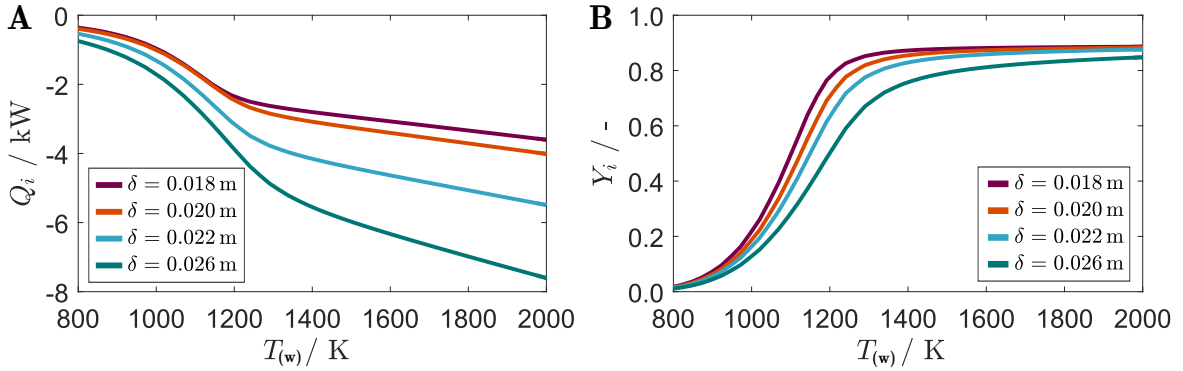
Fig. 5.2 Heat flow across the bounding wall (A) and yield of HCN (B) of a single compartment versus tube wall surface temperatures $T_{(w)}$ for HCN synthesis and four outer tube diameters: $\delta = 0.018\,\mathrm{m}$ (magenta), $\delta = 0.020\,\mathrm{m}$ (red-orange), $\delta = 0.022\,\mathrm{m}$ (blue) and $\delta = 0.026\,\mathrm{m}$ (green).

close to the benchmark scenario: $W_{(s)} \in \{0.016,\ 0.018,\ 0.020,\ 0.024\}\,\mathrm{m}$. where $W_{(s)} = 0.018\,\mathrm{m}$ is the same width as in the first part of the single compartment simulations in chapter 4. Their equivalent inner tube diameters are defined equal to these channel widths and the wall heat flux Q_i for each tube is converted assuming equal surface areas of channel and cylinder as described in the appendix in Sec. C.1. Assuming a tube wall thickness of $0.001\,\mathrm{m}$, the outer equivalent tube diameters are obtained as $\delta := d_{(s),\mathrm{out}} \in \{0.018,\ 0.020,\ 0.022,\ 0.026\}\,\mathrm{m}$ that are indicated in Fig. 5.2. For the smallest equivalent diameter of $\delta = 0.018\,\mathrm{m}$ (magenta) the maximum yield is attained at $T_{(w)} = 1243\,\mathrm{K}$ whereas the yield of HCN for the largest channel width of $\delta = 0.026\,\mathrm{m}$ (green) increases up to the maximum temperature of $2000\,\mathrm{K}$ due to the transport limitations inside the channel. In between are $\delta = 0.020\,\mathrm{m}$ (red-orange) that is close to the smallest diameter and $\delta = 0.022\,\mathrm{m}$ (blue): surface wall temperatures above $1400\,\mathrm{K}$ are required to reach the maximum yield.

5.2.2 Energy Balances for Individual Tubes

The two-dimensional furnace model is based on energy balances for each individual tube as illustrated in Fig. 5.1 B: the heat of reaction inside the i-th tube is supplied by three types of heat flows: convective heat flow from its surroundings $\dot{Q}_i^{(cv)}$, radiative heat exchange with hot flue gas between the tube and furnace walls $\dot{Q}_{\mathrm{g},iw}^{(r)}$ and radiative heat exchange with gas between the tubes $\dot{Q}_{\mathrm{g},ij}^{(r)}$. The index "g" denotes the flue gas. The distinction between wall facing and tube facing radiative heat flows is made because flue gas temperatures close to walls and burner inlets are assumed higher than between tubes as shown in CFD studies of reformers [193]. Conductive heat flows are neglected because the previous chapter 4 showed that conduction becomes negligible for distances above one centimeter which is fulfilled within

the furnace. The energy balance for each tube i is therefore formulated as

$$\dot{Q}_i^{(cv)} + \sum_{w \in \mathcal{N}_w} \dot{Q}_{g,iw}^{(r)} + \sum_{j \in \mathcal{N}_t,\, j \neq i} \dot{Q}_{g,ij}^{(r)} + Q_i = 0 \qquad \forall i \in \mathcal{N}_t \quad . \tag{5.1}$$

Similar to the single compartment level $\mathcal{N}_c$ is the set of all components inside the tubes. While the heat flows supply heat to the tubes, the endothermic synthesis reaction inside the tubes requires the heat duty

$$Q_i = V_i \sum_{\alpha \in \mathcal{N}_c} h_\alpha \sigma_{\alpha,i} \tag{5.2}$$

where V_i, h_α and $\sigma_{\alpha,i}$ denote the volume of tube i, the enthalpy and volume specific source term of component α. This heat consumption in dependence of the wall surface temperature is obtained from the single compartment level. The three heat flows in the single tube energy balance (5.1) are calculated as

$$\dot{Q}_i^{(cv)} = \alpha_{g,i}^{(cv)} A_i (T_{g,w} - T_{(w),i}) \quad , \tag{5.3a}$$

$$\dot{Q}_{g,iw}^{(r)} = \frac{1}{R_{g,iw}} \sigma (T_{g,w}^4 - T_{(w),i}^4) \quad \text{and} \tag{5.3b}$$

$$\dot{Q}_{g,ij}^{(r)} = \frac{1}{R_{g,ij}} \sigma (T_{g,j}^4 - T_{(w),i}^4) \quad . \tag{5.3c}$$

Convective heat flows are determined by the convective heat transfer coefficient $\alpha_{g,i}^{(cv)}$ and the surface area A_i of tube i. $T_{(w),i}$ denotes the surface temperature of tube i. Furthermore, the analogy of radiative heat transfer to electrical currents is used [190]: the current i.e. the radiative heat flow from for example the gas to tube i is determined as the potential difference given by the blackbody emissivity divided by the total resistance. $R_{g,iw}$ and $R_{g,ij}$ represent the total radiative resistances between flue gas, wall w and tube i and between flue gas and tubes i and j respectively. Throughout this chapter, the higher temperature $T_{g,w}$ between tubes and walls is used to estimate the convective heat transfer to all tubes. The radiative resistances between tubes and walls are dependent on the furnace geometry i.e. on the wall areas A_w as well as the tube diameters that result in tube surface areas A_i. In addition, they are a function of the emissivities of the tubes ϵ_i and the furnace gas emissivity ϵ_g which is modeled as an absorbing and emitting gray gas. Lastly, the overall resistances are dependent on view factors between tube i and walls w – φ_{iw} – as well as between tubes i and j – φ_{ij}. The view factor is defined as the fraction of the heat flow leaving surface A_i that is exchanged with surface A_j:

$$\mathrm{d}\dot{Q}_{ij} = \varphi_{ij} \mathrm{d}\dot{Q}_i \quad . \tag{5.4}$$

For a given furnace geometry, the furnace walls A_w are fixed. In total the radiative resistances of tube i are therefore dependent on

$$
\begin{aligned}
R_{\mathrm{g},iw} &= R_{\mathrm{g},iw}\left(\epsilon_{\mathrm{g}}, \epsilon_i, \varphi_{iw}(x_i, y_i, x_j, y_j), A_i, A_j\right) \qquad \text{and} \\
R_{\mathrm{g},ij} &= R_{\mathrm{g},ij}\left(\epsilon_{\mathrm{g}}, \epsilon_i, \varphi_{ij}(x_i, y_i, x_j, y_j), A_i, A_j\right) \quad \forall j \in \mathcal{N}_t, i \neq j \quad .
\end{aligned}
\tag{5.5}
$$

It is crucial to keep in mind that the total resistance between any wall w and any tube i is in general dependent on all other tube positions as they may obstruct the visibility of wall w by tube i and analog for inter-tube resistances.

Fig. 5.3 illustrates the wiring scheme that constitute $R_{\mathrm{g},iw}$ and $R_{\mathrm{g},ij}$ for the example of $R_{\mathrm{g},iw}$. The total radiative resistance $R_{\mathrm{g},iw}$ consists of two resistances in series where the first
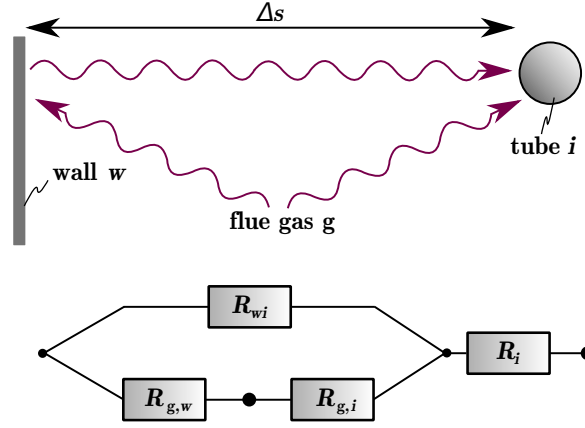
Fig. 5.3 Radiative heat transfer from the flue gas g of thickness Δs to tube i (top) and the corresponding resistance wiring scheme (bottom): the radiation is partly reflected by the wall w and partly emitted directly toward tube i.

resistance is a parallel arrangement of the resistances $R_{\mathrm{g},w}$, R_{wi} and $R_{\mathrm{g},i}$ [190]. The total resistance is calculated analog to electrical engineering as

$$
R_{\mathrm{g},iw} = \cfrac{1}{\cfrac{1}{R_{\mathrm{g},i}} + \cfrac{1}{R_{\mathrm{g},w} + R_{wi}}} + R_i
\tag{5.6}
$$

where the surface resistance of the tube surface is calculated as

$$
R_i = \frac{1 - \epsilon_i}{\epsilon_i \varphi_{iw} A_i} \quad .
\tag{5.7}
$$

The transmission resistance for the radiative intensity that passes the gas unnoticed is determined as

$$
R_{wi} = \frac{1}{A_i \varphi_{iw}(1 - \epsilon_{\mathrm{g}})}
\tag{5.8}
$$

and the resistances between the surface of tube i, the surface of wall w and the flue gas are derived as

$$R_{\mathrm{g},i} = \frac{1}{\varphi_{iw}A_i\epsilon_{\mathrm{g}}} \qquad \text{and} \qquad R_{\mathrm{g},w} = \frac{1}{\varphi_{wi}A_w\epsilon_{\mathrm{g}}} = \frac{1}{\varphi_{iw}A_i\epsilon_{\mathrm{g}}} \quad . \tag{5.9}$$

All surfaces are assumed to be homogeneous and to emit diffusely which means that the directional distribution of the radiative intensity leaving the surface is described by Lambert's law [174]. Consequently,

$$\varphi_{ij}A_i \equiv \varphi_{ji}A_j \tag{5.10}$$

applies to the view factors of two surfaces. $R_{\mathrm{g},w}$ is simplified using this view factor reciprocity: $\varphi_{wi}A_w \equiv \varphi_{iw}A_i$. As a consequence, the total resistances between the flue gas, a tube i, a wall w and another tube j are formulated as

$$\begin{aligned} R_{\mathrm{g},iw} &= \frac{1}{\varphi_{iw}A_i\epsilon_{\mathrm{g}}(2-\epsilon_{\mathrm{g}})} + \frac{1-\epsilon_i}{\epsilon_i\varphi_{iw}A_i} \qquad \text{and} \\ R_{\mathrm{g},ij} &= \frac{1}{\varphi_{ij}A_i\epsilon_{\mathrm{g}}(2-\epsilon_{\mathrm{g}})} + \frac{1-\epsilon_i}{\epsilon_i\varphi_{ij}A_i} \quad . \end{aligned} \tag{5.11}$$

It is important to note that radiative heat transfer from the hot furnace gas to all tubes is independent of the emissivity of the furnace wall surfaces. Surface emissivities for typical tube materials are tabulated whereas the gas emissivity is calculated using Lambert-Beer's law [120]:

$$\epsilon_{\mathrm{g}} = 1 - \exp\left(-\sum_{\alpha} \kappa_\alpha p_\alpha \Delta s\right) \quad . \tag{5.12}$$

In this equation κ_α and p_α represent the temperature dependent absorption coefficient and the partial pressure of component α. The thickness of the gas layer is denoted as Δs. Planck mean absorption coefficients that are introduced in chapter 4 are used as gray gas absorption coefficients [177, 197]. In addition to the parameters above, view factors of each tube i and all other tubes and walls are required which are described next.

5.2.3 Modeling of View Factors

The radiative resistances in Eq. (5.5) depend on the view factors defined by Eq (5.4) that are illustrated schematically in Fig. 5.4 (left). The tubes in the tube bundle have equal surface areas $A_i \equiv A_j$. Therefore, Eq. (5.10) reduces to

$$\varphi_{ij} \equiv \varphi_{ji} \quad . \tag{5.13}$$

The challenge of the view factor determination in a tube bundle is the correct description of shadowing effects between tubes. For a given arrangement of tubes, the view factors are readily calculated using trigonometric functions and careful switching when shadowing occurs. In order to use the tube bundle model for mathematical optimization, however, smooth
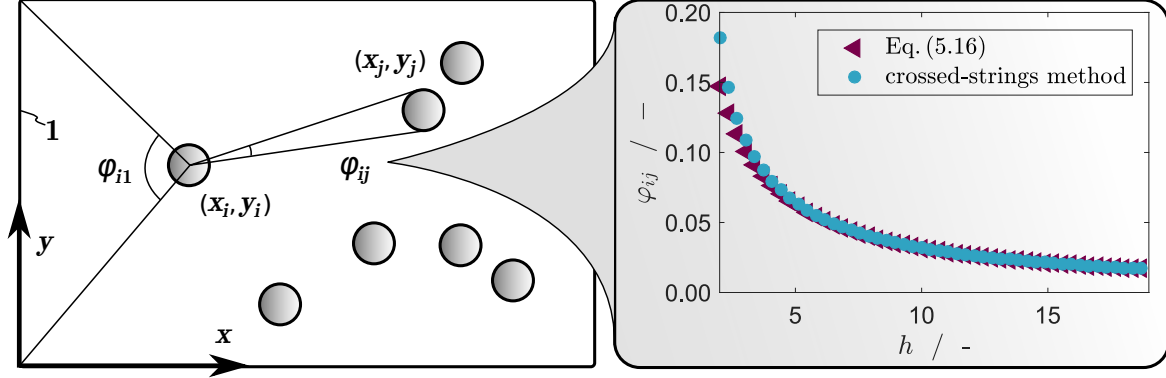
Fig. 5.4 View factors between tube i and the wall $1 - \varphi_{i1}$ – and between tubes i and $j - \varphi_{ij}$ – for a random arrangement of tubes (left) and comparison of view factor calculation according to Eq. (5.16) (red triangles) with the crossed-strings method (blue circles) versus the distance ratio $h := D_{ij}/R_i$.

functions that incorporate shadowing are required. This is achieved using hyperbolic tangent functions as switching functions in the interval $\phi \in [0, 2\pi)$ where the viewing angle between two tubes is described by the product of the two functions

$$\underline{f}_{ij} = \xi_1 \tanh\left(\frac{\phi - \underline{\theta}_{ij}}{\xi_2}\right) + \xi_3 \qquad \text{and} \qquad \overline{f}_{ij} = 1 - \left(\xi_1 \tanh\left(\frac{\phi - \overline{\theta}_{ij}}{\xi_2}\right) + \xi_3\right) \qquad (5.14)$$

where $\underline{\theta}_{ij}(x_i, y_i, x_j, y_j)$ and $\overline{\theta}_{ij}(x_i, y_i, x_j, y_j)$ represent the lower and upper bound of the view angle of i toward j that are dependent on the positions of both tubes. The two parameters ξ_1 and ξ_3 are set to 0.5 to ensure that the visual angle function values remain in $[0, 1]$ and that the function attains unity if tube j is visible from position x_i, y_i and zero if it is not visible. The third parameter ξ_2 is set as small as possible because it determines the steepness of the function switch: the steeper the function, the more accurate the view factor representation but also the harder the integration of the stiffer view factor function. The angular function describing the visual angle from i to j is then given by the product of the lower and upper bound functions

$$f_{ij} = \underline{f}_{ij} \overline{f}_{ij} \quad . \qquad (5.15)$$

The view factor φ_{ij} is then determined as the integration of this function over the entire angular space divided by 2π

$$\varphi_{ij} = \frac{1}{2\pi} \int_0^{2\pi} f_{ij} \mathrm{d}\phi \quad . \qquad (5.16)$$

In order to quantify shadowing it is irrelevant for the total inter-tube view factor if tube i is shaded by tube j or vice versa. Instead, the total inter-tube view factors of each tube i and of the overall bundle are of interest. Using the formulation shown in Eq. (5.15), the total visual angle of tubes j and k from i is given as the sum of the functions subtracted by their product as illustrated in Fig. 5.5

$$f_{ijk} = f_{ij} + f_{ik} - f_{ij}f_{ik} \quad . \tag{5.17}$$

In this illustration, the angular functions that describe the visual angle of tubes j and k from tube i – f_{ij} (red) and f_{ik} (blue) – are illustrated on the left. the sum and product of both functions is shown in the center (green) and the corresponding total visual angle function of tubes j and k from tube i – f_{ijk} (orange) – is displayed at the right. In this manner, the total tube view factor of all tubes that are visible by tube i can be calculated and is obtained as a continuous and differentiable function. This method of view factor calculation between tubes
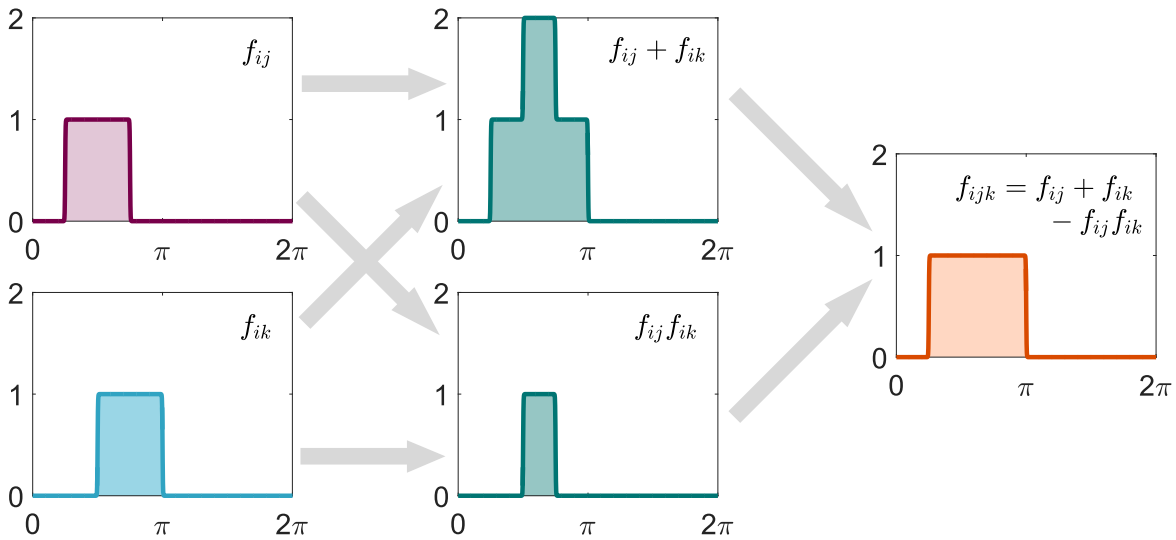
Fig. 5.5 Angular functions f_{ij} and f_{ik} describing the visual angle of tubes j and k from tube i (left) are added and multiplied in the center yielding the combined visual angle function f_{ijk} on the right.

is compared with the crossed-strings method versus the ratio $h := D_{ij}/R_i$ in Fig. 5.4 (right) [174]. In this ratio, R_i is the radius of tube i and D_{ij} the distance between tubes i and j. At the minimum allowed tube distance of $h = 3$ the error of the proposed view factor calculation methodology accounts for $6.2\,\%$. At $h = 4$, the error drops already below $4.0\,\%$ making this deviation negligible. In the crossed-strings method, the diagonals and sides of a hypothetical trapezoid need to be calculated which is valid as long as the diagonals form straight lines [174]. However, the shadowing of tubes by a multitude of other tubes with flexible positions is contrary to this assumption and areas of exchange would have to be recalculated for every new positioning in order to guarantee straight diagonals. As a consequence, the proposed

method of view factor calculation is preferred over the crossed-strings method despite its small deviations for densely packed tube arrangements.

With the derivation of the view factor calculation procedure, the tube bundle furnace model is complete. In the following section, possible solution approaches in order to identify the optimal tube bundle arrangement are introduced and analyzed.

5.3   Bundle Design Strategy

An intuitive strategy to identify the optimal bundle arrangement using the tube bundle furnace model is to formulate an optimization problem. This is either possible using the full tube bundle furnace model or a sub-problem of the heat transfer optimization problem – the minimization of inter-tube view factors provided that shadowing is the principle obstacle in the identification of intensified tube bundle designs. Both optimization problems are introduced first followed by the analysis of the relevance of convective heat transfer and of the objective functions. At the end of this section, the bundle design strategy for the optimization of the tube bundle arrangement in the HCN case study is outlined.

5.3.1   Heat Transfer Optimization Problem

Product yields of the individual tubes in the tube bundle attain their optimum if the heat uptake of each tube is maximized. As a consequence, the optimal tube arrangement maximizes the heat flux into every tube i. This is formulated as an optimization problem in Eq. (5.18)

$$
\begin{aligned}
\max_{\mathbf{x}, \mathbf{y}} \quad & \sum_{i \in \mathcal{N}_t} Y_i(\mathbf{x}, \mathbf{y}) \\
\text{s.t.} \quad & \dot{Q}_i^{(cv)} + \sum_{w \in \mathcal{N}_w} \dot{Q}_{\text{g},iw}^{(r)} + \sum_{j \in \mathcal{N}_t, j \neq i} \dot{Q}_{\text{g},ij}^{(r)} + Q_i = 0 \qquad \forall i \in \mathcal{N}_t \qquad (5.18) \\
& g(\mathbf{x}, \mathbf{y}) \leq 0
\end{aligned}
$$

where Y_i denotes the yield of tube i. Distance constraints are formulated in $g(\mathbf{x}, \mathbf{y})$ where δ_{iw} denotes the minimum tube-wall and δ_{ij} the minimum inter-tube distance to ensure the

feasibility of the bundle arrangement according to Eq. (5.19):

$$g(\mathbf{x}, \mathbf{y}) := \begin{bmatrix} -(x_i - x_j)^2 - (y_i - y_j)^2 & + \delta_{ij}^2 \\ -(L_x - x_i) & + \delta_{iw} \\ -(L_y - y_i) & + \delta_{iw} \\ -x_i & + \delta_{iw} \\ -y_i & + \delta_{iw} \\ \dots & \dots \end{bmatrix} \quad \forall i, j \in \mathcal{N}_t, i \neq j \quad . \tag{5.19}$$

L_x and L_y denote the dimensions of the furnace. The vectors $\mathbf{x} = [x_1, x_2, ..., x_i, ..., x_{N_t}]$ and $\mathbf{y} = [y_1, y_2, ..., y_i, ..., y_{N_t}]$ contain the x and y coordinates of each tube center position as illustrated in Fig. 5.1. Eq. (5.18) with Eq. (5.19) constitutes a nonlinear optimization problem because the energy balance and inter-tube distance constraints as well as the objective function are nonlinear.

5.3.2 View Factor Optimization Problem

Besides design aspects that affect the temperature distribution and convective heat transfer coefficients in the furnace, key design parameters are evident from the calculation of radiative resistances in Eq. (5.11): the radiative heat fluxes $\dot{Q}_{\mathrm{g},iw}^{(r)}$ and $\dot{Q}_{\mathrm{g},ij}^{(r)}$ attain their maxima if the corresponding total resistances R_{giw} and R_{gij} are minimized. One possibility is to increase the tube surface areas A_i but increasing the tube surface area corresponds to higher tube diameters which increases transport barriers inside the tubes which in turn may cause a drop in product yield. The next parameter in Eq. (5.11) – tube surface emissivities ϵ_i – are material parameters and should be selected as high as possible in order to minimize the second term of the resistance calculation in Eq. (5.11).

Three parameters remain that are a direct consequence of the tube bundle arrangement for a specified furnace geometry and tube surface area A_i: ϵ_g, φ_{iw} and φ_{ij}. High inter-tube view factors φ_{ij} correspond to low tube-wall view factors φ_{iw} and vice versa but under the practical constraint that burner outlets must be outside of the bundle arrangement – i.e. between walls and tubes – it is desirable to maximize overall tube-wall view factors. Higher gas temperatures in between burners and tubes compared with gas temperatures between tubes are also reported in literature [193, 154, 194]. If it is justified that the impact of view factors prevail over flue gas emissivities, it is desirable to minimize shadowing between tubes. This leads to the optimization problem in Eq. (5.20):

$$\min_{\mathbf{x}, \mathbf{y}} \quad \hat{\varphi} = \sum_{i \in \mathcal{N}_t} \sum_{j \in \mathcal{N}_t, j \neq i} \varphi_{ij}(\mathbf{x}, \mathbf{y})$$

$$\text{s.t.} \quad g(\mathbf{x}, \mathbf{y}) \leq 0 \quad . \tag{5.20}$$

$\hat{\varphi}$ is referred to as total inter-tube view factor and this optimization problem is a sub-problem of the heat transfer optimization problem (5.18). In Eq. (5.20), $g(\mathbf{x}, \mathbf{y})$ contains the inter-tube distance constraints as well as constraints for the distances between tubes and walls according to Eq. (5.19). The extent of the temperature difference between $T_{g,w}$ and $T_{g,i}$ depends on the specific layout of the furnace chamber and burner arrangement. It is important to keep in mind that the optimization problem in Eq. (5.20) neglects the impact of the flue gas emissivity ϵ_g which depends on the placement of tubes according to Eq. (5.12).

Prior to the bundle design itself it is important to analyze if radiation is the dominant mode of heat transfer in the furnace allowing to solve the reduced problem in Eq. (5.20) instead of Eq. (5.18). Therefore, the relevance of convective and radiative heat transfer in the furnace in combination with the impact of the tube emissivity ϵ_i is discussed next.

5.3.3   Relevance of Convective and Radiative Heat Transfer

It is often assumed that radiation dominates heat transfer on the furnace side [192, 154]. Consequently, the reduction of the heat flux optimization problem from Eq. (5.18) to Eq. (5.20) would be justified. In order to investigate the prevalence of either convective or radiative heat transfer on the furnace side, heat flows are calculated for the Endter BMA reactor design shown in Fig. 5.1 B. The convective heat transfer coefficient $\alpha_g^{(cv)}$ is estimated with correlations for the Nusselt numbers of tube bundles that are in turn functions of Reynolds and Prandtl numbers. These correlations are reported in literature [190, 120]. Based on typical furnace velocities in steam methane reformers where similar reactor designs exist, $\alpha_g^{(cv)}$ values are estimated and illustrated in Fig. 5.6 [193, 156, 191]. Maximum velocity magnitudes
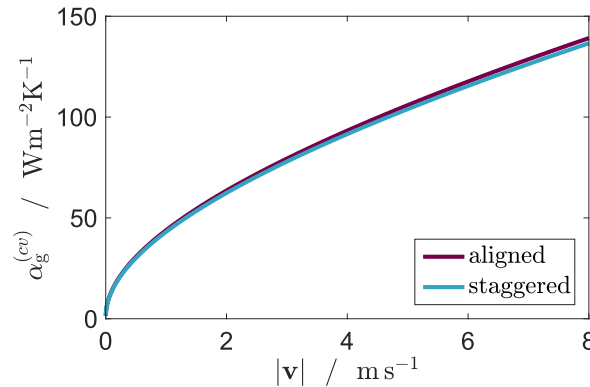
Fig. 5.6 Convective heat transfer coefficient $\alpha_g^{(cv)}$ for aligned (red) and staggered (blue) tube bundle arrangements and typical furnace-side velocities [193, 156].

on the furnace side at the inlet of steam reformers are in the range of $|\mathbf{v}|_{\max} \in [8,\ 10]\,\mathrm{m\,s^{-1}}$ decreasing rapidly below $1\,\mathrm{m\,s^{-1}}$ at bends and in turbulent regions. In between tubes, there is hardly any flue gas flow. These velocity magnitudes correspond to convective heat transfer

coefficients $\alpha_{\mathrm{g}}^{(cv)} \in [0, 140]\,\mathrm{W\,m^{-2}\,K^{-1}}$ as illustrated in Fig. 5.6 where $\alpha_{\mathrm{g}}^{(cv)}$ for aligned (red) and staggered (blue) bundle arrangements are shown. There is a minor difference between both bundle arrangements: convection in aligned bundles is estimated to be slightly higher than in staggered arrangements. Besides, furnace temperatures vary between $1700\,\mathrm{K}$ at the burner inlet up to $800\,\mathrm{K}$ in the narrow space between tubes [193, 156, 191].

The prevalence of the individual mechanisms for heat transfer is estimated using dimensionless numbers [174, 197]: to analyze the impact of convective heat transfer on the overall heat that is transferred from the flue gas to the tube bundle, the dimensionless Boltzmann number at the wall based on simulation $\mathrm{Bo}_{\mathrm{sim},i}$ is introduced which – analog to the original Boltzmann number – indicates the importance of convective and radiative heat transfer to the tubes. It
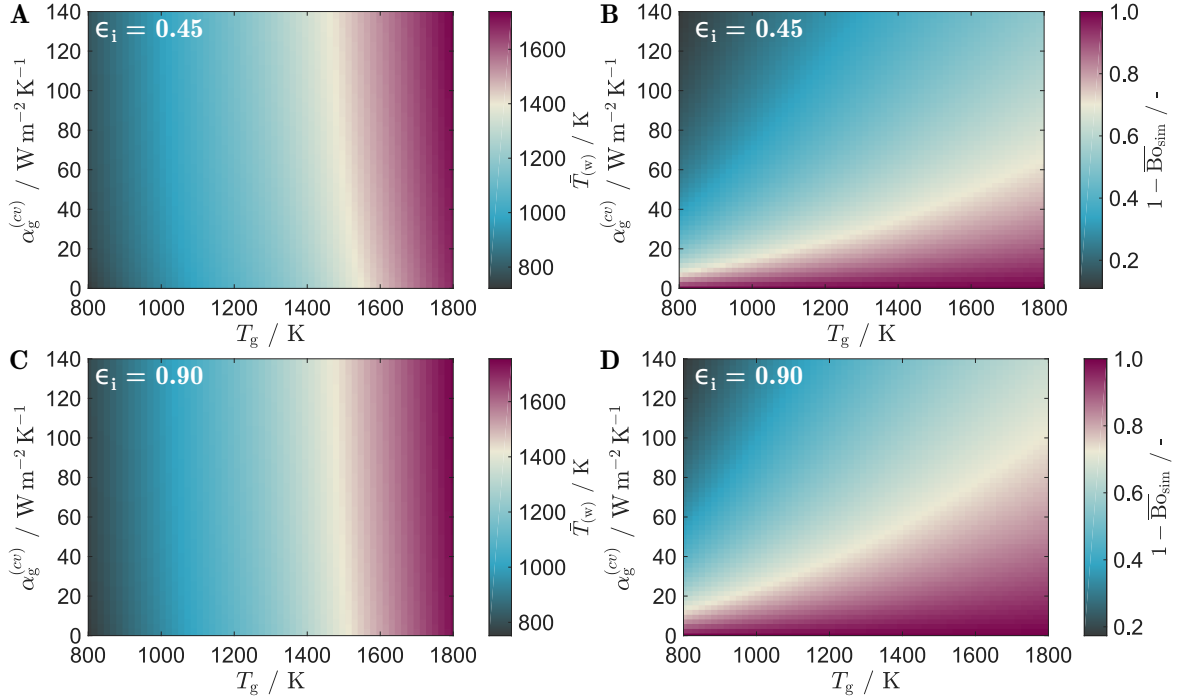
Fig. 5.7 Tube average wall temperature $\bar{T}_{\mathrm{(w)}}$ of the Endter bundle arrangement (A and C) and prevalence of radiative heat transfer given by $1 - \overline{\mathrm{Bo}}_{\mathrm{sim}}$ (B and D) for typical values of convective heat transfer coefficients $\alpha_{\mathrm{g}}^{(cv)}$ and homogeneous flue gas temperatures T_{g} in the furnace. A and B display results for low tube surface emissivities of $\epsilon_i = 0.45$ and C and D for high emissivities $\epsilon_i = 0.90$.

is defined as for the single tube i as:

$$\mathrm{Bo}_{\mathrm{sim},i} := \frac{\dot{Q}_i^{(cv)}}{\dot{Q}_i^{(cv)} + \sum_{w \in \mathcal{N}_w} \dot{Q}_{\mathrm{g},iw}^{(r)} + \sum_{j \in \mathcal{N}_t, j \neq i} \dot{Q}_{\mathrm{g},ij}^{(r)}} \qquad \forall i \in \mathcal{N}_t \quad . \tag{5.21}$$

Fig. 5.7 illustrates the mean tube surface temperature $\overline{T}_{(w)}$ (Fig. 5.7 A,C) as well as the mean of $1 - \overline{Bo}_{sim}$ (Fig. 5.7 B, D) of all 13 tubes in the bundle for two different homogeneous flue gas temperatures T_g and tube surface emissivities: $\epsilon_i = 0.45$ corresponds to alumina at $T_{(w),i} = 1600\,K$ (Fig. 5.7 A, B) and $\epsilon_i = 0.90$ corresponds to silicon carbide (SiC) whose emissivity versus temperature is nearly constant (Fig. 5.7 C, D). These values represent the minimal and maximal attainable values because the emissivity of alumina is $\epsilon_i = 0.90$ at temperatures $T_{(w),i} = 700\,K$. [190, 120]. Evidently, the mean tube surface temperatures increase with rising flue gas temperatures in Fig. 5.7 A and C. However, the increase in temperature with enhanced convection is of secondary importance: strong convection with $\alpha_g^{(cv)} = 140\,W\,m^{-2}K^{-1}$ results in minor increases in temperature compared with $\alpha_g^{(cv)} = 20\,W\,m^{-2}K^{-1}$. SiC as the tube material leads to an increase of mean tube surface temperatures by $40 - 50\,K$. The impact of convection on temperature changes seems less emphasized for the SiC in Fig. 5.7 C.

At the low emissivity of alumina in Fig. 5.7 B, the prevalence of radiative heat transfer is clearly visible for convective heat transfer coefficients below $20\,W\,m^{-2}K^{-1}$: even at flue gas temperatures as low as $800\,K$, radiation dominates overall heat transport clearly with an exponential increase with flue gas temperature. Unless the tube is placed directly within a convection zone and corresponding high $\alpha_g^{(cv)}$ values, radiation accounts for $50 - 100\,\%$ of total heat transferred for any flue gas temperature in the vicinity of flue gas velocities below $2\,m\,s^{-1}$. The highly emissive SiC material leads to a stronger dominance of radiation: while radiation accounts for $80\,\%$ at $800\,K$ up to $\alpha_g^{(cv)} = 7\,W\,m^{-2}K^{-1}$ at the low tube emissivity, this value increases to $\alpha_g^{(cv)} = 12\,W\,m^{-2}K^{-1}$ for high emissivities and the exponential curve increases more steeply.

In addition to the maximization of heat transfer to the tubes, material temperature strains have to be considered for the reactor designs both in HCN synthesis and MSR. Therefore, tubes are typically not placed directly at the burner inlet because this would result in a reduction of the lifetime of the synthesis tubes. Instead, the main convective flow is close but adjacent to the tubes. For furnace temperatures between $1200\,K$ and $1500\,K$, radiative heat transfer dominates with $80\,\%$ or more if the velocities in the vicinity of the tube remain below $3\,m\,s^{-1}$ which is more than justified in MSR furnaces [193]. The investigation for tube bundle design for MSR confirms that the error in heat transfer remains below $10\,\%$ if convection is neglected [92]. Therefore, assuming a prevalence of radiative heat transfer for the majority of the synthesis tubes in the BMA reactor is justified.

As a consequence, two options exist for the optimization problem: the convective heat flow in Eq. (5.18) could be neglected or Eq. (5.20) could be selected for the optimization of the tube bundle arrangement. Prior to the optimization of the tube bundle, the objective function of the sub-problem (5.20) is analyzed.

5.3.4 Analysis of the View Factor Objective Function

The view factor optimization problem Eq. (5.20) is a sub-problem of the overall heat flux optimization problem in Eq. (5.18) and is illustrated using tube bundle arrangements in a square furnace enclosure. The objective function is analyzed because the view factor is dominated by two aspects: the distance between surface areas that exchange radiation as well as shadowing effects through objects in-between these surface. The total view factor objective function $\hat{\varphi}$ is illustrated using four scenarios in Fig. 5.8. In the first scenario (Fig. 5.8 A) four tubes are placed at a minimal distance from the wall in the corner of a square enclosure and the normalized total view factor $\hat{\varphi}_N$ is illustrated for the placement of the fifth tube. In all four scenarios in Fig. 5.8 A, B, C and D, the normalized total view factor corresponds to the total view factor normalized with the maximum total view factor of all four scenarios in Fig. 5.8. White space denotes positions where the inter-tube and tube-wall distance constraints of the fifth tube are not fulfilled (comp. Eq. (5.19)). The total view factor decreases exponentially with distance from other tubes and in addition shadowing occurs if the fifth tube is placed in between other tubes: at all four walls of the square enclosure as well as in diagonal lines across the enclosure center. If the fifth tube is placed at the center of the enclosure, it shades all four tubes from their diagonal neighbor leading to the smallest objective function value. Fig. 5.8 B, C and D illustrate similar results for the placement of the sixth, tenth and fourteenth tubes.

It is evident, that the objective function exhibits a large number of local optima that increases strongly with tube numbers even if the degrees of freedom of the optimization of the tube arrangement are reduced to the positioning x_i, y_i of a single tube i as in Fig. 5.8. Within the real optimization scenario, however, it is the task to optimize all tube positions at the same time. This large number of local optima renders a single, locally optimal result of Eq. (5.20) obsolete. Three possibilities exist to resolve this problem: (i) the repeated local optimization with random initial conditions increases the chances of finding the globally optimum, (ii) use of a global NLP solver such as a branch and bound or stochastic algorithms and (iii) simulation-based optimization i.e. systematic screening of practically feasible tube arrangements to reduce the search space. The computation time for a single solution of the reduced view factor NLP in Eq. (5.20) with 10 tubes and a local NLP solver are in the range of an hour. For local NLP solvers, however, a large number of solutions is required in order to identify overall optimal designs and on top of that, the reduced model does not take the effect of gas layer emissivities ϵ_g into account. Computations on the cluster "mechthild" of the Max Planck Institute using the sub-problem (5.20) proved computationally inefficient and could not be interpreted systematically for the lack of sufficient datapoints. Therefore, within this chapter, simulation-based optimization in Matlab/CasADi is selected because it is computationally efficient allowing for large tube numbers and accounting for both key
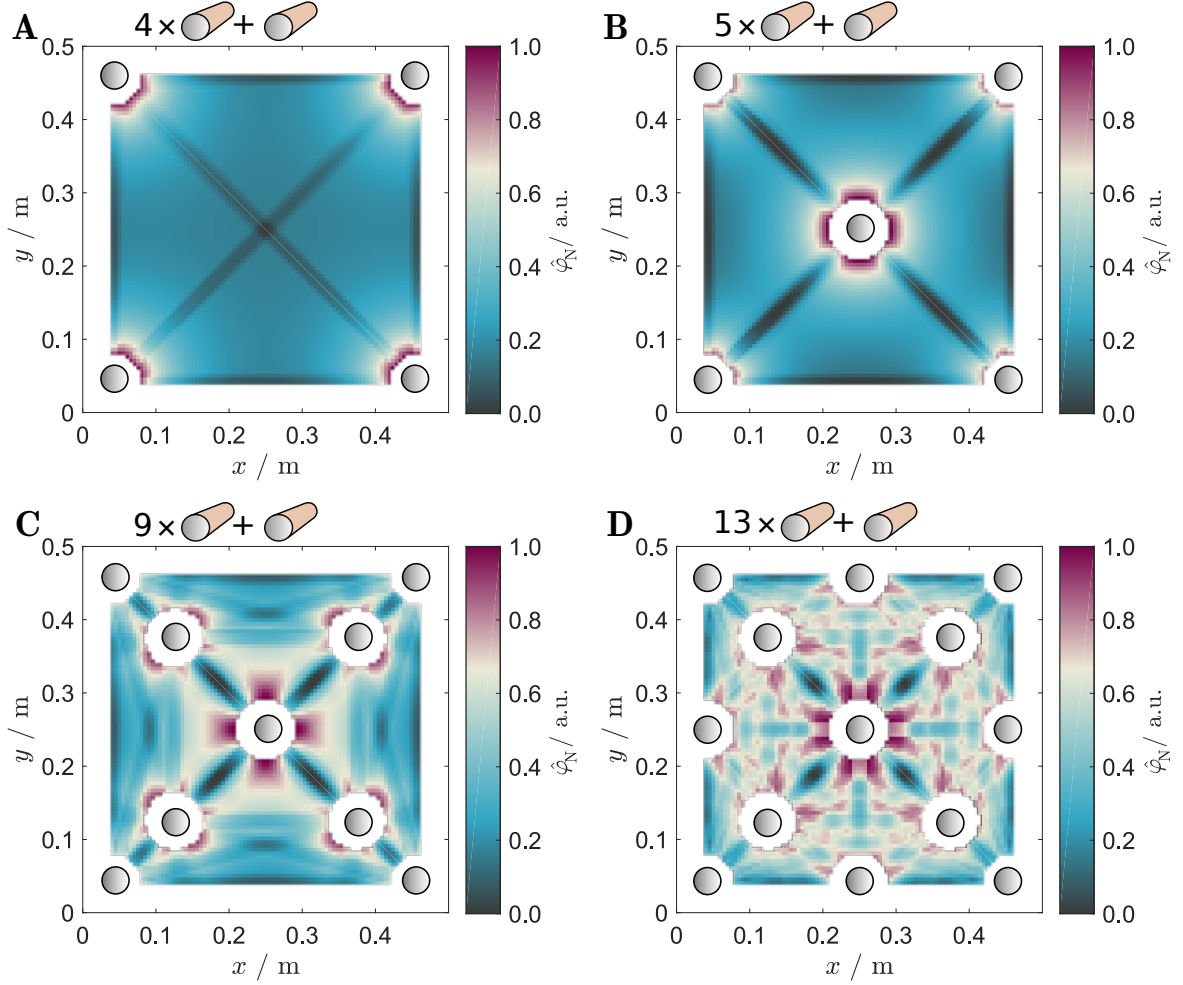
Fig. 5.8 Normalized objective function values $\hat{\varphi}_N$ in arbitrary units of Eq. (5.20) for the placement of the fifth (A), sixth (B), tenth (C) and fourteenth (D) tube in a furnace with a square cross-section and an edge length of 0.5 m.

parameters: total view factor $\hat{\varphi}$ and flue gas emissivity ϵ_g. An additional argument for simulation-based optimization is the rectangular furnace geometry of the case study enabling a systematic screening of the design search space which is not the case if the furnace topology is included as additional degree of freedom as pointed out in the appendix in Sec. C.2.

5.4 Radiation-based Bundle Design for the BMA Reactor

In the following results, flue gas temperatures near walls are approximated with $T_{g,w} = 1500\,\text{K}$ and gas temperatures between tubes as $T_{g,i} = 1200\,\text{K}$ which are values that correspond to steam methane reforming [191, 193]. Equivalent outer tube diameters of $\delta = 0.020\,\text{m}$ are used that correspond to single compartment simulations plus the tube wall thickness of 1 mm in

chapter 4. The remaining simulation parameters are provided in Tab. 5.1. Partial pressures of the radiating gases CO_2 and H_2O are assumed analog to the furnace compartment in chapter 4. It is the goal to enable a comparison between different tube arrangements without emphasis on absolute values of tube surface temperatures and product yields because to achieve more accurate results, the reduction to two dimensions would have to be omitted.

Tab. 5.1 Simulation parameters for the optimal bundle design inspired by the Endter reactor [104].

equivalent outer tube diameter	δ	=	0.020	m
tube length (z)	L_z	=	2.00	m
furnace width (x)	L_x	=	0.32	m
furnace depth (y)	L_y	=	0.21	m
flue gas temperature near burner inlets	$T_{g,w}$	=	1500	K
flue gas temperature between tubes	$T_{g,i}$	=	1200	K
tube surface emissivity	ϵ_i	=	0.5	-
partial pressure CO_2	p_{CO_2}	=	0.09	bar
partial pressure H_2O	p_{H_2O}	=	0.18	bar

5.4.1   Simulation Study of Bundle Arrangements

In addition to the Endter base case scenario, three tube bundle arrangements – a rhombus, a circle and a rectangle arrangement – are simulated and illustrated in Fig. 5.9. Tube colors correspond to tube temperatures and the same colorbar ranges are illustrated for all scenarios for better comparability. The furnace chamber described in literature is a rectangle with the dimensions given in Tab. 5.1 and tube surface temperatures are thus symmetric [104]. In addition to the individual tube surface temperatures $T_{(w),i}$, mean tube surface temperatures $\bar{T}_{(w)}$ and mean tube product yields $\bar{Y}$ including their standard deviations σ_T and σ_Y are indicated above each graph:

$$\bar{T}_{(w)} = \frac{1}{N_t} \sum_{i \in \mathcal{N}_t} T_{(w),i} \qquad \text{and} \qquad \sigma_T = \sqrt{\frac{1}{N_t - 1} \sum_{i \in \mathcal{N}_t} \left| T_{(w),i} - \bar{T}_{(w)} \right|} \qquad (5.22)$$

and analog for the product yields. The bundle arrangements are ordered with decreasing objective function value from A to D attaining values between 5.42 and 3.34. Low objective function values and thus total view factors correspond to scenarios where tubes are located in corners of the rectangle furnace. Despite its low objective function value, the tube arrangement with the least $\hat{\varphi}$ value in Fig. 5.9 D attains the lowest mean surface temperature, mean product yield and a high standard deviation among all tubes which is an additional disadvantage due to strains of the tube material. This detrimental effect despite a reduction
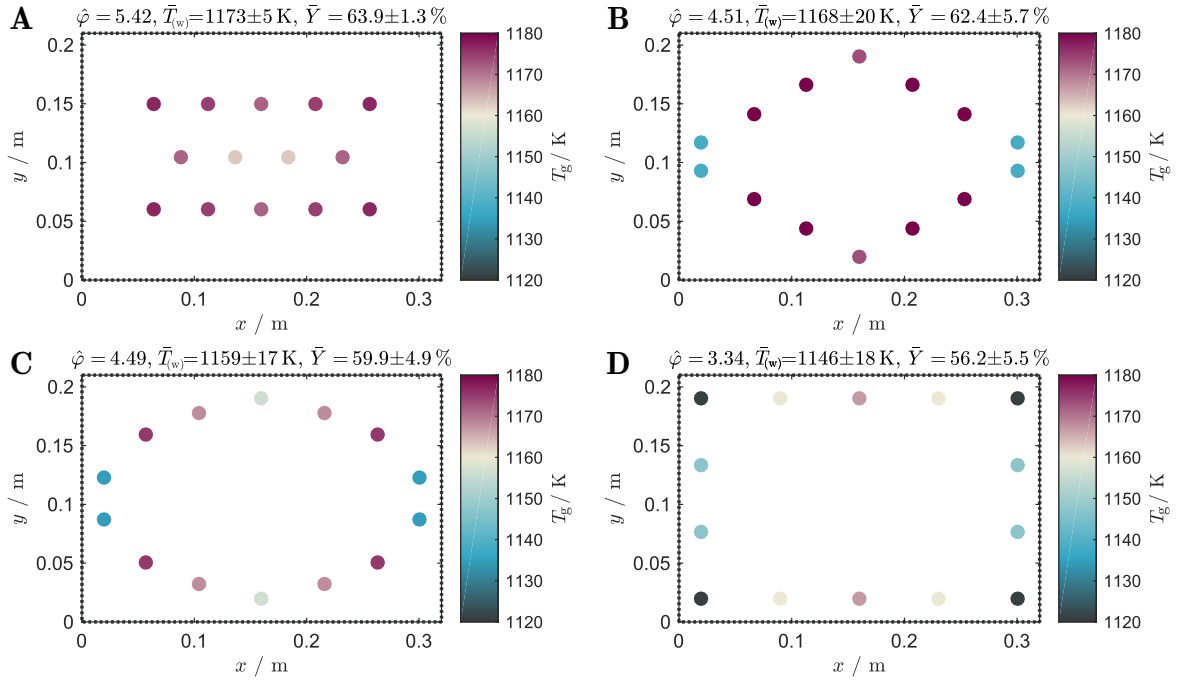
Fig. 5.9 Tube bundle arrangements with decreasing view factor objective function value from A to D. Endter base case arrangement (A), rhombus (B), circle (C) and rectangle arrangements with minimum distances to walls (D).

in view factor is caused by the reduction in the flue gas layer emissivities ϵ_g of tubes located near walls: larger distances and shadowing represent a reduction in view factors which is, however, compensated by a reduction in gas layer emissivities if tubes are located too close to walls.

5.4.2 Systematic Variation of Distances

In order to identify the turning point where a reduction in view factor is compensated by the reduction in gas layer emissivities, a systematic variation of distances is performed for the tube bundle. An equidistant grid is considered and Δx and Δy denote the distance in x and y between tube centers. The reduction of view factor objective values shown in Fig. 5.9 B, C and D is accompanied by larger temperature and thus yield variations among tubes within the bundle. Therefore, and to compare the results with the Endter benchmark reactor, the distance study is performed using aligned and staggered tube arrangements.

Results for the systematic variation of tube distances are illustrated in Fig. 5.10 and distance in x and y as well as objective function values are contained in Tab. 5.2. Starting with the most narrow arrangement in Fig. 5.10 A with distances of $\Delta x = \Delta y = 0.028\,\mathrm{m}$, a strong variation of temperature is evident: tubes at the center of the bundle are shadowed by their

Tab. 5.2 Distances, total view factor value, bundle average surface temperatures and yields of staggered tube arrangements shown in Fig. 5.10 in comparison with the Endter benchmark reactor [104].

	Δx / m	Δy / m	$\hat{\varphi}$ / -	$\bar{T}_{(\mathrm{w})}$ / K	$\bar{Y}$ / %
Endter	0.048	0.045	5.42	1173 ± 5	63.9 ± 1.3
Fig. 5.10 A	0.028	0.028	7.76	1157 ± 25	59.4 ± 7.3
Fig. 5.10 B	0.035	0.035	6.75	1165 ± 17	61.6 ± 4.9
Fig. 5.10 C	0.045	0.045	5.61	1171 ± 6	63.5 ± 1.7
Fig. 5.10 D	0.052	0.054	4.86	1174 ± 5	64.4 ± 1.4
Fig. 5.10 E	0.055	0.060	4.52	1174 ± 8	64.3 ± 2.2
Fig. 5.10 F	0.060	0.090	3.62	1161 ± 29	60.3 ± 8.0

neighbors whereas tubes at the outer corner positions attain maximum temperatures due to both their large view factors of walls and gas layers with high emissivities around them. Turquoise colored tubes are equally surrounded by these gas layers but their view factors are much lower as they "see" more of their neighbors.

Considering the next two scenarios in Fig. 5.10 B and C, both effects are reduced: the thickness of the gas layer is reduced as the distance among tubes is increased but at the same time, the shadowing from the surrounding tubes decreases. Thus, the average yield increases and the standard deviation of all tubes decreases. Fig. 5.10 C is similar to the Endter base case scenario. Increasing the distances between tubes to $\Delta x = 0.052\,\mathrm{m}$ and $\Delta y = 0.054\,\mathrm{m}$, the average yield attains its maximum with $\bar{Y} = 64.4 \pm 1.4\,\%$ and a tipping point becomes visible: with higher inter-tube distances, tubes in the center row have higher temperatures than their neighbors that are located at the outer corners of the bundle arrangement. Increasing the distances in x and y further in the scenarios shown in Fig. 5.10 E and F intensifies this trend. Starting from scenario E, tubes that are located in the center line attain maximum values out of all tubes and the center line tubes of scenario F attain the overall maximum tube surface temperature of $1200\,\mathrm{K}$. In both scenarios, their counterparts close to the walls are relatively cold leading to low average surface temperatures and yields and an increase in standard deviations of the bundle designs. The scenarios Fig. 5.10 D and Fig. 5.10 E attain the same mean surface temperatures but the mean yield of Fig. 5.10 E is slightly lower due to the larger variations in tube temperatures as can be seen from the standard deviation. Consequently, Fig. 5.10 D contains the best result out of all staggered arrangements with an increase in average yield by $0.5\,\%$ compared to the Endter benchmark reactor.

Results for the aligned arrangement are illustrated in Fig. 5.11. An additional tube is added in order to have three complete lines. The results of the aligned bundle arrangement are similar to the staggered arrangement: initially, shadowing of the inner tubes causes lower
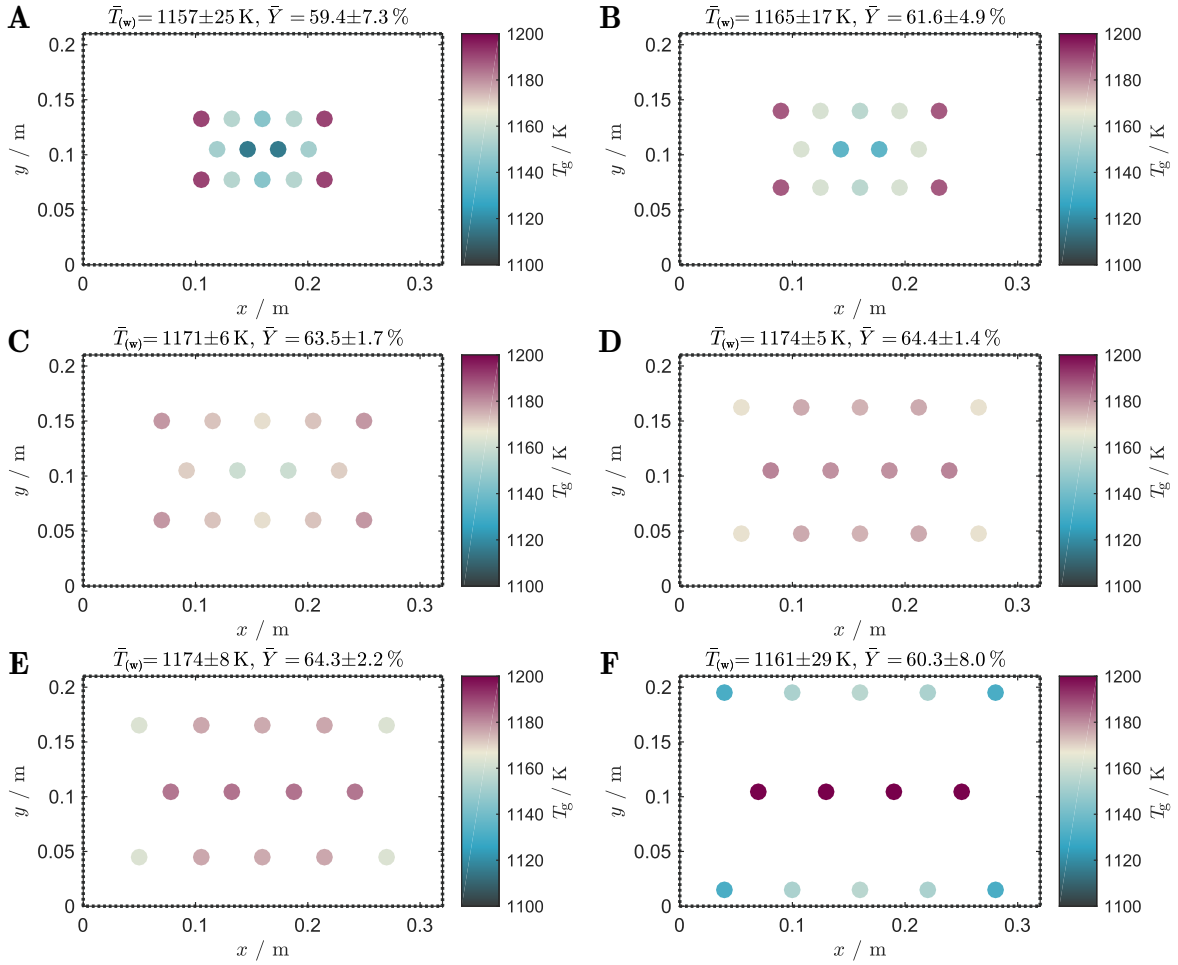
Fig. 5.10 Systematic variation of inter-tube distance for a staggered bundle arrangement with inter-tube distances Δx and Δy provided in Tab. 5.2.

temperatures at the center compared to tubes located at corners. This inequality is reduced as the distances increase. Fig. 5.11 D denotes the turning point with the lowest variations among all tubes and the highest overall yield and temperature with similar Δx and Δy as shown before in Tab. 5.2. In the last two aligned bundle arrangements temperatures of the inner tubes increase while tubes at the periphery cool down. As before, this leads to reduced mean surface temperatures and yields and eventually higher standard deviations of the bundles. Overall, the aligned arrangements attain lower average yields and slightly lower standard deviations than their staggered counterparts. Fig. 5.12 summarizes the findings for aligned and staggered bundle arrangements: it illustrates mean surface temperatures (left) and mean product yields (right) including the standard deviations for both aligned (red) and staggered (blue) bundle arrangements versus Δx. The turning point where a reduction in total view factors leads to no further improvement in temperature and yield is clearly visible at $\Delta x = 0.052\,\mathrm{m}$. The inter-tube distance at the turning point is equal
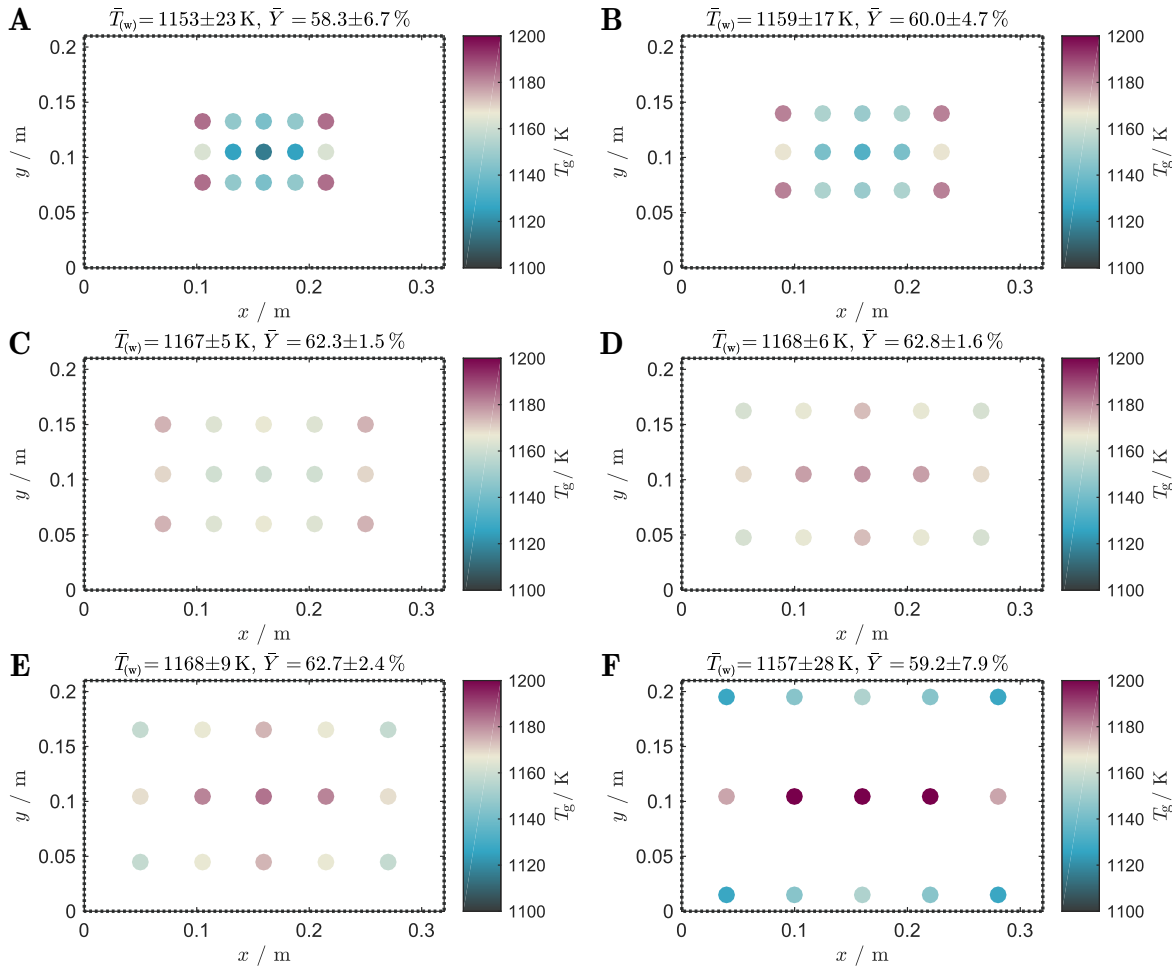
Fig. 5.11 Systematic variation of inter-tube distances for an aligned bundle arrangement. Distances equal the ones of the staggered arrangement in Tab. 5.2.

for aligned and staggered arrangements and corresponds to objective function values of $\hat{\varphi} = 4.86$ for the staggered and $\hat{\varphi} = 5.39$ for the aligned arrangement. These objective function values correspond to total inter-tube view factors of 0.34 and 0.36 for an individual tube in the optimal staggered and aligned scenarios. At the same time, variations in tube surface temperatures among the 14/15 individual tubes decline up to this point and increase for tube distances beyond 0.052 m. The optimal distance in a bundle does not only provide maximum yields but also the best homogeneity of surface temperatures and yields among all tubes. As a consequence, this distance is optimal for the Endter furnace geometry and 14/15 tubes. At this tube distance, the tube arrangement minimizes overall material strain caused by inhomogeneous tube surface temperatures and thus increases the long-term performance of the tubes. Staggered bundle arrangements are superior to aligned bundle arrangements which is evident by an increase in tube surface temperatures by $4-6$ K leading to an increase
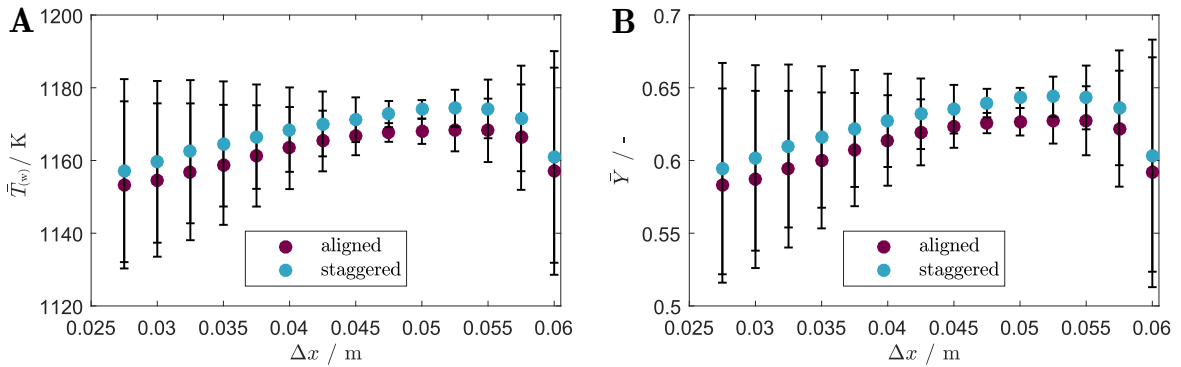
Fig. 5.12 Comparison of distance variation for staggered (blue) and aligned (red) bundle arrangements. Mean tube surface temperatures (left) and mean yields of the product HCN (right) including their standard deviations.

in average yield by 1-3 %. This systematic difference is constant for any inter-tube distances Δx and Δy that are selected.

5.4.3   Impact of Tube Diameter and Flue Gas Temperatures

The previous section identified the optimal bundle arrangement for given tube diameters and flue gas temperature fields. Both assumptions are relaxed in this section in order to analyze the impact of tube diameters and of the flue gas temperature field assumption on the bundle performance.

The comparison of staggered bundle arrangements for the four equivalent outer tube diameters of Fig. 5.2, $\delta = 0.018$ m (magenta), $\delta = 0.020$ m (red-orange), $\delta = 0.022$ m (blue) and $\delta = 0.026$ m (green), are illustrated in Fig. 5.13 A and B. The mean surface temperature profiles of bundle designs with all four diameters are similar but the maximum at $\Delta x = 0.052$ m is more pronounced for smaller diameters and a slight shift toward shorter inter-tube distances is visible. The narrow tubes attain maximum tube surface temperatures of 1187 K whereas tubes with the largest of all four diameters reach a maximum surface temperature of 1150 K despite their larger heat exchange area. The difference between the diameters is emphasized more mean product yields due to the increase in the relevance of transport limitations with increasing tube diameters on the inner tube sides as shown above in Fig. 5.13: increasing the tube diameter increases the heat exchange area with the surrounding furnace but the cross-sectional area increases square-fold resulting in lower cross-sectional averaged yields at the reactor outlet. As shown in the derivation of the total resistance in Eq. (5.6), the tube surface area A_i appears in most of the contributing resistances. An overall increase in all heat exchange areas thus reduces the impact of the view factor on mean tube outlet temperatures and yields corresponding to the flat profiles in Fig. 5.13 for large tube diameters. In chapter 4, the reduction of channel width by 1-3 mm was proposed and the effect on the
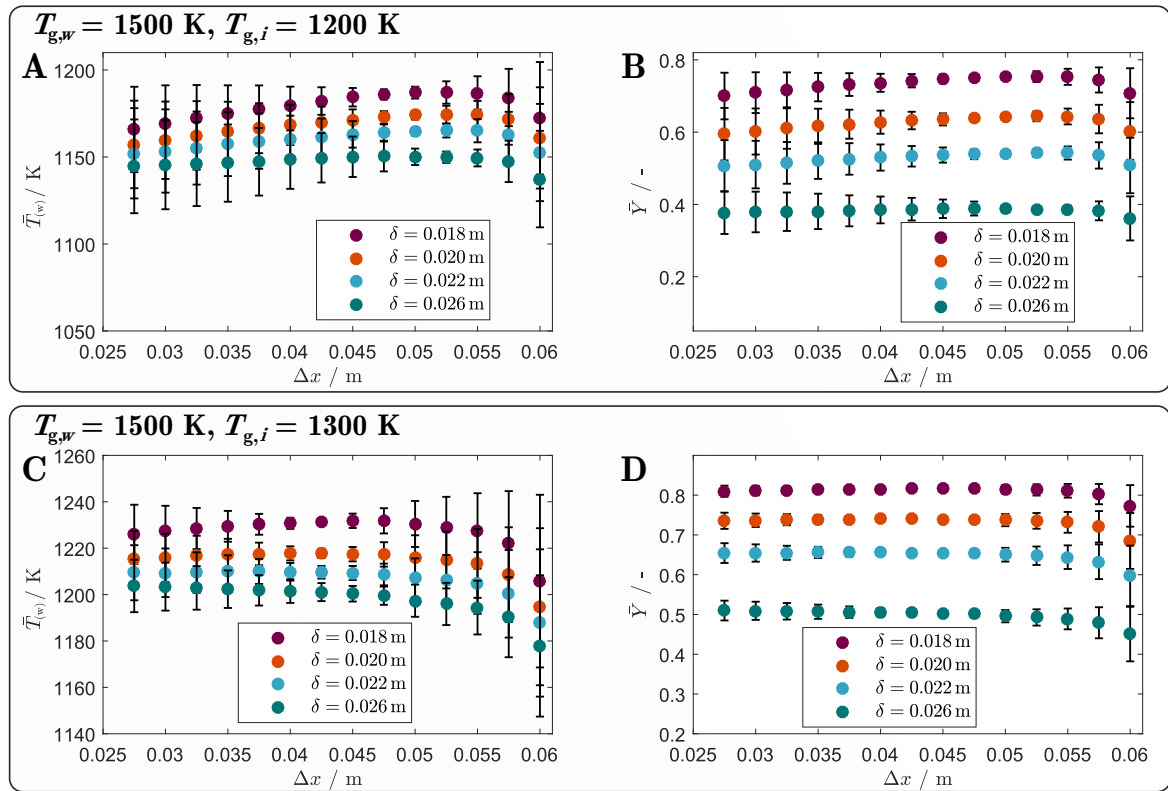
Fig. 5.13 Mean tube surface temperatures $\bar{T}_{(w)}$ (A, C) and mean yield $\bar{Y}$ (B, D) for staggered bundle arrangements and three equivalent outer tube diameters δ: $0.018\,\mathrm{m}$ (magenta), $0.020\,\mathrm{m}$ (red-orange), $0.022\,\mathrm{m}$ (blue) and $0.026\,\mathrm{m}$ (green) for two different flue gas temperature combinations: $T_{g,w} = 1500\,\mathrm{K}$, $T_{g,i} = 1200\,\mathrm{K}$ (A, B) and $T_{g,w} = 1500\,\mathrm{K}$, $T_{g,i} = 1300\,\mathrm{K}$ (C, D).

bundle is visible irrespective of the inter-tube distance: due to the shape of the product yield profiles in Fig. 5.2, a strong increase in product yield by 9-11 % is visible in Fig. 5.13 B.

Assuming – in average – a smaller flue gas temperature gap with $T_{g,w} = 1500\,\mathrm{K}$ in near the burner inlets and $T_{g,i} = 1300\,\mathrm{K}$ between tubes, the mean surface temperatures and yields of Fig. 5.13 C and D are obtained: the tipping point remains but is less emphasized and shifts to lower tube distances between $0.040\,\mathrm{m}$ and $0.042\,\mathrm{m}$. The reason is that as the temperature of the flue gas becomes more homogeneous, view factors play a lesser role compared to the overall maximization of gas emissivities. Decreasing the temperature gap further causes the switching point to vanish. If a homogeneous temperature field is assumed it is thus optimal to reduce tube distances. An additional effect of a reduction in temperature gap between inner and outer areas is that the curves in Fig. 5.13 C and D flatten out compared to Fig. 5.13 A and B. Consequently, the average yields attain almost constant values for the diameters $\delta = 0.018\,\mathrm{m}$, $\delta = 0.020\,\mathrm{m}$ and $\delta = 0.022\,\mathrm{m}$.

Similar to the outer diameter of $\delta = 0.020\,\mathrm{m}$ that was discussed above, aligned tube bundle arrangements have a slightly lower performance but show no qualitative difference to the

results presented for staggered arrangements. A good estimate of the prevailing temperature field in the furnace is thus crucial to decide between a closely arranged bundle and a bundle arrangement with larger distances between tubes irrespective of the diameter of the tubes.

5.5   Chapter Summary

Modeling of high temperature reactors involves a large variety of physical effects including complex geometries, radiation and reactive flow with fast reaction kinetics. As a consequence, high fidelity simulations and the optimization of the operating and design parameters can hardly be achieved simultaneously. Instead, detailed CFD models are utilized to obtain precise and accurate information whereas reduced models enable the identification of optimal operating and design parameter intervals. In this chapter, the overall bundle-furnace optimization was reduced to the simulation-based optimization of the tube bundle arrangement within a given furnace geometry. Based on the quantitative analysis of radiative heat transfer using the analogy of radiation modeling to a system of resistances used in electrical engineering, a model reduction toward view factor-based optimization of the tube bundle arrangement was proposed. Depending on the tube position and the flue gas velocity distribution in the furnace, radiation accounts for 80 % and more of the total heat transferred to individual tubes.

It was demonstrated that a rigorous optimization is unhelpful due to the abundance of local optima already for a reduced model of view factors alone. Therefore, the impact of three key parameters – surface emissivity, gas layer emissivity and view factors – was investigated using simulation-based optimization because wall emissivities are redundant for near-adiabatic furnaces. Variations in tube emissivities are insignificant compared to the minimization of the total inter-tube view factors and compared to the gas layer emissivities: optimal bundle arrangements are obtained for low total inter-tube view factors while maintaining high emissivities of the flue gas around the tube bundle either through an increase in the gas layer width or partial pressures of the radiating species in the furnace. Both effects vary depending on the tube bundle and furnace flue gas temperatures. For this reason, they have to be identified and weighed for each specific furnace bundle combination.

In the case study of HCN synthesis in a BMA reactor with the dimensions of the Endter reactor flue gas temperatures near burners and walls were assumed to be 300 K higher than the flue gas in between tubes. Under these circumstances the staggered arrangements for tubes with outer diameters of 0.02 m are optimal with an inter-tube distance of 0.052 m. This design is slightly superior to the formerly industrially applied tube bundle design with an average improvement of the tube yield of HCN by 0.5 % and a minor reduction of the standard deviation across the tube bundle. Staggered bundle arrangements are generally

superior to aligned arrangements in terms of attainable surface temperatures and product yields. The optimal inter-tube distance of $0.052\,\mathrm{m}$ is similar for any of the investigated outer tube diameters. Reducing the benchmark width by $2\,\mathrm{mm}$ results in an increase in HCN product yield of nearly $10\,\%$ which is stronger than was predicted by Fig. 4.15 but this distortion is partly due to the cylinder-channel conversion and the flue gas temperatures that are assumed in the furnace.

Chapter 6

Process Synthesis at the Plant Level

Having addressed the research questions (I), (II) and (III) at the single compartment and tube bundle reactor levels, it is the objective of this chapter to identify the optimal production process for HCN at the plant level in order to address the remaining aspects (IV) and (V): design of efficient processes and its application to HCN production. Besides the two most common reactors – the BMA and the Andrussow reactor – the product reactant supply and product purification are included at this level opening the space for heat and mass recycling opportunities. As mentioned in the introductory chapter, the reactants of both reactor types include CH_4 and NH_3 and both yield H_2 as a byproduct. Three principle recycling pathways are thus considered for this analysis: the energetic recycling of H_2 and the synthesis of the reactants CH_4 and NH_3 according to the Sabatier and Haber-Bosch reactions:

$$N_2 + 3\,H_2 \rightleftharpoons 2\,NH_3 \qquad \Delta_R h^{\ominus} = -46 \;\; \text{kJ/mol} \qquad (6.1)$$

$$CO_2 + 4\,H_2 \rightleftharpoons CH_4 + 2\,H_2O \qquad \Delta_R h^{\ominus} = -151 \;\text{kJ/mol} \quad . \qquad (6.2)$$
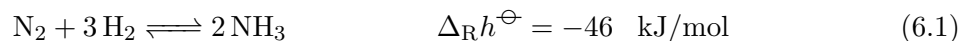
In order to identify the optimal production pathway, the simultaneous consideration of heat and mass integration is required during the process synthesis step. Prior to the identification of the resource optimal plant for HCN synthesis, it is thus the objective of this chapter to introduce the FluxMax approach (FMA) which is a simultaneous process synthesis and heat integration approach. The FMA was developed in collaboration with Dominik Schack of the PSE group at the Max Planck Institute for Dynamics of Complex Technical Systems (MPI) in the context of our dissertation projects. The scope of the plant design is set on resource efficiency which is split into energy efficiency, raw material efficiency as well as variable cost which represents a weighing of the other two efficiencies. This chapter on process synthesis

at the plant level (comp. Fig. 2.2) is directly linked to chapter 4 because the heat duties for the BMA reactor originate from single compartment simulations of that chapter. Following this introduction, literature for process and plant design is reviewed followed by the method section where the FMA is introduced. Subsequently, the results for the case study of HCN production are presented.

6.1 Literature Context

Optimal process design – in the sense of most efficient, cost-optimal or any other optimality criteria – can be achieved via two distinct pathways: simulation-based and optimization-based approaches. Simulation-based methods for plant design include LCA, definition and evaluation of plant layouts along key performance indicators such as energy duties or cost and exergy analyses that are nowadays integrated in process simulators such as Aspen [198–201]. The advantages of simulation-based approaches for process synthesis comprise the large availability of ready-to-use software and databases for example for LCA. Additionally, the problem size is not constrained by an optimization algorithm. Nevertheless, a drawback consists of the potential limitations of the process design search space if insufficient simulations are made. Then, the risk of missing the optimal process candidate exists.

On the other hand, optimization-based approaches formulate the process synthesis problem as MINLPs and can include a larger or even the full process design search space [88, 202, 203]. A key characteristic of efficient chemical processes are high levels of mass and energy integration except for examples where heat integration is not considered a priori because it is rather negligible. This is the case if all participating process units operate at similar or even near-ambient temperatures such as in some biotechnological applications [204–206]. In most industrially-relevant scenarios, however, neglecting heat integration may not lead to optimal process design decisions.

Within the computer-aided process engineering community, there are two principle approaches toward heat integrated chemical production processes. In the first approach, the process synthesis problem is solved in a sequential fashion and can be split into two consecutive steps: a design step where the overall synthesis pathway is optimized and an integration step where energy is integrated for example via a pinch analysis [207–211]. Nowadays, there is a large community that investigates an expansion of heat exchanger networks (HEN) toward work and heat exchanger networks (WHEN) where waste heat is upgraded to electricity via organic Rankine cycles [212–216]. The separation of the design and integration problem is generally easier to solve because the number of constraints is smaller compared to the combined optimization problem of simultaneous design and integration. However, it does not necessarily provide the overall optimal solution.

Therefore, the second perspective is to combine the process synthesis and heat integration in a single step [217, 202, 218]. The fundamental idea of the Duran-Grossmann model is to include all feasible and non-feasible pinch combinations as potential candidates and to identify the feasible pinch combination through maximization of overall utility requirements. These are formulated as additional inequality constraints in the overall MINLP process synthesis problem. Refinements include the treatment of large problems via a split of all heat flows in different zones where heat is exchanged separately as well as extensions with regards to fixed and variable temperature limits [219–221]. Additionally, accurate HEN design and area calculations are reported in literature [222, 223]. Latest developments include a systematic step-wise approach of the synthesis or extension to power-plant applications where the assumption of constant utility temperatures is not applicable [57, 224].

The major disadvantage of the Duran-Grossmann formulation is that the complexity of the inequality constraints of the MINLP increases exponentially with the number of heat flows in the system making it necessary to split heat integration into zones for example. Another potential disadvantage is that the solution of the integrated process synthesis and heat integration problem requires the solution of a MINLP where convergence and optimality depend to a large extent on the non-linearities of the underlying model, heat flows and the objective function.

Besides the inclusion of the heat integration problem into the synthesis problem in form of additional inequality constraints of the MINLP, simultaneous process synthesis and heat integration has been recently addressed within the infinitely dimensional state space framework (IDEAS) by Pichardo and Manousiouthakis [225]. A disadvantage of that contribution is the required prescreening and subsequent exclusion of all internal heat flows that cannot be integrated entirely. In a separate contribution Friedler et al. [226] combined HEN synthesis with their process network synthesis approach of p-graphs [227]. Their solution entails direct heat exchange among the heat flows of the network resulting in as much as 10,227 potential heat exchanging units in their MILP example of a single reactor with three separator stages.

In contrast to the methods just discussed, the simultaneous process synthesis and heat integration approach that is introduced in this chapter overcomes the described drawbacks through an effective decoupling of non-linearities contained in the process synthesis models: the system equations – i.e. the constraints of the optimization problem – are linearized and depending on the user's requirements for the objective function one obtains a nonlinear or linear optimization problem. The flux optimization problem is formulated in such a way that integer decision variables are avoided. The FMA constitutes the generalization of the LP formulation for the cost and energy flux distribution optimization of a chemical production network whose feasibility has already been exemplified for process unit design [228–230].

6.2   Introduction of the FluxMax Approach

The underlying idea of the FMA is an effective decoupling of modeling non-linearities – that originate for example from chemical rate expressions, temperature dependencies of transport coefficients as well as equations of state – and a subsequent flux optimization within the network that is bounded by linear constraints. The methodology is structured into three steps and is illustrated in Fig. 6.1 (left). The decoupling of modeling non-linearities is achieved via a discretization of the thermodynamic state space into thermodynamic state points in the first step (1.). These discretized state points are connected through elementary process functions (EPF) in a second step (2.) as shown in Fig. 6.1 (center, left) that form a superstructure of all possible transitions within the network of discretized state points. In a last step (3.), the flux optimization problem from the initial to the final state point is solved. The EPF methodology that was developed within our research group addresses the same transition problem from an initial to a final state point at the process unit level. However, it identifies the optimal trajectory in the thermodynamic state space via the solution of a dynamic optimization problem as was shown for catalytic and multiphase reactor design [231–233]. The advantage of the FMA is that any type of transition can be easily considered as demonstrated previously with reactor design [230]. In this chapter the FMA is applied to simultaneous process synthesis and heat integration [234]. Step 1 and 2 in Fig. 6.1 are closely linked and their order is not strictly defined. In contrary to the reactor design example where the thermodynamic grid was defined a priori, the discretization grid of the simultaneous process synthesis and heat integration example results from the modeling of transitions among state points. This modeling of transitions corresponds to modeling of process units that can be described either with shortcut and rigorous physics-based unit models or by data driven models that are based on experimental or plant data (Fig. 6.1 center right). The process unit modeling results in a plant superstructure that contains all state points as well as connecting process units. In this manner the process synthesis problem is transformed into a flux optimization problem on a network represented by a directed graph (digraph). The third step (3.) is the formulation and solution of the flux optimization problem (Fig. 6.1 bottom left and right). Having decoupled all modeling non-linearities results in a convex linear feasible region because constraints of the optimization problem are linear in terms of the fluxes that are decision variables. Therefore, for any convex objective function a convex optimization problem is obtained. An additional advantage of this formulation is the applicability across scales as was shown previously at the process unit and production system levels [229, 230]. Through this versatility, the FMA can be used either for the identification of the globally optimal process for a chemical production system or for the retrofitting and process intensification of existing processes using a relatively coarse grid as shown in this chapter.
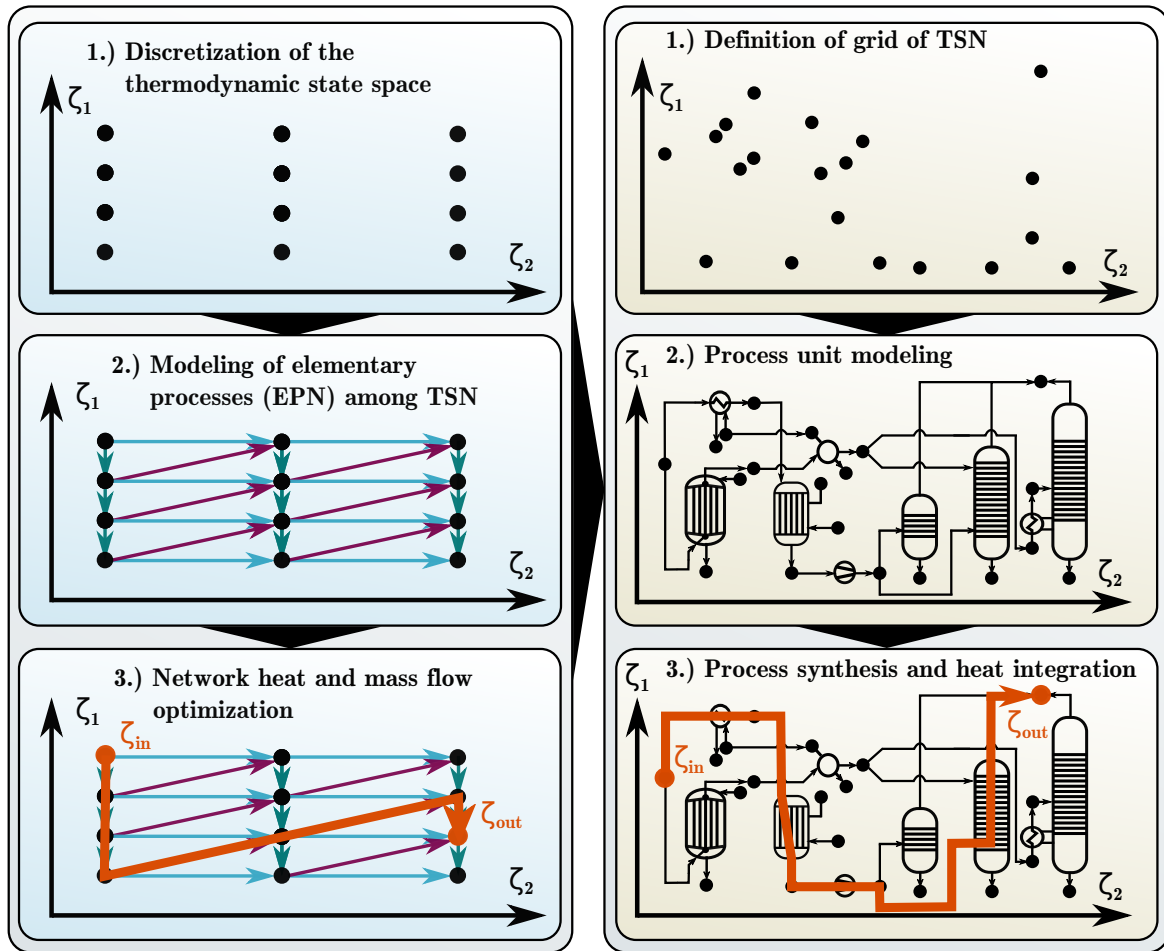
Fig. 6.1 Illustration of the three-step FluxMax approach (left) for process design with simultaneous energy integration (right): discretization of the thermodynamic state space for two arbitrary thermodynamic properties ζ_1 and ζ_2 (1.), modeling of elementary processes respective process units leading to a superstructure (2.) and network mass and energy flow optimization representing process design and integration (3.).

6.2.1 Digraph Representation of the Process Network Flux Problem

The digraph representation of the chemical process network consists of nodes and edges where the nodes represent storage or transformation of chemical substances or energy and the edges allow for mass and energy fluxes between the nodes. In contrast to the p-graph approach by Cabezas et al. [235] where material and operating nodes are defined, four distinct types of nodes (or vertices) are distinguished: the first group of nodes constitutes the discretized points within the thermodynamic state space that are defined as thermodynamic substance nodes (TSN) $M_i \in \mathcal{M}$ where $\mathcal{M}$ is the set of all TSNs that exist within the chemical process network. Any thermodynamic coordinates ζ are conceivable (comp. Fig 6.1) for the TSN but

temperature T, pressure p and composition $\mathbf{x}$ are selected for the introduction of the FMA in this chapter.

The second set of vertices is the set of elementary process nodes (EPN) $E_j \in \mathcal{E}$ where $\mathcal{E}$ comprises all feasible transformations among TSNs caused for example by chemical reactions, separation as well as a change in temperature or pressure. As a consequence, TSNs can only be linked via EPNs but EPNs may have connections to several TSN. The third group of vertices are the utility nodes (UN) $U_l \in \mathcal{U}$ where the set $\mathcal{U}$ contains all utility nodes within the network that correspond to temperature levels. UNs can link different EPNs but do not interact with discretized state space points TSNs directly. In addition to the three sets of nodes, all edges that are rated with molar, heat and work fluxes are contained in the set $\mathcal{F}$. A fourth group of nodes – the work utility nodes (WUN) S_k – are contained in the set $\mathcal{S}$. WUNs exchange work duties with process nodes but their detailed description is not relevant for the current example which consists only of work utility consuming EPNs.
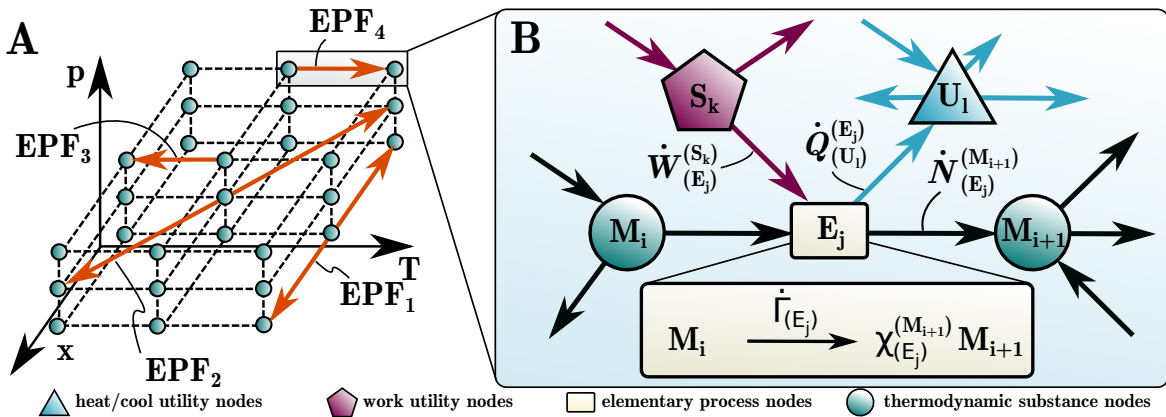
Fig. 6.2 Grid of thermodynamic state points (A) in the thermodynamic state space with p, T and $\mathbf{x}$ coordinates. Thermodynamic substance nodes (green) are linked via elementary process functions (orange): isobaric heating (EPF$_4$) and cooling (EPF$_3$), isobaric-isothermal absorption (EPF$_1$) and isobaric distillation (EPF$_2$). Two TSN (green circles) M_i and M_{i+1} are linked via EPN E_j (yellow box) (B). Work utility nodes (red pentagon) and heat utility nodes (blue triangle) supply the EPN with duties. Work fluxes (red arrows), heat fluxes (blue arrows) and molar fluxes (black arrows) link the four node types. The conversion from M_i to M_{i+1} inside the elementary process node E_j is described by a stoichiometric reaction equation and a process extent number $\dot{\Gamma}_{(E_j)}$.

Thermodynamic Substance Nodes

The TSN are discretized points within the thermodynamic state space as introduced in [230]. Consequently, a TSN is characterized by its thermodynamic coordinates for example temperature T, pressure p and its molar composition $[x_1, x_2, ..., x_i]$. Therefore, pure substances are special cases of TSNs. For each temperature, pressure or composition change from an existing TSN via an elementary process node, a new TSN is introduced. Thermodynamic properties

of pure components and mixtures in particular enthalpy and entropy are calculated a priori with a (nonlinear) equation of state of choice. EPNs link TSN in order to travel from one TSN to another in the thermodynamic state space, EPNs that perform the duty of process functions (EPF) are required as illustrated in Fig. 6.2 A. Nodes represent TSNs whereas red arrows denote feasible EPFs: EPF_1 is an isobaric-isothermal absorption, EPF_2 an isobaric distillation, EPF_3 and EPF_4 represent isobaric cooling and heating respectively.

Elementary Process Nodes

Elementary process nodes E_j are introduced to describe the transformation among TSNs. EPNs link at least two TSNs via mass flux edges that are illustrated as black arrows in Fig. 6.2 B. Stoichiometric reaction equations using the TSN are formulated to describe the transition between TSNs via a EPN. As indicated in Fig 6.2 B, generalized stoichiometric coefficients are denoted as $\chi_{(E_j)}^{(M_i)}$ with the indices of the EPN and TSN that they link. Analog to the extent of reaction $\dot{\xi}$ of chemical reactors a generalized process extent number (PEN) $\dot{\Gamma} \in \mathbb{R}_0^+$ is introduced that links the participating TSNs of an EPN. It represents the extent of the elementary process and is defined analog to the extent of reaction as:

$$d\dot{\Gamma}_{(E_j)} := \chi_{(E_j)}^{(M_i)} d\dot{N}_{(E_j)}^{(M_i)} \quad . \tag{6.3}$$

A characteristic flow of the EPN obtains the stoichiometric coefficient $\left| \chi_{(E_j)}^{(M_i)} \right| = 1$ and it is negative if the flow is directed toward the EPN, and vice versa for an outward pointing flow direction. Based on the definition (6.3), the PEN has the unit of a molar flow. If the transition among TSNs is inactive it takes the value of zero $\dot{\Gamma}_{E_j} = 0$. It is important to note, however, that PENs should not be confused with the extent of reaction which affects the outlet composition of a reactor flow directly. Instead, the PEN is a scaling variable that enables an elegant flow problem formulation because all flows via an EPN E_j are related to the unique PEN of E_j.

Utility Nodes

The third vertex set $\mathcal{U}$ of utility nodes U_l represents the heat exchange system within a process network because heat is often not transferred between process units or streams directly. Instead, heat is transferred indirectly via a network of utilities such as steam lines or cooling water bodies. This has the added advantage that from a modeling perspective, a high number of heat flows can be integrated without an exponential increase in combinatorial complexity such as in the example of Nagy et al. [227]. Heating and cooling duties to and from elementary process nodes are therefore only supplied via suitable UNs, i.e. they must

have matching temperature to fulfill the second law of thermodynamics. Surplus or demands of utilities are supplied with external heat flows denoted with full blue lines in Fig. 6.2. Heat integration among EPNs occurs indirectly via heat exchange with UNs. Consequently, UNs connect EPNs but not TSNs.

Digraph Edges

Based on the three sets of nodes that were introduced above for the digraph representation of a chemical process, edges that are evaluated by mass (Fig. 6.2 black arrows), heat (Fig. 6.2 blue arrows) and work (Fig. 6.2 red arrows) fluxes are introduced as connections among nodes. These fluxes are the decision variables of the optimization problem and constraints ensure the feasibility of the results. Upon definition of a process network of interest, internal edges are connections among nodes that are responsible for the internal distribution of mass and energy whereas external edges provide external supplies to the process network. External supplies can be either work duties supplied to WUNs, heating and cooling duties supplied to UNs or mass fluxes supplied to or extracted from TSNs.

6.2.2 Formulation of Node Conservation Laws

Conservation laws for each node of the three node types TSN, EPN and UN are set up whereas no energy balances are required for WUNs because no work integration is considered. Mass and energy balances are formulated for each EPN based on its stoichiometric reaction equation. Whereas the conventional modeling (comp. chapter 4) of component balances (CB) requires one CB per pure substance, one CB per TSN is required in the discretized thermodynamic state space grid of the FMA. Integration of Eq. (6.3) yields

$$\chi_{(E_j)}^{(M_i)} \dot{\Gamma}_{(E_j)} = \dot{N}_{(E_j)}^{(M_i)} - \dot{N}_{(E_j),0}^{(M_i)} \quad . \tag{6.4}$$

Furthermore, full conversion of thermodynamic substances inside an EPN is assumed – the thermodynamic substance entering the EPN from M_i is fully converted to a different thermodynamic substance, say M_{i+1} – resulting therefore in the following CB for each TSN M_i that is connected to an EPN E_j:

$$0 = -\text{sgn}\left(\chi_{(E_j)}^{(M_i)}\right)\dot{N}_{(E_j)}^{(M_i)} + \chi_{(E_j)}^{(M_i)}\dot{\Gamma}_{(E_j)} \quad . \tag{6.5}$$

In addition to the CBs, an energy balance for each EPN E_j is formulated containing molar heat (φ) and work (ω) duties

$$0 = \left(-\omega_{(E_j)}^{\text{in}} + \omega_{(E_j)}^{\text{out}}\right)\dot{\Gamma}_{(E_j)} + \dot{W}_{(E_j)}^{\text{ext, in}} - \dot{W}_{(E_j)}^{\text{ext, out}} \tag{6.6a}$$

$$0 = \left[\varphi_{(E_j)}^{\text{out}} + \left(1 - \eta_{(E_j)}^{\text{in}} \right) \omega_{(E_j)}^{\text{in}} + \left(\frac{1}{\eta_{(E_j)}^{\text{out}}} - 1 \right) \omega_{(E_j)}^{\text{out}} \right] \dot{\Gamma}_{(E_j)} - \sum_{\forall U_l} \dot{Q}_{(U_l)}^{(E_j)} \tag{6.6b}$$

$$0 = -\varphi_{(E_j)}^{\text{in}} \dot{\Gamma}_{(E_j)} + \sum_{\forall U_l} \dot{Q}_{(E_j)}^{(U_l)} \tag{6.6c}$$

$$\text{where} \quad \dot{Q}_{(U_l)}^{(E_j)}, \dot{Q}_{(E_j)}^{(U_l)}, \dot{W}_{(E_j)}^{\text{ext, out}}, \dot{W}_{(E_j)}^{\text{ext, in}} \in \mathbb{R}_0^+ \quad .$$

The superscript of an internal heat flow $\dot{Q}_{(E_j)}^{(U_l)}$ indicates the node from which it originates and the subscript denotes its destination node. In Eqs. (6.6), the assumption is made that simultaneous work in- and outflows do not occur and all flux variables are defined as non-negative quantities. The energy balance is thus split into three equations in order to avoid the formulation of additional entropy balances: Eq. (6.6a) contains work duties only. For EPNs that do not require work in- or output flows such as distillation columns, this equation is omitted. The second equation (Eq. (6.6b)) contains the net cooling duty which is composed of three contributions for a EPN E_j: cooling duty for example due to condensation and cooling duties resulting from waste heat for work in- and output flows which is accounted for by means of two efficiency factors $\eta_{(E_j)}^{\text{in}}$ and $\eta_{(E_j)}^{\text{out}}$:

$$\eta_{(E_j)}^{\text{in}} := \frac{\omega_{(E_j)}^{\text{in, rev}}}{\omega_{(E_j)}^{\text{in}}} \qquad \text{and} \qquad \eta_{(E_j)}^{\text{out}} := \frac{\omega_{(E_j)}^{\text{out}}}{\omega_{(E_j)}^{\text{out, rev}}} \quad . \tag{6.7}$$

The third part of the energy balancing concept accounts for net heating duties (Eq. (6.6c)). TSNs may interact with any EPN via internal mass fluxes $\dot{N}_{(E_j)}^{(M_i)}$ as well as with external supplies via external mass fluxes $\dot{N}_{\text{ext, in}}^{(M_i)}$, $\dot{N}_{\text{ext, out}}^{(M_i)} \in \mathbb{R}_0^+$. CBs for TSNs are therefore formulated as

$$0 = \sum_{E_j \in \mathcal{E}} \text{sgn}\left(\chi_{(E_j)}^{(M_i)} \right) \dot{N}_{(E_j)}^{(M_i)} + \dot{N}_{\text{ext, in}}^{(M_i)} - \dot{N}_{\text{ext, out}}^{(M_i)} \quad . \tag{6.8}$$

Energy balances for TSNs are not required because fluxes in- and out of a TSN are per definition in the same thermodynamic state.

UNs are connected via heat fluxes and therefore require no CBs. The energy balance for each UN U_l is formulated as

$$0 = \sum_{E_j \in \mathcal{E}} \left(\dot{Q}_{(U_l)}^{(E_j)} - \dot{Q}_{(E_j)}^{(U_l)} \right) + \dot{Q}_{(U_l)}^{\text{ext,in}} - \dot{Q}_{(U_l)}^{\text{ext,out}} \qquad \forall \, U_l \in \mathcal{U} \quad . \tag{6.9}$$

The sum of all heat fluxes entering an utility U_l – heat fluxes from elementary node E_j towards U_l and externally provided heat fluxes $\dot{Q}_{(U_l)}^{\text{ext,in}}$ – needs to be equal to the sum of all heat fluxes leaving an utility U_l towards E_j as well as externally removed heat fluxes $\dot{Q}_{(U_l)}^{\text{ext,out}}$.

6.2.3 Inequality Constraints for Heat Integration

The feasibility of the heat integration is assured with inequality constraints. Three different cases for all hot and cold streams are distinguished: case I streams can be integrated entirely with utility U_l, case II partially and for case III no heat integration is possible because either heat is required at a higher temperature or the temperature of the utilities is too high to be convenient for cooling. The three cases are summarized for hot and cold streams in Tab. 6.1 and illustrated in Fig. 6.3. For case I and case II streams internal heat flows
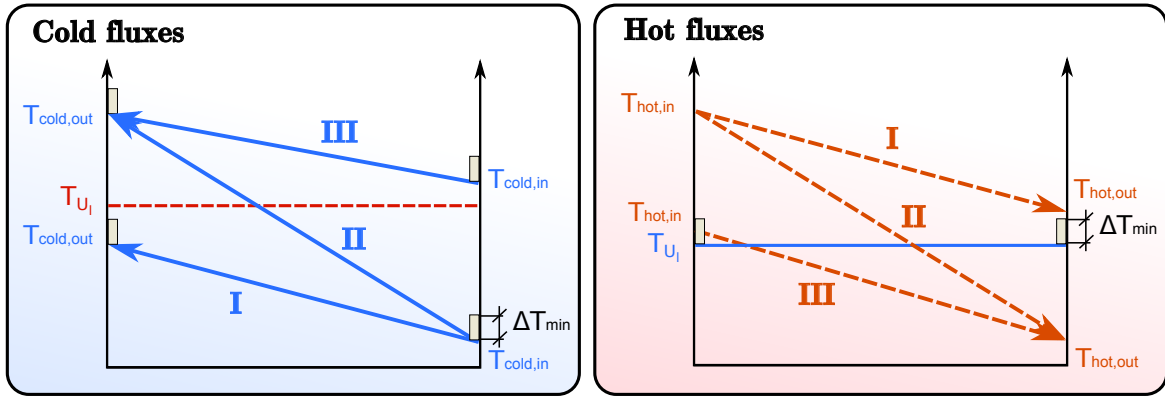
Fig. 6.3 Illustration of heat integration inequality constraints for heat integration via utilities as summarized in Tab. 6.1 (cold fluxes: blue, full lines; hot fluxes: red, dashed lines): cold fluxes are heated by the hot utility U_l (left) and hot fluxes are cooled by a cold utility (right). I, II and III represent totally and partially feasible as well as infeasible heat exchange.

$\dot{Q}_{(E_j)}^{(U_l)}$ or $\dot{Q}_{(U_l)}^{(E_j)}$ are created and added to the energy balance Eq. (6.6). To account for the maximum amount of internally transferable heat fluxes of case II streams, two subsets of $\mathcal{F}$ that contain all graph edges are introduced as: $\mathcal{F}_{II}^{UE} := \{\dot{Q}_{(E_j)}^{(U_l)} \in \mathbb{R}_0^+ \mid \text{case II satisfied}\}$ and $\mathcal{F}_{II}^{EU} := \{\dot{Q}_{(U_l)}^{(E_j)} \in \mathbb{R}_0^+ \mid \text{case II satisfied}\}$. In order to ensure the feasibility of case II streams, they must fulfill the following inequalities:

$$0 \leq \frac{T_{(U_l)} - T_{\text{cold,in},(E_j)} - \Delta T_{\min}}{T_{\text{cold,out},(E_j)} - T_{\text{cold,in},(E_j)}} \varphi_{(E_j)}^{\text{in}} \dot{\Gamma}_{(E_j)} - \dot{Q}_{(E_j)}^{(U_l)} \qquad \forall \dot{Q}_{(E_j)}^{(U_l)} \in \mathcal{F}_{II}^{UE} \qquad (6.10a)$$

$$0 \leq \frac{T_{\text{hot,in},(E_j)} - T_{(U_l)} - \Delta T_{\min}}{T_{\text{hot,in},(E_j)} - T_{\text{hot,out},(E_j)}} \varphi_{(E_j)}^{\text{out}} \dot{\Gamma}_{(E_j)} - \dot{Q}_{(U_l)}^{(E_j)} \qquad \forall \dot{Q}_{(U_l)}^{(E_j)} \in \mathcal{F}_{II}^{EU} \qquad . \qquad (6.10b)$$

Eq. (6.10a) is used to constrain the maximum heat flux that can be provided from utility U_l to the cold flux that belongs to elementary process E_j utilizing the temperature ratio in the first term that depends on the constant temperature level $T_{(U_l)}$ of U_l. Similarly, Eq. (6.10b) quantifies the maximum heat that can be transferred from the hot stream of elementary process E_j to the cooling utility U_l.

Tab. 6.1 Case differentiation of heat flows according to their temperature conditions.

Case	Condition			Heat Integration
Cold Fluxes				
I	$T_{(U_l)}$ $\geq$	$T_{\mathrm{cold,\,out}} + \Delta T_{\min}$		total
II	$T_{(U_l)}$ $<$	$T_{\mathrm{cold,\,out}} + \Delta T_{\min}$		partial
	$T_{(U_l)}$ $> T_{\mathrm{cold,\,in}}$	$+ \Delta T_{\min}$		
III	$T_{(U_l)}$ $\leq T_{\mathrm{cold,\,in}}$	$+ \Delta T_{\min}$		infeasible
Hot Fluxes				
I	$T_{(U_l)}$ $+\Delta T_{\min} \leq$	$T_{\mathrm{hot,\,out}}$		total
II	$T_{(U_l)}$ $+\Delta T_{\min} >$	$T_{\mathrm{hot,\,out}}$		partial
	$T_{(U_l)}$ $+\Delta T_{\min} <$	$T_{\mathrm{hot,\,in}}$		
III	$T_{(U_l)}$ $+\Delta T_{\min} \geq$	$T_{\mathrm{hot,\,in}}$		infeasible

6.2.4 Formulation of the Flux Optimization Problem

Within the discretized thermodynamic state space, the process synthesis and heat integration problem is formulated as a constrained flux optimization problem. The mass and energy conservation laws for all node types constitute a linear system of equality constraints. The inequality constraints that result from the heat integration formulation are also linear resulting in a convex feasible region. Therefore, a convex objective function leads to a convex optimization problem and for the special case of a linear objective function to a linear programming problem as stated in Eq. (6.11):

$$
\begin{aligned}
\min_{\mathbf{x}} \quad & f(\mathbf{x}) = \mathbf{c}^\top \mathbf{x} \\
\text{s.t.} \quad & \mathbf{A}_{\mathrm{eq}} \mathbf{x} = \mathbf{b}_{\mathrm{eq}} \\
& \mathbf{A}_{\mathrm{iq}} \mathbf{x} \leq \mathbf{b}_{\mathrm{iq}} \\
& \mathbf{x}_{\mathrm{lb}} \leq \mathbf{x} \leq \mathbf{x}_{\mathrm{ub}} \; .
\end{aligned}
\tag{6.11}
$$

f is the objective function and $\mathbf{x} = (\dot{\mathbf{N}}, \dot{\mathbf{\Gamma}}, \dot{\mathbf{Q}}, \dot{\mathbf{W}})^\top$ denotes the vector of all decision variables: internal and external mass fluxes $\dot{\mathbf{N}}$, internal and external heat fluxes $\dot{\mathbf{Q}}$, work fluxes $\dot{\mathbf{W}}$ and PENs $\dot{\mathbf{\Gamma}}$. The influence of the decision variables on the objective function is determined by the vector of cost factors $\mathbf{c}^\top = (\mathbf{c}_{\dot{N}}, \mathbf{c}_{\dot{\Gamma}}, \mathbf{c}_{\dot{Q}}, \mathbf{c}_{\dot{W}})$.

The equality constraints, described by the incidence matrix $\mathbf{A}_{\mathrm{eq}}$ and the vector of right-hand sides $\mathbf{b}_{\mathrm{eq}}$, contain the entire information about the coupling of nodes and edges of the superstructure – i.e. the energy and mass balances of EPNs, TSNs and UNs. The pattern of the equality constraint matrix $\mathbf{A}_{\mathrm{eq}}$ is illustrated in Eq. (6.12). The equality constraint matrix has the dimensions $\mathbf{A}_{\mathrm{eq}} \in \mathbb{R}^{m \times n}$ where m is the total number of nodes and n the total number of fluxes. It consists of block entries per elementary process node E_j, external mass

fluxes $\mathbf{A}_{\mathrm{eq}}^{\mathrm{ext}}$ as well as matrix entries for heat fluxes (HI).

$$\mathbf{A}_{\mathrm{eq}} = \begin{bmatrix} \mathbf{0} & \mathbf{A}_{\mathrm{eq}}^{(\mathrm{E}_1)} & & & & \mathbf{A}_{\mathrm{eq}}^{(\mathrm{E}_1),\mathrm{HI}} & \mathbf{0} \\ \cdots & & \cdots & & & \cdots & \cdots \\ \mathbf{0} & & & \mathbf{A}_{\mathrm{eq}}^{(\mathrm{E}_j)} & & \mathbf{A}_{\mathrm{eq}}^{(\mathrm{E}_j),\mathrm{HI}} & \mathbf{0} \\ \cdots & & & & \cdots & \cdots & \cdots \\ \mathbf{A}_{\mathrm{eq}}^{\mathrm{ext}} & -\mathbf{A}_{\mathrm{eq}}^{\mathrm{mb},(\mathrm{E}_1)} & \cdots & -\mathbf{A}_{\mathrm{eq}}^{\mathrm{mb},(\mathrm{E}_j)} & \cdots & \mathbf{0} & \mathbf{0} \\ \mathbf{0} & \mathbf{0} & \cdots & \mathbf{0} & \cdots & -\mathbf{A}_{\mathrm{eq}}^{\forall(\mathrm{E}_j),\mathrm{HI}} & \mathbf{A}_{\mathrm{eq}}^{\mathrm{ext},\mathrm{HI}} \end{bmatrix} \tag{6.12}$$

Top entries correspond to conservation laws of process nodes (EPNs) followed by TSNs and at the bottom UNs. Each process node equality constraint matrix contains a PEN scaling variable $\dot{\boldsymbol{\Gamma}}$, internal mass fluxes $\dot{\mathbf{N}}^{(\mathrm{int})}$ as well as external work fluxes $\dot{\mathbf{W}}^{(\mathrm{ext})}$. External molar flows to the thermodynamic substance node M_i, $\dot{\mathbf{N}}_{(\mathrm{M}_i)}^{(\mathrm{ext})}$, are contained in the plant-wide mass balance in the second block from the bottom. Equality constraints for a EPN E_j inside the equality constraint matrix consist of a mass (mb) and energy balance (eb) as shown in Eq. (6.13)

$$\mathbf{A}_{\mathrm{eq}}^{(\mathrm{E}_j)} = \begin{bmatrix} \mathbf{A}_{\mathrm{eq}}^{\mathrm{mb},(\mathrm{E}_j)} \\ \mathbf{A}_{\mathrm{eq}}^{\mathrm{eb},(\mathrm{E}_j)} \end{bmatrix} \tag{6.13}$$

and the order of the variables for each EPN is $\dot{\Gamma}_{(\mathrm{E}_j)}$, $\dot{N}_{(\mathrm{E}_j)}^{(\mathrm{M}_i)}$, $\dot{N}_{(\mathrm{E}_j)}^{(\mathrm{M}_{i+1})}$, ..., $\dot{W}_{(\mathrm{E}_j)}^{(\mathrm{ext})}$. The second-to-last column of Eq. (6.12) contains all internal heat fluxes i.e. EPN-UN couplings whereas the last column entries contains the external heat fluxes. Both entries constitute the heat integration formulation highlighted with superscripts HI.

$$\mathbf{A}_{\mathrm{iq}} = \begin{bmatrix} \mathbf{0} & \mathbf{A}_{\mathrm{iq}}^{\dot{\Gamma},\mathrm{E}_1} & \cdots & \mathbf{A}_{\mathrm{iq}}^{\dot{\Gamma},\mathrm{E}_j} & \cdots & \mathbf{A}_{\mathrm{iq}}^{\mathrm{HI}} & \mathbf{0} \end{bmatrix} \quad . \tag{6.14}$$

Inequality constraints originating from the heat integration formulation (Eq. (6.10)) are contained in $\mathbf{A}_{\mathrm{iq}}$ which is shown in Eq. (6.14): it contains entries at $\dot{\Gamma}$ positions of each EPN and at heat flux positions coupling EPNs with UNs. The right hand sides of both equality and inequality constraints in Eq. (6.11) are zero vectors: $\mathbf{b}_{\mathrm{eq}} = \mathbf{0}$, $\mathbf{b}_{\mathrm{iq}} = \mathbf{0}$.

6.3   Plant Model of the HCN Production Plant

The plant model for the HCN production plant is illustrated schematically with the super-structure flowsheet in Fig 6.4. The flowsheet is structured into two parts: the top section (A) comprises both the BMA and Andrussow reactor nodes for the synthesis of HCN: mixing of reactants, synthesis reactor which is either a BMA reactor at variable temperature or an Andrussow reactor, acidic absorption of unreacted NH_3, absorption of product HCN and
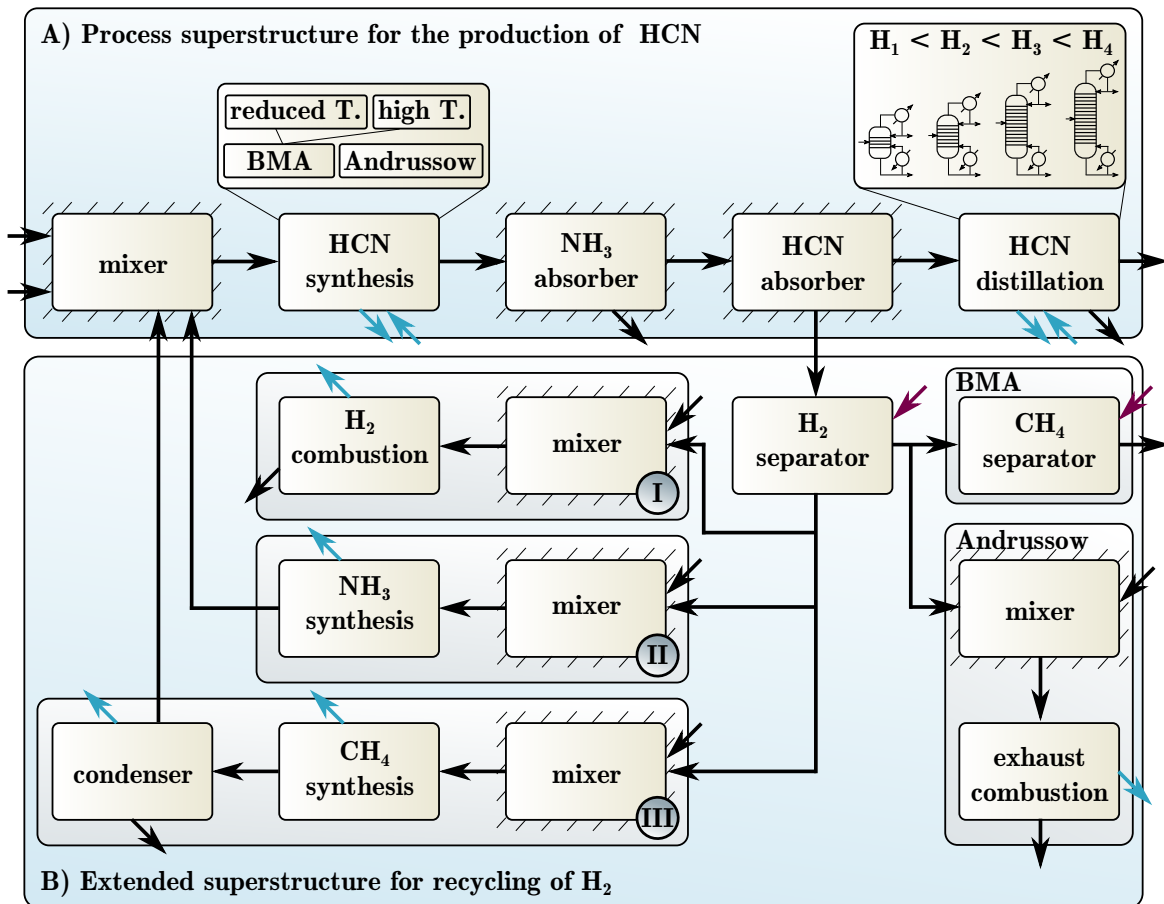
Fig. 6.4 Schematic flowsheet of process synthesis for the production of HCN (top section) including the selection of the reactor type (BMA or Andrussow) and design decisions such as number of trays of the product purification distillation column. The bottom section illustrates three possible recycling possibilities upon separation of H_2 from the byproduct gas stream: energetic coupling via combustion of H_2 (I) and two synthesis routes using the surplus H_2 towards NH_3 (II) and CH_4 (III). Additionally, for low temperatures of the BMA reactor, CH_4 may be recycled and additional exhaust gases of the Andrussow such as CO require combustion prior to release to the environment. Arrows correspond to mass (black), heat (blue) and work (red) fluxes. Hatched process units indicate adiabatic units.

purification in a distillation column with variable number of stages. Hatched borders around a unit indicate an adiabatic process unit, black arrows represent mass flows and colored arrows illustrate heat (blue) and work (red) demands. The discretized EPNs of the reactor and distillation process units are sketched in the two insets.

Besides the production route toward HCN at the top (A), three possible recycling pathways of hydrogen are illustrated below in section (B) of Fig. 6.4. Off-gases of the HCN absorber are separated from the byproduct H_2 and the remaining gas may be stripped off CH_4 in the BMA, or fully oxidized in the Andrussow process variant. Purified H_2 may undergo the following recycling options: combustion for generation of heat (I), production of reactant NH_3 (II) according to Eq. (6.1) or production of reactant CH_4 (III) according to the Sabatier

reaction (Eq. (6.2)). The byproduct H_2O from the methanation is separated in a condenser. Both reactant synthesis routes comprise the idealized assumption of the utilization of pure H_2 without the need of further pretreatment such as additional purification steps.

6.3.1 Elementary Process Node Calculation: BMA Reactor Nodes

The formulation of reaction equations for EPN is demonstrated for the example of the BMA reactor node. All other EPN descriptions including the other reactor process nodes are described in the appendix in section D.2. The reactor process node is described by the stoichiometric equation Eq. (6.15)

$$M_i \longrightarrow \chi_{(R_j)}M_{i+1} \tag{6.15}$$

where M_i specifies the mixture of reactants and M_{i+1} the mixture of products and reactants in the outlet of the reactor. The inlet composition (M_1) is set to the standard inlet conditions of $x_{CH_4} = 0.48$ and $x_{NH_3} = 0.52$ that were used in single compartment modeling in chapter 4 and the constant wall temperature is set to either 1200 K or 1500 K. Then, the outlet compositions (M_2 and M_3) that are presented in Tab. 6.2 are obtained. Furthermore, the extent of reaction $\dot{\boldsymbol{\xi}} = \begin{pmatrix} \dot{\xi}_1 & \dot{\xi}_2 \end{pmatrix}$ for each of the two chemical reactions (Eq. (3.6a) and Eq. (3.6b)) and the stoichiometric coefficients for the transition between the TSN of Eq. (6.15), $\chi_{(R_j)}^{(M_i)}$, are provided. Heat duties that are required for each reactor EPN are equally indicated

Tab. 6.2 Characteristic data of BMA reactor EPNs: inlet and outlet composition, extent of reaction, stoichiometric coefficient and heat duty.

T_w	TSN	molar fraction					$\dot{\xi}$	$\chi_{(R_j)}^{(M_i)}$	q
		CH_4	NH_3	HCN	N_2	H_2			
K	-	-	-	-	-	-	$mol\,s^{-1}$	-	$kJ\,mol^{-1}$
1200	M_1	0.48	0.52	0	0	0	$\begin{pmatrix} 0.28 & 0.07 \end{pmatrix}$	1.61	114
	M_2	0.12	0.11	0.17	0.02	0.58			
1500	M_1	0.48	0.52	0	0	0	$\begin{pmatrix} 0.41 & 0.08 \end{pmatrix}$	1.91	172
	M_3	0.03	0.01	0.22	0.02	0.72			

in Tab. 6.2: comparison of the heating duties from the kinetic reactor simulation with the product of reaction extents and reaction enthalpies shows that heating duties based on the reactor simulation are approximately 50 % higher compared to the reaction enthalpies at standard conditions due to the heating and additional effects that are considered in the kinetic reactor model.

The formulation of the conservation laws for the two BMA reactor EPN yields two mass balances – one per TSN –

$$
\begin{aligned}
0 &= \dot{N}^{(M_1)}_{(R_j)} &&- &&\dot{\Gamma}_{(R_j)} \\
0 &= &&-\dot{N}^{(M_2)}_{(R_j)} &&+\chi_{(R_j)}\dot{\Gamma}_{(R_j)}
\end{aligned}
\tag{6.16}
$$

and one energy balance per BMA reactor EPN:

$$
0 = -\varphi^{\text{in}}_{(R_j)}\dot{\Gamma}_{(R_j)} + \sum_{U_l \in \mathcal{U}} \dot{Q}^{(U_l)}_{(E_j)} \quad .
\tag{6.17}
$$

6.3.2 Discretization Grid for the HCN Case Study

The EPF that link TSN in this case study are described using a combination of shortcut and rigorous models. The discretized thermodynamic state space for the case study of HCN is 13-dimensional because it comprises temperature, pressure and the following 11 chemical species: H_2O, CH_4, H_2, N_2, O_2, NH_3, HCN, CO, CO_2, NO and H_2SO_4. Sulfuric acid is used in the ammonia absorption and to maintain a safe pH value smaller five in all flows that contain HCN. With this high dimensionality it is not desirable to identify the globally optimal process through an equidistant, infinitesimal refining of the thermodynamic grid that was applied in the design of process units [230]. Instead, the state space discretization grid is refined for key process units by incorporating different design and operating points. For recycling reactors at the plant periphery, however, no such distinctions are made in the first step to enable a quick identification of promising recycling pathways. This combination is possible because the FMA allows for the combination of any types of models irrespective of their levels of detail. The recycling section that is of lesser importance is described using short-cut reactor models and the separate reactor operating conditions of recycling reactors are not distinguished. As such the FMA enables the fast identification of the most promising process candidates. Fig. 6.4 illustrates this split into key components and periphery: the main process routes towards HCN are considered in more detail (Fig. 6.4 A) with two different reactor types and two temperatures for the BMA reactor as well as four different distillation column designs with increasing number of trays. This level of detail is also reflected by the kinetic reactor models. In addition to the detailed two-dimensional model for the BMA reactor, the Andrussow reactor is characterized using a steady-state and one-dimensional reactor model using the system of reaction equations by Schmidt et al. [122, 123, 125]. Reaction equations as well as the Andrussow reactor model are described in the appendix in Sec. A.2 and Sec. D.1. Absorber units are discretized with single units since their operation does not involve neither heating nor cooling duties.

Overall, this state space discretization is coarse but allows for a good interpretation of results due to the complex interplay of different process units particularly when simultaneous heat integration is considered. In order to attain a finer discretization grid or a larger superstructure, one could perform more simulations of all process units – for example of key units such as reactor and distillation units – or extend the scope to additional unit operations. An increase in grid refinement would increase the accuracy of the solution for a defined superstructure but is beyond the scope of this chapter. Instead, a proof-of-concept is provided in combination with the demonstration that significant process intensification potentials can be identified with a relatively coarse discretization grid.

6.3.3 Case Study Parameters for the Optimization

All case study parameters are summarized in Tab. 6.3. Costs of heating utilities at temperatures above ambient temperatures are approximated via an estimation of the heat that is usable at this temperature from combustion of natural gas. In this manner, high temperature utilities require more natural gas because not all of the heating value can be used to achieve the utility temperature. Not all commodity prices are generally available because they often depend on local supplier situations. To maintain comparability among cost values, raw material prices are therefore obtained from Sigma-Aldrich in August 2018 and scaled with the Index Mundi price of CH_4 [236]. Water prices are obtained from Statista and CO_2 emission prices are taken from August 2018 price of European CO_2 emission allowances [237, 238].

6.4 Optimal Design of a HCN Production Plant

The results are split into two main sections after a brief discussion of the optimality criteria for the process designs. At first, the identification of the most resource-efficient HCN synthesis process is shown leaving recycling of H_2 aside. In a subsequent step, recycling pathways of H_2 via energetic coupling as well as the production of reactants from the side product H_2 are included in the process synthesis.

6.4.1 Objective Functions and System Constraints

Externally supplied resources i.e. external fluxes into the whole process system that are consumed upon the production of HCN are grouped into raw materials and energy fluxes consisting of heating, cooling and work duties. In addition, both variable costs of material and energy fluxes are combined in the total variable cost. Raw material optimization is achieved with an objective function for atom efficiency and the Sheldon E-factor of the

Tab. 6.3 Case study parameters for simultaneous process synthesis and heat integration for the production of HCN.

parameter	symbol	unit	value
simulation parameters			
H_2 separation efficiency	$\eta_{(E_j)}$	-	0.01
minimum temperature difference	$\Delta T_{\min}$	K	20
utility temperatures	$T_{(U_l)}$	K	[290, 500, 1600]
lower heating value of CH_4	h_{CH_4}	$kJ\,mol^{-1}$	800
cost values			
work duty	$p_{\dot{W},\text{ext,in}}$	$EUR\,kJ^{-1}$	2.8×10^{-5}
cooling duty	$p_{\dot{Q},\text{ext,out}}$	$EUR\,kJ^{-1}$	1.7×10^{-6}
purchase methane	$p_{CH_4,\text{ext,in}}$	$EUR\,mol^{-1}$	1.6×10^{-3}
purchase ammonia	$p_{NH_3,\text{ext,in}}$	$EUR\,mol^{-1}$	1.5×10^{-2}
purchase hydrogen cyanide	$p_{HCN,\text{ext,in}}$	$EUR\,mol^{-1}$	$-$
purchase air	$p_{air,\text{ext,in}}$	$EUR\,mol^{-1}$	0
purchase hydrogen	$p_{H_2,\text{ext,in}}$	$EUR\,mol^{-1}$	1.0×10^{-3}
purchase water	$p_{H_2O,\text{ext,in}}$	$EUR\,mol^{-1}$	1.7×10^{-5}
purchase carbon dioxide	$p_{CO_2,\text{ext,in}}$	$EUR\,mol^{-1}$	1.4×10^{-3}
discharge water	$p_{H_2O,\text{ext,out}}$	$EUR\,mol^{-1}$	-2.5×10^{-5}
discharge carbon dioxide	$p_{CO_2,\text{ext,out}}$	$EUR\,mol^{-1}$	-4.8×10^{-4}

process [239]. For this purpose all mass flows that leave the network are multiplied with their respective atom numbers $n_{\text{atom},i}$ to evaluate the objective function for atom efficiency and with their respective molar masses $\tilde{M}_i$ to obtain the E-factor. Energy optimization is achieved via minimization of total energy inputs and heating utility inputs. Variable cost are minimized through pricing of all raw materials and utility duties according to the data in Tab. 6.3. Conflicting objectives are identified and analyzed with multiobjective optimization via weighted objective functions. The objective functions are summarized in Tab. 6.4. Atom efficiency is defined as atoms in the target product(s) divided by the total input of atoms. It is maximized if the number of output atoms is minimized for a constant production amount of HCN. E-factor minimization is the mass equivalent in kg_{waste} per kg_{product} to the atom efficiency. Minimization of total duty comprises both in- and outward pointing duty supplies whereas heating minimization comprises solely the externally supplied heating duties which is of particular interest for the selected case study where endo- and exothermic reactor options exist. The index "ext,out" indicates fluxes that leave the process toward its environment whereas fluxes with indices "ext" refer to in- and outward pointing fluxes. Variable cost minimization prices all external edges with corresponding material and duty cost.

Tab. 6.4 Objective functions of this chapter: maximization of the atom efficiency of the overall process, minimization of the E-factor, minimization of total duties, minimization of heating duties and the minimization of variable cost.

objective function		cost vector definition		
$f_{\text{atom efficiency}}$	$:= \sum\limits_{\text{M}_i \in \mathcal{M}} n_{\text{atom}}^{(\text{M}_i)}\ \dot{N}_{\text{ext,out}}^{(\text{M}_i)}$	$c_{\dot{N}_{\text{ext,out}}^{(\text{M}_i)}}$	$=$	$n_{\text{atom}}^{(\text{M}_i)}$
		$\mathbf{c}_{\dot{\Gamma}}$	$=$	$\mathbf{0}$
		$\mathbf{c}_{\dot{Q}}$	$=$	$\mathbf{0}$
		$\mathbf{c}_{\dot{W}}$	$=$	$\mathbf{0}$
$f_{\text{E-factor}}$	$:= \sum\limits_{\text{M}_i \in \mathcal{M}} \tilde{M}^{(\text{M}_i)}\ \dot{N}_{\text{ext,out}}^{(\text{M}_i)}$	$c_{\dot{N}_{\text{ext,out}}^{(\text{M}_i)}}$	$=$	$\tilde{M}^{(\text{M}_i)}$
		$\mathbf{c}_{\dot{\Gamma}}$	$=$	$\mathbf{0}$
		$\mathbf{c}_{\dot{Q}}$	$=$	$\mathbf{0}$
		$\mathbf{c}_{\dot{W}}$	$=$	$\mathbf{0}$
$f_{\text{total duty}}$	$:= \sum\limits_{\text{U}_l \in \mathcal{U}} \dot{Q}_{(\text{U}_l)}^{\text{ext}} + \sum\limits_{\text{E}_j \in \mathcal{E}} \dot{W}_{(\text{E}_j)}^{\text{ext,in}}$	$\mathbf{c}_{\dot{N}}$	$=$	$\mathbf{0}$
		$\mathbf{c}_{\dot{\Gamma}}$	$=$	$\mathbf{0}$
		$\mathbf{c}_{\dot{Q}^{\text{ext}}}$	$=$	$\mathbf{1}$
		$\mathbf{c}_{\dot{W}^{\text{ext}}}$	$=$	$\mathbf{1}$
f_{heating}	$:= \sum\limits_{\text{U}_l \in \mathcal{U}} \dot{Q}_{(\text{U}_l)}^{\text{ext,in}}$	$\mathbf{c}_{\dot{N}}$	$=$	$\mathbf{0}$
		$\mathbf{c}_{\dot{\Gamma}}$	$=$	$\mathbf{0}$
		$\mathbf{c}_{\dot{Q}^{\text{ext,in}}}$	$=$	$\mathbf{1}$
		$\mathbf{c}_{\dot{W}}$	$=$	$\mathbf{0}$
$f_{\text{var, cost}}$	$:= \sum\limits_{\text{M}_i \in \mathcal{M}} c_{\dot{N}_{\text{ext}}^{(\text{M}_i)}}\ \dot{N}_{\text{ext}}^{(\text{M}_i)} + \sum\limits_{\text{U}_l \in \mathcal{U}} c_{\dot{Q}_{(\text{U}_l)}^{\text{ext}}}\ \dot{Q}_{(\text{U}_l)}^{\text{ext}}$ $+ \sum\limits_{\text{E}_j \in \mathcal{E}} c_{\dot{W}_{(\text{E}_j)}^{\text{ext}}}\ \dot{W}_{(\text{E}_j)}^{\text{ext}}$	$c_{\dot{N}_{\text{ext}}^{(\text{M}_i)}}$	$=$	$p_{(\text{M}_i),\text{ext}}$
		$\mathbf{c}_{\dot{\Gamma}}$	$=$	$\mathbf{0}$
		$c_{\dot{Q}_{(\text{U}_l)}^{\text{ext}}}$	$=$	$p_{\dot{Q},\text{ext}}$
		$c_{\dot{W}_{(\text{E}_j)}^{\text{ext,in}}}$	$=$	$p_{\dot{W},\text{ext,in}}$

The production capacity of HCN is set to 200,000 $\text{t}_{\text{HCN}}\ \text{a}^{-1}$. Furthermore, reactants as well as auxiliary materials such as water and air can enter the process in contrast to TSNs that represent process intermediates such as for example a H_2O-HCN mixture. In addition, all processes must have equal conditions for outward pointing flows in order to enable a fair comparison among all process alternatives. Therefore, outward flows must be at reference state and must not contain hazardous substances. For example the off-gases of the Andrussow reactor must undergo a complete oxidation in order to prevent emission of carbon monoxide.

6.4.2 Process Design Without H_2 Recycling

The first goal of process synthesis for the production of HCN is to identify the most resource-efficient reactor-separator combination as shown in Fig. 6.4 A. Therefore, the recycling of the byproduct H_2 is neglected at this stage. Three reactor configurations, a BMA reactor $R_{(1)}$ with reactor wall temperatures $T_{(\text{w})} = 1500$ K, a BMA reactor $R_{(2)}$ with reactor wall temperatures $T_{(\text{w})} = 1300$ K and an Andrussow reactor are considered in combination with

four different distillation column designs of 8, 11, 14 and 17 stages. The idea behind the reduced temperature BMA is to sacrifice product yield in exchange for a reduction of heat duty requirements thus achieving a quasi intermediate between the BMA reactor at operating temperature and the Andrussow reactor. As discussed in chapter 5, the heat requirements for the BMA reactors are based on the single compartment level of chapter 4 because the quantitative information at the tube bundle level is inaccurate. The reflux ratios of the distillation columns are set to achieve a purity of 99.9 % of HCN in the separator distillate. In order to illustrate the impact of the selected objective function, all possible configurations – i.e. 12 optimization scenarios – are compared in Fig. 6.5 and in Fig. 6.6.

Identification of Competing Objectives

Weighted optimization results of the five objective functions – atom efficiency, total duty, heating duty, E-factor and variable cost – are illustrated in Fig. 6.5 where optimal scenarios are always located in the bottom left corner of the diagrams. The legend is illustrated at the top: the color of a data point denotes the reactor node – red for high temperature BMA, green for BMA with reduced temperature and blue for Andrussow reactor nodes – whereas the shape of the data point represents the selected HCN distillation column. Black filled symbols denote results without simultaneous heat integration whereas heat integration is applied in optimization results with colored symbols.

BMA reactors obtain high yields whereas Andrussow reactors do not require heating. Therefore, atom efficiency versus total duty (Fig. 6.5 A) as well as atom efficiency versus heating duties (Fig. 6.5 B) are both competing objectives. The results thus form a Pareto front that is indicated with the dotted line in both figures. With regard to total duties, both BMA reactors constitute the Pareto front whereas high temperature BMA and Andrussow reactor make up the Pareto front when heating is examined. For the twelve possible scenarios under consideration, atom efficiency and E-factor (Fig. 6.5 C) yield exactly the same results no matter if simultaneous heat integration is considered or not which is also illustrated in Fig. 6.6. High atom efficiencies mean less waste and indicate often but not always good E-factors. The former is a quantification of this effect in terms of moles whereas the E-factor is mass-based. Atom efficiency and E-factor are therefore not competing objectives. Similar results apply for atom efficiency and variable cost (Fig. 6.5 D): material flows are the key contributor to variable cost as shown in Fig. 6.6 D. Therefore, low variable cost also means high atom efficiency.
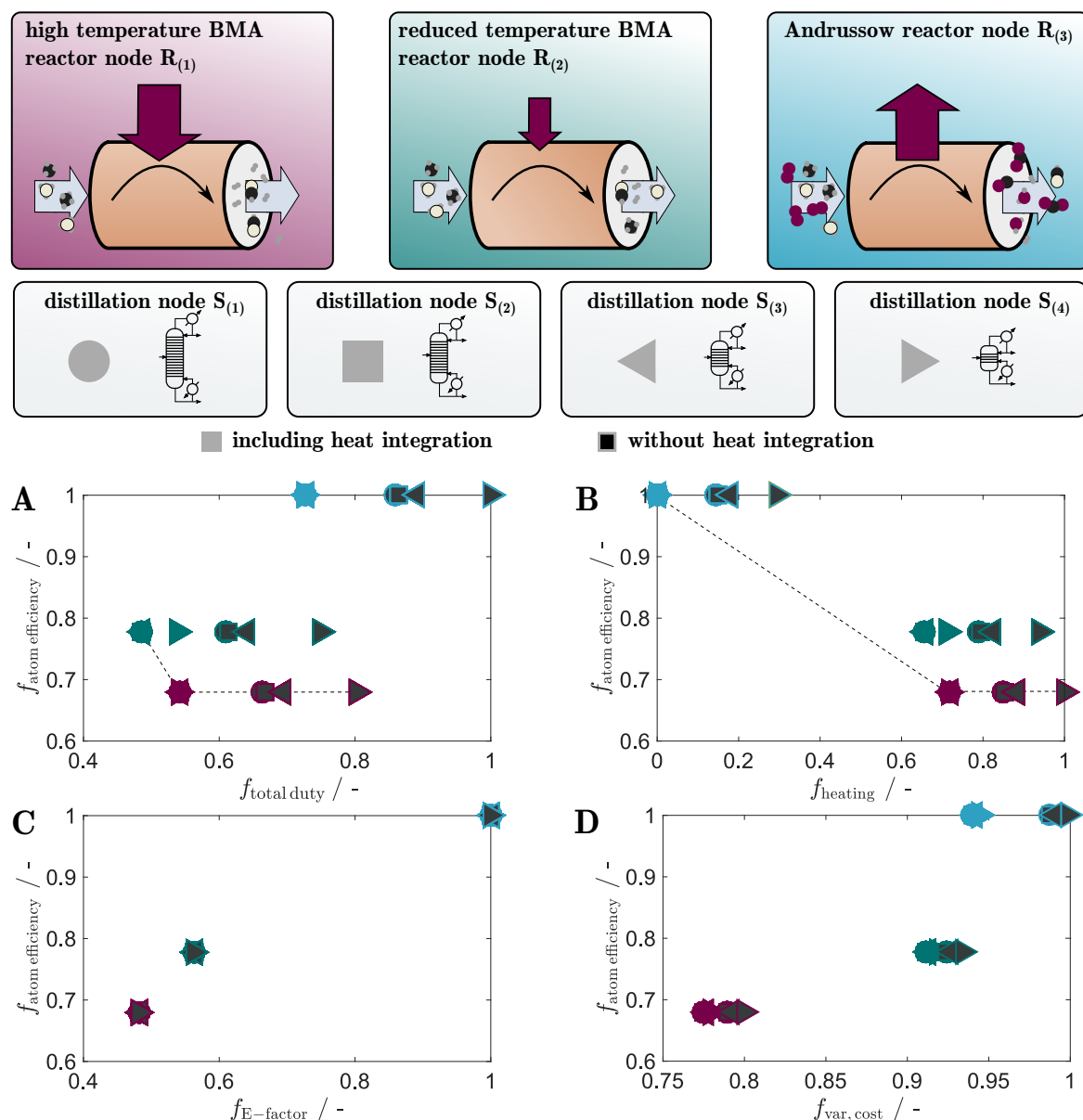
Fig. 6.5 Weighted optimization of two objectives: atom efficiency versus total duties (A), atom efficiency versus heating duties (B), atom efficiency versus E-factor (C) and atom efficiency versus total variable cost (D). A, B form Pareto curves where the front is indicated with a dotted line; C, D are not competing objectives and form no Pareto front. Shapes correspond to the four distillation column process nodes and colors to the three reactor process nodes highlighted at the top. Symbols that are filled with color include heat integration in their calculation, symbols that are filled with black color highlight results without simultaneous heat integration.

Impact of the Reactor Node

A comparison of the twelve scenarios is provided in more detail in Fig. 6.6: the results illustrate atom efficiency, E-factor, utility demands and variable cost for the minimization
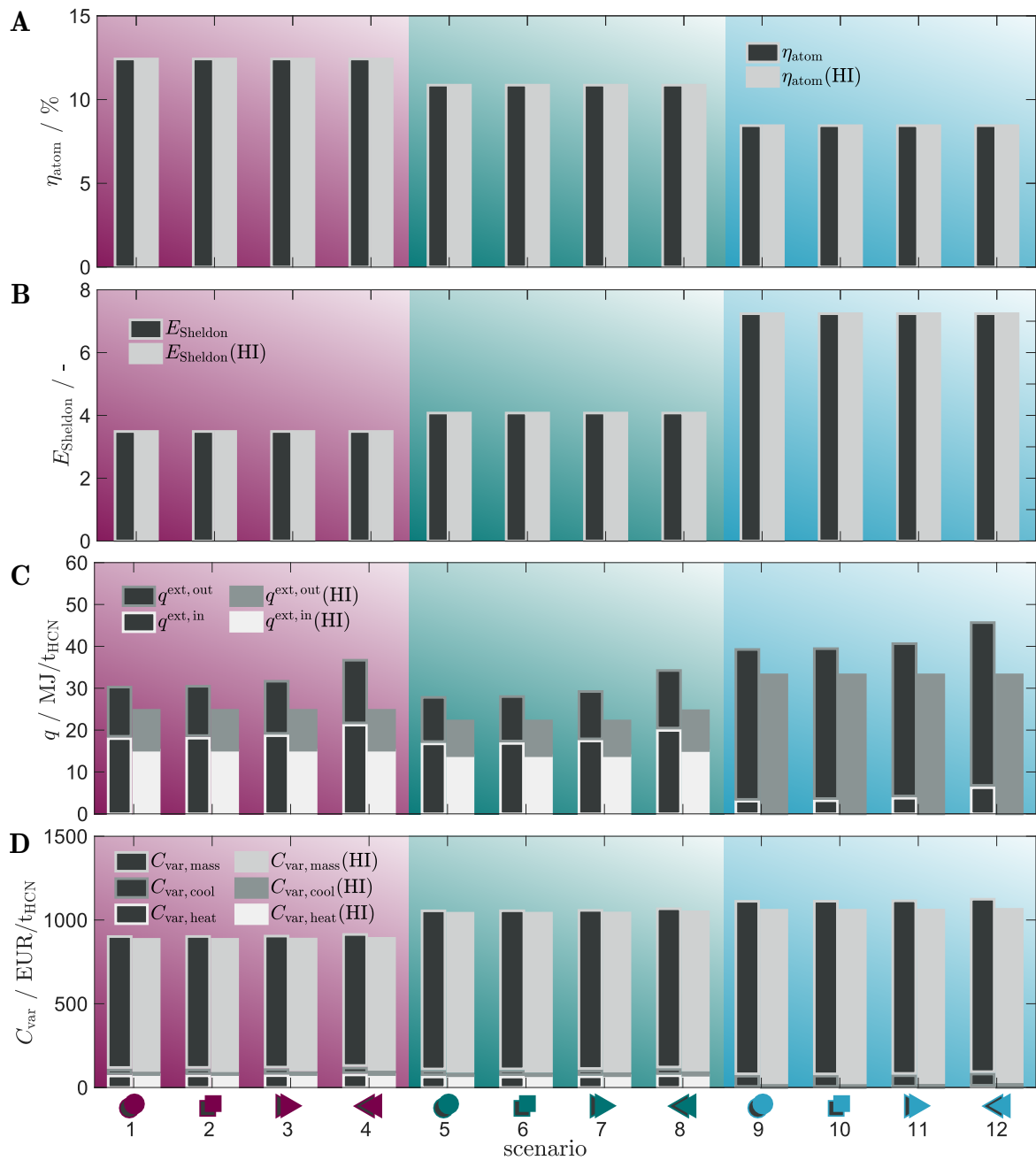
Fig. 6.6 Optimal atom efficiency (A), E-factor (B), duties (C) and variable cost (D). The legend of the 12 scenarios corresponds to the one of Fig. 6.5: the symbol and background color indicate the reactor node and the shape denotes the distillation column node. The gray shade of the bar edges denotes the type of property and the filling with or without heat integration.

of variable cost. As mentioned above, processes with high temperature BMA reactors (red) attain the highest atom efficiencies (Fig. 6.6 A) of $\eta_{atom} = 12.4\,\%$ and lowest E-factors (Fig. 6.6 B) of $E_{Sheldon} = 3.5$ followed by low temperature BMA reactors (green) with $\eta_{atom} = 10.9\,\%$ and $E_{Sheldon} = 4.2$. All reactor-separator combinations that are based on

Andrussow reactors (blue) are significantly less raw material efficient with $\eta_{\text{atom}} = 8.4\%$ and they produce twice as much waste per kilogram product with $E_{\text{Sheldon}} = 7.2$. The results for the E-factor of the BMA reactors are within the range generally applicable to bulk chemicals whereas the Andrussow process is already in the range of fine chemical production [239]. All these results are not dependent neither on the type of the distillation column nor on heat integration.

Comparison of the duties involved in each scenario (Fig. 6.6 C) shows that low temperature BMA processes (green) have the lowest total duty consumption both with and without heat integration. Therefore, they constitute the low-duty-edge of the Pareto front in (Fig. 6.5 A) with the high temperature BMA reactors at the high-atom-efficiency edge (red). With respect to heating, the Andrussow processes (blue) are optimal due to the exothermal reactor nodes. The general idea of operating the BMA reactor at lower temperature is to reduce heating cost while sacrificing product yield as introduced at the end of chapter 4. The reduction in atom efficiency, however, is not compensated by the advantage of having lower heating duties. Processes that employ low temperature BMA reactors thus lie within the Pareto region in Fig. 6.5 B. Consequently, if one desires to operate an atom efficient and total duty efficient process, one has to choose either the high temperature BMA, the low temperature BMA reactor or a mixture of both. If – on the other hand – one wants to minimize heating instead of total duties one has to weigh between high temperature BMA and Andrussow reactors.

Including simultaneous heat integration in the process synthesis reduces variable cost for all process possibilities (Fig. 6.6 D): around 2.5 % for both BMA reactor types and roughly 4.5 % for the Andrussow reactor even though all have a similar reduction in total duties as shown in Fig. 6.6 C. The reason for the enhanced reduction of variable costs for the Andrussow process are the temperature levels: heat integration aside, the heating demand of BMA reactors is at high temperatures whereas the Andrussow reactor requires less costly cooling duties. In total, heat integration does reduce variable cost but the key contributor to variable costs are mass flow costs. Therefore, different recycling pathways for H_2 are considered below.

Impact of the Distillation Column Node

Prior to the discussion of the impact of H_2 recycling, the impact of the distillation column on the overall process performance is highlighted. Comparing the processes without simultaneous heat integration (black-filled) in Fig. 6.5 A and B it is evident that the column with the least number of stages requires the highest amount of duties and vice versa for the column with the highest number of stages (17 stages). Process design without taking simultaneous heat integration into account would clearly identify the column with 17 stages as the most resource-efficient process. In a subsequent pinch analysis one would find out that its heating

and cooling duties can be fully integrated using the internal heat flows within the overall process.

Considering heat integration simultaneously to the process synthesis, however, reveals that no difference in the process performance among all four column designs exist in terms of neither heating nor total duties. This is due to the fact, that all duty requirements of the columns can be integrated with internal heat flows of the processes for all column designs and reactor designs with one exception. The column with the minimum number of eight theoretical stages in combination with the low temperature BMA reactor cannot be fully integrated which is visible in Fig. 6.6 C: the white bar of scenario 8 is higher than its benchmark scenarios 5,6 and 7. Consequently, resource-efficient process design without access to simultaneous process synthesis and heat integration identifies the process with the distillation column with 17 stages to be optimal while all distillation columns within this plant context are equally resource-efficient. The approach of simultaneous process synthesis and heat integration thus enables to identify process pathways that are structurally different and cannot be identified using a sequential approach of mass flow optimization and subsequent heat integration.

6.4.3   Process Design Including H_2 Recycling

Within this section the room for improvement with respect to the five target objectives through consideration of the three recycling pathways shown in Fig. 6.4 B is illustrated. The results are structured into three parts: first, the recycling pathways are compared with regard to their effect on the objective functions. Subsequently, Pareto optimal scenarios are identified through multi-objective optimization and in the last part the Pareto optimal results are analyzed in more detail.

Comparison of Recycling Pathways

Fig. 6.7 demonstrates the impact of heat integration and the three recycling pathways on the process performance for the three reactor types. As shown above, the selection of the distillation column within this specific process context is of minor importance and thus not discussed in detail. Background colors in Fig. 6.7 correspond to the three reactor nodes that are available, and the five bars for each reactor node type correspond to the standard process without heat integration, with heat integration, with energetic H_2 recycling through combustion, with production of the reactant NH_3 and with production of the reactant CH_4. Heating duties of the Andrussow process are effectively reduced to zero by heat integration (indicated with 0). The combustion of its byproduct H_2 provides thus no benefits for the process and is not included in the diagram (indicated with X). It is common practice in
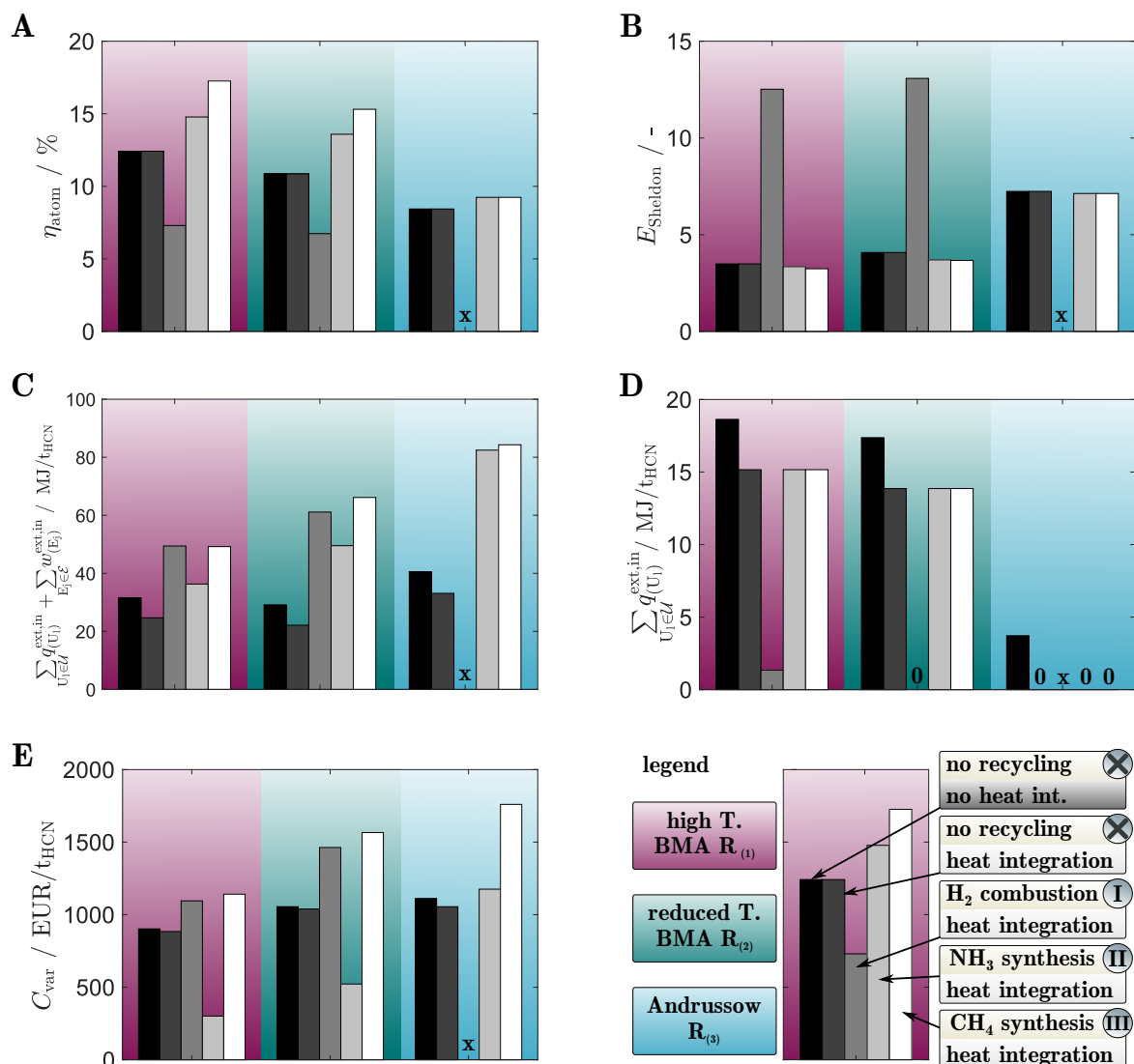
Fig. 6.7 Impact of heat integration and three different recycle pathways on the three available reactor nodes (background color: red – high temp. BMA, green – low temp. BMA, blue – Andrussow) and on the five objectives: atom efficiency (A), E-factor (B), total duties (C) and heating duties (D) as well as total variable cost (E). Bars in each group represent (from left to right): no recycling and no heat integration, no recycling with heat integration, combustion of H_2 with heat integration, production of NH_3 with heat integration and CH_4 production with heat integration. Zero values are indicated with 0 and "x" denotes the Andrussow reactor node with H_2 combustion which provides no benefit for any objective function.

industry to recycle the byproduct H_2 energetically in the synthesis furnaces of BMA reactors [93]. Fig. 6.7 D confirms that combustion of H_2 reduces heating duties to 13 % for high and to 0 % for low temperature BMA reactors. However, at the same time, cooling and work duties from the separation of H_2 (Fig. 6.7 C) increase due to the assumption of a combustion of pure H_2 and cooling requirements for plant waste streams. Overall, this pathway deteriorates variable cost by 20 % and 38 % for the reactor nodes $R_{(1)}$ and $R_{(2)}$. The effect is larger for the

low temperature BMA reactor because its reactor outlet stream contains considerably less H_2 resulting in an increase in H_2 separating cost. The boundary conditions that cause these results are required to maintain general comparability of the results. Otherwise a case by case selection of waste streams would be required according to local country- and site-specific legislation with respect to hazardous substance regulations for example. Another negative side-effect of the combustion of H_2 is the decrease in atom efficiency (Fig. 6.7 A) by 39% and 38% and an increase in E-factors (Fig. 6.7 B) by 256% and 233% due to air flow that is required for combustion leading to large waste streams. The difference in atom efficiency and E-factor results from the strong difference in molar masses of for example O_2 compared with H_2. The reason why this process alternative is often selected in industrial processes is that the purification step of the H_2 separator is omitted leading to a mixed combustion of non-reacted CH_4 and fuel gas streams in the furnace with a combined flue gas cleaning of the off-gases of the furnace. In this manner, the total variable cost may be reduced by a few percent. For this modeling scenario, two drawbacks of the combustion of H_2 remain due to the requirement of a H_2 purification and the boundary conditions of the process synthesis: atom efficiency and waste streams deteriorate and the H_2 separation and cooling duties increase. In addition, heating cost account for a minor contribution of the total variable cost as was shown in Fig. 6.6 D.

The second recycling alternative is the production of NH_3 from the side product H_2 to improve atom efficiency and reduce waste. Fig. 6.7 A shows improvements in atom efficiency by 19%, 23% and 9% for the base processes of the three reactor nodes $R_{(1)}$, $R_{(2)}$ and $R_{(3)}$. The reduction in waste mass is smaller (Fig. 6.7 B) accounting for 4%, 9% and 1.5% because of the low molar mass of H_2. The production of NH_3 is exothermal requiring additional cooling duties (Eq. (6.1)) but the temperature levels are not sufficiently high to provide heat to the endothermal BMA reactors. Therefore, no improvement is attained in terms of heating duties when NH_3 is produced. The most significant effect of the on-site production of NH_3 is the decline of total variable cost. Reactant cost and in particular the cost of NH_3 are the key drivers of variable cost. Production of NH_3 leads to a decrease in 67% and 51% for $R_{(1)}$ and $R_{(2)}$. On the other hand, variable cost of the Andrussow process are increased by 6% if NH_3 is produced. The reason for this range from strong decrease to an increase in variable cost originates from the different purities of H_2 in the reactor outlet streams of the base case processes and subsequent requirements for purification prior to production of NH_3: whereas the outlet streams of $R_{(1)}$ and $R_{(2)}$ are rich in H_2 as indicated in Tab. 6.2, the outlet stream of $R_{(3)}$ has a hydrogen outlet molar fraction of $x_{H_2} = 12\%$. Therefore, cost for purification of H_2 are low for $R_{(1)}$ and higher for $R_{(2)}$ and $R_{(3)}$. In total, production of NH_3 has strong benefits for processes with BMA but not with Andrussow reactors.

The third recycling pathway is the production of CH_4 via the Sabatier reaction where an additional benefit exists in the consumption of the greenhouse gas CO_2. Atom efficiencies

(Fig. 6.7 A) are increased by 40 % for both $R_{(1)}$ and $R_{(2)}$ and 9 % for $R_{(3)}$. At first sight it is surprising that the increase in atom efficiency for the BMA reactors is higher than for production of NH_3 because a comparison of the reaction equations (Eq. (6.1), Eq. (6.2)) shows that for equal amounts of H_2 to be recycled, 100 % of the H_2 is converted to reactants for the former and a mere 50 % of H_2 is converted to reactants in the Sabatier reaction. In the context of the entire process, however, also the side product H_2O from the Sabatier reaction can be used for the absorption of NH_3 and HCN in the downstream processing and thus the atom efficiency saving potentials of both recycling pathways are equally high. Improvements in atom efficiency for CH_4 production are larger compared to NH_3 for $R_{(1)}$ and $R_{(2)}$, because more H_2 is available than can be used as NH_3 in the reactor whereas the full amount of H_2 can be exploited if both CH_4 and H_2O are used. The process with the Andrussow reactor node $R_{(3)}$ does not show this behavior because H_2 is not available in sufficient amounts to cover the consumption of NH_3 in the reactor: therefore, both recycling pathways exhibit the same increase in atom efficiency.

As before, heating duties are not affected (Fig. 6.7 D) and total duties increase if CH_4 is produced on-site. The increase in duties is stronger compared to the production of NH_3 because the reaction enthalpy of the Sabatier reaction is considerably larger requiring more cooling. Contrary to the gains in atom efficiency for production of CH_4, an increase in total variable cost for any type of reactor node is obtained: 26 % $R_{(1)}$, 48 % for $R_{(2)}$ and 58 % for $R_{(3)}$. The reason is, that the separation H_2 from the off-gas stream is more expensive than the procurement of the reactant CH_4 which is available at low prices on the world market. The increase in variable cost is more pronounced for $R_{(2)}$ and $R_{(3)}$ because the separation cost in the H_2 separator are higher for those processes. In summary, globally optimal scenarios include either production of CH_4 to attain high atom efficiencies or production of NH_3 for high atom efficiencies and low total variable cost.

Pareto-Optimal Process Pathways

Having discussed the impact of the three recycling pathways on the objective functions, it is the focus of this section to identify the overall most resource-efficient process. The objectives atom efficiency and total variable cost are weighted with heating and total duty objective functions in a multi-objective optimization and the results are shown in Fig. 6.8 where the illustrated processes are limited to process candidates that lie at the edge of the Pareto fronts. As in Fig. 6.5, colors represent the type of reactor node whereas an additional color – orange-red – identifies processes that employ a combination of the reactor nodes. Shapes correspond to recycling pathways: H_2 combustion, NH_3 production, CH_4 production, any combination thereof and no recycling at all. Results with and without heat integration are highlighted with color- and gray-filled symbols and the resulting two Pareto fronts are

indicated with a dashed line (no heat integration) and a dotted line (heat integration). The
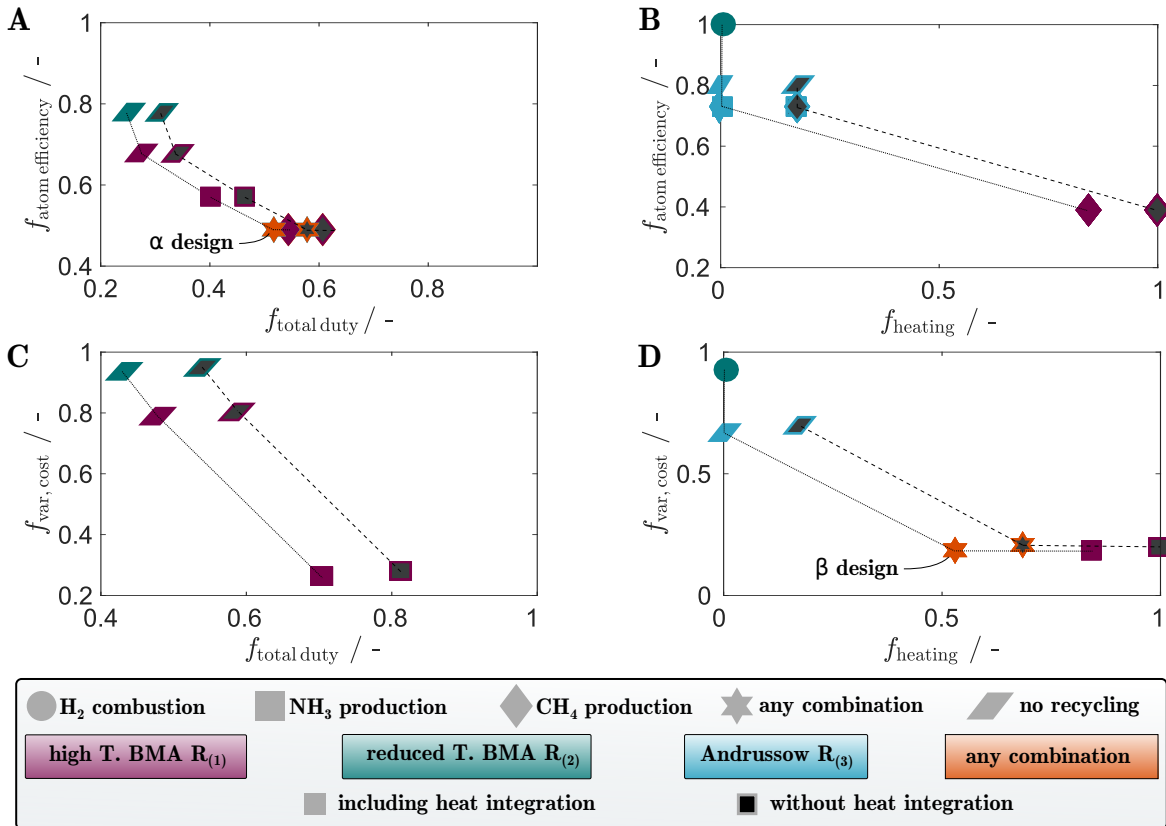
Fig. 6.8 Pareto optimal results for the entire process scheme of Fig. 6.4: symbols denote recycling pathways and colors the reactor type. Pareto fronts are indicated with a dashed line (no heat integration) and a dotted line (including heat integration). Four scenarios are compared: atom efficiency versus total duty (A), atom efficiency versus heating duty (B), total variable cost versus total duty (C) and total variable cost versus heating duty (D).

results for atom efficiency versus total duty requirement (Fig. 6.8 A) confirm the observations above: recycling leads to higher total duty requirements and thus no recycling is at the total duty optimal range whereas the production of CH_4 for the reactor node $R_{(1)}$ leads to the best atom efficiency which is better than for the production of NH_3. Heat integration leads to a shift of all scenarios to lower duty requirements. A novel process – the α design – is identified which has a lower total duty at similar minimal atom efficiency. Results for atom efficiency versus heating are shown in Fig. 6.8 B which correspond to a horizontal shift of the results of A: Andrussow reactor nodes require no heating and their atom efficiency is improved through either NH_3 or CH_4 production to the same extent as was mentioned above and high temperature BMA and production of CH_4 remain at the optimal atom efficient corner where also the α design is located because its requirements for heating duty equal the $R_{(1)}$-CH_4 combination. Interestingly, another structurally new process is identified due to the simultaneous heat and mass optimization which would not appear in a two-step consecutive

approach. The heat duty requirements of the process that involves the low temperature BMA reactor are effectively reduced to zero through combustion of its side product H_2.

The calculation is repeated for variable cost versus energy (Fig. 6.8 C) which is similar to atom efficiency versus energy (Fig. 6.8 A): no recycling for the two BMA-type reactors for minimal energy requirements but now the production of NH_3 in combination with $R_{(1)}$ at the minimal variable cost as was shown in Fig. 6.7 E. Replacing total duty with heating duty in Fig. 6.7 D is similar to B and C: Andrussow designs replace low temperature BMA and NH_3 production replaces the production of CH_4. In addition to these expected results a second new process – the β design – is identified: it has equally low variable cost like the $R_{(1)}$-NH_3 combination at significantly lower heating duties. The novel plant designs α and β are discussed in more detail in the following section.

Analysis of Optimal Plant Designs

The flowsheets of the two novel designs – α and β are illustrated in Fig. 6.9 A and B. The α design attains the same globally optimal atom efficiency as the BMA $R_{(1)}$ reactor in combination with the production of CH_4 through a combination of the same reactor node with both production of NH_3 and CH_4. As both recycling processes have equal resource-saving potential the application of more NH_3 production results in lower total duty requirements due to lower reaction enthalpy of the NH_3 synthesis reaction. The β design has similarly low variable cost as the $R_{(1)}$-NH_3 process at lower heating duty requirements. This is achieved through a combination of the benefits of both the BMA and the Andrussow reactor concepts: the H_2 outlet of the high temperature BMA reactor is exploited for the maximum production of NH_3 while zero-heating-duty Andrussow reactor is applied to reduce heating requirements. Overall duty is with $40.6\,\mathrm{MJ/t_{HCN}}$ $10\,\%$ below the $R_{(1)}$-NH_3 combination.

Both new designs are compared in Fig. 6.9 C, D, E and F with respect to atom efficiencies, E-factor, duty requirements and variable cost. Both designs represent resource-efficient designs because they have high atom efficiencies and low total variable cost. Their heating and total duty requirements are inferior to for example the Andrussow reactor without recycling but the impact of raw material efficiency is prioritized over energy efficiency due to its larger contribution to total variable cost for the case study under consideration.

The BMA reactor $R_{(1)}$ is applied in both the α and β designs and is thus considered as a benchmark process. The results of the objectives relative to this benchmark process are presented in Tab. 6.5. The direct comparison of the results shows that heat integration reduces utility requirements significantly but has a minor effect on total variable cost whereas recycling of H_2 to produce valuable NH_3 may reduce the total variable cost by $55\,\%$ (α design) or $68\,\%$ (β design) despite higher total duty requirements. Depending on the specific site
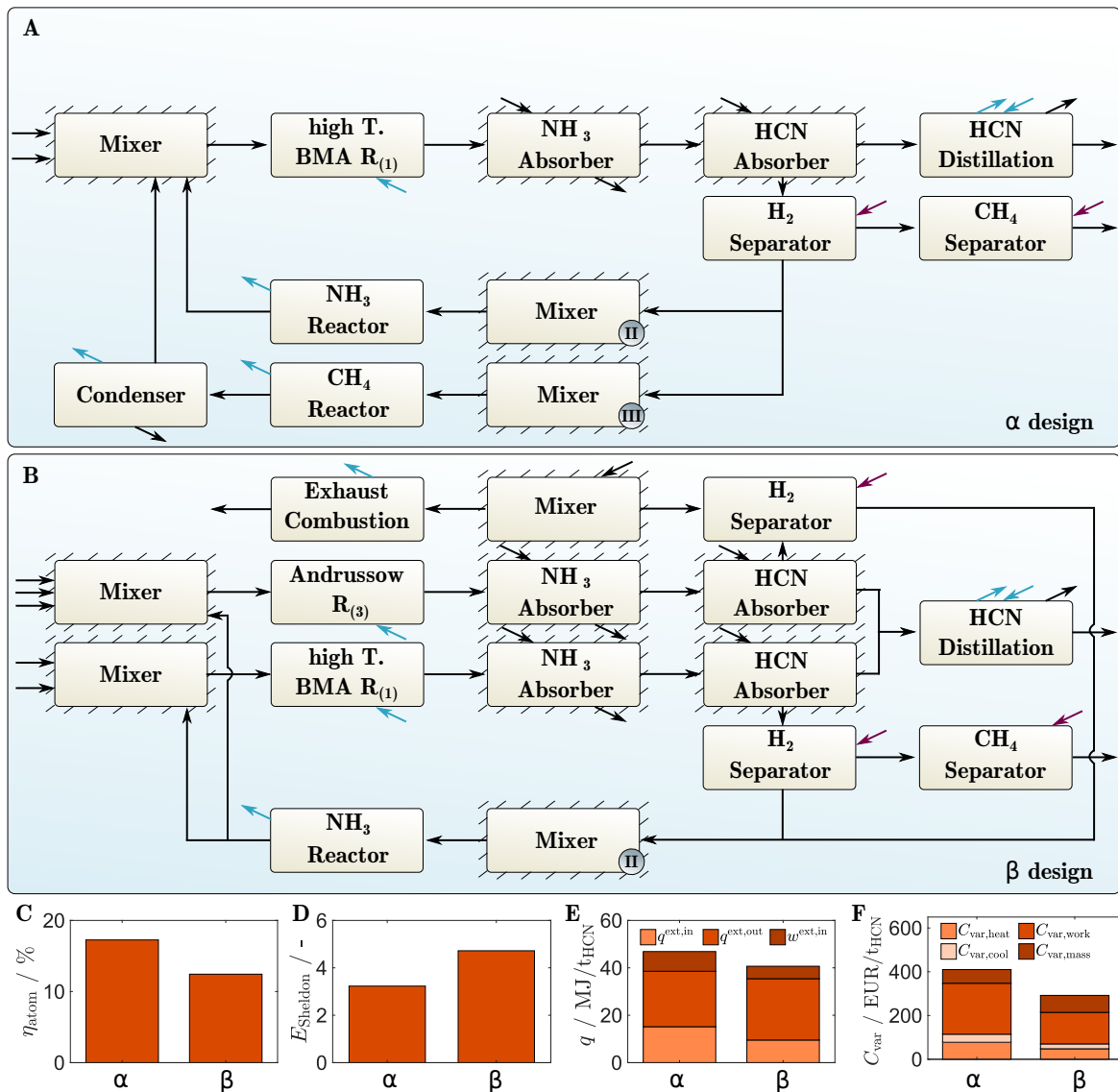
Fig. 6.9 Flowsheets of the α and β process designs for production of HCN from Fig. 6.8. Combination of NH_3 and CH_4 production for minimal atom efficiency at low energy duties (A) and parallel operation of high temperature BMA and Andrussow reactors with NH_3 production for minimal total variable cost and heating duties. Atom efficiencies (C), E-factors (D), heating, cooling, work duties (E) and variable cost (F) of the two designs are presented at the bottom.

requirements and regulations either the more reactant-efficient α design or the more heating and variable cost efficient β process design is of interest.

It has to be kept in mind, that a significantly larger amount of process units is required for the β process design due to the parallel operation of both the Andrussow and the BMA reactors and the related downstream process units. In this study, however, the most resource-efficient production processes are identified from the technological perspective. In practice, various aspects may lead to different results: HCN and NH_3 are often traded and exchanged locally

Tab. 6.5 Relative changes of objective values of scenarios $i \in \{\alpha, \beta\}$ compared with objective values of the benchmark process R_1 with (HI) and without heat integration and with NH_3 synthesis.

	$R_{(1)}$	$R_{(1)}$(HI)	$R_{(1)}+NH_3$(HI)	α(HI)	β(HI)
$\dfrac{\eta_{\text{atom}}(i)}{\eta_{\text{atom}}\left(R_{(1)}\right)} - 1 \Big/ \%$	0	0	+19.3	+39.5	−2.1
$\dfrac{E_{\text{Sheldon}}(i)}{E_{\text{Sheldon}}\left(R_{(1)}\right)} - 1 \Big/ \%$	0	0	−4.0	−7.5	+35.2
$\dfrac{\displaystyle\sum_{U_l \in \mathcal{U}} q_{(U_l)}^{\text{ext,in}}(i)}{\displaystyle\sum_{U_l \in \mathcal{U}} q_{(U_l)}^{\text{ext,in}}\left(R_{(1)}\right)} - 1 \Big/ \%$	0	−18.6	−18.6	−18.6	−48.8
$\dfrac{\displaystyle\sum_{U_l \in \mathcal{U}} q_{(U_l)}^{\text{ext}} + \sum_{E_j \in \mathcal{E}} w_{(E_j)}^{\text{ext,in}}(i)}{\displaystyle\sum_{U_l \in \mathcal{U}} q_{(U_l)}^{\text{ext}} + \sum_{E_j \in \mathcal{E}} w_{(E_j)}^{\text{ext,in}}\left(R_{(1)}\right)} - 1 \Big/ \%$	0	−21.8	+14.9	+48.4	+28.7
$\dfrac{C_{\text{var}}(i)}{C_{\text{var}}\left(R_{(1)}\right)} - 1 \Big/ \%$	0	−2.0	−66.7	−54.6	−67.6

resulting in strongly different cost scenarios; fixed cost, maintenance, insurance and other regulatory aspects may lead to strongly different results as well. Nonetheless, the results that are presented here demonstrate the potential of the FMA of identifying and optimizing a priori non-intuitive process structures.

6.5 Chapter Summary

This chapter addressed the research questions (IV) and (V) that were identified in the introductory chapter 1. Therefore, a method for designing resource-efficient processes called the FluxMax approach was introduced. This method enables a simultaneous heat and mass flux optimization through the discretization of the thermodynamic state space. Model inherent nonlinearities are effectively decoupled from the optimization problem leading to a convex feasible region where the heat integration problem is formulated as a system of linear inequality constraints. By use of linear objective functions, globally optimal solutions are identified within the discretized network. The case study of HCN production reveals that there is not a single but instead there are multiple optimal process pathways. It does not suffice to consider neither energy efficiency nor raw material efficiency in an isolated fashion. A comprehensive consideration of resource efficiency incorporating energy, raw material and financial resources as a whole is required instead because mutual dependencies between objectives and competing objectives are significant as the case study demonstrates. Five objective functions were considered: atom efficiency and E-factor for raw material efficiency, heating and total duty to assess the energetic performance and total variable cost to provide a

comparative framework of material and energy efficiency. Using multi-objective optimization, competing objectives are identified as utility versus raw material requirement whereas variable cost and waste minimization point in the same direction because the procurement of the reactant NH_3 is the most significant contributor to total variable cost within the case study of HCN synthesis.

The case study demonstrated that structurally non-intuitive processes can be found with the FMA that are not identifiable using a sequential approach of plant synthesis and subsequent heat integration: this concerns all process steps where heat integration is crucial. As such, the design of the distillation column with respect to the investigated objective functions is irrelevant in the HCN process context due to heat integration potential. Besides, the energetic recycling of H_2 is activated within the process synthesis only if heat integration is considered simultaneously. This process design example also illustrates that no chemical process design is superior in all five objectives but resource efficiency contributes significantly more to variable cost than utility duties for this example. Consequently, the most resource-efficient process which is the high temperature BMA process is selected as a benchmark scenario. Two novel process designs – the most atom-efficient and the most variable cost efficient – lead to improvements in atom efficiency by 39.5 % and variable cost reduction by 67.6 %, however, at the price of an increase in overall utility duties between 28.7 % and 48.4 %. This increase in utility requirement, however, is related to the system boundaries: the introduction of additional resource recycling steps comes at the expense of an increase in cooling utility requirements.

Chapter 7

Conclusion

High temperature gas phase reactors are characterized by high enthalpies of reaction which renders heat transfer essential for reactor design. Fixed bed reactors dominate in MSR and wall reactors in the BMA reactor at the single compartment level but the both are built as tube bundle furnace reactors at the aggregate tube bundle level. The reactants are CH_4 and an oxidizing agent – H_2O in MSR and NH_3 in HCN production – which is added in excess to prevent coking. However, coking is not reflected in the reaction kinetic expressions, particularly in HCN synthesis and the excess amount can thus not be identified in a model-based analysis. Instead, reactor design problems emphasize enhancing the heat transfer. Besides, high temperature reactors are of interest for heat integration at the plant level due to the availability of hot heat flows at high temperature levels. Five target research questions were identified in the introduction of this thesis and they are addressed at their corresponding process hierarchy. After that, this thesis is concluded from the combined multi-level perspective.

7.1 Conclusions at the Single Compartment Level

The first three aspects refer to heat transfer characteristics of high temperature reactors (I), the scale dependency of heat transfer (II) and reactor design implications based on these insights (III). Within chapter 4 and 5 these aspects were addressed at the single compartment and tube bundle levels. It was found for the single reactor compartment that the flow is predominantly in the laminar and forced flow region. Total heat transfer into the reactor gas mixture is dominated by conduction accounting for 80 % and radiation accounting for 20 %. This ratio is caused by the endothermic chemical synthesis reactions at the catalytic surface of the reactor walls. Careful modeling of radiative heat transfer is nonetheless essential because

it is highly relevant in the inlet region of the reactor. For this reason, gray gas absorption coefficients were calculated based on molecular absorption spectra that are provided in HITRAN and HITEMP databases for all relevant species. For both case studies, MSR and HCN synthesis, the reactants H_2O and NH_3 have high absorption coefficients and thus favor a fast heat uptake of the gas mixture which is important particularly for HCN synthesis to avoid the decomposition of the reactant NH_3 to N_2. Increasing wall emissivities is one possibility to achieve a faster heating-up of the reactants and the doubling of the surface emissivity from 0.45 to 0.90 which could be achieved through addition of SiC in the inlet region of the reaction tubes would lead to an overall increase in the gas outlet temperature of 30 K. A channel width of 16 mm was identified to be optimal: more narrow channels reduce the space time yield without providing significant improvements in yield for the example of HCN. The ensemble of the channel and absorption coefficient model as well as its application to HCN synthesis were presented in chapter 4 and published in the course of this thesis [197]. Furthermore, this method was also applied to MSR to discuss the onset of transport limitations for microreactors [91]. Both examples illustrate that optimality criteria for the reactor design are not straightforward at the single compartment level: product purity and quantity must be balanced as well as the fuel efficiency. Therefore, despite the implementation of the channel model in Matlab/CasADi that enables a fast model solution and rigorous optimization compared to a model in commercial CFD software, no optimization results are presented at the single reactor compartment level.

Overall, additional experimental data with respect to two aspects would be of interest to further increase the predictive power of the single compartment model: firstly, mass flow and temperature measurements using inert gas flows through the reaction compartment would enable a validation of the heat transfer model. Subsequently, the setup of a microkinetic reaction mechanism for the methane-ammonia system on platinum including coking and decomposition reactions would enable a rigorous optimization of the synthesis compartment through dosing of reactants or optimization of the temperature profile along the reactor. This enhanced reactor design could then be identified using dynamic optimization on the existing model implementation that is presented in this thesis for example by utilizing the EPF methodology or the concept of parsimonious input parametrization to reduce computational cost that was developed within our group [240]. In the context of this thesis, however, validation with literature data as well as the dialogue with the industrial partner Evonik Industries substituted own experimental data. In order to access more sophisticated geometries using advanced CFD solvers while maintaining accessibility of the underlying model equations, an implementation of the synthesis compartment model in the open source software OpenFOAM could be considered [241].

7.2   Conclusions at the Tube Bundle Level

Based on the two-dimensional single compartment model, the analysis and design of the reactor at the superordinate tube bundle reactor level was achieved. Utilizing correlations of wall heat flux versus tube wall temperature from the single synthesis compartment, the influence of the arrangement of multiple tubes in a tube bundle were investigated and optimized. While the correlations for each individual tube in the bundle are based on a channel model they were converted to tubes using equal surface areas. The complexity of the full-scale furnace was reduced to a two-dimensional tube bundle furnace model. Depending on the position of tubes and burners in the furnace, radiative heat transfer accounts for 80 % or more of the total heat transferred to the tubes unless a tube was placed directly in the burner flue gas stream which is prohibited by material strain constraints. This is a sharp contrast to the single compartment channel reactor model where conductive heat transfer is dominant. By means of switching functions the view factors between tubes and walls were formulated as smooth functions. Based on the tube bundle furnace model, two optimization problems were formulated based on heat transfer maximization and on inter-tube view factor minimization. Two aspects, however, led to a simulation-based optimization of the tube bundle: the large abundance of local optima in the objective function of the view factor optimization problem and the computational cost of a single solution to the optimization problem. Using manual simulations, it was found that different geometric arrangements of tubes have a minor impact compared to the inter-tube distances. For the case study of the Endter reactor, the optimal inter-tube distance was identified as 0.052 m irrespective of the tube diameter for the Endter furnace layout. With a staggered tube arrangement of this distance, the average tube yield is augmented by 0.5 % and the standard deviation of the tube bundle is reduced. Generally, staggered bundle arrangements are superior by 2-3 % product yield compared to aligned arrangements because the view factors are smaller.

In a follow-up study that is currently investigated, the temperature field and convection assumptions are relaxed using CFD solvers in Star-CCM+ to model the flue gas flow inside the furnace in collaboration with Sebastian Engel of the chair of fluid dynamics at the Otto-von-Guericke University. Preliminary results indicate that the assumption that radiative heat transfer is dominant in the furnace is justified. This validation motivates future industrial applications of the radiation-based design approach for tube bundle furnaces that is presented in chapter 5 of this thesis. Nonetheless, the modeling of the hot flue gas flow in the furnace enables the consideration of the fuel efficiency of a bundle design which will be investigated alongside. Besides, the furnace boundary has been modeled as a polygonal line which enables the systematic variation of the furnace topology. Variation of the bundle and the furnace at the same time, however, increases the search space drastically depending on the number of elements of the polygonal line. This topology optimization of the furnace, however, is only

purposeful in combination with the modeling of the flow field: consideration of radiative heat transfer alone returns the trivial results that the gas layer around the bundle arrangement shall attain its maximum values on all sides.

The modeling of the furnace in CFD emphasizes that high model precision and optimization need to be balanced despite the fast technological developments and the strong increase in computational power over the last decades. Similar and even more pronounced than for the single compartment, experimental validation of the tube bundle model results is expensive and difficult. One possibility for industrial applications would therefore be the optimization of the tube bundle using the tool described in this thesis and subsequent validation of the results using selected high fidelity simulations for the three-dimensional furnace.

7.3 Conclusions at the Plant Level

Utilizing the heat duty requirements per product of the single compartment level, the remaining two research questions (IV) and (V) with respect to design of efficient processes were addressed. The realization that simultaneous heat and mass flux optimization are essential for efficient process design lead to the development of the FMA for simultaneous process synthesis and heat integration in collaboration with Dominik Schack. Its main characteristics include the discretized thermodynamic state space, the representation of any EPF transition between state points as chemical reaction enabling a unified problem formulation as a digraph. Thereby, a linear feasible region for the network flow optimization is obtained. The proof-of-concept of this approach for the identification of efficient chemical processes in a single step was demonstrated for both process unit design and plant synthesis emphasizing its applicability across characteristic length-scales [230, 234].

Multi-objective optimization was used for the process synthesis of the HCN case study in order to balance material, energy and the combination of both i.e. variable cost. It was found that despite the zero heating requirements of the Andrussow reactor, processes that involve high temperature BMA reactors are superior with respect to total duty consumption, waste production, material efficiency and variable cost. Reducing the temperature of the BMA reactor does reduce total energy consumption but causes higher variable cost because material cost account for the majority of all variable cost. From an economic perspective it is thus not recommendable to utilize neither the Andrussow reactor alone nor the BMA reactor at reduced temperatures. Instead, recycling of the byproduct H_2 to produce the reactants CH_4 and particularly NH_3 have the best material and cost efficiency: combination of both recycling pathways with the high temperature BMA reactor increases the atom efficiency by 40 % and variable cost by 55 % whereas a combination of BMA, Andrussow and on-site synthesis of NH_3 reduces variable cost by 68 % without sacrificing atom efficiency.

While heating duties are reduced for both designs, total duties increase by 29 % and 48 % respectively due to the boundary conditions of the optimization that do not allow the emission of for example hot water and steam to enable a fair comparison of all processes within the same framework.

The identification of structurally non-intuitive process alternatives is possible due to the simultaneous heat integration within the FMA: as such, the column design is irrelevant in the HCN plant context and the combustion of excess H_2 to reduce heating duties of the endothermic reactors is utilized only if simultaneous heat integration is considered. This feature is particularly relevant for complex examples with multiple heat sources and sinks that cannot be easily overlooked. The successful development of the FMA and the findings for the case study raised a number of continuative research questions. The idea at the origins of the FMA – the discretization of the search space in a thermodynamic grid and a priori calculation of elementary edges – requires further research because the grid limits the search space in the optimization step. Grid design and refinement for both coarse screening and global optimization need to be formulated more systematically. Engineering know-how remains crucial for the identification of the most areas within the search space that provide the greatest process intensification potentials. These need to be discretized in a fine manner whereas other areas can be covered more coarsely. The HCN example has 13 dimensions making an equidistant search grid computationally prohibitive. In addition, the solution time for a single problem is shifted from the optimization – which occurs within seconds for linear objective functions – toward the preprocessing for both simulations that are required and toward the creation of the constraint matrices. The former can be accelerated through smart decisions on the kind of available edges. The latest developments of the FMA for methanol synthesis utilize idealized edges that can be set up rapidly and enable quick refinement of the grid within the thermodynamic state space [242, 243]. The constraint matrices on the other hand could be assembled more quickly by exploiting for example sparsity patterns within the large matrices or model reduction techniques which could be investigated further in collaboration with "computational methods in systems and control theory" group of the MPI. A decisive aspect for the interpretation of results are the system boundaries that concern both material take-up and discharge: the supplier situation at a specific site, emission limits for byproduct or waste off-gases and temperature limits for cooling water all have a significant impact on the results. Context-independent system boundaries were proposed but it is evident that the performance of a process is substantially site dependent for industrial applications.

Further research questions in the context of the novel methodology include the identification of globally optimal processes benchmarking the method with the IDEAS approach. In addition, fix cost can be included via the process extent numbers enabling a comparison of the FMA with the with existing approaches such as the p-graph method and MINLP approaches that

exploit the Duran-Grossmann formulation for heat integration. The inclusion of fix cost can lead to a generalization of the objective function to quadratic or other nonlinear functions. Based on the structure of utility and work utility nodes, it is a logical next step to close the gap between the two node types using heat pumps for example organic Rankine cycles in order to couple work and heat integration and compare the FMA with other WHEN synthesis methodologies because they are currently of high interest within the PSE community. The case study shows that weighing of material and energy efficiency is currently required within the FMA and variable cost offers one possibility of combining the two. In the context of sustainable process design, however, ecological aspects of process design are equally important for example the types of waste streams and their related hazards, the global warming potential and many other criteria. These aspects are considered in LCA approaches and a link of LCA databases with the FMA enables better decision making through a combination of the advantage of detailed LCA databases with process synthesis through optimization.

7.4   Conclusions from a Multi-Level Perspective

All three level hierarchies that were examined – the single compartment, tube bundle and plant level – are both interconnected and stand-alone: the correlation of heat flux versus reactor output is both essential for the bundle optimization and to estimate heat requirements at the process scale. The bundle level, however, is independent of the results at the plant level and vice versa. This one-way, bottom-up connection is suitable for the connection of length-scales and hierarchies that are considered in this thesis but it is not universal for any application. Instead, this approach illustrates that both the model selection and its assumptions as well as the coupling of research questions of different hierarchical levels remain key aspects of process engineering that require engineering know-how and weighing of the objectives and preferences in order to obtain both computationally manageable and meaningful problem formulations. For example, it was shown that the selection of the design objectives for decision making in the current case study can hardly be addressed at the single compartment reactor stage where yield and efficiency are strongly competing. Instead, objective selection is most reasonable at the superordinate plant level. As such, this aspect can hardly be automated. In addition to the systemic and combined consideration of results, the results of each hierarchical level are stand-alone for example for designing reactors with enhanced heat transfer at the single compartment and tube bundle levels. Besides, the FMA for simultaneous process synthesis and heat integration is not limited to neither the plant level nor high temperature applications. This was successfully demonstrated with applications at the process unit, plant and production system levels for the example of methanol synthesis [229, 242, 243, 230].

7.5   Impact of This Thesis

Despite its high heating duty requirements, the most efficient HCN production process involves high temperature BMA reactors irrespective of the design of the specific tube bundle furnace. The bundle design can in turn improve the process performance by few percent. The synthesis of reactants from recycled H_2 is reasonable from a technological perspective since it reduces the resource footprint in terms of waste, heating and variable cost of the process but may not be the best alternative from a LCA, an overall economic or from a specific plant perspective where for example a local provider of NH_3 is available or strict cooling duty constraints exist.

It was shown how the tube bundle in the furnace is optimized through the optimal arrangement of individual tubes but separate reactor intensification strategies may provide additional benefits: oxygen-rich combustion to increase the partial pressure of radiating components H_2O and CO_2 or soot particles to enhance the emissivity of the flue gas. The furnace topology in two as well as three dimensions are also degrees of freedom that could be considered in the future. The impact of the feed composition, aspect ratio and temperature of individual tubes were considered and were utilized at the bundle and process scales but the scrutiny of existing reactor concepts using microkinetic reaction mechanisms may enable a hybrid BMA-Andrussow reactor. Preliminary steps toward the development of a microkinetic reaction mechanism in collaboration with Matteo Maestri seem promising but they could not be completed due to the scope of this work. These considerations show clearly, that by answering the five key questions that were formulated in the introduction, several new questions arose in the context of this dissertation. It is likely that HCN remains an important intermediate of the chemical value chain and thus its efficient production remains important. This applies even more to synthesis gas and H_2 which are required for a wide range of products both in the production of conventional chemicals and with an increasing use of alternative energy and material sources. The quick-wins of CO_2 emission reductions in the chemical industry have already been achieved in order to fulfill a first share of the Paris agreement. Examples include heat integration of large-scale interconnected plants and the emphasis of resource efficiency as a whole. However, more steps are required to achieve a further overall reduction in greenhouse gas emissions in the chemical industry. As such, there may be an economic incentive to utilize dry reforming or mixed reforming in order to include CO_2 as a large-scale feedstock in the future.

The multi-level perspective that was illustrated using a pyramid in the introduction of this thesis shows that it is not just the PSE perspective but instead an interdisciplinary perspective because expertise of specialists is required to address the research questions at each individual level – from chemists, experts on fluid dynamics up to economists at the

plant level. In addition, the three hierarchical levels of this thesis exemplify, that a balance between models with high levels of detail and models that are suitable for mathematical optimization is important showing the proximity of PSE and mathematics. In order to enable the formulation of the right models and enable their solution interdisciplinary research and collaborations remain crucial particularly for the PSE community: as each individual research area gains depth due to new insights and findings, bridging know-how and exchange between experts from different fields is even more relevant than in the past in order to address global challenges: attending several national and international conferences, collaborating with experts on fluid dynamics as well as linear optimization techniques as well as joining lectures of the faculty of natural sciences as well as mathematics in the context of the graduate school IMPRS were keys to the successful outcome of this thesis. Furthermore, the dialogue with industry provided useful insights into the practical application. In addition, it served as a benchmark for the findings.

It was shown how process improvements – from minor at the bundle level to significant at the process scale – can be achieved at the individual hierarchical levels but the total efficiency gains were nowhere close to the factor of 10 in resource reduction that is postulated in the introduction. Rising process efficiencies in the chemical industry can indeed be a significant contributor but they will not suffice to achieve the factor 10 reduction: instead, all societal levels must contribute their share: industry sectors from construction to agriculture to mobility; individuals and private households as well as societies as a whole in order to set the policy and market framework to achieve this ambitious target. The design methodologies that were presented here but also life cycle analysis and more holistic concepts such as the true cost of nature and societal ecological footprints are important tools and concepts that help achieve this goal because it is evident that the best resource efficiency is achieved if the resources are not consumed but saved for future use instead.

Appendix A

Supplement to Chapter 3

A.1 HCN Synthesis Reaction Mechanism

Mechanistic investigations of Diefenbach et al. [128] suggest that the principle reaction pathway from the reactants CH_4 and NH_3 toward HCN proceeds via the addition of NH_3 to an adsorbed CH_2 species. The major pathway follows the desorption of a neutral formimine species and CH_2NH and its successive dehydrogenation in the gas phase to yield gaseous HCN as shown in Fig. A.1.
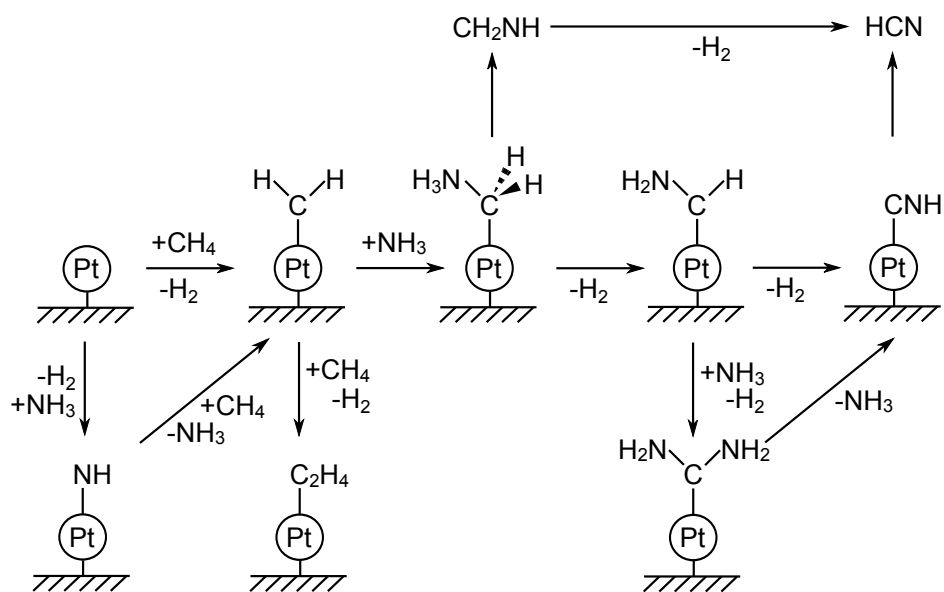
Fig. A.1 Elementary steps that are involved in the HCN synthesis in the BMA route according to Diefenbach et al. [128].

A.2 Reaction Rate Expressions in the Andrussow Reactor

Table A.1 contains the chemical reactions and corresponding reaction rate expressions that were discussed in Fig. 3.2 and that are considered for the Andrussow reactor model.

Tab. A.1 Chemical reactions and rate expressions in the Andrussow reactor according to Waletzko and Schmidt [125].

reaction	rate expression
$NH_3 \longrightarrow \frac{3}{2}\,H_2 + \frac{1}{2}\,N_2$	$\dfrac{4.9 \times 10^{18}\,\exp\left(-2130/T\right) p_{NH_3}}{\left(1 + 0.044\,\exp\left(2390/T\right) p_{CH_4}/p_{NH_3}^{1/2}\right)^4}\,{}^{*}$
	$\dfrac{4.9 \times 10^{18}\,\exp\left(-2130/T\right) p_{NH_3}}{\left(1 + 4.35 \times 10^{-5}\,\exp\left(8400/T\right) p_{NH_3} + 9.85 \times 10^{-6}\exp\left(13850/T\right) p_{H_2}^{3/2}\right)^4}\,{}^{\dagger}$
$CH_4 + NH_3 \longrightarrow HCN + 3\,H_2$	$\dfrac{7.8 \times 10^{18}\,\exp\left(-1950/T\right) p_{CH_4} p_{NH_3}^{1/2}}{\left(1 + 0.044\,\exp\left(2390/T\right) p_{CH_4}/p_{NH_3}^{1/2}\right)^4}$
$NH_3 + \frac{5}{4}\,O_2 \longrightarrow NO + \frac{3}{2}\,H_2O$	$\dfrac{2.1 \times 10^{16}\,\exp\left(10850/T\right) p_{NH_3} p_{O_2}^{1/2}}{1 + 4.0 \times 10^{-5}\,\exp\left(12750/T\right) p_{NH_3}}$
$NH_3 + \frac{3}{2}\,NO \longrightarrow \frac{5}{4}\,N_2 + \frac{3}{2}\,H_2O$	$\dfrac{1.48 \times 10^{17}\,\exp\left(3875/T\right) p_{NO} p_{NH_3}^{1/2}}{\left(1 + 5.0 \times 10^{-5}\,\exp\left(7950/T\right) p_{NO} + 0.0145\,\exp\left(2880/T\right) p_{NH_3}^{1/2}\right)}$
$\frac{1}{2}\,O_2 + H_2 \longrightarrow H_2O$	$1.5 \times 10^{19} p_{O_2} p_{H_2}$
$CH_4 + \frac{3}{2}\,O_2 \longrightarrow CO + 2\,H_2O$	$\dfrac{4 \times 10^{19}\,\exp\left(-5000/T\right) p_{CH_4} p_{O_2}^{1/2}}{1 + 5.0 \times 10^{-10}\,\exp\left(15000/T\right) p_{CH_4}}$
$NO + H_2 \longrightarrow \frac{1}{2}\,N_2 + H_2O$	$\dfrac{3.5 \times 10^{18}\,\exp\left(7300/T\right) p_{H_2} p_{NO}}{\left(1 + 2.7 \times 10^{-4}\,\exp\left(9750/T\right) p_{NO} + 15\,\exp\left(1100/T\right) p_{H_2}^{0.7}\right)^2}$
$NO \longrightarrow \frac{1}{2}\,N_2 + \frac{1}{2}\,O_2$	$\dfrac{5.53 \times 10^{16}\,\exp\left(-2625/T\right) p_{NO}}{\left(1 + 6.95 \times 10^{-4}\,\exp\left(4125/T\right) p_{NO} + 1.56\,\exp\left(4775/T\right) p_{O_2}\right)}$
$NO + CO \longrightarrow \frac{1}{2}\,N_2 + CO_2$	$\dfrac{3.5 \times 10^{17}\,\exp\left(2900/T\right) p_{NO}}{1 + 4.0 \times 10^{-9}\,\exp\left(15000/T\right) p_{CO}}$
$CO + \frac{1}{2}\,O_2 \longrightarrow CO_2$	$\dfrac{2.5 \times 10^{15}\,\exp\left(16000/T\right) p_{CO} p_{O_2}}{\left(3 \times 10^{-7}\,\exp\left(15000/T\right) p_{CO} + 300\,\exp\left(6000/T\right) p_{O_2}\right)^2}$
$CH_4 + NO \longrightarrow HCN + \frac{1}{2}\,H_2 + H_2O$	$\dfrac{1.8 \times 10^{20}\,\exp\left(5000/T\right) p_{CH_4} p_{NO}}{1 + 5.0 \times 10^{-10}\,\exp\left(15000/T\right) p_{CH_4}}$
$CO + H_2O \longrightarrow CO_2 + H_2$	$\dfrac{3.65 \times 10^{17}\,\exp\left(-1595/T\right) p_{CO} p_{H_2O}^{1/2}}{\left(1 + 0.048\,\exp\left(3037/T\right) p_{CO}\right)^2}$
$CH_4 + 3\,NO \longrightarrow \frac{3}{2}\,N_2 + CO + H_2O$	$\dfrac{1.25 \times 10^{15}\,\exp\left(5000/T\right) p_{CH_4} p_{NO} + 3 \times 10^{20}\,\exp\left(-750/T\right) p_{NO} p_{CH_4}^{1/2}}{1 + 1 \times 10^{-11}\,\exp\left(20000/T\right) p_{CH_4}}$

---

*if $p_{CH_4} > 0$
†if $p_{CH_4} = 0$

A.3   Derivation of the Differential Selectivity

$$S_{\text{diff}}^{\text{HCN}} := \frac{\mathrm{d}[\mathrm{P}_1]/\mathrm{d}t}{\mathrm{d}[\mathrm{P}_2]/\mathrm{d}t} = \frac{r_1}{r_2} \tag{A.1}$$

$$= \frac{7.8 \times 10^{18} \exp\left(\frac{-1950}{T}\right) p_{\mathrm{CH_4}} p_{\mathrm{NH_3}}^{1/2}}{\left(1 + 0.044 \exp\left(\frac{2390}{T}\right) p_{\mathrm{CH_4}}/p_{\mathrm{NH_3}}^{1/2}\right)^4} \frac{\left(1 + 0.044 \exp\left(\frac{2390}{T}\right) p_{\mathrm{CH_4}}/p_{\mathrm{NH_3}}^{1/2}\right)^3}{4.9 \times 10^{18} \exp\left(\frac{-2130}{T}\right) p_{\mathrm{NH_3}}} \tag{A.2}$$

$$= \frac{7.8 \times 10^{18} \exp\left(\frac{-1950}{T}\right) p_{\mathrm{CH_4}} p_{\mathrm{NH_3}}^{1/2}}{1 + 0.044 \exp\left(\frac{2390}{T}\right) p_{\mathrm{CH_4}}/p_{\mathrm{NH_3}}^{1/2}} \frac{1}{4.9 \times 10^{18} \exp\left(\frac{-2130}{T}\right) p_{\mathrm{NH_3}}} \quad . \tag{A.3}$$

Definition of the Arrhenius-type expressions in Eq. (A.3) as

$$k_1(T) := 7.8 \exp\left(\frac{-1950}{T}\right) \tag{A.4}$$

$$k_2(T) := 0.044 \exp\left(\frac{2390}{T}\right) \tag{A.5}$$

$$k_3(T) := 4.9 \exp\left(\frac{-2130}{T}\right) \tag{A.6}$$

enables the reformulation of the differential selectivity to

$$S_{\text{diff}}^{\text{HCN}} = \frac{k_1(T) p_{\mathrm{CH_4}} p_{\mathrm{NH_3}}^{1/2}}{1 + k_2(T) p_{\mathrm{CH_4}}/p_{\mathrm{NH_3}}^{1/2}} \frac{1}{k_3(T) p_{\mathrm{NH_3}}} \tag{A.7}$$

$$= \frac{k_1(T) p_{\mathrm{CH_4}} p_{\mathrm{NH_3}}^{1/2}}{k_3(T) p_{\mathrm{NH_3}} + k_2(T) k_3(T) p_{\mathrm{CH_4}} p_{\mathrm{NH_3}}^{1/2}} \tag{A.8}$$

$$= \frac{k_1(T) p_{\mathrm{CH_4}}}{k_3(T) p_{\mathrm{NH_3}}^{1/2} + k_2(T) k_3(T) p_{\mathrm{CH_4}}} \quad . \tag{A.9}$$

Appendix B

Supplement to Chapter 4

B.1 Discretization of the Component Balance

The discretization of the BLF model is exemplified for the component balance of α that is solved for the corresponding mass fraction w_α using the discretization scheme that is illustrated in Fig. 4.5. Finite volume integration is illustrated for a non-wall element Λ

$$\int_\Lambda \rho v_z \frac{\partial w_\alpha}{\partial z} \mathrm{d}y + \int_\Lambda \rho v_y \frac{\partial w_\alpha}{\partial y} \mathrm{d}y = -\int_\Lambda \frac{\partial j_{y,\alpha}}{\partial y} \mathrm{d}y \tag{B.1}$$

where two spatial coordinates y and z are sufficient for the description of the reactor as outlined in the modeling assumptions:

$$\int_{\Delta z} \int_{j-1/2}^{j+1/2} \rho v_z \frac{\partial w_\alpha}{\partial z} \mathrm{d}y \mathrm{d}z + \int_{\Delta z} \int_{j-1/2}^{j+1/2} \rho v_y \frac{\partial w_\alpha}{\partial y} \mathrm{d}y \mathrm{d}z = -\int_{\Delta z} \int_{j-1/2}^{j+1/2} \frac{\partial j_{y,\alpha}}{\partial y} \mathrm{d}y \mathrm{d}z \quad . \tag{B.2}$$

In a first step of the solution procedure, integration in the transverse coordinate y assuming piecewise constant state functions is shown exemplarily for the first term of Eq. (B.2):

$$\int_{\Delta z} \int_{j-1/2}^{j+1/2} \rho v_z \frac{\partial w_\alpha}{\partial z} \mathrm{d}y \mathrm{d}z \tag{B.3a}$$

$$= \int_{\Delta z} \frac{\partial w_\alpha}{\partial z}\bigg|_j \left(\int_{j-1/2}^{j} \rho v_z \mathrm{d}y + \int_{j}^{j+1/2y} \rho v_z \mathrm{d}y \right) \mathrm{d}z \tag{B.3b}$$

$$= \int_{\Delta z} \frac{\partial w_\alpha}{\partial z}\bigg|_j \left(\left[\rho_{j-1/2} v_{z,j-1/2} + \rho_j v_{z,j} \right] \frac{1}{4} \Delta y + \left[\rho_j v_{z,j} + \rho_{j+1/2} v_{z,j+1/2} \right] \frac{1}{4} \Delta y \right) \mathrm{d}z \tag{B.3c}$$

$$= \int_{\Delta z} \frac{\partial w_\alpha}{\partial z}\bigg|_j \left(\left[\rho_{j-1/2} v_{z,j-1/2} + 2\rho_j v_{z,j} + \rho_{j+1/2} v_{z,j+1/2} \right] \frac{1}{4} \Delta y \right) \mathrm{d}z \quad . \tag{B.3d}$$

Variables at the boundaries $j+1/2$ and $j-1/2$ are evaluated according to the piece-wise linear state function assumption. The remaining two terms of Eq. (B.2) are integrated accordingly, transforming Eq. (B.2) into an ordinary differential equation in w_α:

$$\int_{\Delta z} \frac{\partial w_\alpha}{\partial z}\bigg|_j \, \mathrm{d}z = \int_{\Delta z} \left(\cdots \right) \frac{4}{\left[\rho_{j-1/2} v_{z,j-1/2} + 2\rho_j v_{z,j} + \rho_{j+1/2} v_{z,j+1/2} \right] \Delta y} \mathrm{d}z \quad . \tag{B.4}$$

The term in brackets $(\cdots)$ in Eq. (B.4) represents the remaining second and third terms of Eq. (B.2) integrated for Δy. In the final step, the ordinary differential equation Eq. (B.4) is integrated in Matlab/CasADi using IDAS.

B.2 Validation of Single Compartment Model for Methane Steam Reforming

The single synthesis compartment model that is validated for HCN synthesis in Fig. 4.8 was also utilized to describe MSR in microchannels using the kinetics of Xu and Froment [136, 91]. The validation with microchannel experimental data from Karakaya et al. is shown in Fig. B.1 [135]. Near isothermal reaction conditions at $T_{\mathrm{ref}} = 1023 \, \mathrm{K}$ and a catalyst amount of $m_{\mathrm{Ni}} = 14.2 \, \mathrm{mg}$ were used in the experimental studies of Karakaya et al. [135].

The agreement of simulation and experimental data is excellent with respect to conversion of the limiting reactant CH_4 (Fig. B.1 A) and good for the selectivity toward CO (Fig. B.1 B). The deviation of the selectivity in Fig. B.1 B cannot be entirely clarified: in contrast to the experimental values by Karakaya et al. [135], selectivities of CO of the reactor model (Fig. B.1 B) increase with space time and approach the thermodynamic equilibrium values as shown in Liesche and Sundmacher [91]. Results at different S/C rations and space times show similar behavior. Despite this deviation for selectivities, the general agreement of the model with the experimental data is good which increases the credibility of the model also for the HCN example in chapter 4.
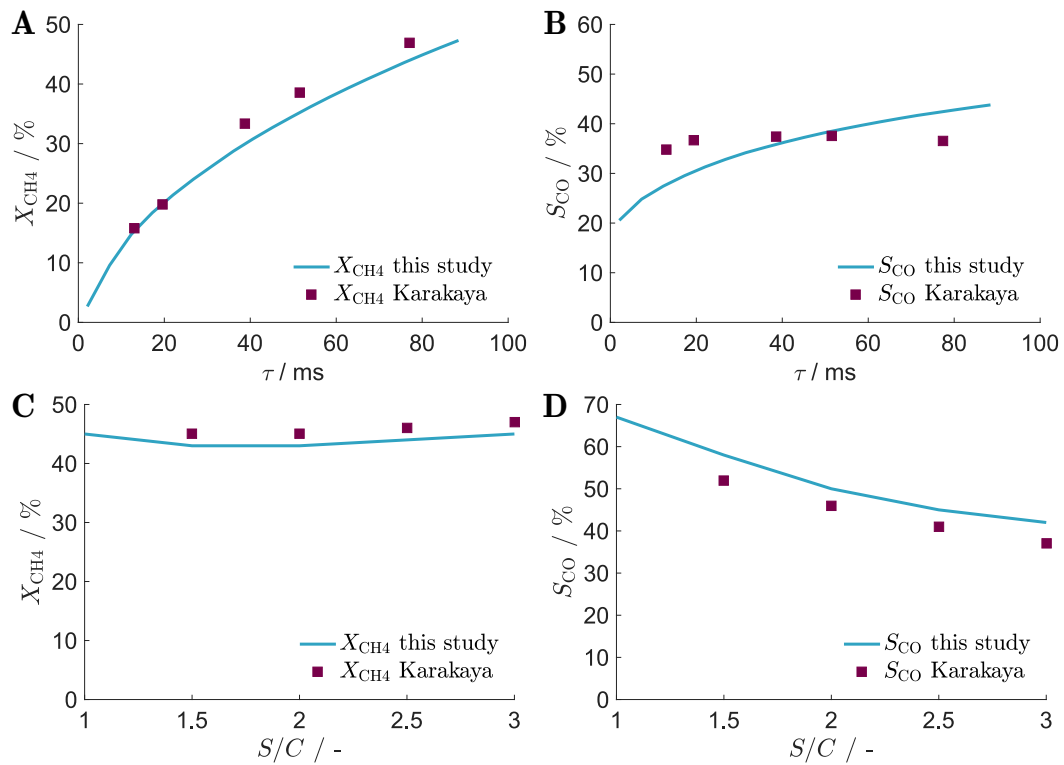
Fig. B.1 Validation of the channel model for MSR using experimental data of Karakaya et al. [135]: conversion of limiting reactant CH_4 (A,C) and selectivity toward target product CO (B,D) versus space times and steam-to-carbon ratios (S/C) at isothermal and ambient pressure reaction conditions ($T = 1023\,\mathrm{K}$). Space times (A,B) are compared at $S/C = 3$ and steam-to-carbon ratios (C,D) at $\tau = 77\,\mathrm{ms}$.

Appendix C

Supplement to Chapter 5

C.1 Channel to Cylinder Conversion

The tube bundle optimization requires a quantitative correlation of wall heat fluxes in dependence of the wall boundary temperature for a cylinder geometry. The conversion of the wall heat fluxes from the channel model is achieved using the following assumptions: (i) inner channel height and inner tube diameter are equal $d_{(s),in} = W_{(s)}$ to ensure comparability of size-dependent flow behavior of both compartments and (ii) equal wall areas for channel and cylinder are prioritized over equal reaction volumes due to the wall heat flux that is of interest. As a consequence, the reactor volumes of cylinder and channel compartments differ but this does not affect the qualitative findings of chapter 5. The outer equivalent tube diameter that is used in chapter 5 is defined as $\delta := d_{(s),out} = d_{(s),in} + 2t_{(w)}$. The cylinder and
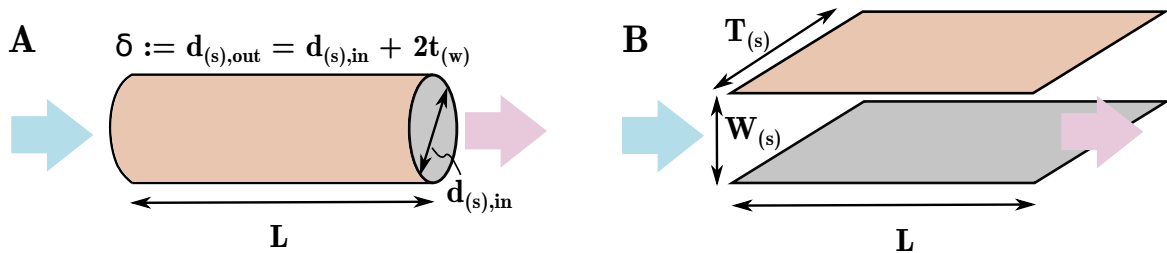
Fig. C.1 Geometric measures of the cylinder (A) and channel (B) geometries: equal length L and a tube diameter equal to the channel height $d_{(s),in} = W_{(s)}$ are assumed. The principle flow direction is indicated with arrows.

channel geometries are illustrated in Fig. C.1. The assumption of equal wall surface areas means that the cylinder circumference equals two times the channel depth $T_{(s)}$ because both reactors have an identical length L and because side walls $(2W_{(s)})$ are not considered in the

channel model:

$$U_{\text{cylinder}} = \pi\delta = 2T_{(s)} = U_{\text{channel}} \quad . \tag{C.1}$$

resulting in the conversion factor $T_{(s)} = 1/2\pi d_{(s),\text{in}}$. Consequently, the reactor volumes – described by the cross-sectional area are not equal:

$$A_{\text{cylinder}} = \frac{1}{4}\pi d_{(s),\text{in}}^2 \quad \text{and} \quad A_{\text{channel}} = HT = d_{(s),\text{in}}\frac{1}{2}\pi d_{(s),\text{in}} = \frac{1}{2}\pi d_{(s),\text{in}}^2 \quad . \tag{C.2}$$

Instead, the reactor volume of the channel is twice as large as the cylinder volume.

C.2 Comparison of Furnace Cross-Sections

The furnace geometry is discussed in this section with the example of five different furnace cross-sectional geometries: square, rectangle, circle, ellipse and trapezoid. This analysis is an extension to the optimal arrangement of the tubes within the furnace and the two-dimensional model is utilized that is introduced in chapter 5. The simulations of the five furnace cross-sections are obtained by modeling the furnace wall as a polygon chain. All geometries have equal cross-sectional areas with 0.51 m^2 thus achieving equal flue gas amounts. As a case study, tube bundles of five tubes with equivalent tube diameters of $\delta = 0.020$ m are investigated in two arrangement patterns: 'dice' and regular pentagon arrangements.

C.2.1 Tube Bundle Arrangement in a Circular Furnace Geometry

Two tube-tube distance studies for a circular cross-section exemplify the results for the geometry comparison in Fig. C.2 and Fig. C.3. The bundle properties of the dice-shaped arrangement in Fig. C.2 are similar to the Endter rectangular reactor: view factors decrease with increasing tube-tube distances while improvements in average tube surface temperature and yields exhibit a maximum and decrease for tube-tube distances that are larger than 0.12 m. At this distance shadowing is overcome and further increase in tube distance simply reduces the flue gas emissivity around the tubes.

Pentagon shaped bundle arrangements do not shadow a center tube from the outside radiating gas layer for five tubes. Instead, all five tubes have greater visibility of their surrounding tubes than for the 'dice'-type arrangements as shown by the total view factors $\hat{\varphi}$ in Fig. C.3. Consequently, average temperatures and yields increase up to the largest pentagon edge length of 0.16 m where they achieve equal tube average temperatures and yields as the dice-shaped arrangement. Direct comparison shows that the standard deviation of pentagon shaped arrangements is lower than for the dice-shaped arrangements because of their equal
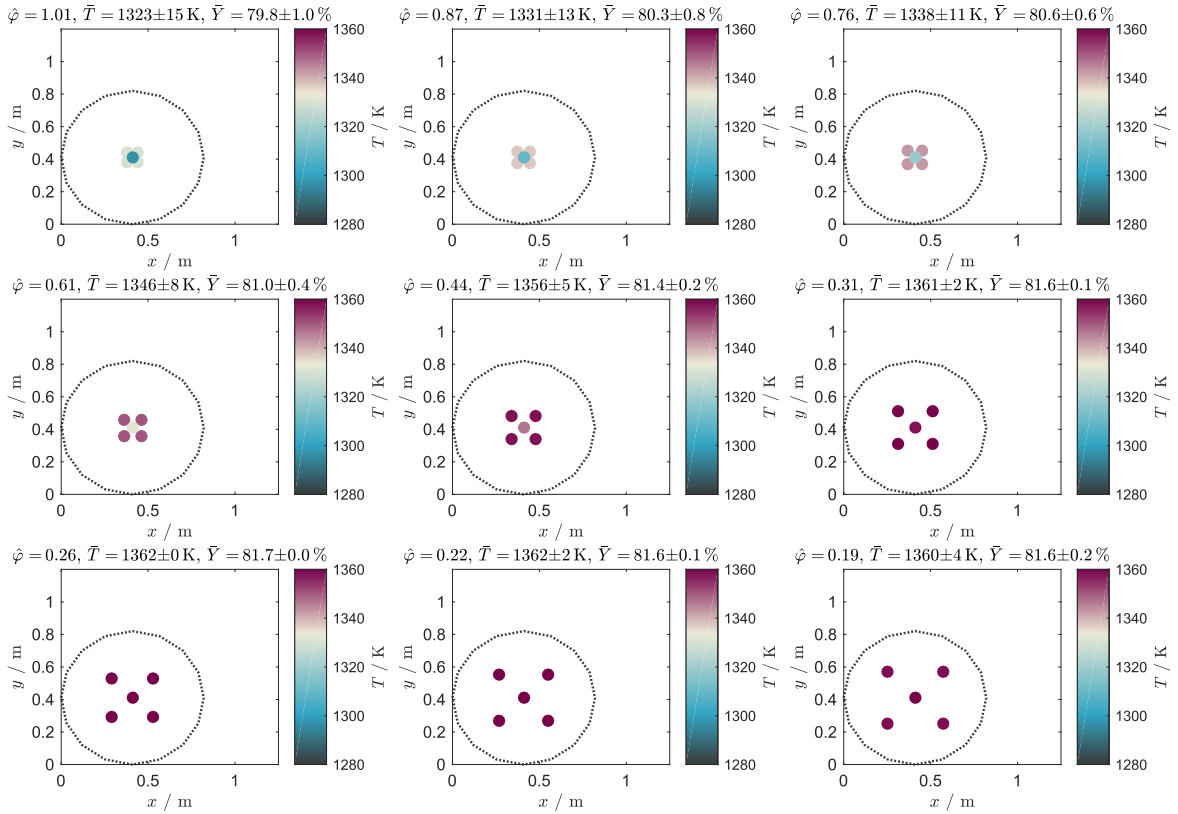
Fig. C.2 Bundle arrangements with decreasing view factor objective function for 'dice'-type arrangement of five tubes and a circular furnace.

view factors. Similar results are obtained for the other four cross-sections and they are compared in the following section.

C.2.2 Systematic Comparison of Furnace Geometries

In Fig. C.4 mean tube surface temperatures and mean product yields versus inter-tube distance for 'dice'-type and pentagon-type arrangements are compared for all five furnace cross-sections. The results for are similar independent of the furnace cross-section: 'Dice'-type arrangements (Fig. C.4 A,B) exhibit a maximum where the reduction in view factor starts to be compensated by the reduction of the gas emissivity around the bundle. Pentagon-type arrangements (Fig. C.4 C,D) on the other hand have higher view factors but lower standard deviations attaining equal performance for their maximum tube-tube distances. Thus, the view factor cannot be the only performance indicator – for the heat flux and tube temperature correlations – because it is not sufficiently sensitive to change in tube temperature and vice versa. Comparison of the five cross-sections indicates that a rectangular shaped furnace is generally disadvantageous whereas a circle or square are the optimal furnace cross-sectional
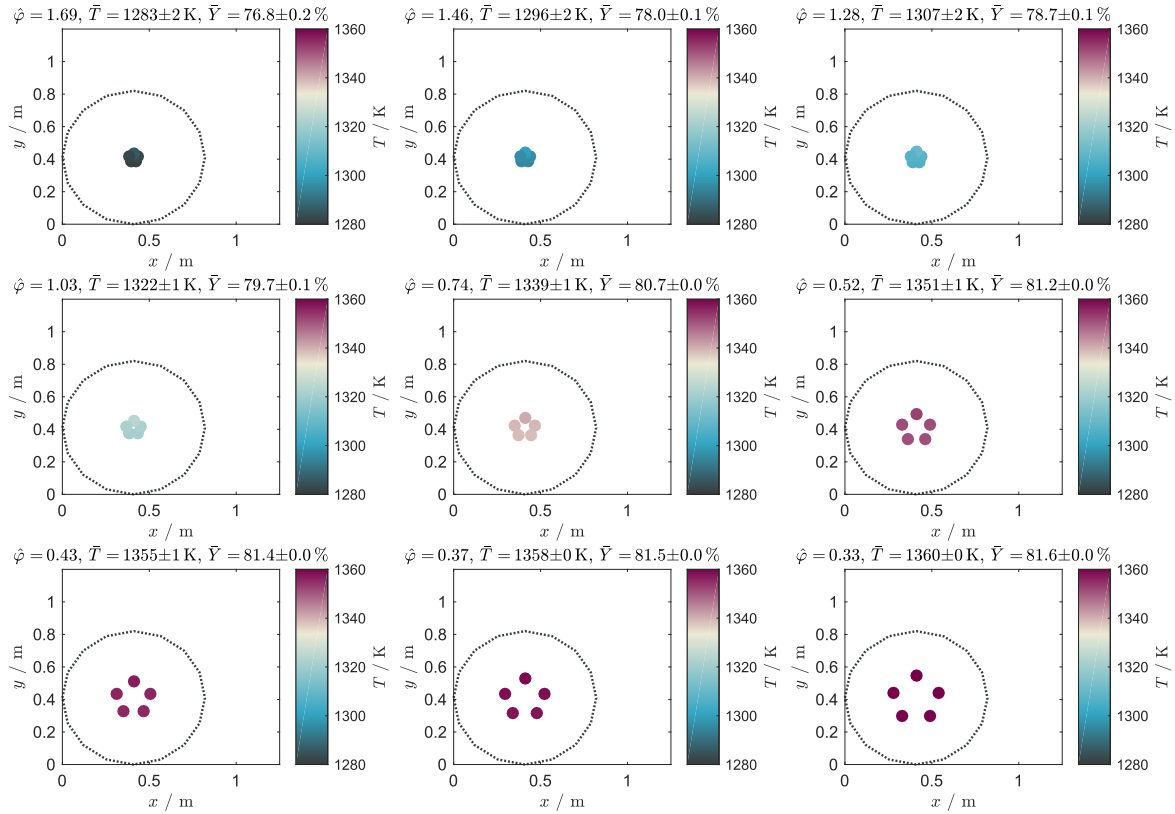
Fig. C.3 Bundle arrangements with decreasing view factor objective function for 'pentagon'-type arrangement of five tubes and a circular furnace.

areas. It is true that wide radiating gas layers from all sides result in high gas emissivities and are thus optimal if shadowing is not the limiting factor of a bundle arrangement. On the other hand, equal tube arrangements where compared for all five cross-sections in order to enable their fair comparison. This assumption, however, means that cross-sections with small aspect ratios have a disadvantage (trapezoid, ellipse and rectangle) because the selected tube arrangement is compact and causes narrow gas layers on the sides and thus overall lower tube surface temperatures.

In general, these results show that compact cross-sections with aspect ratios close to unity are favorable for compact bundle arrangements but the tube bundle arrangement can be adapted to each individual furnace cross-section. As such, the Endter reactor bundle arrangement attains a similar performance as the dice and pentagon shaped arrangements for square and circular cross-sections.
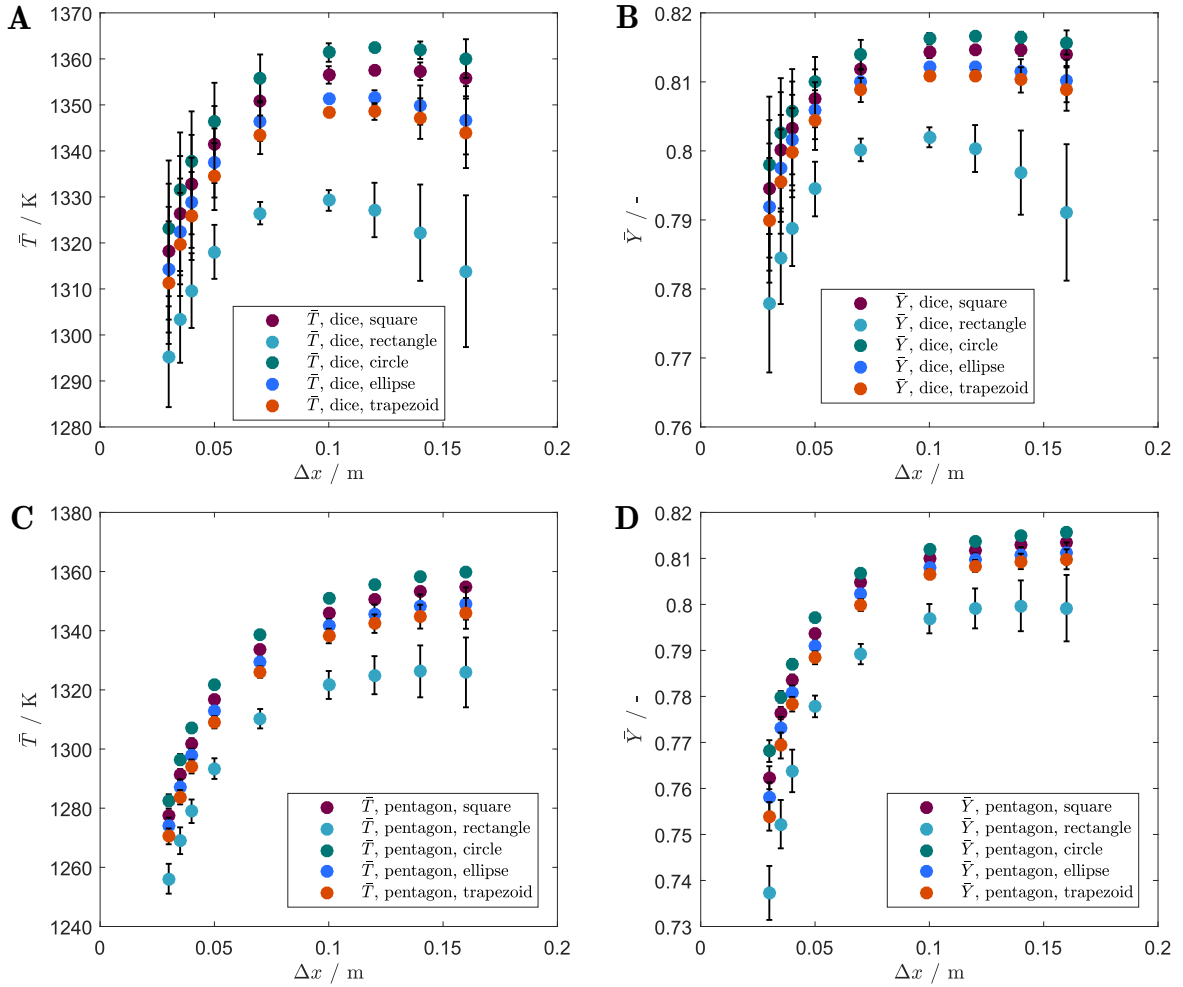
Fig. C.4 Tube mean temperature (A,C) and tube mean yield (B,D) versus tube-tube distance for five furnace cross-sections – square, rectangle, circle, ellipse and trapezoid. 'Dice'-type tube arrangement (A,B) and pentagon-shape tube arrangement (C,D).

Appendix D

Supplement to Chapter 6

D.1 Andrussow Reactor Model

The Andrussow reactor is modeled as a plug flow reactor and in steady state: the synthesis of HCN in the Andrussow reactor occurs in the millisecond range on a Pt gauze as shown in Fig. 3.1 on the right. The target is to determine the heat output of the reactor at a defined utility temperature level of $600\mathrm{\dot{K}}$ which is sufficient for heat integration of any other unit in the HCN process context. The model of Waletzko and Schmidt was thus modified for a cooled instead of an adiabatic reactor. The mass balance is a simplification of Eq. (4.3) and formulated as

$$\rho_{(A)} v_{(A)} \frac{\partial w_{\alpha,(A)}}{\partial z} = \sigma_{\alpha,(A)}$$

where the index (A) denotes the Andrussow reactor. The energy balance of the reactor is given as

$$\rho_{(A)} c_{p,(A)} v_{(A)} \frac{\partial T_{(A)}}{\partial z} = -\sum_{\alpha=1}^{N_c} h_\alpha^0 \sigma_{\alpha,(A)} - k_{(A)} \left(T_{(A)} - T_{(Ac)} \right) \quad .$$

For a stoichiometric feed to the Andrussow reactor according to Eq. (3.3) the cooling duty accounts for $66\,\mathrm{kJ\,mol^{-1}}$ of the combined reactor outlet flow i.e. the outlet TSN of the reactor.

D.2 Elementary Process Node Modeling

The formulation of conservation equations was exemplified for the BMA reactor nodes in Sec. 6.3.1. Based on the general conservation laws of the FluxMax formulation, characteristic parameters of each EPN include stoichiometric coefficients $\chi_{(E_j)}^{(M_i)}$, heating and cooling duties $\varphi_{(E_j)}^{\text{in}}$ and $\varphi_{(E_j)}^{\text{out}}$ as well as work duties $\omega_{(E_j)}^{\text{out}}$, $\omega_{(E_j)}^{\text{out}}$. Mass and energy balances are formulated for each specific unit type of the HCN process in Fig. 6.4 and the results are summarized in Tab. D.1. The first column contains the name of the process node, followed by the corresponding stoichiometric equation that links the associated TSNs. The third and fourth columns contain the mass and energy balances.

D.2.1 Mixing Nodes

Mixing EPNs L_j provide the reactant gas mixtures for HCN formation, NH_3 formation and methanation at equal temperatures and near-ambient pressures. At these conditions, an ideal gas and thus adiabatic mixing is assumed which means that energy balances for mixing nodes are not required. PMBs of an adiabatic static mixing node L_j are the reverse of the separation edge shown below. One PMB is required for each TSN that is associated with the mixing node. In this example the maximum number of reactants that are mixed is three. The stoichiometric coefficients $\chi_{(L_j)}^{(M_2)}$ and $\chi_{(L_j)}^{(M_3)}$ correspond to the molar fractions of the inlet TSNs M_2 and M_3 in the outlet TSN M_1. The stoichiometric coefficient of the inlet TSN M_1 equals 1.

D.2.2 Reactor Nodes

In addition to the BMA reactor node description that was provided in chapter 6 EPNs for the Andrussow and all reactors of the recycling pathways need to be formulated: The Andrussow reactor is characterized with a steady-state model as described in Sec. D.1 in order to quantify heat release and byproduct formation. The Andrussow reactor is operated at a single temperature due to its combustion-like behavior. Specific cooling duty requirements $\varphi_{(R_{\text{Andr}})}^{\text{out}}$ are obtained from the Andrussow reactor model.

The HCN synthesis pathway is emphasized in chapter 6. Therefore, the HCN synthesis reactors are modeled in more detail than the additional reactors that are involved in the recycling pathways – combustion of Andrussow off-gases, H_2 combustion, formation of NH_3 and CH_4 – are described using stoichiometric reactors as shortcut models and the corresponding heat duties are obtained from enthalpy differences between in- and outlet mass flows. Both heating and cooling duties occur and therefore two PMBs and one energy balance

Tab. D.1 Unit types, stoichiometric equations, partial mass and energy balances for process unit types that are present in the superstructure of the production system of HCN.

process unit type	stoichiometric reaction equation	partial molar balance	energy balance
adiabatic mixer L_j	$\chi_{(L_j)}^{(M_2)} M_2 + \chi_{(L_j)}^{(M_3)} M_3 \longrightarrow M_1$	$0 = -\dot{N}_{(L_j)}^{(M_1)} + \dot{\Gamma}_{(L_j)}$ $0 = \dot{N}_{(L_j)}^{(M_2)} - \chi_{(L_j)}^{(M_2)} \dot{\Gamma}_{(L_j)}$ $0 = \dot{N}_{(L_j)}^{(M_3)} - \chi_{(L_j)}^{(M_3)} \dot{\Gamma}_{(L_j)}$	—
chemical reactor R_j	$M_1 \longrightarrow \chi_{(R_j)} M_2$	$0 = \dot{N}_{(R_j)}^{(M_1)} - \dot{\Gamma}_{(R_j)}$ $0 = -\dot{N}_{(R_j)}^{(M_2)} + \chi_{(R_j)} \dot{\Gamma}_{(R_j)}$	$0 = \left(-\varphi_{(R_j)}^{in} + \varphi_{(R_j)}^{out}\right) \dot{\Gamma}_{(R_j)} + \sum_{\forall U_l} \left(\dot{Q}_{(E_j)}^{(U_l)} - \dot{Q}_{(U_l)}^{(E_j)}\right)$
adiabatic absorption A_j with entrainer M_2	$M_1 + e_{(A_j)} M_2 \longrightarrow$ $\left(e_{(A_j)} + \chi_{(A_j)}^{(M_3)}\right) M_3 + \chi_{(A_j)}^{(M_4)} M_4$	$0 = \dot{N}_{(A_j)}^{(M_1)} - \dot{\Gamma}_{(A_j)}$ $0 = \dot{N}_{(A_j)}^{(M_2)} - e_{(A_j)} \dot{\Gamma}_{(A_j)}$ $0 = -\dot{N}_{(A_j)}^{(M_3)} + \left(e_{(A_j)} + \chi_{(A_j)}^{(M_3)}\right) \dot{\Gamma}_{(A_j)}$ $0 = -\dot{N}_{(A_j)}^{(M_4)} + \chi_{(A_j)}^{(M_4)} \dot{\Gamma}_{(A_j)}$	—
distillation column S_j	$M_1 \longrightarrow \chi_{(S_j)}^{(M_2)} M_2 + \chi_{(S_j)}^{(M_3)} M_3$	$0 = \dot{N}_{(S_j)}^{(M_1)} - \dot{\Gamma}_{(S_j)}$ $0 = -\dot{N}_{(S_j)}^{(M_2)} + \chi_{(S_j)}^{(M_2)} \dot{\Gamma}_{(S_j)}$ $0 = -\dot{N}_{(S_j)}^{(M_3)} + \chi_{(S_j)}^{(M_3)} \dot{\Gamma}_{(S_j)}$	$0 = -\varphi_{(S_j)}^{in} \dot{\Gamma}_{(S_j)} + \sum_{\forall U_l} \dot{Q}_{(E_j)}^{(U_l)}$ $0 = \varphi_{(S_j)}^{out} \dot{\Gamma}_{(S_j)} - \sum_{\forall U_l} \dot{Q}_{(U_l)}^{(E_j)}$
generic elementary process node: G_j	$M_1 \longrightarrow \chi_{(G_j)}^{(M_2)} M_2 + \chi_{(G_j)}^{(M_3)} M_3$	$0 = \dot{N}_{(G_j)}^{(M_1)} - \dot{\Gamma}_{(G_j)}$ $0 = -\dot{N}_{(G_j)}^{(M_2)} + \chi_{(G_j)}^{(M_2)} \dot{\Gamma}_{(G_j)}$ $0 = -\dot{N}_{(G_j)}^{(M_3)} + \chi_{(G_j)}^{(M_3)} \dot{\Gamma}_{(G_j)}$	$0 = \left(-\omega_{(G_j)}^{in} + \omega_{(G_j)}^{out}\right) \dot{\Gamma}_{(G_j)} + \dot{W}_{(G_j)}^{ext,\,in} - \dot{W}_{(G_j)}^{ext,\,out}$ $0 = \Big[\varphi_{(G_j)}^{out} + \left(1 - \eta_{(G_j)}^{in}\right) \omega_{(G_j)}^{in} +$ $\left(\frac{1}{\eta_{(G_j)}^{out}} - 1\right) \omega_{(G_j)}^{out}\Big] \dot{\Gamma}_{(G_j)} - \sum_{\forall U_l} \dot{Q}_{(U_l)}^{(E_j)}$
temperature state changer D_j	$M_1 \longrightarrow M_2$	$0 = \dot{N}_{(D_j)}^{(M_1)} - \dot{\Gamma}_{(D_j)}$ $0 = -\dot{N}_{(D_j)}^{(M_2)} + \dot{\Gamma}_{(D_j)}$	$0 = \left(-\varphi_{(D_j)}^{in} + \varphi_{(D_j)}^{out}\right) \dot{\Gamma}_{(D_j)} + \sum_{\forall U_l} \left(\dot{Q}_{(E_j)}^{(U_l)} - \dot{Q}_{(U_l)}^{(E_j)}\right)$

are required for the correct EPN description within the FluxMax approach. It is assumed that reactants enter as a mixture and therefore two TSNs participate in each reactor node R_j.

D.2.3 Absorber Process Nodes

Absorber columns A_j are modeled as adiabatic units and the heat of absorption as well as dissociation is contained in the outlet molar flows. Two different absorbers are present as illustrated in Fig. 6.4: the absorption of non-reacted NH_3 using a diluted solution of H_2SO_4 in H_2O and the consecutive absorption of the product HCN from the gas stream. Both absorbers are modeled with equilibrium stages and in order to account for dissociation reactions in the liquid phase, the electrolyte non-random-two-liquid model combined with the Redlich-Kwong equation of state (ENRTL-RK) for vapor phase properties is used. Exact design parameters of both absorbers are not available in literature and are thus approximated.

The absorption of NH_3 is based on the neutralization reaction of NH_3 in a sulfuric acid solution

$$NH_3 + H_3O^+ \rightleftharpoons NH_4^+ + H_2O \quad .$$
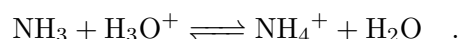
The equilibrium is entirely on the right hand side and therefore few equilibrium stages are required. The absorber is modeled with 6 equilibrium stages, an entrainer ratio of $e_{A_j} = 0.5$ and in- and outlet streams have the following temperatures: $T_{gas,in} = 700\,K$, $T_{gas,out} = 346\,K$, $T_{liq,in} = 340\,K$ and $T_{liq,out} = 349\,K$. With these parameters the loss of HCN in the resulting ammonium sulfate solution is minimized and accounts for approximately 4%. The absorption of HCN relies on the condensation of gaseous HCN and is modeled with 10 equilibrium stages requiring an entrainer ratio of $e_{A_j} \geq 6$. The resulting temperatures of in- and outlet streams in order to reduce the content of HCN in the gas stream to trace amounts are: $T_{gas,in} = 313\,K$, $T_{gas,out} = 295\,K$, $T_{liq,in} = 295\,K$ and $T_{liq,out} = 307\,K$.

Four associated TSNs are present in the description of an absorber EPN: the inlet TSN mixture, the entrainer at an entrainer-to-feed ratio $e_{(A_j)}$ and the two outlet TSNs. Consequently, four PMBs are formulated and no energy balance is required for an adiabatic absorber EPN.

D.2.4 Distillation Process Nodes

Distillation column nodes S_j are described with the Winn-Underwood-Gilliland shortcut model in ASPEN Plus. The minimum number of stages and reflux ratio and the required reflux ratio for a specified number of stages and distillate composition are obtained using

the ENRTL-RK property model. This property method is selected because trace amounts of H_2SO_4 must be present to maintain the pH of the dilute HCN mixture close to two for two reasons: to avoid dissociation of the target molecule and to prevent its subsequent exothermal polymerization reactions. The property data for this mixture within Aspen is taken from the Chemical Engineer's Handbook [244]. In order to achieve a recovery of HCN of 99.9 %, the minimum number of stages is 7 at a reflux ratio of 0.72. Four different distillation columns are taken into account in the process superstructure: 8, 11, 14 and 17 stages.

Three associated TSNs are connected with a distillation process node – feed, distillate and bottom product – and therefore three PMBs are required as shown in Tab. D.1. In addition to that, two energy balance equations, Eq. (6.6b) and Eq. (6.6c) are required to account for reboiler and condenser duties.

D.2.5   Hydrogen and Methane Separator Nodes

The gas separations of H_2 and CH_4 in order to recycle byproduct and non-converted reactants in Fig. 6.4 are modeled with a shortcut model because they are part of the recycle section of the superstructure. The work duty of the gas separation is estimated using the molar Gibbs enthalpy of mixing $\Delta_M g$ of the TSN inlet assuming an ideal gas mixture (Eq. (D.1)):

$$\Delta_M g := \sum_\alpha RT x_\alpha \ln x_\alpha \quad .\tag{D.1}$$

The separation duty $\omega_{(E_j)}^{in}$ is then approximated using the definition of the separation efficiency $\eta_{(E_j)}$ in Eq. (D.2) and the Gibbs enthalpy of mixing. The separation efficiency is approximated with 0.01 (comp. Tab. 6.3):

$$\eta_{(E_j)} := \frac{\Delta_M g}{\omega_{(E_j)}^{in}} \quad .\tag{D.2}$$

Both gas separations are modeled with a generic unit type G_j of Tab. D.1 with three PMBs and two energy balances (Eq. (6.6a), Eq. (6.6b)).

D.2.6   Temperature State Changer Process Nodes

Temperature state changer process nodes D_j are required in order to link TSNs of similar composition among EPNs. Isobaric change of temperature is assumed for the participating TSNs and the required duties are the enthalpy difference between in- and outlet TSNs of the economizer, $\varphi_{(D_j)}^{in/out} := \Delta h_{(M_{i+1})}^{(M_i)}$. The condenser is modeled in a similar way except that it has two outward-pointing TSN mass flows, because the separation of H_2O results from

cooling the inlet stream entering via the inlet TSN. Two PMBs for regular temperature change and three PMBs for condensers are required and either Eq. (6.6b) or Eq. (6.6c) to account for heating and cooling duties. Stoichiometric coefficients of temperature changer process nodes equal one because in- and outlet mass flows are equal.

References

[1] Wackernagel, M. and Browne, S. Earth overshoot day, accessed: June 15th, 2018. URL https://www.overshootday.org/.

[2] European Commission. *Communication from the Commission to the European Parliament, the Council, the European Economic and Social Committee and the Committee of the Regions on the 2017 List of Critical Raw Materials for the EU.* Brussels, 2017.

[3] Halada, K., Shimada M., and Ijima, K. Decoupling Status of Metal Consumption from Economic Growth. *Materials Transactions*, 49(3):411–418, 2008.

[4] Wiegandt, K. *Mut zur Nachhaltigkeit: 12 Wege in die Zukunft.* Fischer, Frankfurt a.M., 2016.

[5] Maxton, G., Randers, J., and Suzuki, D. *Reinventing Prosperity: Managing Economic Growth to Reduce Unemployment, Inequality and Climate Change.* Greystone Books, Vancouver, 2016.

[6] Rockström, J., Steffen, W., Noone, K., Persson, A., Chapin, F. S., Lambin, E., Lenton, T., Scheffer, M., Folke, C., Schellnhuber, H. J., Nykvist, B., de Wit, C., Hughes, T., van der Leeuw, S., Rodhe, H., Sörlin, S., Snyder, P. K., Costanza, R., Svedin, U., Falkenmark, M., Karlberg, L., Corell, R. W., Fabry, V. J., Hansen, J., Walker, B., Liverman, D., Richardson, K., Crutzen, P., and Foley, J. Planetary Boundaries: Exploring the Safe Operating Space for Humanity. *Ecology and Scoeity*, 14(2), 2009.

[7] Schmidt-Bleek, F. and Wiegandt, K. *Nutzen wir die Erde richtig?: die Leistungen der Natur und die Arbeit des Menschen.* Fischer, Frankfurt a.M., 2007.

[8] Bazzanella, A. M. and Ausfelder, F. *Technology Study: Low Carbon Energy and Feedstock for the European Chemical Industry.* DECHEMA Gesellschaft für Chemische Technik und Biotechnologie e.V., Frankfurt a.M., 2017.

[9] Box, G. Science and Statistics. *Journal of the American Statistical Association*, 71 (356):791–799, 1976.

[10] Cajot, S. *Interactive Optimization for Supporting Multicriteria Decisions in Urban and Energy System Planning.* PhD Thesis, EPFL, Lausanne, 2018.

[11] Fazlollahi, S., Becker, G., and Maréchal, F. Multi-Objectives, Multi-Period Optimization of District Energy Systems: III. Distribution Networks. *Computers & Chemical Engineering*, 66:82–97, 2014.

[12] Fazlollahi, S., Becker, G., Ashouri, A., and Maréchal, F. Multi-Objective, Multi-Period Optimization of District Energy Systems: IV – A Case Study. *Energy*, 84:365–381, 2015.

[13] Chung, P. S., Smith, R., Vemuri, S. H., Jhon, Y. I., Tak, K., Moon, I., Biegler, L. T., and Jhon, M. S. Multi-Scale/Multi-Physical Modeling in Head/Disk Interface of Magnetic Data Storage. *Journal of Applied Physics*, 111(7):07B712, 2012.

[14] Karakasidis, T. E. and Charitidis, C. A. Multiscale Modeling in Nanomaterials Science. *Materials Science and Engineering: C*, 27(5-8):1082–1089, 2007.

[15] Walpole, J., Papin, J. A., and Peirce, S. M. Multiscale Computational Models of Complex Biological Systems. *Annual review of biomedical engineering*, 15:137–154, 2013.

[16] Rollié, S., Mangold, M., and Sundmacher, K. Designing Biological Systems: Systems Engineering Meets Synthetic Biology. *Chemical Engineering Science*, 69(1):1–29, 2012.

[17] Vlachos, D. G. A Review of Multiscale Analysis: Examples from Systems Biology, Materials Engineering, and Other Fluid–Surface Interacting Systems. In *Advances in Chemical Engineering - Multiscale Analysis*, volume 30 of *Advances in Chemical Engineering*, pages 1–61. Elsevier, 2005.

[18] Charpentier, J.-C. Among the Trends for a Modern Chemical Engineering, the Third Paradigm: The Time and Length Multiscale Approach as an Efficient Tool for Process Intensification and Product Design and Engineering. *Chemical Engineering Research and Design*, 88(3):248–254, 2010.

[19] Grossmann, I. E. and Westerberg, A. W. Research Challenges in Process Systems Engineering. *AIChE Journal*, 46(9):1700–1703, 2000.

[20] Vlachos, D. G. Multiscale Modeling for Emergent Behavior, Complexity, and Combinatorial Explosion. *AIChE Journal*, 58(5):1314–1325, 2012.

[21] Partopour, B. and Dixon, A. G. Integrated Multiscale Modeling of Fixed Bed Reactors: Studying the Reactor Under Dynamic Reaction Conditions. *Chemical Engineering Journal*, DOI: 10.1016/j.cej.2018.08.124, 2018.

[22] Gilles, E. D. Network Theory for Chemical Processes. *Chemical Engineering & Technology*, 21(2):121–132, 1998.

[23] Mangold, M., Motz, S., and Gilles, E. A Network Theory for the Structured Modeling of Chemical Processes. *Chemical Engineering Science*, 57(19):4099–4116, 2002.

[24] Sundmacher, K. Multi-Level Design of Process Systems for Efficient Chemicals Production and Energy Conversion. In *12th International Symposium on Process Systems Engineering and 25th European Symposium on Computer Aided Process Engineering*, volume 37 of *Computer Aided Chemical Engineering*, pages 25–34. Elsevier, 2015.

[25] Freund, H. and Sundmacher, K. Process Intensification, 2. Phase Level. In *Ullmann's Encyclopedia of Industrial Chemistry*. Wiley-VCH, Weinheim, 2000.

[26] Charpentier, J. C. and McKenna, T. F. Managing Complex Systems: Some Trends for the Future of Chemical and Process Engineering. *Chemical Engineering Science*, 59 (8-9):1617–1640, 2004.

[27] Floudas, C. A., Niziolek, A. M., Onel, O., and Matthews, L. R. Multi-Scale Systems Engineering for Energy and the Environment: Challenges and Opportunities. *AIChE Journal*, 62(3):602–623, 2016.

[28] Miller, D. C., Siirola, J. D., Agarwal, D., Burgard, A. P., Lee, A., Eslick, J. C., Nicholson, B., Laird, C., Biegler, L. T., Bhattacharyya, D., Sahinidis, N. V., Grossmann, I. E., Gounaris, C. E., and Gunter, D. Next Generation Multi-Scale Process Systems Engineering Framework. In *13th International Symposium on Process Systems Engineering (PSE 2018)*, volume 44 of *Computer Aided Chemical Engineering*, pages 2209–2214. Elsevier, 2018.

[29] Dudukovic, M. P. Reaction Engineering: Status and Future Challenges. *Chemical Engineering Science*, 65(1):3–11, 2010.

[30] Salciccioli, M., Stamatakis, M., Caratzoulas, S., and Vlachos, D. G. A Review of Multiscale Modeling of Metal-Catalyzed Reactions: Mechanism Development for Complexity and Emergent Behavior. *Chemical Engineering Science*, 66(19):4319–4355, 2011.

[31] Ricardez-Sandoval, L. A. Current Challenges in the Design and Control of Multiscale Systems. *The Canadian Journal of Chemical Engineering*, 89(6):1324–1341, 2011.

[32] Raimondeau, S. and Vlachos, D. Recent Developments on Multiscale, Hierarchical Modeling of Chemical Reactors. *Chemical Engineering Journal*, 90(1-2):3–23, 2002.

[33] Deutschmann, O., Tischer, S., Correa, C., Chatterjee, D., Kleditzsch, S., Janardhanan, V. M., Mladenov, N., Minh, H. D., Karadeniz, H., and Hettel, M. DETCHEM Software package 2.5 ed., 2014. URL www.detchem.com.

[34] Hettel, M., Diehm, C., Bonart, H., and Deutschmann, O. Numerical Simulation of a Structured Catalytic Methane Reformer by DUO: The New Computational Interface for OpenFOAM and DETCHEM. *Catalysis Today*, 258:230–240, 2015.

[35] Maestri, M. Escaping the Trap of Complication and Complexity in Multiscale Microkinetic Modelling of Heterogeneous Catalytic Processes. *Chemical communications (Cambridge, England)*, 53(74):10244–10254, 2017.

[36] Mhadeshwar, A. B. and Vlachos, D. G. Hierarchical Multiscale Mechanism Development for Methane Partial Oxidation and Reforming and for Thermal Decomposition of Oxygenates on Rh. *Journal of Physical Chemistry B*, 109(35):16819–16835, 2005.

[37] Chen, D., Lødeng, R., Svendsen, H., and Holmen, A. Hierarchical Multiscale Modeling of Methane Steam Reforming Reactions. *Industrial & Engineering Chemistry Research*, 50(5):2600–2612, 2011.

[38] Borchert, C. and Sundmacher, K. Morphology Evolution of Crystal Populations: Modeling and Observation Analysis. *Chemical Engineering Science*, 70:87–98, 2012.

[39] Samad, N. A. F. A., Singh, R., Sin, G., Gernaey, K. V., and Gani, R. A Generic Multi-Dimensional Model-Based System for Batch Cooling Crystallization Processes. *Computers & Chemical Engineering*, 35(5):828–843, 2011.

[40] Eisenschmidt, H., Bajcinca, N., and Sundmacher, K. Optimal Control of Crystal Shapes in Batch Crystallization Experiments by Growth-Dissolution Cycles. *Crystal Growth & Design*, 16(6):3297–3306, 2016.

[41] Prasad, V. and Vlachos, D. G. Multiscale Model and Informatics-Based Optimal Design of Experiments: Application to the Catalytic Decomposition of Ammonia on Ruthenium. *Industrial & Engineering Chemistry Research*, 47(17):6555–6567, 2008.

[42] Prasad, V., Karim, A. M., Ulissi, Z., Zagrobelny, M., and Vlachos, D. G. High Throughput Multiscale Modeling for Design of Experiments, Catalysts and Reactors: Application to Hydrogen Production from Ammonia. *Chemical Engineering Science*, 65(1):240–246, 2010.

[43] Karst, F., Maestri, M., Freund, H., and Sundmacher, K. Reduction of Microkinetic Reaction Models for Reactor Optimization Exemplified for Hydrogen Production from Methane. *Chemical Engineering Journal*, 281:981–994, 2015.

[44] Subramanian, A., Gundersen, T., and Adams, T. Modeling and Simulation of Energy Systems: A Review. *Processes*, 6(12):238, 2018.

[45] Terrazas-Moreno, S. and Grossmann, I. E. A Multiscale Decomposition Method for the Optimal Planning and Scheduling of Multi-Site Continuous Multiproduct Plants. *Chemical Engineering Science*, 66(19):4307–4318, 2011.

[46] Jung, J., von der Assen, N., and Bardow, A. Comparative LCA of Multi-Product Processes with Non-Common Products: a Systematic Approach Applied to Chlorine Electrolysis Technologies. *The International Journal of Life Cycle Assessment*, 18(4): 828–839, 2013.

[47] Marechal, F., Palazzi, F., Godat, J., and Favrat, D. Thermo-Economic Modelling and Optimisation of Fuel Cell Systems. *Fuel Cells*, 5(1):5–24, 2005.

[48] Quaglia, A., Sarup, B., Sin, G., and Gani, R. Integrated Business and Engineering Framework for Synthesis and Design of Enterprise-Wide Processing Networks. *Computers & Chemical Engineering*, 38:213–223, 2012.

[49] Susarla, N. and Karimi, I. A. Integrated Supply Chain Planning for Multinational Pharmaceutical Enterprises. *Computers & Chemical Engineering*, 42:168–177, 2012.

[50] Mitra, S., Pinto, J. M., and Grossmann, I. E. Optimal Multi-Scale Capacity Planning for Power-Intensive Continuous Processes Under Time-Sensitive Electricity Prices and Demand Uncertainty. Part I: Modeling. *Computers & Chemical Engineering*, 65:89–101, 2014.

[51] Mitra, S., Pinto, J. M., and Grossmann, I. E. Optimal Multi-Scale Capacity Planning for Power-Intensive Continuous Processes Under Time-Sensitive Electricity Prices and Demand Uncertainty. Part II: Enhanced Hybrid Bi-Level Decomposition. *Computers & Chemical Engineering*, 65:102–111, 2014.

[52] Pfafferodt, M., Heidebrecht, P., Sundmacher, K., Würtenberger, U., and Bednarz, M. Multiscale Simulation of the Indirect Internal Reforming Unit (IIR) in a Molten Carbonate Fuel Cell (MCFC). *Industrial & Engineering Chemistry Research*, 47(13): 4332–4341, 2008.

[53] Pfafferodt, M., Heidebrecht, P., and Sundmacher, K. Stack Modelling of a Molten Carbonate Fuel Cell (MCFC). *Fuel Cells*, 10(4):619–635, 2010.

[54] Heidebrecht, P., Pfafferodt, M., and Sundmacher, K. Multiscale Modelling Strategy for Structured Catalytic Reactors. *Chemical Engineering Science*, 66(19):4389–4402, 2011.

[55] Holl, P., Marquardt, W., and Gilles, E. D. DIVA - A Powerful Tool for Dynamic Process Simulation. *Computers & Chemical Engineering*, 12(5):421–426, 1988.

[56] Tränkle, F., Zeitz, M., Ginkel, M., and Gilles, E. D. PROMOT: A Modeling Tool for Chemical Processes. *Mathematical and Computer Modelling of Dynamical Systems*, 6 (3):283–307, 2000.

[57] Bertran, M.-O., Frauzem, R., Sanchez-Arcilla, A.-S., Zhang, L., Woodley, J. M., and Gani, R. A Generic Methodology for Processing Route Synthesis and Design Based on Superstructure Optimization. *Computers & Chemical Engineering*, 106:892–910, 2017.

[58] Kravanja, Z. and Grossmann, I. E. Multilevel-Hierarchical MINLP Synthesis of Process Flowsheets. *Computers & Chemical Engineering*, 21:S421–S426, 1997.

[59] Pouransari, N., Bocquenet, G., and Maréchal, F. Site-Scale Process Integration and Utility Optimization with Multi-Level Energy Requirement Definition. *Energy Conversion and Management*, 85:774–783, 2014.

[60] Kumar, A., Edgar, T. F., and Baldea, M. Multi-Resolution Model of an Industrial Hydrogen Plant for Plantwide Operational Optimization with Non-Uniform Steam-Methane Reformer Temperature Field. *Computers & Chemical Engineering*, 107: 271–283, 2017.

[61] Kumar, A., Baldea, M., and Edgar, T. F. A Physics-Based Model for Industrial Steam-Methane Reformer Optimization with Non-Uniform Temperature Field. *Computers & Chemical Engineering*, 105:224–236, 2017.

[62] Onel, O., Niziolek, A. M., Butcher, H., Wilhite, B. A., and Floudas, C. A. Multi-Scale Approaches for Gas-to-Liquids Process Intensification: CFD Modeling, Process Synthesis, and Global Optimization. *Computers & Chemical Engineering*, 105:276–296, 2017.

[63] Gassner, M. and Maréchal, F. Thermo-Economic Process Model for Thermochemical Production of Synthetic Natural Gas (SNG) from Lignocellulosic Biomass. *Biomass and Bioenergy*, 33(11):1587–1604, 2009.

[64] Hanes, R. J. and Bakshi, B. R. Process to Planet: A Multiscale Modeling Framework Toward Sustainable Engineering. *AIChE Journal*, 61(10):3332–3352, 2015.

[65] Peschel, A., Jörke, A., Sundmacher, K., and Freund, H. Optimal Reaction Concept and Plant Wide Optimization of the Ethylene Oxide Process. *Chemical Engineering Journal*, 207-208:656–674, 2012.

[66] Karst, F., Freund, H., Maestri, M., and Sundmacher, K. Multiscale Chemical Process Design Exemplified for a PEM Fuel Cell Process. *Chemie Ingenieur Technik*, 86(12): 2075–2088, 2014.

[67] Hentschel, B., Peschel, A., Freund, H., and Sundmacher, K. Simultaneous Design of the Optimal Reaction and Process Concept for Multiphase Systems. *Chemical Engineering Science*, 115:69–87, 2014.

[68] Naseri, A. T., Peppley, B. A., and Pharoah, J. G. Computational Analysis of the Reacting Flow in a Microstructured Reformer Using a Multiscale Approach. *AIChE Journal*, 60(6):2263–2274, 2014.

[69] Pantoleontos, G., Skevis, G., Karagiannakis, G., and Konstandopoulos, A. G. A Heterogeneous Multiscale Dynamic Model for Simulation of Catalytic Reforming Reactors. *International Journal of Chemical Kinetics*, 48(5):239–252, 2016.

[70] Singhal, A., Cloete, S., Quinta-Ferreira, R., and Amini, S. Multiscale Modeling of Packed Bed Chemical Looping Reforming. *Energy Procedia*, 136:349–355, 2017.

[71] da Cruz, F. E., Karagöz, S., and Manousiouthakis, V. I. Parametric Studies of Steam Methane Reforming Using a Multiscale Reactor Model. *Industrial & Engineering Chemistry Research*, 56(47):14123–14139, 2017.

[72] Medrano-García, J. D., Ruiz-Femenia, R., and Caballero, J. A. Multi-Objective Optimization of Combined Synthesis Gas Reforming Technologies. *Journal of CO_2 Utilization*, 22:355–373, 2017.

[73] Vlachos, D. G. Homogeneous-Heterogeneous Oxidation Reactions Over Platinum and Inert Surfaces. *Chemical Engineering Science*, 51(10):2429–2438, 1996.

[74] Weinan, E., Engquist, B., and Huang, Z. Heterogeneous Multiscale Method: A General Methodology for Multiscale Modeling. *Physical Review B*, 67(9):783, 2003.

[75] Kevrekidis, I. G. and Samaey, G. Equation-Free Multiscale Computation: Algorithms and Applications. *Annual Review of Physical Chemistry*, 60:321–344, 2009.

[76] Zhou, T., McBride, K., Zhang, X., Qi, Z., and Sundmacher, K. Integrated Solvent and Process Design Exemplified for a Diels-Alder Reaction. *AIChE Journal*, 61(1):147–158, 2015.

[77] Zhou, T., Zhou, Y., and Sundmacher, K. A Hybrid Stochastic–Deterministic Optimization Approach for Integrated Solvent and Process Design. *Chemical Engineering Science*, 159:207–216, 2017.

[78] Daróczy, L., Janiga, G., and Thévenin, D. Systematic Analysis of the Heat Exchanger Arrangement Problem Using Multi-Objective Genetic Optimization. *Energy*, 65:364–373, 2014.

[79] Bodenstein, M. Eine Theorie der photochemischen Reaktionsgeschwindigkeiten. *Zeitschrift für physikalische Chemie*, 85U(1):329–397, 1913.

[80] Zhou, T., Wang, J., McBride, K., and Sundmacher, K. Optimal Design of Solvents for Extractive Reaction Processes. *AIChE Journal*, 62(9):3238–3249, 2016.

[81] Harper, P. M., Gani, R., Kolar, P., and Ishikawa, T. Computer-Aided Molecular Design with Combined Molecular Modeling and Group Contribution. *Fluid Phase Equilibria*, 158-160:337–347, 1999.

[82] Harper, P. M. and Gani, R. A Multi-Step and Multi-Level Approach for Computer Aided Molecular Design. *Computers & Chemical Engineering*, 24(2-7):677–683, 2000.

[83] Bremer, J., Rätze, K. H. G., and Sundmacher, K. CO_2 Methanation: Optimal Start-Up Control of a Fixed-Bed Reactor for Power-to-Gas Applications. *AIChE Journal*, 63(1): 23–31, 2017.

[84] Rätze, K. H. G., Bremer, J., Biegler, L. T., and Sundmacher, K. Physics-Based Surrogate Models for Optimal Control of a CO_2 Methanation Reactor. In Espuña, A., Graells, M., and Puigjaner, L., editors, *27th European Symposium on Computer Aided Process Engineering*, volume 40 of *Computer Aided Chemical Engineering*, pages 127–132. Elsevier, Amsterdam, 2017.

[85] McBride, K. and Sundmacher, K. Data Driven Conceptual Process Design for the Hydroformylation of 1-Dodecene in a Thermomorphic Solvent System. *Industrial & Engineering Chemistry Research*, 54(26):6761–6771, 2015.

[86] Biegler, L. T. and Lang, Y. Multi-Scale Optimization for Advanced Energy Processes. In *11th International Symposium on Process Systems Engineering*, volume 31 of *Computer Aided Chemical Engineering*, pages 51–60. Elsevier, 2012.

[87] Biegler, L. T., Lang, Y.-d., and Lin, W. Multi-Scale Optimization for Process Systems Engineering. *Computers & Chemical Engineering*, 60:17–30, 2014.

[88] Biegler, L. T. and Grossmann, I. E. Retrospective on Optimization. *Computers & Chemical Engineering*, 28(8):1169–1192, 2004.

[89] Houghton Mifflin Harcourt. The American Heritage Dictionary, accessed: February 14, 2019. URL https://www.ahdictionary.com/word/search.html?q=efficient.

[90] de Hemptinne, J.-C., Ferrasse, J.-H., Gorak, A., Kjelstrup, S., Maréchal, F., Baudouin, O., and Gani, R. Energy Efficiency as an Example of Cross-Discipline Collaboration in Chemical Engineering. *Chemical Engineering Research and Design*, 119:183–187, 2017.

[91] Liesche, G. and Sundmacher, K. Productivity versus Product Quality: Exploring the Limits of Autothermal Microchannel Reactors in Methane Steam Reforming. *Chemical Engineering Journal*, DOI: 10.1016/j.cej.2018.09.209, 2018.

[92] Engel, S., Liesche, G., Janiga, G., and Sundmacher, K. Optimal Tube Bundle Arrangements in Side-fired Methane Steam Reforming Furnaces. *Energy*, under internal review, 2019.

[93] Gail, E., Gos, S., Kulzer, R., Lorösch, J., Rubo, A., Sauer, M., Kellens, R., Reddy, J., Steier, N., and Hasenpusch, W. Cyano Compounds, Inorganic. In *Ullmann's Encyclopedia of Industrial Chemistry*. Wiley-VCH, Weinheim, 2000.

[94] Sauer, J., Bewersdorf, M., Köstner, M., Rinner, M., and Wolf, D. Hydrocyanic Acid (HCN) Production. In Ertl, G., editor, *Handbook of Heterogeneous Catalysis*, pages 2592–2609. Wiley-VCH, 2008.

[95] Shine, N. Fluohmic Process for Hydrogen Cyanide. *Chemical Engineering Progress*, 67 (2):52–55, 1971.

[96] Johnson, H. and Andersen, A. Process for Preparation of Hydrogen Cyanide - Procédé pour la préparation d'acide hydrocyanique, No. CA573348, 1959.

[97] Kennedy, D. J. and Shine, N. Production of Hydrogen Cyanide, No. US3097921, 1963.

[98] Bipp, H. and Kieczka, H. Formamides. In *Ullmann's Encyclopedia of Industrial Chemistry*, volume 73, pages 1–12. Wiley-VCH, Weinheim, 2000.

[99] von Öhsen, U., Stecher, K., Köhler, W., Müller, B., Brunnmüller, F., and Schneider, R. Process for the Decomposition of Formamide into Cyanic Acid and Water, No. EP0209039A3, 1987.

[100] Brazdil, J. F. Acrylonitrile. In *Ullmann's Encyclopedia of Industrial Chemistry*, volume 23, page 1841. Wiley-VCH, Weinheim, 2000.

[101] Andrussow, L. Über die katalytische Oxydation von Ammoniak-Methan-Gemischen zu Blausäure. *Angewandte Chemie*, 48(37):593–604, 1935.

[102] Andrussow, L. Blausäuresynthese und die schnell verlaufenden katalytischen Prozesse in strömenden Gasen. *Chemie Ingenieur Technik*, 27(8/9):469–472, 1955.

[103] Kautter, C. T. and Leitenberger, W. Großtechnische Herstellung von Cyanwasserstoff nach Andrussow. *Chemie Ingenieur Technik*, 25(12):697–701, 1953.

[104] Endter, F. Die technische Synthese von Cyanwasserstoff aus Methan und Ammoniak ohne Zusatz von Sauerstoff. *Chemie Ingenieur Technik*, 30(5):305–310, 1958.

[105] Hoffmann, G., Kokert, E., and Wendlandt, R. Verfahren zur Durchführung katalytischer Reaktionen insbesondere zur Herstellung von Blausäure, No. DE882985, 1953.

[106] Endter, F. Vorrichtung zur Durchführung von endothermen Gasreaktionen, No. DE959364C, 1957.

[107] Endter, F. Unteres Ofenverschlussteil für Öfen, insbesondere Reaktionsöfen, No. DE1007300, 1957.

[108] von Hippel, L., Bussek, C., and Arntz, D. Verfahren zur Herstellung von Blausäure, No. EP 0752390 B1, 1998.

[109] von Hippel, L., Gutsch, A., Schaffer, R., Sauer, M., and Vanheertum, R. Verfahren zur Herstellung von Blausäure, No. EP 0922674 A1, 1999.

[110] Schulze, G. and Weiß, G. Verfahren zur Herstellung von Blausäure, No. DE1143497, 1963.

[111] Velenyi, L. J., Hardman, H. F., and Pesa, F. A. Process for the Production of Hydrocyanic Acide from Carbon Monoxide and Ammonia, No. US 4423023, 1983.

[112] Riegert, R. J. and Mehdizadeh, M. Preparation of Hydrogen Cyanide, No. WO1995021126, 1995.

[113] Herbertz, H. A., Bockhorn, H., and Fetting, F. Synthese von Cyanwasserstoff aus leichten Kohlenwasserstoffen und Ammoniak durch Flammenreaktionen. *Chemie Ingenieur Technik*, 42(2):63–72, 1970.

[114] Bockhorn, H., Coy, R., Fetting, F., and Prätorius, W. Chemische Synthesen in Flammen. *Chemie Ingenieur Technik*, 49(11):883–895, 1977.

[115] Koberstein, E. Model Reactor Studies of the Hydrogen Cyanide Synthesis from Methane and Ammonia. *Industrial & Engineering Chemistry Process Design & Development*, 12 (4):444–448, 1973.

[116] Burgess, D. R. Thermochemical data. In Lindstrom, P. J. and Mallard, W. G., editors, *NIST Chemistry WebBook: NIST Standard Reference Database Number 69*. Gaithersburg, 2017.

[117] Stephan, P., Schaber, K., Stephan, K., and Mayinger, F. *Thermodynamik - Grundlagen und technische Anwendungen: Band 2: Mehrstoffsysteme und chemische Reaktionen*. Springer, Berlin Heidelberg, 2010.

[118] Baehr, H. D. and Kabelac, S. *Thermodynamik*. Springer, Berlin Heidelberg, 2012.

[119] Rumble, J. *CRC Handbook of Chemistry and Physics*. Taylor & Francis, Abingdon, 99th edition, 2018.

[120] Verein Deutscher Ingenieure, VDI-Gesellschaft Verfahrenstechnik und Chemieingenieurwesen. *VDI-Wärmeatlas*. Springer, Berlin, 11th edition, 2013.

[121] Pfeil, E. and Hoffmann, P. Über die Synthese von Blausäure aus Methan und Ammoniak. *Berichte der Bunsengesellschaft*, 67(2):229–235, 1963.

[122] Hasenberg, D. and Schmidt, L. D. HCN Synthesis from CH_4 and NH_3 on Clean Rh. *Journal of Catalysis*, 91(1):116–131, 1985.

[123] Hasenberg, D. and Schmidt, L. D. HCN Synthesis from CH_4 and NH_3 on Platinum. *Journal of Catalysis*, 97(1):156–168, 1986.

[124] Hasenberg, D. and Schmidt, L. D. HCN Synthesis from CH_4, NH_3, and O_2 on Clean Pt*. *Journal of Catalysis*, 104(2):441–453, 1987.

[125] Waletzko, N. and Schmidt, L. D. Modeling Catalytic Gauze Reactors: HCN Synthesis. *AIChE Journal*, 34(7):1146–1156, 1988.

[126] Herceg, E. and Trenary, M. Formation of Surface CN from the Coupling of C and N Atoms on Pt(111). *Journal of the American Chemical Society*, 125(51):15758–15759, 2003.

[127] Delagrange, S. and Schuurman, Y. HCN Synthesis from Methane and Ammonia over Platinum. *Catalysis Today*, 121(3-4):204–209, 2007.

[128] Diefenbach, M., Brönstrup, M., Aschi, M., Schröder, D., and Schwarz, H. HCN Synthesis from Methane and Ammonia: Mechanisms of Pt^+-Mediated C-N Coupling. *Journal of the American Chemical Society*, 121(45):10614–10625, 1999.

[129] Horn, R. *Investigation of Heterogeneously Catalyzed Reactions using Molecular Beam Sampling Mass Spectrometry with Threshold Ionization.* PhD Thesis, Technische Universität Berlin, Berlin, 2003.

[130] Horn, R., Mestl, G., Thiede, M., Jentoft, F. C., Schmidt, P. M., Bewersdorf, M., Weber, R., and Schlögl, R. Gas Phase Contributions to the Catalytic Formation of HCN from CH_4 and NH_3 over Pt: An In Situ Study by Molecular Beam Mass Spectrometry with Threshold Ionization. *Physical chemistry chemical physics*, 6(18):4514–4521, 2004.

[131] Reimert, R., Marschner, F., Renner, H.-J., Boll, W., Supp, E., Brejc, M., and Liebner, W. Gas Production, 2. Processes. In *Ullmann's Encyclopedia of Industrial Chemistry*, pages 423–482. Wiley-VCH, Weinheim, 2000.

[132] Davy, H. Some New Experiments and Observations on the Combustion of Gaseous Mixtures, with an Account of a Method of Preserving a Continued Light in Mixtures of Inflammable Gases and Air Without Flame. *Philosophical Transactions of the Royal Society of London*, 107(77), 1817.

[133] Rostrup-Nielsen, J. R. Catalytic Steam Reforming. In Anderson, J. R. and Boudart, M., editors, *Catalysis: Volume 5*, pages 1–117. Springer, Berlin, 1984.

[134] Mond, L. and Langer, C. Dampfreformierung mit einem Nickel Katalysator, No. DRP 51572, 1889.

[135] Karakaya, M., Keskin, S., and Avci, A. K. Parametric Study of Methane Steam Reforming to Syngas in a Catalytic Microchannel Reactor. *Applied Catalysis A: General*, 411-412:114–122, 2012.

[136] Xu, J. and Froment, G. F. Methane Steam Reforming, Methanation and Water-Gas Shift: I. Intrinsic Kinetics. *AIChE Journal*, 35(1):88–96, 1989.

[137] Xu, J. and Froment, G. F. Methane Steam Reforming: II. Diffusional Limitations and Reactor Simulation. *AIChE Journal*, 35(1):97–103, 1989.

[138] Wei, J. and Iglesia, E. Mechanism and Site Requirements for Activation and Chemical Conversion of Methane on Supported Pt Clusters and Turnover Rate Comparisons among Noble Metals. *Journal of Physical Chemistry*, 108(13):4094–4103, 2004.

[139] Zeppieri, M., Villa, P. L., Verdone, N., Scarsella, M., and de Filippis, P. Kinetic of Methane Steam Reforming Reaction Over Nickel- and Rhodium-Based Catalysts. *Applied Catalysis A: General*, 387(1-2):147–154, 2010.

[140] Schädel, B. T., Duisberg, M., and Deutschmann, O. Steam Reforming of Methane, Ethane, Propane, Butane, and Natural Gas Over a Rhodium-Based Catalyst. *Catalysis Today*, 142(1-2):42–51, 2009.

[141] Maier, L. I., Schädel, B., Herrera Delgado, K., Tischer, S., and Deutschmann, O. Steam Reforming of Methane Over Nickel: Development of a Multi-Step Surface Reaction Mechanism. *Topics in Catalysis*, 54(13-15):845–858, 2011.

[142] Irani, M., Alizadehdakhel, A., Pour, A. N., Hoseini, N., and Adinehnia, M. CFD Modeling of Hydrogen Production Using Steam Reforming of Methane in Monolith Reactors: Surface or Volume-Base Reaction Model? *International Journal of Hydrogen Energy*, 36(24):15602–15610, 2011.

[143] Dybkjaer, I. Tubular Reforming and Autothermal Reforming of Natural Gas - an Overview of Available Processes. *Fuel Processing Technology*, 42:85–107, 1995.

[144] Krummnow, A. *Modellierung, Simulation und Modelldimensionsanalyse eines Festbet-treaktors für die Dampfreformierung von Methan.* Master thesis, Otto-von-Guericke Universität, Magdeburg, 2019.

[145] Bhat, S. A. and Sadhukhan, J. Process Intensification Aspects for Steam Methane Reforming: An Overview. *AIChE Journal*, 55(2):408–422, 2009.

[146] Venkataraman, K., Wanat, E. C., and Schmidt, L. D. Steam Reforming of Methane and Water-Gas Shift in Catalytic Wall Reactors. *AIChE Journal*, 49(5):1277–1284, 2003.

[147] Tonkovich, A. Y., Perry, S., Wang, Y., Qiu, D., LaPlante, T., and Rogers, W. A. Microchannel Process Technology for Compact Methane Steam Reforming. *Chemical Engineering Science*, 59(22-23):4819–4824, 2004.

[148] Ricca, A., Palma, V., Martino, M., and Meloni, E. Innovative Catalyst Design for Methane Steam Reforming Intensification. *Fuel*, 198:175–182, 2017.

[149] Wanat, E. C., Venkataraman, K., and Schmidt, L. D. Steam Reforming and Water–Gas Shift of Ethanol on Rh and Rh–Ce Catalysts in a Catalytic Wall Reactor. *Applied Catalysis A: General*, 276(1-2):155–162, 2004.

[150] Galvita, V. and Sundmacher, K. Hydrogen Production from Methane by Steam Reforming in a Periodically Operated Two-Layer Catalytic Reactor. *Applied Catalysis A: General*, 289(2):121–127, 2005.

[151] Wolf, D., Höhenberger, M., and Baerns, M. External Mass and Heat Transfer Limitations of the Partial Oxidation of Methane over a Pt/MgO Catalyst – Consequences for Adiabatic Reactor Operation. *Industrial & Engineering Chemistry Research*, 36: 3345–3353, 1997.

[152] Wehinger, G. D. Radiation Matters in Fixed-Bed CFD Simulations. *Chemie Ingenieur Technik*, 91(5):583–591, 2019.

[153] Jurtz, N., Kraume, M., and Wehinger, G. D. Advances in Fixed-Bed Reactor Modeling Using Particle-Resolved Computational Fluid Dynamics (CFD). *Reviews in Chemical Engineering*, 35(2):139–190, 2019.

[154] Lao, L., Aguirre, A., Tran, A., Wu, Z., Durand, H., and Christofides, P. D. CFD Modeling and Control of a Steam Methane Reforming Reactor. *Chemical Engineering Science*, 148:78–92, 2016.

[155] Schwaab, M., Alberton, A. L., Fontes, C. E., Bittencourt, R. C., and Pinto, J. C. Hybrid Modeling of Methane Reformers. 2. Modeling of the Industrial Reactors. *Industrial & Engineering Chemistry Research*, 48(21):9376–9382, 2009.

[156] Tran, A., Aguirre, A., Durand, H., Crose, M., and Christofides, P. D. CFD Modeling of a Industrial-Scale Steam Methane Reforming Furnace. *Chemical Engineering Science*, 171:576–598, 2017.

[157] Frauhammer, J., Eigenberger, G., von Hippel, L., and Arntz, D. A New Reactor Concept for Endothermic High-Temperature Reactions. *Chemical Engineering Science*, 54:3661–3670, 1999.

[158] Kolios, G., Frauhammer, J., and Eigenberger, G. A Simplified Procedure for the Optimal Design of Autothermal Reactors for Endothermic High-Temperature Reactions. *Chemical Engineering Science*, 56(2):351–357, 2001.

[159] Kolios, G., Frauhammer, J., and Eigenberger, G. Efficient Reactor Concepts for Coupling of Endothermic and Exothermic Reactions. *Chemical Engineering Science*, 57(9):1505–1510, 2002.

[160] Piña, J., Schbib, N. S., Bucalá, V., and Borio, D. O. Influence of the Heat-Flux Profiles on the Operation of Primary Steam Reformers. *Industrial & Engineering Chemistry Research*, 40(23):5215–5221, 2001.

[161] Rajesh, J. K., Gupta, S. K., Rangaiah, G. P., and Ray, A. K. Multiobjective Optimization of Steam Reformer Performance Using Genetic Algorithm. *Industrial & Engineering Chemistry Research*, 39(3):706–717, 2000.

[162] de Jong, M., Reinders, A., Kok, J., and Westendorp, G. Optimizing a Steam-Methane Reformer for Hydrogen Production. *International Journal of Hydrogen Energy*, 34(1): 285–292, 2009.

[163] Park, N., Park, M.-J., Baek, S.-C., Ha, K.-S., Lee, Y.-J., Kwak, G., Park, H.-G., and Jun, K.-W. Modeling and Optimization of the Mixed Reforming of Methane: Maximizing CO_2 Utilization for Non-Equilibrated Reaction. *Fuel*, 115:357–365, 2014.

[164] Mundhwa, M., Parmar, R. D., and Thurgood, C. P. A Comparative Parametric Study of a Catalytic Plate Methane Reformer Coated with Segmented and Continuous Layers of Combustion Catalyst for Hydrogen Production. *Journal of Power Sources*, 344: 85–102, 2017.

[165] Arzamendi, G., Diéguez, P. M., Montes, M., Odriozola, J. A., Sousa-Aguiar, E. F., and Gandía, L. M. Methane Steam Reforming in a Microchannel Reactor for GTL Intensification: A Computational Fluid Dynamics Simulation Study. *Chemical Engineering Journal*, 154(1-3):168–173, 2009.

[166] Karim, A., Bravo, J., Gorm, D., Conant, T., and Datye, A. Comparison of Wall-Coated and Packed-Bed Reactors for Steam Reforming of Methanol. *Catalysis Today*, 110(1-2): 86–91, 2005.

[167] Zhai, X., Ding, S., Cheng, Y., Jin, Y., and Cheng, Y. CFD Simulation with Detailed Chemistry of Steam Reforming of Methane for Hydrogen Production in an Integrated Micro-Reactor. *International Journal of Hydrogen Energy*, 35(11):5383–5392, 2010.

[168] Stutz, M. J., Hotz, N., and Poulikakos, D. Optimization of Methane Reforming in a Microreactor—Effects of Catalyst Loading and Geometry. *Chemical Engineering Science*, 61(12):4027–4040, 2006.

[169] Jischa, M. *Konvektiver Impuls-, Wärme- und Stoffaustausch.* Springer, Wiesbaden, 1982.

[170] Krause, E., Schlichting, H., Oertel, H. J., and Gersten, K. *Grenzschicht-Theorie.* Springer, Berlin, 10th edition, 2013.

[171] Taylor, R. and Krishna, R. *Multicomponent Mass Transfer.* John Wiley and Sons, New York, 1993.

[172] Wilke, C. R. A Viscosity Equation for Gas Mixtures. *Journal of Chemical Physics*, 18 (4):517, 1950.

[173] Kee, R. J., Dixon-Lewis, G., Warnatz, J., Coltrin, M. E., and Miller, J. A. A FORTRAN Computer Code Package for the Evaluation of Gas-Phase, Multicomponent Transport Properties. *SAND86-8246*, pages 3–39, 1986.

[174] Modest, M. F. *Radiative Heat Transfer.* Elsevier, New York, 3rd edition, 2013.

[175] Howell, J. R., Menguc, M. P., and Siegel, R. *Thermal Radiation Heat Transfer*. CRC Press - Taylor and Francis, Boca Raton, 5th edition, 2010.

[176] Kochanov, R. V., Gordon, I. E., Rothman, L. S., Wcisło, P., Hill, C., and Wilzewski, J. S. HITRAN Application Programming Interface (HAPI): A Comprehensive Approach to Working with Spectroscopic Data. *Journal of Quantitative Spectroscopy & Radiative Transfer*, 177:15–30, 2016.

[177] Zhang, H. and Modest, M. F. Evaluation of the Planck-Mean Absorption Coefficients from HITRAN and HITEMP Databases. *Journal of Quantitative Spectroscopy & Radiative Transfer*, 73(6):649–653, 2002.

[178] Rothman, L. S., Gordon, I. E., Barber, R. J., Dothe, H., Gamache, R. R., Goldman, A., Perevalov, V. I., Tashkun, S. A., and Tennyson, J. HITEMP, the High-Temperature Molecular Spectroscopic Database. *Journal of Quantitative Spectroscopy & Radiative Transfer*, 111(15):2139–2150, 2010.

[179] Rothman, L. S., Gordon, I. E., Babikov, Y., Barbe, A., Chris Benner, D., Bernath, P. F., Birk, M., Bizzocchi, L., Boudon, V., Brown, L. R., Campargue, A., Chance, K., Cohen, E. A., Coudert, L. H., Devi, V. M., Drouin, B. J., Fayt, A., Flaud, J.-M., Gamache, R. R., Harrison, J. J., Hartmann, J.-M., Hill, C., Hodges, J. T., Jacquemart, D., Jolly, A., Lamouroux, J., Le Roy, R. J., Li, G., Long, D. A., Lyulin, O. M., Mackie, C. J., Massie, S. T., Mikhailenko, S., Müller, H., Naumenko, O. V., Nikitin, A. V., Orphal, J., Perevalov, V., Perrin, A., Polovtseva, E. R., Richard, C., Smith, M., Starikova, E., Sung, K., Tashkun, S., Tennyson, J., Toon, G. C., Tyuterev, V., and Wagner, G. The HITRAN2012 Molecular Spectroscopic Database. *Journal of Quantitative Spectroscopy & Radiative Transfer*, 130:4–50, 2013.

[180] Chu, H., Gu, M., Zhou, H., and Liu, F. Calculations of Narrow-Band Transimissities and the Planck Mean Absorption Coefficients of Real Gases Using Line-by-Line and Statistical Narrow-Band Models. *Front. Energy*, 8(1):41–48, 2014.

[181] Brenan, K. E., Campbell, S. L., and Petzold, L. R. *Numerical Solution of Initial-Value Problems in Differential-Algebraic Equations*. Society for Industrial and Applied Mathematics, Philadelphia, 1996.

[182] Hindmarsh, A. C., Brown, P. N., Grant, K. E., Lee, S. L., Serban, R., Shumaker, D. E., and Woodward, C. S. SUNDIALS: Suite of Nonlinear and Differential/Algebraic Equation Solvers. *ACM Transactions on Mathematical Software (TOMS)*, 31(3):363–396, 2005.

[183] Andersson, J. *A General-Purpose Software Framework for Dynamic Optimization*. Phd thesis, KU Leuven, Heverlee, Belgium, 2013.

[184] Patankar, S. *Numerical Heat Transfer and Fluid Flow*. Taylor & Francis, London, 1980.

[185] Graziani, F., editor. *Computational Methods in Transport: Verification and Validation*. Springer, Berlin, 2008.

[186] Roache, P. J. Perspective: A Method for Uniform Reporting of Grid Refinement Studies. *Journal of Fluids Engineering*, 116(3):405–413, 1994.

[187] Drazin, P. G. and Reid, W. H. *Hydrodynamic Stability*. Cambridge University Press, Cambridge, 2nd edition, 2004.

[188] Kays, W., Crawford, M., and Weigand, B. *Convective Heat & Mass Transfer*. McGraw-Hill, New York, 4th edition, 2005.

[189] Levenspiel, O. *Chemical Reaction Engineering*. Wiley-VCH, New York, 1999.

[190] Specht, E. *Heat and Mass Transfer in Thermoprocessing: Fundamentals, Calculations, Processes.* Vulkan, Essen, 2017.

[191] Zhang, Y. *Theory and Calculation of Heat Transfer in Furnaces.* Elsevier, Boston MA, 2016.

[192] Olivieri, A. and Vegliò, F. Process Simulation of Natural Gas Steam Reforming: Fuel Distribution Optimisation in the Furnace. *Fuel Processing Technology*, 89(6):622–632, 2008.

[193] Zheng, D., Wu, B., Fleitz, J., Trajkovski, R., and Zhou, C. Q. CFD Simulation of a Hydrogen Reformer Furnace. In *2010 14th International Heat Transfer Conference, Volume 3*, pages 233–244. ASME, August 8–13, 2010.

[194] Latham, D. A., McAuley, K. B., Peppley, B. A., and Raybold, T. M. Mathematical Modeling of an Industrial Steam-Methane Reformer for On-Line Deployment. *Fuel Processing Technology*, 92(8):1574–1586, 2011.

[195] Tran, A., Aguirre, A., Crose, M., Durand, H., and Christofides, P. D. Temperature Balancing in Steam Methane Reforming Furnace via an Integrated CFD/Data-Based Optimization Approach. *Computers & Chemical Engineering*, 104:185–200, 2017.

[196] Yu, Z., Cao, E., Wang, Y., Zhou, Z., and Dai, Z. Simulation of Natural Gas Steam Reforming Furnace. *Fuel Processing Technology*, 87(8):695–704, 2006.

[197] Liesche, G. and Sundmacher, K. Identification of Key Transport Phenomena in High-Temperature Reactors: Flow and Heat Transfer Characteristics. *Industrial & Engineering Chemistry Research*, 57(46):15884–15897, 2018.

[198] Sternberg, A. and Bardow, A. Power-to-What? – Environmental Assessment of Energy Storage Systems. *Energy & Environmental Science*, 8(2):389–400, 2015.

[199] Otto, A., Grube, T., Schiebahn, S., and Stolten, D. Closing the Loop: Captured CO_2 as a Feedstock in the Chemical Industry. *Energy & Environmental Science*, 8(11): 3283–3297, 2015.

[200] Deutz, S., Bongartz, D., Heuser, B., Kätelhön, A., Schulze Langenhorst, L., Omari, A., Walters, M., Klankermayer, J., Leitner, W., Mitsos, A., Pischinger, S., and Bardow, A. Cleaner Production of Cleaner Fuels: Wind-to-Wheel – Environmental Assessment of CO_2-Based Oxymethylene Ether as a Drop-in Fuel. *Energy & Environmental Science*, 11(2):331–343, 2018.

[201] Roh, K., Frauzem, R., Nguyen, T. B., Gani, R., and Lee, J. H. A Methodology for the Sustainable Design and Implementation Strategy of CO_2 Utilization Processes. *Computers & Chemical Engineering*, 91:407–421, 2016.

[202] Papoulias, S. A. and Grossmann, I. E. A Structural Optimization Approach in Process Synthesis—III. *Computers & Chemical Engineering*, 7(6):723–734, 1983.

[203] Hartono, B., Heidebrecht, P., and Sundmacher, K. Combined Branch and Bound Method and Exergy Analysis for Energy System Design. *Industrial & Engineering Chemistry Research*, 51(44):14428–14437, 2012.

[204] Voll, A. and Marquardt, W. Reaction Network Flux Analysis: Optimization-Based Evaluation of Reaction Pathways for Biorenewables Processing. *AIChE Journal*, 58(6): 1788–1801, 2012.

[205] Martín, M. and Grossmann, I. E. Energy Optimization of Bioethanol Production via Gasification of Switchgrass. *AIChE Journal*, 57(12):3408–3428, 2011.

[206] Kim, J., Sen, S. M., and Maravelias, C. T. An Optimization-Based Assessment Framework for Biomass-to-Fuel Conversion Strategies. *Energy & Environmental Science*, 6(4):1093, 2013.

[207] Linnhoff, B. and Flower, J. R. Synthesis of Heat Exchanger Networks: I. Systematic Generation of Energy Optimal Networks. *AIChE Journal*, 24(4):633–642, 1978.

[208] Kokossis, A. C., Tsakalova, M., and Pyrgakis, K. Design of Integrated Biorefineries. *Computers & Chemical Engineering*, 81:40–56, 2015.

[209] Gençer, E. and Agrawal, R. Synthesis of Efficient Solar Thermal Power Cycles for Baseload Power Supply. *Energy Conversion and Management*, 133:486–497, 2017.

[210] Gençer, E. and Agrawal, R. Toward Supplying Food, Energy and Water Demand: Integrated Solar Desalination Process Synthesis with Power and Hydrogen Coproduction. *Resources, Conservation and Recycling*, 133:331–342, 2018.

[211] Ulonska, K., Skiborowski, M., Mitsos, A., and Viell, J. Early-Stage Evaluation of Biorefinery Processing Pathways Using Process Network Flux Analysis. *AIChE Journal*, 62(9):3096–3108, 2016.

[212] Fu, C., Vikse, M., and Gundersen, T. Challenges in Work and Heat Integration. *Chemical Engineering Transactions*, 61:601–606, 2017.

[213] Fu, C., Vikse, M., and Gundersen, T. Work and Heat Integration: An Emerging Research Area. *Energy*, 158:796–806, 2018.

[214] Huang, K. and Karimi, I. A. Work-Heat Exchanger Network Synthesis (WHENS). *Energy*, 113:1006–1017, 2016.

[215] Yu, H., Eason, J., Biegler, L. T., and Feng, X. Simultaneous Heat Integration and Techno-Economic Optimization of Organic Rankine Cycle (ORC) for Multiple Waste Heat Stream Recovery. *Energy*, 119:322–333, 2017.

[216] Kermani, M., Wallerand, A. S., Kantor, I. D., and Maréchal, F. Generic Superstructure Synthesis of Organic Rankine Cycles for Waste Heat Recovery in Industrial Processes. *Applied Energy*, 212:1203–1225, 2018.

[217] Papoulias, S. A. and Grossmann, I. E. A Structural Optimization Approach in Process Synthesis—II. *Computers & Chemical Engineering*, 7(6):707–721, 1983.

[218] Duran, M. A. and Grossmann, I. E. Simultaneous Optimization and Heat Integration of Chemical Processes. *AIChE Journal*, 32(1):123–138, 1986.

[219] Colberg, R. D. and Morari, M. Area and Capital Cost Targets for Heat Exchanger Network Synthesis with Constrained Matches and Unequal Heat Transfer Coefficient. *Computers & Chemical Engineering*, 14(1):1–22, 1990.

[220] Yee, T. F., Grossmann, I. E., and Kravanja, Z. Simultaneous Optimization Models for Heat Integration - I. Area and Energy Targeting and Modeling of Mulit-Stream Exchangers. *Computers & Chemical Engineering*, 14(10):1151–1164, 1990.

[221] Dowling, A. W. and Biegler, L. T. A Framework for Efficient Large Scale Equation-Oriented Flowsheet Optimization. *Computers & Chemical Engineering*, 72:3–20, 2015.

[222] Huang, B., Li, Y., Gao, R., Zuo, Y., Dai, Z., and Wang, F. Simultaneous Optimization and Heat Integration of the Coal-to-SNG Process with a Branched Heat Recovery Steam Cycle. *Computers & Chemical Engineering*, 117:117–128, 2018.

[223] Kong, L., Wu, Y., and Maravelias, C. T. Simultaneous Utility and Heat Exchanger Area Targeting for Integrated Process Synthesis and Heat Integration. *Industrial & Engineering Chemistry Research*, 56(41):11847–11859, 2017.

[224] Martelli, E., Elsido, C., Mian, A., and Marechal, F. MINLP Model and Two-Stage Algorithm for the Simultaneous Synthesis of Heat Exchanger Networks, Utility Systems and Heat Recovery Cycles. *Computers & Chemical Engineering*, 106:663–689, 2017.

[225] Pichardo, P. and Manousiouthakis, V. I. Infinite DimEnsionAl State-Space as a Systematic Process Intensification Tool: Energetic Intensification of Hydrogen Production. *Chemical Engineering Research and Design*, 120:372–395, 2017.

[226] Friedler, F., Tarján, K., Huang, Y. W., and Fan, L. T. Graph-Theoretic Approaches to Process Synthesis: Axioms and Theorems. *Chemical Engineering Science*, 47:1973–1988, 1992.

[227] Nagy, A. B., Adonyi, R., Halasz, L., Friedler, F., and Fan, L. T. Integrated Synthesis of Process and Heat Exchanger Networks: Algorithmic Approach. *Applied Thermal Engineering*, 21(13-14):1407–1427, 2001.

[228] Schack, D., Rihko-Struckmann, L., and Sundmacher, K. Structure Optimization of Power-to-Chemicals (P2C) Networks by Linear Programming for the Economic Utilization of Renewable Surplus Energy. In Kravanja, Z. and Miloš Bogataj, editors, *26th European Symposium on Computer Aided Process Engineering*, volume 38 of *Computer Aided Chemical Engineering*, pages 1551–1556. Elsevier, 2016.

[229] Schack, D., Rihko-Struckmann, L., and Sundmacher, K. Linear Programming Approach for Structure Optimization of Renewable-to-Chemicals (R2Chem) Production Networks. *Industrial & Engineering Chemistry Research*, 57(30):9889–9902, 2018.

[230] Liesche, G., Schack, D., Rätze, K. H. G., and Sundmacher, K. Thermodynamic Network Flow Approach for Chemical Process Synthesis. In Friedl, A., Klemeš, J., Radl, S., Varbanov, P., and Wallek, T., editors, *28th European Symposium on Computer Aided Process Engineering*, volume 43 of *Computer Aided Chemical Engineering*, pages 881–886. Elsevier, 2018.

[231] Freund, H. and Sundmacher, K. Towards a Methodology for the Systematic Analysis and Design of Efficient Chemical Processes: Part 1 - From Unit Operations to Elementary Process Functions. *Chemical Engineering and Processing: Process Intensification*, 47 (12):2051–2060, 2008.

[232] Peschel, A. *Model-Based Design of Optimal Chemical Reactors*. PhD Thesis, Otto-von-Guericke University, Magdeburg.

[233] Kaiser, N. M., Flassig, R. J., and Sundmacher, K. Reactor-Network Synthesis Via Flux Profile Analysis. *Chemical Engineering Journal*, 335:1018–1030, 2018.

[234] Liesche, G., Schack, D., and Sundmacher, K. The FluxMax Approach for Simultaneous Process Synthesis and Heat Integration: Production of Hydrogen Cyanide. *AIChE Journal*, 65(7):e16554, 2019.

[235] Cabezas, H., Argoti, A., Friedler, F., Mizsey, P., and Pimentel, J. Design and Engineering of Sustainable Process Systems and Supply Chains by the P-Graph Framework. *Environmental Progress & Sustainable Energy*, 37(2):624–636, 2018.

[236] Barrientos, M. and Soria, C. Index Mundi - Commodity Prices Indices, accessed: August 15th, 2018. URL https://www.indexmundi.com.

[237] Statista Ltd. Statista - Average US Industrial Water and Sewage Costs, accessed: August 15th, 2018. URL https://www.statista.com/.

[238] finanzen.net GmbH. CO$_2$ European Emission Allowances, accessed: August 15th, 2018. URL https://www.finanzen.net/rohstoffe/co2-emissionsrechte.

[239] Sheldon, R. A. Atom Efficiency and Catalysis in Organic Synthesis. *Pure and Applied Chemistry*, 72(7):1233–1246, 2000.

[240] Aydin, E., Bonvin, D., and Sundmacher, K. Toward Fast Dynamic Optimization: An Indirect Algorithm That Uses Parsimonious Input Parameterization. *Industrial & Engineering Chemistry Research*, 57(30):10038–10048, 2018.

[241] OpenFOAM, accessed: June 16th, 2019. URL https://openfoam.org/.

[242] Schack, D., Liesche, G., and Sundmacher, K. The FluxMax Approach: Simultaneous Flux Optimization and Heat Integration by Discretization of Thermodynamic State Space Illustrated on Methanol Synthesis Process. *Computers & Chemical Engineering*, under review, 2019.

[243] Schack, D., Liesche, G., and Sundmacher, K. Simultaneous Heat and Mass Flow Optimization of a Distillation Column Applying the FluxMax Approach. *Chemical Engineering Transactions*, 76:1–6, 2019.

[244] Perry, R. H. and Chilton, C. H. *Chemical Engineer's Handbook.* McGraw Hill, New York, 6th edition, 1984.

List of Figures

List of Tables

Publications and Statements of Authorship

Journal Publications

Liesche, G., Sundmacher, K. (2018). Identification of Key Transport Phenomena in High-Temperature Reactors: Flow and Heat Transfer Characteristics, *Industrial & Engineering Chemistry Research*, **57**, 15884-15897.
Liesche, G. developed the model, carried out the simulations and wrote the manuscript.

Liesche, G., Sundmacher, K. (2018). Productivity versus Product Quality: Exploring the Limits of Autothermal Microchannel Reactors in Methane Steam Reforming, *Chemical Engineering Journal*, DOI: 10.1016/j.cej.2018.09.209.
Liesche, G. developed the model, carried out the simulations and wrote the manuscript.

Liesche, G., Schack, D., Sundmacher, K. (2019). The FluxMax Approach for Simultaneous Process Synthesis and Heat Integration: Production of Hydrogen Cyanide, *AIChE Journal*, **65**, 7, e16554.
Schack, D. and **Liesche, G.** developed the FluxMax approach with equal contributions and the advice of Sundmacher, K. **Liesche G.** carried out the simulations for the HCN case study, analyzed the results and wrote the manuscript.

Liesche, G., Sundmacher, K. (2019). Radiation-Based Model Reduction for the Optimziation of High Temperature Tube Bundle Reactors: Synthesis of Hydrogen Cyanide, *Computers & Chemical Engineering*, accepted article.
Liesche, G. developed the model, carried out the simulations and wrote the manuscript.

Schack, D., **Liesche, G.**, Sundmacher, K. (2019). The FluxMax Approach: Simultaneous Flux Optimization and Heat Integration by Discretization of Thermodynamic State Space Illustrated on Methanol Synthesis Process, *Computers & Chemical Engineering*, under review.
Schack, D. and **Liesche, G.** developed the FluxMax approach with equal contributions and

the advice of Sundmacher, K. **Liesche G.** provided parts of the figures and methods section to the final manuscript.

Engel, S., **Liesche, G.**, Janiga, G., Sundmacher, K. (2019). Optimal Tube Bundle Arrangements in Side-fired Methane Steam Reforming Furnaces, *Energy*, under internal review. **Liesche, G.** carried out simulations with the radiation-based model, analyzed and compared data with the CFD study and wrote part of the manuscript.

Conference Proceedings

Liesche, G., Schack, D., Rätze, K., Sundmacher, K.: Thermodynamic Network Flow Approach for Chemical Process Synthesis, *Proceedings of the 28th European Symposium on Computer Aided Process Engineering (ESCAPE28)*, volume 43 of *Computer Aided Chemical Engineering*, Graz, Austria, June 10 - 13, 2018

Schack, D., **Liesche, G.**, Sundmacher, K.: Simultaneous Heat and Mass Flow Optimization of a Distillation Column Applying the FluxMax Approach, *22nd Conference on Process Integration for Energy Saving and Pollution Reduction - PRES'19*, volume 76 of *Chemical Engineering Transactions*, Agios Nikolaos, Greece, October 20 - 23, 2019

Conference Contributions

Liesche, G., Sundmacher, K.: Multiscale Modeling for High Temperature Heterogeneous Gas Phase Synthesis Reactions: HCN Synthesis, *AIChE Annual Meeting 2016*, San Francisco, USA, November 13 - 18, 2016 (Oral presentation).

Liesche, G., Sundmacher, K.: Analysis of Key Heat Transport Phenomena in a High Temperature Catalytic Reactor, *Société Francaise de Génies de Procédés (SFGP) Meeting 2017*, Nancy, France, July 11 - 13, 2017 (Oral presentation).

Liesche, G., Sundmacher, K.: Optimization of a High Temperature Catalytic Wall Reactor: Synthesis of Hydrogen Cyanide, *10th World Congress of Chemical Engineering and 27th European Symposium on Computer Aided Process Engineering*, Barcelona, Spain, October 1 - 5, 2017 (Poster presentation).

Liesche, G., Sundmacher, K.: Design of a High Temperature Catalytic Wall Reactor for Methane Steam Reforming, *25th International Conference on Chemical Reaction Engineering*, Florence, Italy, May 20 - 23, 2018 (Oral presentation).

Liesche, G., Sundmacher, K.: Conduction-Convection-Radiation Heat Transfer in High Temperature Catalytic Reactors, *5th International Conference on Fluid Flow, Heat and Mass Transfer (FFHMT'18)*, Niagara Falls, Canada, June 7 - 9, 2018 (Oral presentation - "Best Paper Award")

Liesche, G., Schack, D., Sundmacher, K.: Thermodynamic Network Flow Approach for Chemical Process Synthesis, *28th European Symposium on Computer Aided Process Engineering (ESCAPE28)*, Graz, Austria, June 10 - 13, 2018, (Oral presentation - upgraded to keynote lecture and held by K. Sundmacher)

Schack, D., **Liesche, G.**, Sundmacher, K.: Renewables-to-Chemicals: Optimaler Prozessentwurf für eine nachhaltige Methanolproduktion unter Einsatz von CO_2, *ProcessNet-Jahrestagung und 33. DECHEMA-Jahrestagung der Biotechnologen*, Aachen, Germany, September 10 - 13, 2018 (Oral presentation).

Liesche, G., Schack, D., Sundmacher, K.: Integriertes Prozessdesign und Wärmeintegration am Beispiel der Blausäuresynthese, *Jahrestreffen der ProcessNet-Fachgruppe Energieverfahrenstechnik*, Frankfurt a.M., Germany, March 6 - 7, 2019 (Oral presentation).

Schack, D., **Liesche, G.**, Sundmacher, K.: Optimaler Prozessentwurf für eine nachhaltige Methanolproduktion unter Einsatz von CO_2 und erneuerbaren Energien, *Jahrestreffen der ProcessNet-Fachgruppe Energieverfahrenstechnik*, Frankfurt a.M., Germany, March 6 - 7, 2019 (Oral presentation).

Liesche, G., Schack, D., Sundmacher, K.: Integrated Process Synthesis and Heat Integration Exemplified for Production of Hydrogen Cyanide, *Young Professionals Conference on Process Engineering*, Magdeburg, Germany, March 18 - 20, 2019 (Oral presentation).

Schack, D., **Liesche, G.**, Sundmacher, K.: Simultaneous Heat and Mass Flow Optimization of a Distillation Column Applying the FluxMax Approach, *22nd Conference on Process Integration for Energy Saving and Pollution Reduction - PRES'19*, Agios Nikolaos, Greece, October 20 - 23, 2019 (Oral presentation)

Schack, D., **Liesche, G.**, Sundmacher, K.: Optimal Process Design for a Sustainable Methanol Production Using Renewable Energies by Applying the FluxMax Approach, *AIChE Annual Meeting 2019*, Orlando, USA, November 10 - 15, 2019 (submitted).

Liesche, G., Schack, D., Sundmacher, K.: The FluxMax Approach: Integrated Process Synthesis and Heat Integration Exemplified for the Production of Hydrogen Cyanide, *AIChE Annual Meeting 2019*, Orlando, USA, November 10 - 15, 2019 (submitted).

Invited Talks

Sundmacher, K., Schack, D., **Liesche, G.**: FluxMax: Process Intensification by Network Flow Optimization in the Thermodynamic State Space, *Process Intensification Colloquium*, Dortmund, Germany, May 7 - 8, 2019.

Schriftliche Erklärung

Ich erkläre hiermit, dass ich die vorliegende Arbeit ohne unzulässige Hilfe Dritter und ohne Benutzung anderer als der angegebenen Hilfsmittel angefertigt habe. Die aus fremden Quellen direkt oder indirekt übernommenen Gedanken sind als solche kenntlich gemacht.

Insbesondere habe ich nicht die Hilfe einer kommerziellen Promotionsberatung in Anspruch genommen. Dritte haben von mir weder unmittelbar noch mittelbar geldwerte Leistungen für Arbeiten erhalten, die im Zusammenhang mit dem Inhalt der vorgelegten Dissertation stehen.

Die Arbeit wurde bisher weder im Inland noch im Ausland in gleicher oder ähnlicher Form als Dissertation eingereicht und ist als Ganzes auch noch nicht veröffentlicht.

Magdeburg, den 21. Juni 2019

Georg Liesche